**The Dissertation Committee for Dongwen Gan Certifies that this is the approved version of the following dissertation :**

# Thermal Stress and Stress Relaxation in Copper Metallization for ULSI Interconnects

**Committee:**

Paul S. Ho, Supervisor

Llewellyn K. Rabenberg

Li Shi

Eric Taleff

Jiehua Zhao

# THERMAL STRESS AND STRESS RELAXATION IN COPPER METALLIZATION FOR ULSI INTERCONNECTS

**by**

**Dongwen Gan, B.S., M.S.**

**Dissertation**

Presented to the Faculty of the Graduate School of

The University of Texas at Austin

in Partial Fulfillment

of the Requirements

for the Degree of

**Doctor of Philosophy**

**The University of Texas at Austin**

**December 2005**

## Dedication

To my family

## Acknowledgements

I would like to thank all the people who were contributory for me to complete this dissertation. First of all, I wish to express my special gratitude to Prof. Paul Ho for his guidance and financial support during my graduate study. His valuable remarks and questions inspired me to identify problems and explore solutions. In addition, I want to acknowledge other committee members, Prof. Llewellyn K. Rabenberg, Prof. Li Shi, Prof. Eric Taleff, and Dr. Jiehua Zhao for taking time to review my dissertation. Special thanks go to Dr. Rabenberg for his valuable inputs.

Special appreciation is extended to Dr. Rui Huang for his helpful discussions. The creep model he developed is included in this dissertation and used to evaluate interfacial diffusivity. I would like to thank Dr. Jihperng Leu for his great effort to provide most of the samples. I am indebted to my friend, Dr. Yi Zheng for proofreading the manuscript and suggesting the correction of numerous errors.

I would like to express my appreciation to Dr. Yong Du and the folks in the Laboratory for interconnect and Packaging for their help and team work. Some of them are Dr. Ennis Ogawa, Dr. Chuan Hu, Dr. Guotao Wang, Junjun Liu, Xia Lu, Bin Li, Ming Ding, Soo Young Choi, Swarnal Borthakur, Meike Hauschildt, Scott Smith, Won-

Chong Beak, JungWoo Pyun, Xuefeng Zhang, Zhiquan Luo, Junjing Bao, Kuan-Hsun Lu, Huang-Lin Chao. Special thanks also go to Jo Ann, who is always warmhearted and has provided numerous helps in the past several years.

Finally, I would like to thank my wife Ye and our families for their love, encouragement and support. Our sons, Lawrence and Ryan have provided me lots of pleasure.

# Thermal Stress and Stress Relaxation in Copper Metallization for ULSI Interconnects

Publication No._____

Dongwen Gan, Ph.D.

The University of Texas at Austin, 2005

Supervisor: Paul S. Ho

Thermal stress and mass transport are key issues for Cu metallization yield and reliability. In this study, thermal stresses in Cu films, and line structures with three types of inter-level dielectric (ILD), SiOF, CDO (carbon doped oxide) and SiLK™, and the linewidths of 0.2μm and 0.4μm, were investigated using a bending beam technique, X-ray diffraction (XRD) and finite element analysis (FEA). During thermal cycling, plastic yield was found to play an important role for the plastic deformation of Cu films. The deformation was strongly affected by the presence of impurities in the films. The stress in Cu lines was found dependent on annealing and the properties of the ILD, but not sensitive to the change of linewidth in submicron range. FEA results indicated that the stresses in the ILD's as a function of Cu linewidth were quite different in the interconnects.

Stress-induced void formation was studied in passivated Cu films during thermal cycling and isothermal annealing. The void density was strongly affected by the ramp rate, film stress and thermal history during thermal cycling. A kinetic model was developed for the void growth, and an activation energy of 0.75eV was deduced. The local stress gradients due to the mechanical anisotropy, and in the void vicinity were evaluated by FEA models.

In order to characterize the Cu/passivation interface diffusivity, isothermal stress relaxations of Cu films and line structures were studied. The isothermal stress relaxation behaviors were shown significantly different for the films with different passivation layers, $SiN_x$, SiC, modified SiC and a metal cap layer. Diffusional kinetic models were developed for the stress relaxation in thin films and then combined with experimental results to deduce the interfacial diffusivities, which were found to be much smaller than the grain boundary diffusivity. In the line structures with different ILD's, the effects of the passivation layers were found to be consistent with the results of the Cu films. The mechanical confinement of the passivation layers on the stress in the Cu lines was evaluated using FEA models. Results from this study demonstrate that stress relaxation measurement is an effective method to evaluate electromigration (EM) performance in Cu metallization.

# Table of Contents

# List of Tables

# List of Figures

# Chapter 1 Introduction

## 1.1 THERMAL STRESS AND ELECTROMIGRATION IN INTERCONNECTS

Millions of active devices are built on a single chip to form modern ultra large scale integrated (ULSI) circuits. A three dimensional network of metal wires insulated by dielectrics provides necessary interconnections for these devices to function in concert. Al alloyed with a small amount of Cu has been used as the conductor in interconnects for decades, since Al has a low resistance and is easy to process. Cu is added to improve the electromigration performance. The dielectric in which the Al lines are embedded has traditionally been silicon oxide, formed by Chemical Vapor Deposition (CVD) with various silicon containing precursors.

Along with the shrinkage of devices for better performance and cost reduction, an increase in interconnect density and decrease in metal line dimension occur, resulting in an increase of the wiring resistance. Consequently, the interconnect RC delay, *i.e.*, the product of the wire resistance and the dielectric capacitance, becomes the bottleneck of the ULSI circuit speed at the 0.13μm technology node and below [1.1]. To address this issue and enable the microelectronic industry to continuously follow "Moore's Law", which predicts that the number of components per integrated circuits (IC) doubles every 18 months [1.2], the parasitic resistance and capacitance associated with the interconnect system need to be reduced.

The Cu/low-k (low dielectric constant) system has been introduced to replace the Al/TEOS interconnect system because the Cu resistivity is about 40% lower. However,

low resistance metal lines are not sufficient for future interconnect requirements. With the introduction of multi-level metallization, where different levels of interconnects are separated by the dielectric and contacted by vertical vias, the interconnect RC delay could be further reduced by keeping the line dimension and reducing the total length of the metal lines. Figure 1.1 is the cross-section of an IBM multi-level interconnect structure.

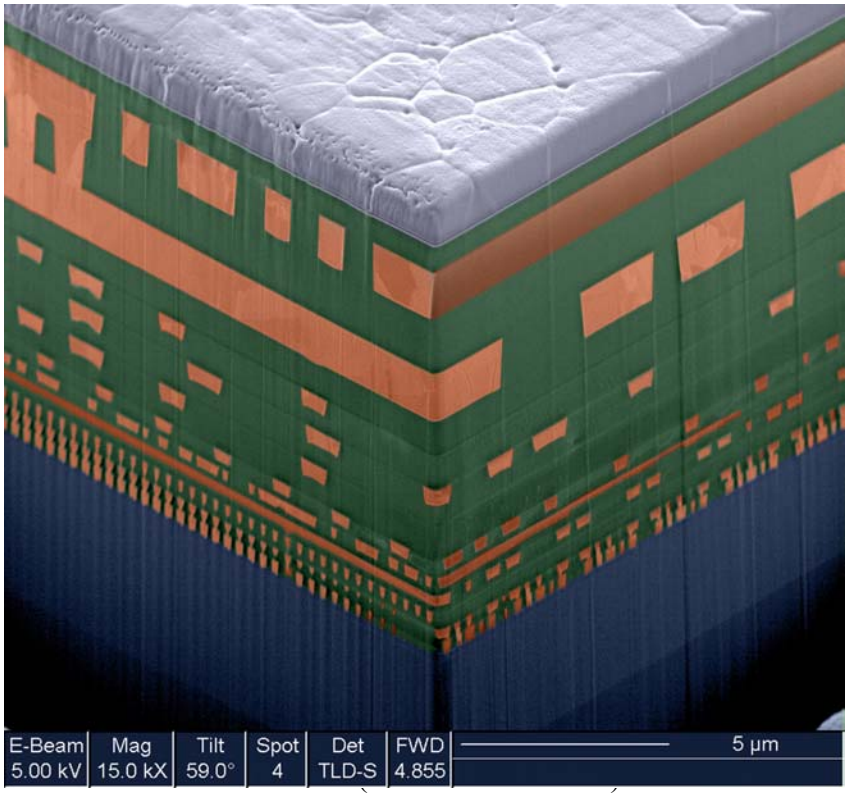


Figure 1.1 Cross-section of a 64-bit high-performance microprocessor chip built in IBM's 90 nm Server-Class CMOS technology with Cu/low-k wiring. Above the transistors, the wiring levels include one W local interconnect, five "1x-scaled" Cu levels in full SiCOH low-k dielectric, three "2x-scaled" Cu/SiCOH levels, two "6x-scaled" Cu levels in FTEOS/SiO2 dielectric, and finally, one Al(Cu) terminal pad and wiring level. The minimum M1 Cu line widths and spaces are 0.12 um. (http://www-03.ibm.com/chips/technology/makechip/breakthroughs/lowk.html, 2005)

While the Cu/low-k interconnect is expected to provide remarkable improvement on the performance of IC's, new reliability and yield issues arise since the conversion from Al to Cu metallization induces many new materials and processes into the manufacturing. The traditionally subtractive dry etching of copper is not practical because of the lack of volatile copper components at room temperature [1.3], and wet etching is impossible for patterning sub-micron trenches due to its isotropic nature. Moreover, unlike the strong, imperious Al oxide layer that can provide self-passivation and suppress surface diffusion, Cu is readily oxidized in air and forms a weak and easily penetrated oxide layer that has no passivation effects. Furthermore, Cu diffuses very fast in dielectrics and Si substrates and causes devices failure. Consequently, Cu interconnects are built using the damascene and dual-damascene processes. Cu lines are encapsulated by a diffusion barrier on the bottom and sidewalls, and a passivation layer on the top. In addition, electroplating at room temperature is chosen to fill Cu into trenches, compared to physical vapor deposition (PVD) of Al. Generally, the Cu overburden and the extract barrier are removed by the chemical mechanical polishing (CMP) process.

While it is quite straightforward to replace Al with Cu as the conductor, the choice of the low-k material to replace TEOS as the dielectric is not easy. In addition to SiOF, CDO and SiLK™ that have so far been integrated into chips, a wide range of low-k candidates have been evaluated in the laboratory for Interconnect and Packaging at the University of Texas at Austin, including polyimide, hydrogen silsesquioxane (HSQ), JSR, methylsilsesquioxane (MSQ), "Black Diamond" and their modified versions etc.

Eventually, micro-pores or air gaps are expected to be introduced to form ultra-low-k materials.

Table 1.1 Isotropic mechanical properties of the related materials at 25°C [1.4-5]

| Material | E (GPa) | $\nu$ | $\sigma_y$ (MPa) | $\alpha$ (ppm/°C) |
|---|---|---|---|---|
| Aluminum | 69 | 0.345 | 150 | 24.0 |
| Copper | 117 | 0.343 | 250 | 17.7 |
| Silicon | 130.2 | 0.28 | - | 2.14 |
| TEOS | 71.7 | 0.16 | - | 0.94 |
| SiLK | 2 | 0.35 | - | 66.0 |
| Black Diamond | 5.6 | 0.3 | - | 20.0 |
| Ta | 185.0 | 0.34 | - | 6.5 |
| W | 411.0 | 0.28 | - | 4.5 |

Mechanical and electrical reliabilities are the major concerns in interconnects. One cause of mechanical failure is the thermal stress induced by the thermal expansion mismatch between the metal lines and the surrounding materials. Isotropic properties of several materials used in interconnects are listed in Table 1.1. Since process temperature can go up to 400°C during annealing and the deposition of dielectrics, the thermal stress in the metal lines can reach a level of hundreds of MPa. The generation of such large compressive stress may lead to the formation of hillocks or increase the driving force for metal out-diffusion through the barrier. On the other hand, the high tensile stress could cause void formation, a major reliability concern in metal lines. Extensive efforts have been made to study the void formation in Al interconnects [1.6-17], and hydrostatic stress is believed to be the driving force for the void formation. Since Cu has a much higher melting point, stress induced void formation was initially expected to be less problematic in Cu metallization. However, the changes of material properties and processes in Cu

interconnects make the mechanism of void formation in Cu lines distinct from that of Al lines; that is, Cu does not have better resistance for voiding. For example, electroplated Cu has very small initial grain size. As grains grow, atomic vacancies form due to the annihilation of grain boundaries and these vacancies can enhance the void formation in Cu interconnects [1.18]. Cu crystals are mechanically anisotropic, and their anisotropy can result in the local stress concentrations and local stress gradients at the boundary between grains with different orientations. Furthermore, interfacial diffusion in Cu metallization plays an important role in the stress-induced void formation. Stress induced void formation has been observed during thermal cycling and isothermal annealing in both Cu films and Cu interconnects [1.18-22]. In addition, since the low-k materials have intrinsically poor adhesion to other materials and are much softer than silicon oxide, thermal stress can more easily cause interface delamination and cracking in Cu/low-k interconnects.

All these issues make it critical to understand the thermal stress in Cu metallization. Many studies have been carried out to investigate the thermal stress evolution mainly in sputter and e-beam Cu films [1.23-28]. A number of factors were found to affect the thermal stress development in Cu films during thermal cycling, including the passivation layer, the film thickness and the microstructure of the film [1.29-31]. Even the presence of a small concentration of alloying element can play an important role [1.32]. Moreover, the surface condition associated with the oxygen exposure is a key factor affecting the yield behavior of Cu films [1.33-1.34].

Various models have been proposed to understand the deformation of Cu films during thermal cycling. Thouless *et al*. [1.24] used the deformation mechanism maps and proposed that the dominant deformation mechanism of Cu films shifts among plasticity, diffusional flow, power-law creep and power-law breakdown during thermal cycling from room-temperature (RT) to 450°C. On the other hand, Keller *et al*. [1.27] believed that power-law creep was the dominant deformation mechanism and the diffusional creep was completely inactive during thermal cycling. More recently, Weiss *et al*. [1.28] suggested that constraints from the substrate limited the grain-boundary diffusion and thus the stress would not relax to zero at high temperature. Although some of the models seams to agree with the experimental data, a comprehensive understanding is still lacking. This leads to disagreements in identifying the dominant deformation mechanism of Cu films during thermal cycling.

Compared to Cu films, quite limited information on the thermal stress measurement of Cu line structure exists [1.35-38]. Differences between Cu films and Cu wires are obvious. The thickness of a Cu film can be quite small, but its in-plane dimension is relatively large, resulting in a bi-axial stress state. In a Cu line, a tri-axial stress state is expected since the sidewalls of the line are confined by the diffusion barrier and the IMD (inter-metal-dielectric). Furthermore, the shrinkage of the dimensions from those of a Cu film is also expected to cause different plastic deformation behaviors in Cu lines. These factors imply that the thermal stress behavior of Cu films might not be suitable for analysis of the stress-related failure mechanism in Cu interconnects. It is important to directly evaluate the thermal stress in Cu line structure. The thermal stress

behavior of Cu/low k damascene line structures has been measured using x-ray diffraction methods [1.35-36]. The barrier and the cap layer were found to play an important role in confining thermal deformation of Cu lines, resulting in a stress state distinctly different from that of AlCu/low k lines not embedded in the damascene structure [1.38].

These studies raise two basic questions concerning thermal stress behavior of Cu/low k damascene structures. First, what is the effect of the dielectric material, particularly when the linewidth is reduced below 0.25μm? The second question concerns the deformation and stress characteristics of the low-k ILD. The stress behavior of the ILD in the confined sub-micron geometry of the damascene structure is also expected to be quite different from that measured on blanket films or large pad structures. So far there exists little such information to evaluate the structural reliability of the low k material.

Electromigration (EM) is another major reliability concern in interconnects and many studies have been carried out, both in Al and Cu metallizations [1.39-54]. EM is the phenomenon of the net diffusion of atoms in the direction of the electron flow caused by the momentum exchange due to collision between the conducting electrons and the atom. As a result, the depletion of atoms may cause the void formation at the cathode and the accumulation of atoms may result in the formation of metal extrusion at the anode, causing an open circuit or an electrical short. During this process, the net atom flux is given by [1.47]

$$J = \frac{D_{eff} C}{kT}(Z^* e\rho j - \Omega d\sigma / dx) \tag{1.1}$$

where $C$ is the concentration of the atoms, $k$ the Boltzmann constant, $T$ the temperature, $Z^*$ the effective charge number, $e$ the fundamental electronic charge, $\rho$ the reisitivity, $j$ the current density, and $\Omega$ is the atomic volume. $Z^* e\rho j$ represents the driving force from the electron wind and $\Omega d\sigma / dx$ represents that from the stress gradient built up due to the depletion and accumulation of atoms at the two ends of the line, respectively. $D_{eff}$ is the effective diffusivity, which depends on the diffusion mechanism and is given by [1.47]

$$D_{eff} = D_b + \sum D_{gb.j}(\delta_{gb.j}) + D_i[2\delta_i(1/w + 1/h)] + D_p \rho_{disl} d^2 \tag{1.2}$$

where $D_b$ , $D_{gb}\delta_{gb}$ , $D_i\delta_i$ and $D_p \rho_{disl} d^2$ are the lattice, grain boundary, interface and dislocation diffusivities, respectively. In Al(Cu) interconnects, the dominant diffusion path is the grain boundary. Thus, Al(Cu) lines with the bamboo-like grain structure have a higher resistance for electromigration. For Cu lines, previous works have shown that the activation energy values for electromigration failure of Cu interconnects are lower than those for grain boundary diffusion [1.55]. Although the barrier material was found to affect the electromigration performance of Cu interconnect due to the diffusion through barrier/Cu interface [1.56-57], the cap/Cu interface was shown to be the dominant diffusion path for electromigration, partially due to defects and contaminations induced by the CMP process [1.58-59]. Therefore, a longer EM lifetime of Cu interconnects can be achieved by improving the quality of the Cu/passivation interface, i.e. decreasing the interfacial diffusivity. Recently, Lane *et al.* [1.60] showed that EM lifetime of Cu

interconnects can indeed be improved by optimizing the interfacial bond using different cap layers and cleaning processes, and their results were supported by a correlation between EM lifetime and interfacial adhesion. This was corroborated by Hu et al. [1.61] who demonstrated a significant improvement in EM lifetime by coating the Cu surface with a thin (20-30nm) metal layer. Thus, evaluation of the diffusion is important for fundamental study of EM behavior and for process development to improve reliability in Cu interconnects. However, so far there have been no reports of effective methods to measure the Cu/passivation interface diffusivity.

## 1.2 SCOPE OF THE DISSERTATION

This dissertation includes studies of thermal stress in Cu films and line structures, stress-induced void formation in Cu films, and stress relaxation and mass transport in Cu metallization. The methods for stress measurement and evaluation, including the bending beam technique, X-ray diffraction and finite element analysis (FEA) are reviewed in chapter 2. The thermal stress of both passivated and unpassivated Cu films during thermal cycling was investigated in chapter 3, where the discussion focused on the deformation mechanisms and the effect of the impurities in Cu films. Chapter 4 focuses on the thermal stress in Cu line structures, including the effects of annealing, ILD and linewidth. Three types of ILD, SiOF, CDO and SiLK™, and two sets of line widths, 0.2 and 0.4μm, were employed in this study with the stress measured by XRD. A three-dimensional FEA model is developed and verified by the experimental results, and then used to evaluate the stress in the dielectric that cannot be measured directly. As one of the

major reliability issues, the stress-induced void formation upon thermal cycling and in isothermal annealing in passivated Cu films is systematically studied in chapter 5. Optical microscopy was used to observe *in-situ* void formation during thermal cycling and to determine the void density while the void size was measured using a SEM. A kinetic model is developed for the void growth and the activation energy is deduced. In addition, FEA is used to analyze the local tri-axial stress states and stress gradients in Cu metallization that are believed to be the important factors for the void formation. Much effort has been made in chapter 6 to study stress relaxation and mass transport in Cu metallization. Both Cu films and Cu line structures passivated with SiN, SiC, modified SiC and Co-based metal layers were used to evaluate the effect of passivation on the stress relaxation, and the Cu/passivation interface diffusivity. Both XRD and the bending beam method were used for stress measurement that reveals the (i) a negligible difference in thermal stress during thermal cycling but (ii) significant differences in isothermal stress relaxation for samples with different passivation layers. The stress relaxation rate was found to correlate well to the EM lifetime of interconnects with the same passivation layer. Interfacial diffusivities can be determined by combining the experimental results with the kinetic models developed by coupling the diffusion through the grain boundaries and the Cu/passivation interface. FEA models are set up to evaluate the effect of the mechanical confinement from the passivation on the stress, and the effective modulus of the line structures. Finally, chapter 7 presents a summary and some suggestions for future work.

# Chapter 2 Methods for Stress Evaluation

In this study, thermal stresses in thin films and line structures were characterized using a combination of the bending beam (BB) technique, X-ray diffraction (XRD) and finite element analysis (FEA). The BB technique is a type of substrate curvature measurement that determines the averaged in-plane stress in thin films or thin interconnect layers from the overall bending of the substrate, while XRD gives the principle stresses in selected grains of the crystal films or lines from direct lattice constant measurement. In contrast to BB or XRD, FEA can be used not only to evaluate the averaged stress but also to reveal the local stress distributions, providing an effective approach to investigate the metallization failure mechanisms related to stress concentration or stress migration driven by local stress gradients. The principles and details of these methods are reviewed in this chapter.

## 2.1 BENDING BEAM TECHNIQUE

### 2.1.1 Stoney's equation and the system set up

Stress can be induced in a film on a Si substrate by several reasons, such as the mismatch of the lattice spacing or thermal expansion. The film in turn applies a force on the substrate that results in the bending of the substrate. This enables film stress to be determined by measuring the curvature of the substrate. Quantitatively, the correlation is well known as Stoney's equation [2.1],

$$\sigma = \frac{E_s t_s^2}{6 t_f R} \tag{1}$$

where σ is the film stress, $E$ Young's modulus, t the thickness, R the radius of the curvature while the subscript "*s*" indicates the substrate and "*f*" the film. The sign of the stress is determined by the sign of 1/R; thus tension and compression of the film bend the substrate forward and backward to the film, respectively. Since equation 1 is derived from beam theory, it must be modified for film/substrate bi-layer structure using the plate theory [2.2]. As a result, Stoney's equation becomes

$$\sigma = \frac{E_s t_s^2}{6(1-\nu_s)t_f R} \tag{2}$$

where $v$ is Poisson's ratio and the biaxial modulus $E_s/(1-\nu_s)$ of the substrate replaces Young's modulus used in equation 1. It should be noted that the above two equations are based on the assumption that the unstressed substrate is perfectly flat. If that assumption is not true, the film stress should be corrected by subtracting the initial curvature $(1/R_0)$ from the measured curvature $(1/R)$, which yields the form of Stoney's equation used in this study

$$\sigma = \frac{E_s t_s^2}{6(1-\nu_s)t_f}\left(\frac{1}{R} - \frac{1}{R_0}\right) \tag{3}$$

This equation is subject to several restrictions. For example, it applies only when the film is much thinner than the substrate and both are elastically isotropic. If the film or the layer on the substrate is elastically anisotropic, such as the interconnect layer with different mechanical response along and across the line directions, Stoney's equation is further modified as [2.3-2.5]

$$\sigma_{\parallel} = \frac{E_s t_s^2}{6(1-\nu_s^2)t_f}\left(\frac{1}{R_{\parallel}} + \nu_s \frac{1}{R_{\perp}}\right) \tag{4a}$$

$$\sigma_{\perp} = \frac{E_s t_s^2}{6(1-\nu_s^2)t_f}\left(\frac{1}{R_{\perp}} + \nu_s \frac{1}{R_{\parallel}}\right) \tag{4b}$$

where $\sigma_{\parallel}$ and $\sigma_{\perp}$ are respectively the stresses along and across the line direction with the correlated radii of curvature $R_{\parallel}$ and $R_{\perp}$. Other parameters have the same meanings as in equation 2. This equation indicates that curvature changes in both directions need to be measured to determine the correct stresses of anisotropic layers.

It should be noted that the above equations do not include any physical constants of the film except its thickness. All other terms are properties of the substrate, all well known for silicon. Therefore, the curvature measurement based on the above equations is a simple yet powerful method to study the mechanical behavior of thin films.

However, the stress induced curvature change is generally very small. To correctly measure it, a bending beam system using an optic lever was set up in our lab. It converts changes in the curvature of a substrate to amplified movements of laser beams and thus makes the measurements feasible. Figure 1 shows the schematic set up of the bending beam system. A laser beam from a He-Ne laser source is split into four beams by a set of cube beam splitters. A mirror is used to reflect the beams into a vacuum chamber, where they are reflected out by the sample surface and finally reach the position sensors. The coordinate values of each laser spot on the sensor coordinator are calculated and shown by the UDT™ position indicator and recorded by a personal computer. The time and the temperature of the chamber are also recorded during experiments.

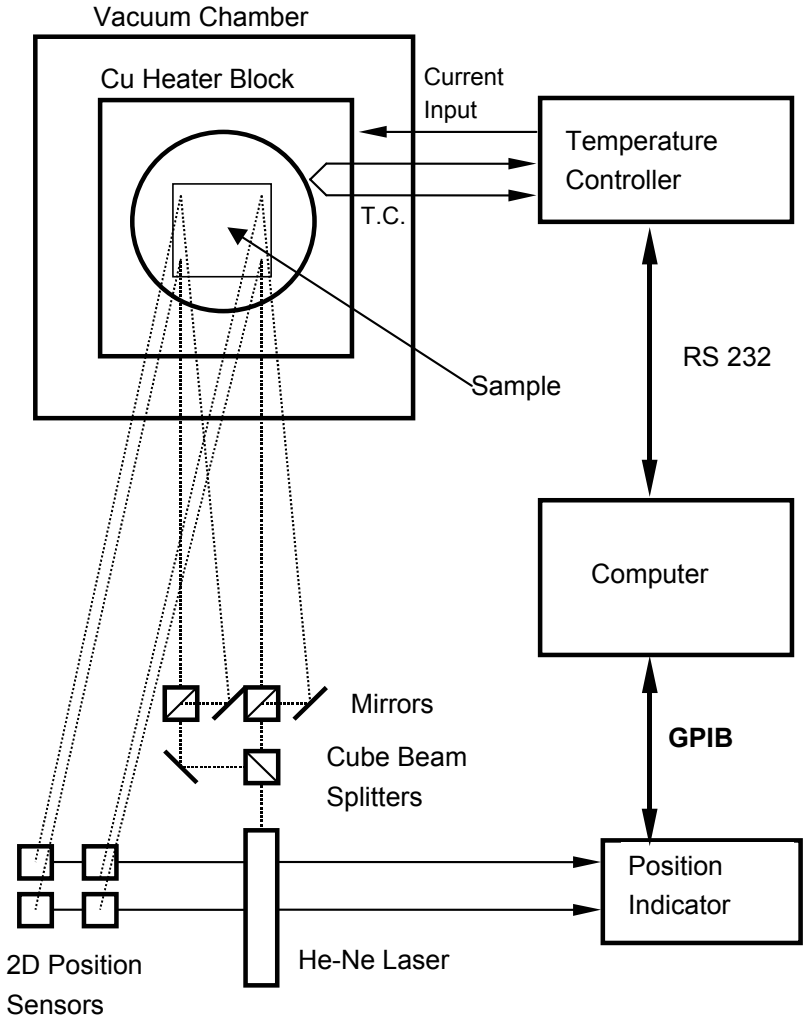


Figure 2.1 Experimental setup of the bending beam system

### 2.1.2 The thermal and long term stability of the BB system

Since the BB system is set up to measure thermal stresses under thermal cycling and isothermal thermal stress relaxations in thin films and line structures, the thermal stability and temporal stability of the BB system are critical. Figure 2 shows the experimental data of a low-dielectric-constant (low-k) thin film deposited on a 720μm thick Si substrate upon heating up with a ramp rate of 2°C/min. The x-axis is the temperature of the chamber, and the y-axis the position of the laser spot on the sensor coordinate that changes during thermal cycling with the curvature change of the substrate. The initial data showed large scatter that became worse at higher temperature. Careful examination revealed that the scatter was caused by vibration of the laser beams due to the formation of an unstable hot air layer on the surface of the top-viewer where the laser beams pass in and out of the chamber. The problem was solved by introducing a stable air flux above the surface to remove the hot air layer. As shown in Fig.3, the data spread became much tighter.

The temporal stability of the BB system was evaluated with a bare Si beam in the chamber at room temperature for a relatively long period. Assuming the curvature of the bare Si remains constant, we expect no movement of the laser spot on the sensor. A poorly aligned system shows significant laser movement over a period of 50 hours, as shown in Fig. 4, indicating some long-term instability in the system. For a 1 μm thick film on a 750μm thick Si substrate, the instability induced stress error could be as large as 40MPa. By comparing the position of the laser spot in Fig.4 with the room temperature recorded in Fig.6 during the test, the instability of the BB system was found to be caused

by variations of ambient temperature, which caused the tilting of the laser source and the thermal expansion or shrinkage of optical components. That the significant variation is observed from a variation of only 1°C of the ambient temperature indicates the high sensitivity of the system. Since controlling room temperature fluctuation to below 1°C is not practical in our lab, we developed a partial solution by changing alignment of the mounting of the laser source and the optic components. As shown in Fig.7 and Fig.8, the movement of the laser spots per degree C change of the ambient temperature was greatly reduced after the system was aligned. Since the bending of a rigid beam is proportional to the inverse of the square of the beam thickness, the signal to noise ratios of the BB system can be further improved by thinning down the substrate. As a result shown in Fig. 9, for a 1 μm thick film deposited on a 300μm thick Si substrate, the correlated stress error due to the instability of the system shown in Fig.7 was reduced to about 1MPa. This enables the BB system to perform the accurate and stable long-term stress relaxation measurements on thin films and line structures.

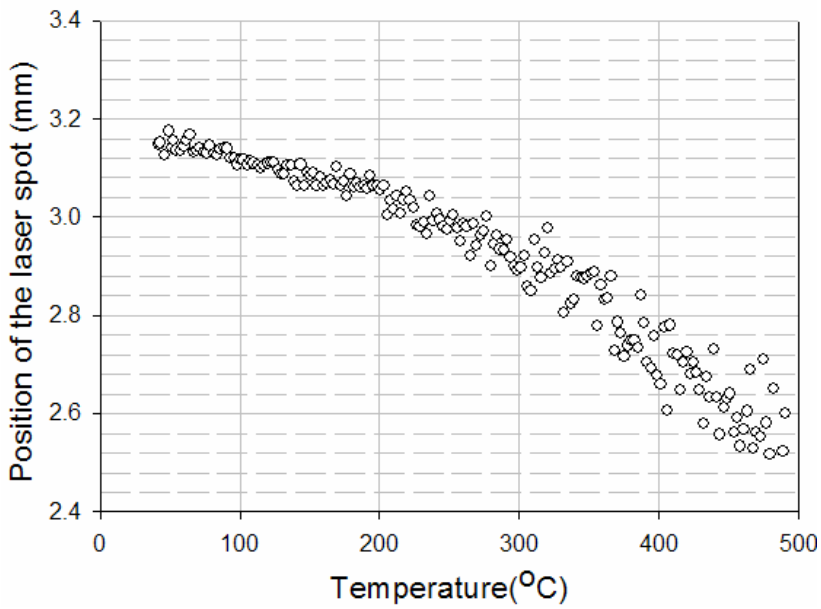


Figure 2.2 Experimental data showing that scatter increases with temperature.

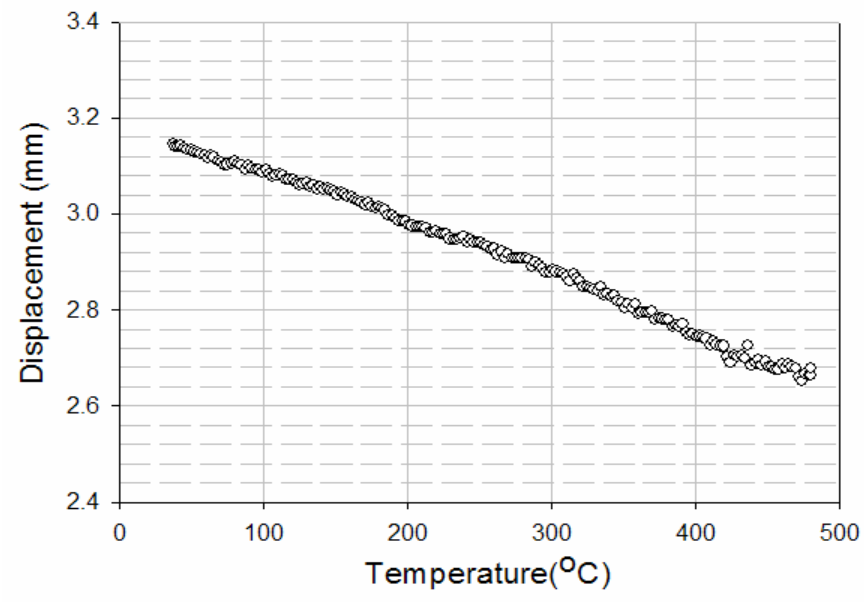


Figure 2.3 Experimental data showing that scatter was reduced using an air flux to prevent the formation of a hot air layer on the chamber surface.

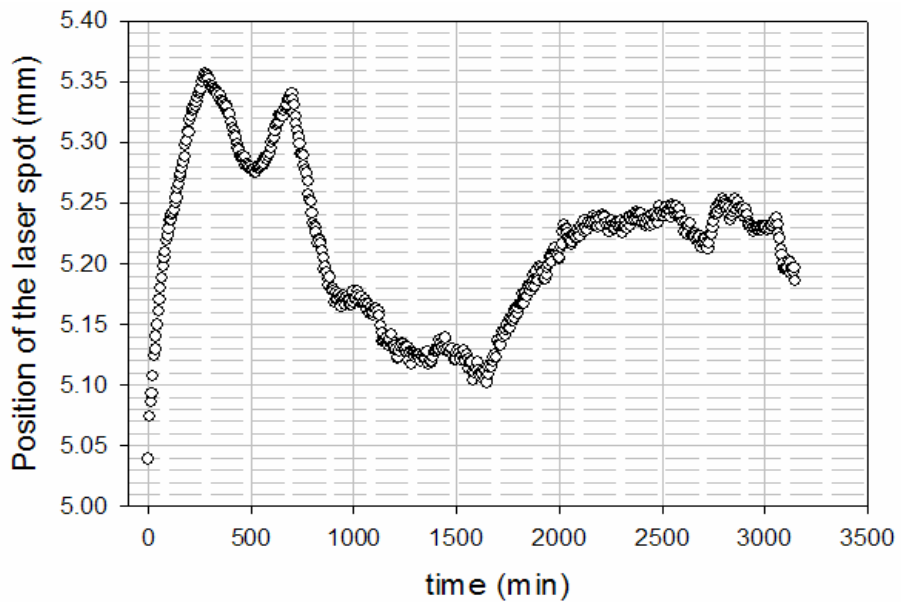


Figure 2.4 A test of the long-term stability of the BB system at room temperature using a bare Si beam

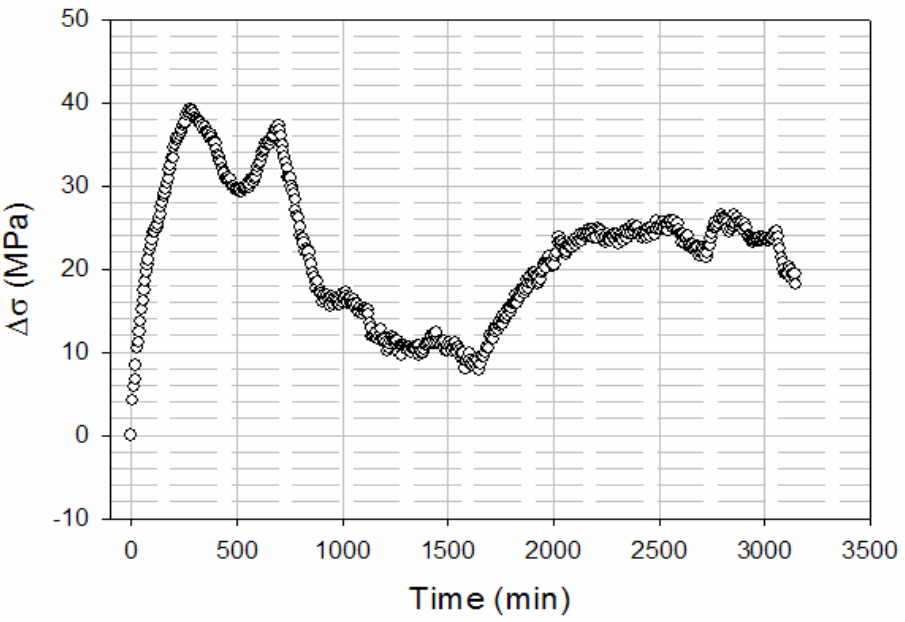


Figure 2.5 Correlated stress error due to the instability of the BB system for a 1μm thick thin film deposited on a 750μm thick Si substrate

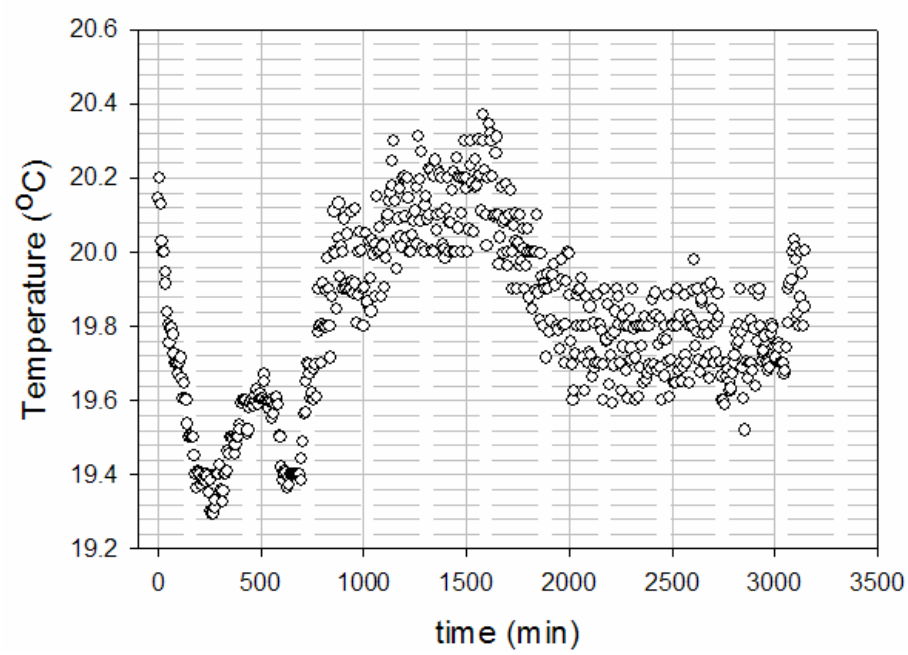


Figure 2.6 Measured ambient temperature during the test of the long-term stability of the BB system

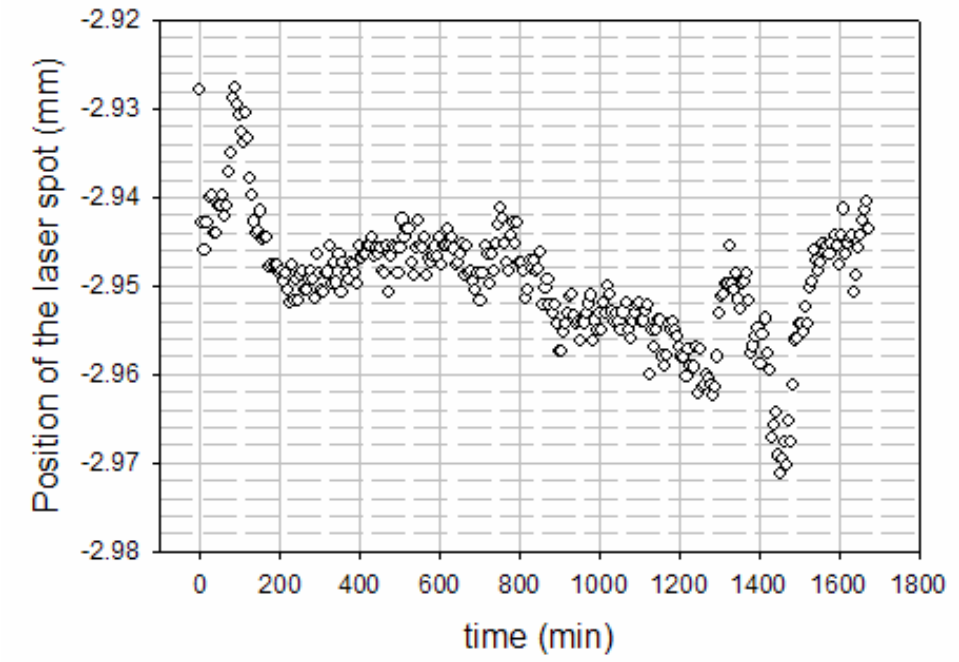


Figure 2.7 A test of the long-term stability of the BB system at room temperature using a bare Si beam after the system alignment

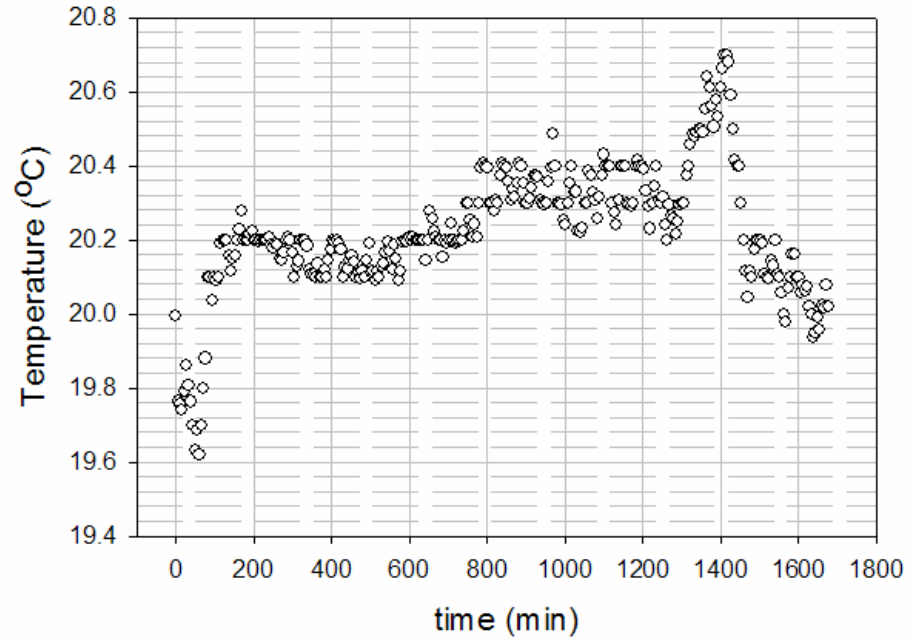


Figure 2.8 Measured ambient temperature during the test of the long-term stability of the BB system after the system alignment

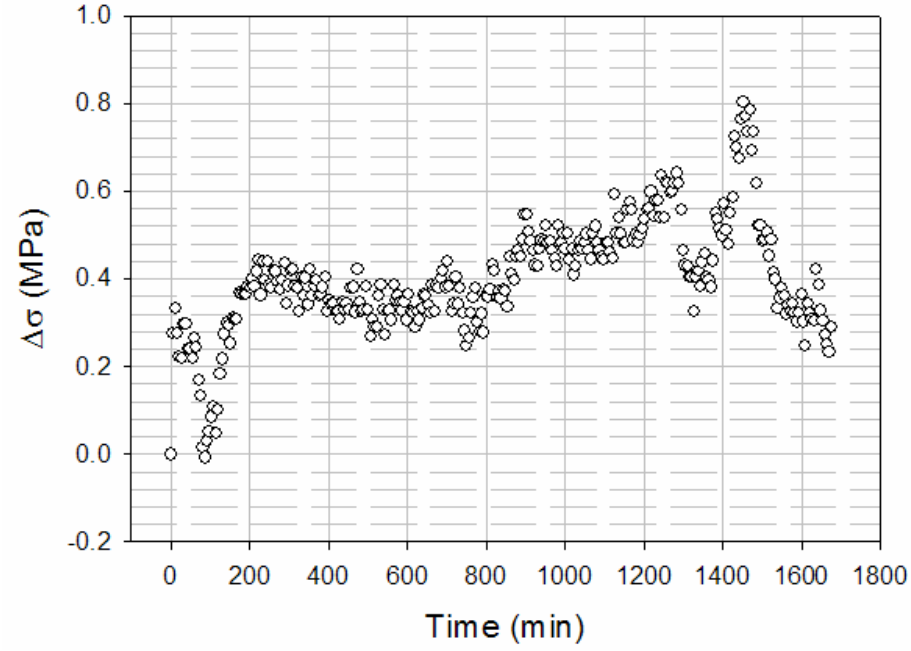


Figure 2.9 Correlated stress error due to the instability of the BB system for a 1μm thick thin film deposited on a 300μm thick Si substrate

## 2.2 X-RAY DIFFRATION FOR STRESS MEASUREMENT

XRD determines the strain in a crystal by measuring the change of the lattice spacing based on Bragg's law,

$$2d\sin\theta = \lambda, \tag{5}$$

where $d$ is the inter-planar spacing, $\theta$ is half of the angle between the incident and diffracted x-ray beams and λ is the wavelength of the x-ray. For a cubic lattice structure, such as Cu, $d$ can be calculated by:

$$d = \frac{a}{\sqrt{h^2 + k^2 + l^2}} \tag{6}$$

where $h$, $k$ and $l$ are the indices of the crystal plane while $a$ is the lattice constant. If the unstressed lattice parameter $a_0$ is known, the strain along a [hkl] direction can be determined by:

$$\varepsilon_{hkl} = \frac{a - a_o}{a_0} = \frac{d - d_o}{d_0} \tag{7}$$

In Cu interconnects, the Cu lines are generally encapsulated by several materials such as inter-level dielectrics (ILD), inter-metal dielectrics (IMD), a diffusion barrier and a passivation layer, resulting in a tri-axial stress state within the Cu lines. Fig.10 shows sample coordinate where x, y and z directions are along, across and normal to the lines, respectively. In order to determine the principle stresses, $\sigma_x$, $\sigma_y$ and $\sigma_z$, of the Cu lines, we need to measure the principle strains, $\varepsilon_x$, $\varepsilon_y$ and $\varepsilon_z$. However, $\varepsilon_y$ and $\varepsilon_z$ cannot be measured directly due to the limitation of the XRD system, but they can be deduced through the following steps.

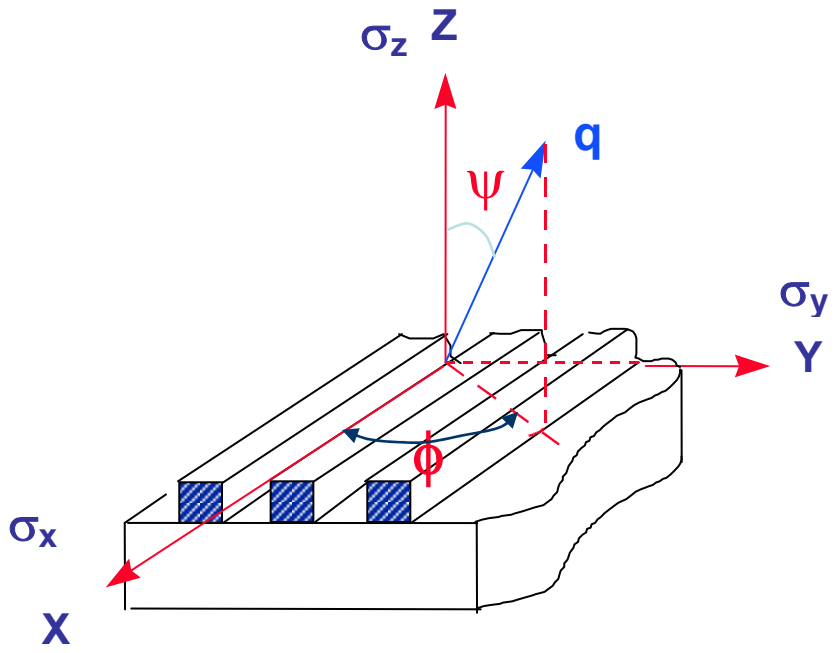


Figure 2.10 Definition of the sample coordinate system

A general strain matrix **[$\varepsilon_{ij}$]** in the sample coordinates can be converted to the lab coordinate related to the sample coordinates by Euler angles $\phi$ and ψ, such that the strain along q is given by

$$\varepsilon_{\phi\psi} = \varepsilon_x \cos^2\phi \sin^2\psi + \varepsilon_{xy} \sin 2\phi \sin^2\psi + \varepsilon_y \sin^2\phi \sin^2\psi + \varepsilon_z \cos^2\psi + \varepsilon_{xz} \cos\phi \sin 2\psi + \varepsilon_{yz} \sin\phi \sin 2\psi \quad (8)$$

The principle stresses of the Cu lines are parallel to the sample coordinate axes and the shear components are zero. Then equation 8 is reduced to

$$\varepsilon_{\psi\phi} = \varepsilon_x \cos^2\phi \sin^2\psi + \varepsilon_y \sin^2\phi \sin^2\psi + \varepsilon_z \cos^2\psi \quad (9)$$

which shows a linear relationship between $\varepsilon_{\psi\phi}$ and $\sin^2\psi$. This relationship is the basis for the XRD stress measurement and also the criterion for the system alignment that is discussed later. By setting $\phi = 0°$ (along the line) and 90° (across the line), equation 8 is further reduced to

$$\varepsilon_{\psi,0} = (\varepsilon_x - \varepsilon_z)\sin^2\psi + \varepsilon_z \tag{10}$$

$$\varepsilon_{\psi,90} = (\varepsilon_y - \varepsilon_z)\sin^2\psi + \varepsilon_z \tag{11}$$

respectively.

Thus, the principle strains of the Cu lines, $\varepsilon_x$, $\varepsilon_y$ and $\varepsilon_z$ can be determined by measuring $\varepsilon_{\psi_1,0}$, $\varepsilon_{\psi_2,0}$ and $\varepsilon_{\psi_2,90}$. They are

$$\varepsilon_x = \frac{\varepsilon_{\psi_1,0}\cos^2\psi_2 - \varepsilon_{\psi_2,0}\cos^2\psi_1}{\sin^2\psi_1\cos^2\psi_2 - \sin^2\psi_2\cos^2\psi_1} \tag{12}$$

$$\varepsilon_z = \frac{\varepsilon_{\psi_1,0}\sin^2\psi_2 - \varepsilon_{\psi_2,0}\sin^2\psi_1}{\sin^2\psi_2\cos^2\psi_1 - \sin^2\psi_1\cos^2\psi_2} \tag{13}$$

$$\varepsilon_y = \frac{\varepsilon_{\psi_2,90} - \varepsilon_z\cos^2\psi_2}{\sin^2\psi_2} \tag{14}$$

Although the above equations suggest that any two different Euler angles $\psi_1$ and $\psi_2$ can be used for the deduction of the principle strains, there are some limitations for choosing them in experiments. One limitation is that Cu lines generally show strong texture, so that only the textured grains can provide enough XRD intensity for the measurement at special Euler angles. For the film and line with (111) texture, which is common in Cu metallization, if the Cu $K\alpha_1$ X-ray source is used, the available crystal

planes for diffraction from the (111) textured grains are (111) at ψ=0° and 70.5°, (200) at ψ=54.7°, (220) at ψ=35.7°, (222) at ψ=0° and (311) at ψ=29.5° and 58.5°. Figure 2.11 illustrates how to determine the principal strains by using (311) diffraction at ψ=29.5° and ψ=58.5°.

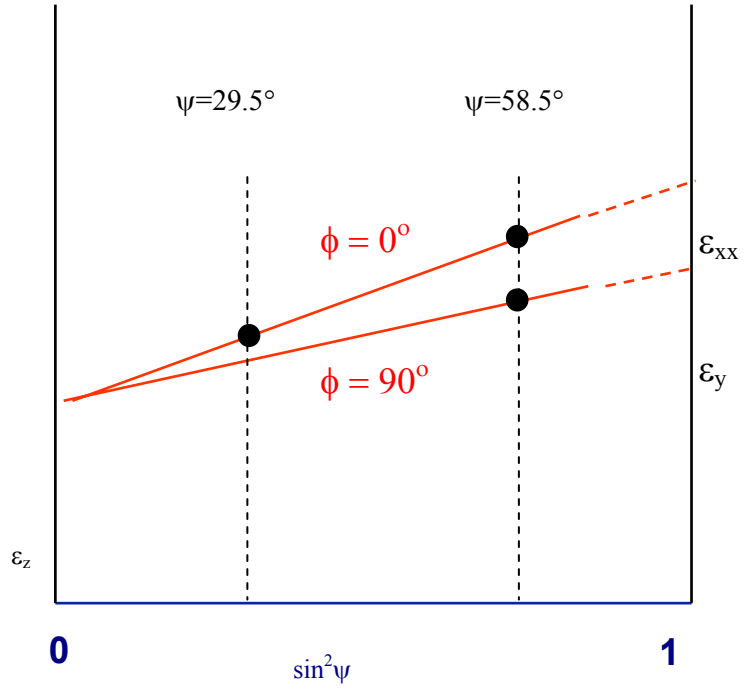


Figure 2.11 Determination of the principle strains by XRD using (311) planes of the <111> textured grains.

Generally, the principle stresses can be calculated using Hooke's law, if the principle strains are determined. Unlike Al, the mechanical properties of Cu single crystals are anisotropic, so that it is the correlated compliance (or stiffness) matrix instead of the bulk or polycrystalline material properties such as Young's modulus and Poisson's

ratio that must be used to convert the strains to the stresses for a textured film or line structure.

Cu crystals show cubic symmetry, so that the fourth order stiffness tensor is reduced to only three independent constants. In the <100> crystal coordinate system where these constants are usually specified, the stiffness tensor would appear as:

$$\begin{matrix} C_{11} & C_{12} & C_{12} & 0 & 0 & 0 \\ C_{12} & C_{11} & C_{12} & 0 & 0 & 0 \\ C_{12} & C_{12} & C_{11} & 0 & 0 & 0 \\ 0 & 0 & 0 & C_{44} & 0 & 0 \\ 0 & 0 & 0 & 0 & C_{44} & 0 \\ 0 & 0 & 0 & 0 & 0 & C_{44} \end{matrix}$$

where $C_{11}$, $C_{12}$ and $C_{44}$ are 168.4GPa, 121.4GPa and 75.4GPa, respectively [2.6] for Cu crystals.

As mentioned above, Cu films and line structures are known to develop strong (111) texture, and the (111) textured grains are generally used for the strain measurement by XRD. The stiffness coefficients in the <100> system need to be transformed for use in the line coordinate system, where the z-axis is along the <111> direction with the x-y directions in the (111) plane. The exact crystal direction for the x and y directions is not

important since the (111) plane is mechanically isotropic for Cu crystal [2.7]. The stiffness tensor in the line coordinate system appears as:

$$\begin{matrix} C'_{11} & C'_{12} & C'_{13} & - & - & - \\ C'_{12} & C'_{11} & C'_{13} & - & - & - \\ C'_{13} & C'_{13} & C'_{33} & - & - & - \\ - & - & - & C'_{44} & - & - \\ - & - & - & - & C'_{44} & - \\ - & - & - & - & - & C'_{44} \end{matrix}$$

where each term in the matrix is given by [2.8]:

$$C'_{11} = (C_{11} + C_{12} + 2C_{44}) / 2 = 220.3 \text{ GPa}$$

$$C'_{12} = (C_{11} + 5C_{12} - 2C_{44}) / 6 = 104.1 \text{ GPa}$$

$$C'_{13} = (C_{11} + 2C_{12} - 2C_{44}) / 3 = 86.8 \text{ GPa}$$

$$C'_{33} = (C_{11} + 2C_{12} + 4C_{44}) / 3 = 237.6 \text{ GPa}$$

$$C'_{44} = (C_{11} - C_{12} + C_{44}) / 3 = 40.8 \text{ GPa}$$

$$C'_{66} = (C_{11} - C_{12} + 4C_{44}) / 6 = 58.1 \text{ GPa}$$

At last, the stresses can be calculated by:

$$[\sigma] = [\mathbf{C'}] \bullet [\varepsilon] \qquad (15)$$

It should be noted that the value of the unstressed lattice parameter must be known in order to use equation 7 to calculate the strain from the measured lattice parameter. Since electroplated (EP) Cu films may be deposited at different conditions, their properties will differ from sample to sample and from bulk Cu. In this case, the unstressed lattice spacing needs to be measured from film samples instead of quoting

standard values from references. Since the entire lattice parameters used in equation 7 are determined by the same system, most of the systematic errors can be canceled out.

The principle to derive the unstressed lattice parameter can be explained below. Based on Hooke's law, for a film under an equal bi-axial tensile or compressive stress state, its strain can vary from positive to negative or negative to positive when ψ changes from $90^o$ to $0^o$, so that there must exist an angle $\psi_0$ at which the strain is zero. For the (111) textured metal films, it is determined by:

$$\sin^2 \psi_0 = \frac{2C_{13}^{'}}{2C_{13}^{'} + C_{33}^{'}} \tag{16}$$

Once $\psi_0$ is determined, the actual unstressed lattice parameter can be interpolated at $\sin^2\psi_0$ from Fig.11.

It is important to note that suitable (hkl) reflections have to be chosen for exact measurements with regards to the systematic error and reflection intensity. If λ is constant, differentiation of equation 5, the Bragg's law, yields,

$$\partial\theta = -\frac{\partial d}{d}\tan\theta \tag{17}$$

which indicates that at a given strain ($\partial d / d$), the reflection that occurs at a higher 2θ will result in a larger peak shift ($\partial\theta$). For example, the thermoelastic strain in a Cu film deposited on a Si substrate is given by

$$\varepsilon = (\alpha_{Si} - \alpha_{Cu})\Delta T \tag{18}$$

where α is the coefficient of thermal expansion (CTE) and ΔT is the temperature excursion. The thermoelastic strain from a 10°C change will cause a 0.0017° peak shift

for a 2θ peak of 89.933° (for Cu (311) plane, Cu $K_{\alpha 1}$ radiation). In comparison, the same strain shifts a 2θ peak at 43.298° (for Cu (111) plane, Cu $K_{\alpha 1}$ radiation) by only 0.0007°. Since XRD determines the strain by measuring the peak shift, a bigger peak shift is desirable for precise measurement, so that theoretically, choosing the high reflection angle will improve the accuracy of the result. However, higher index reflections are less intense than low reflections due to their lower structure factors than low index reflections. The resulting lower signal to noise ratio erodes the benefits of high index reflections. Moreover, as mentioned above, in (111) textured Cu films and lines, only the (111) extured grains provides enough diffraction intensity for the measurement at special Euler angles, setting further limitations for selecting reflections.

Based on the above considerations, the (311) planes of the <111> textured grains are our choice for XRD stress measurements in this study.

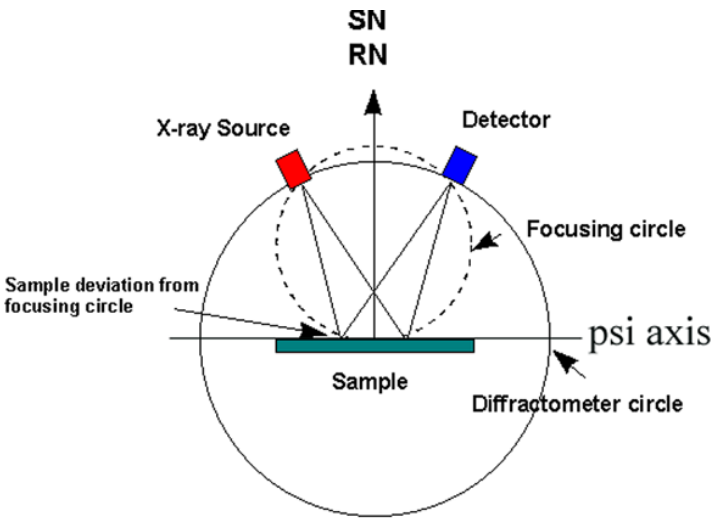


Figure 2.12 Schematic of the XRD system setup

A schematic drawing of the four-circle diffractometer is shown in Fig.12. A rotating anode X-ray source with a maximum power of 18kW was employed to achieve high X ray intensity for the strain measurement on thin films and lines. A copper target was chosen to generate X-ray because the wavelength of copper $K_{\alpha 1}$ is relatively short, and therefore more diffraction is available for the alignment and the measurement. The setup enables the sample to rotate along 3 axes, $\theta$, $\psi$ and $\phi$, while the detector travels along $2\theta$. Besides the rotational freedom, the sample position can be adjusted with high precision along the $\phi$ axis. In addition, the dimension and the tilting of the X-ray beam can be controlled by four high precision slits.

During measurement, changes in sample position with respect to the diffractometer circle induce peak shifts that may cause error in strain measurements. To alleviate this problem, the incident beam and the sample surface must be placed as close as possible to the Euler center of the diffractometer by careful alignment of the system and calibration of the thermal expansion of the sample heating stage. The details of the alignment procedure can be found in Kasthurirangan's dissertation [2.18].

## 2.3 FEA MODELING

As mentioned above, the BB technique can be employed to determine the averaged stress of a thin layer deposited on a rigid substrate using modified Stoney's equation. Since this method cannot directly measure the out-of-plane deformation, it should be complemented by other measurements or calculations to fully evaluate the tri-axial stresses in metal lines. X-ray diffraction, on the other hand, is an independent

method to determine the stresses in Cu lines. However, due to the small amount of copper and the challenging experimental requirements, only the stresses in the (111) textured grains can be measured so far. Neither of the methods can determine the local stress distributions and the stress in patterned dielectric materials. The lack of the experimental means can be compensated by FEA modeling. Modeling can reveal the local stress not only in the metal lines but also in patterned dielectrics and other materials, providing useful insights into the stress-related reliability issues in Cu metallization. In this study, a commercial FEA code, called ABAQUS was used to establish elastic models for stress evaluation.

# Chapter 3 Thermomechanical stress in Cu films

## 3.1 INTRODUCTION

Understanding the mechanical response of materials in small dimensions is critical to process integration and to study device reliability in microelectronic industry that has seen decades of process scaling for better performance and cost reduction. Interconnect structures have been mostly built by thermal processes such as annealing and CVD deposition of dielectric materials. Generally, these processes involve thermal cycles from room temperature to 350–400°C, during which stresses are induced in materials due to the thermal expansion mismatch among the metal lines, dielectrics, barriers and the silicon substrate. These stresses could lead to interconnect failures such as delamination, cracking and stress-induced void or hillock formations, causing manufacturing yield loss or premature product failure. The ever shrinking integrated circuits also propelled the replacement of aluminum alloy interconnect metal lines by copper lines and silicon oxide dielectrics by low dielectric constant (low-k) materials. Along with the new materials, new processes must be introduced to accommodate Cu/low-k, such as the damascene structure, the chemical mechanical polishing (CMP) and the electroplated (EP) Cu. All these lead to novel mechanisms of electromigration and stress migration different from those of Al metallization.

Many studies have addressed the mechanisms of stress development in Cu films under thermal cycling [3.1-3.6]. It is found that stress in copper films changes from tensile to compressive, along with thermoelastic and plastic deformations, resulting in a

stress hysteresis in the stress-temperature curve and the residual stress significantly higher than the yield point of bulk copper at room temperature. While the thermoelastic behavior of a Cu film on a Si substrate is dominated by the mismatch of their coefficient of thermal expansion (CTE) and the Cu elastic modulus, a number of factors may affect the inelastic deformation of Cu films during thermal cycling, including the passivation layer, the film thickness and the microstructure of the film [3.7-3.9]. Even the presence of a small concentration of alloying element was found [3.10] to play an important role. Moreover, the surface condition associated with the oxygen exposure is a key factor affecting the yield behavior of Cu films [3.11-3.12]. Various models have been proposed to understand the underlying deformation mechanisms during thermal cycling of Cu films. Based on the deformation mechanisms map of bulk copper (Frost and Ashby), Thouless *et al*. [3.2] analyzed the stress in thin copper films and proposed that the dominant deformation mechanism shifted among plasticity, diffusional flow, power-law creep and power-law breakdown with temperature during thermal cycling from room-temperature (RT) to 450°C. On the other hand, Keller *et al*. [3.5] believed that the power-law creep was the dominant deformation mechanism and that diffusional creep was completely inactive during thermal cycling. More recently, Weiss *et al*. [3.6] suggested that constraints from the substrate limited the grain-boundary diffusion and thus the stress would not relax to zero at high temperature. Their model of dislocation glide and constrained diffusional creep fits well with the thermal stress data of the self-passivated Cu-1%Al film. In these approaches, the rate equations of steady state creep, which are functions of stress, temperature and material properties but not dependant on time, were

used to predict the stress–temperature curve of Cu films. Although some of the models agreed well with the experimental data, a comprehensive understanding is still lacking, resulting in disagreements in identifying the dominant deformation mechanism of Cu films during thermal cycling.

In this study, a new approach is used to investigate the deformation mechanism of Cu films during thermal cycling. Since a particular plastic deformation mechanism can be correlated to a particular strain rate equation for thin films [3.13], the mechanism can therefore be identified if the plastic strain rate is only a function of stress at known temperature. Following this approach, the strain rate was deduced from the thermal stress in Cu films with different thermal ramp rates. It was found that the stress-temperature curve of EP Cu films during thermal cycling is not sensitive to the ramp rate, suggesting that the dominant mechanism of plastic deformation is the plastic yield in the studied temperature range.

## 3.2 SAMPLES AND EXPERIMENTAL METHODS

Copper film samples were prepared on silicon wafers about 780μm thick. Figure 3.1 shows the schematic of the film structure. A PVD Ta layer was first deposited as a copper diffusion barrier, followed by the deposition of a PVD Cu seed layer. An electroplating process then deposited the main copper film to a total thickness of 0.6μm. Finally, a passivation film of 100nm, named etch stop layer #1 (ES#1), was used as cap layer. Both passivated and unpassivated Cu films were studied for comparison.

The thermal stress in Cu films was measured using the bending beam system. Since the Ta layer is much thinner than the Cu film, Ta effect on substrate curvature can be ignored. The contribution from the passivation layer was determined from a blanket ES#1 film and then subtracted from the total amount. The estimated system error in the measurement is about 5%, largely due to variation in reference curvature.

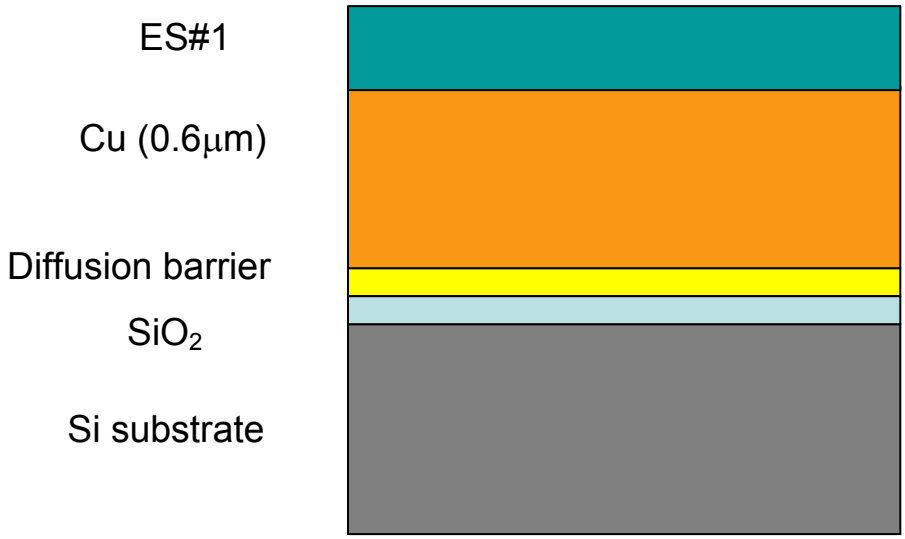


Figure 3.1 Schematic of the passivated EP Cu film structure

The samples were cut into 5mm by 40mm stripes. The surface curvatures were monitored and recorded with respect to time and temperature while the samples were thermally loaded in a vacuum chamber under a nitrogen atmosphere at a pressure of 50 torr. Passivated and unpassivated film samples were placed into the same chamber and measured simultaneously in 4 thermal cycles. In the 1st cycle, the temperature went from room temperature to 410ºC and remained at 410ºC for 30 minutes to stabilize the microstructure of films. Data for the remaining three cycles from RT to 400ºC are shown

with ramp rates of 2ºC/min, 8ºC/min and 0.5ºC/min, respectively. Without an effective cooling system, the actual chamber ramp rate would deviate from the set value when the temperature became lower than a critical point upon cooling down as shown in Fig.2, where the negative values are for cooling down and the positive ones for heating up. The relative critical temperatures indicated in Fig.2 are about 55ºC, 146ºC and 310ºC for the set ramp rates of 0.5ºC/min, 2ºC/min and 8°C /min, respectively.

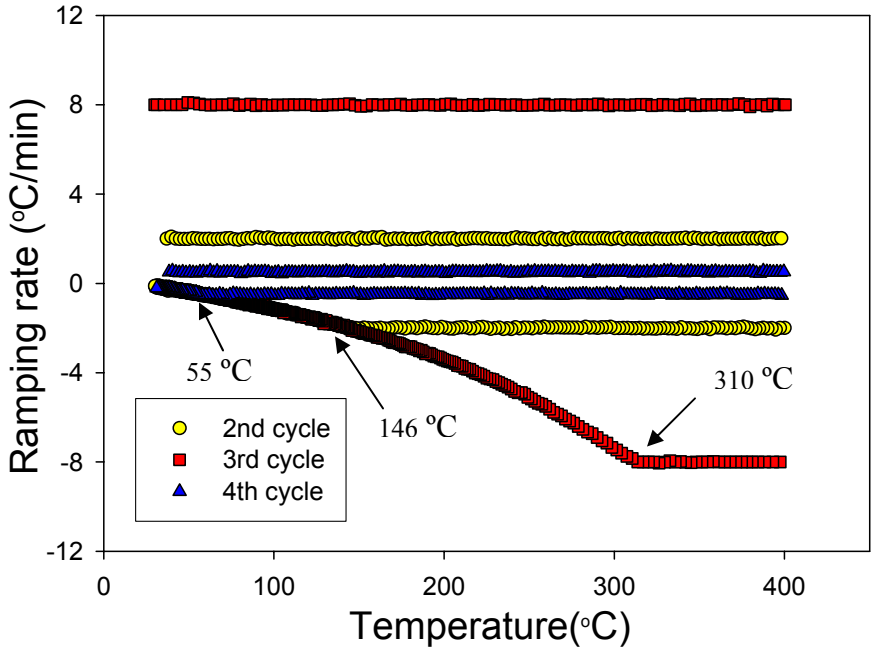


Figure 3.2. Actual ramp rates for the stress measurement in three thermal cycles

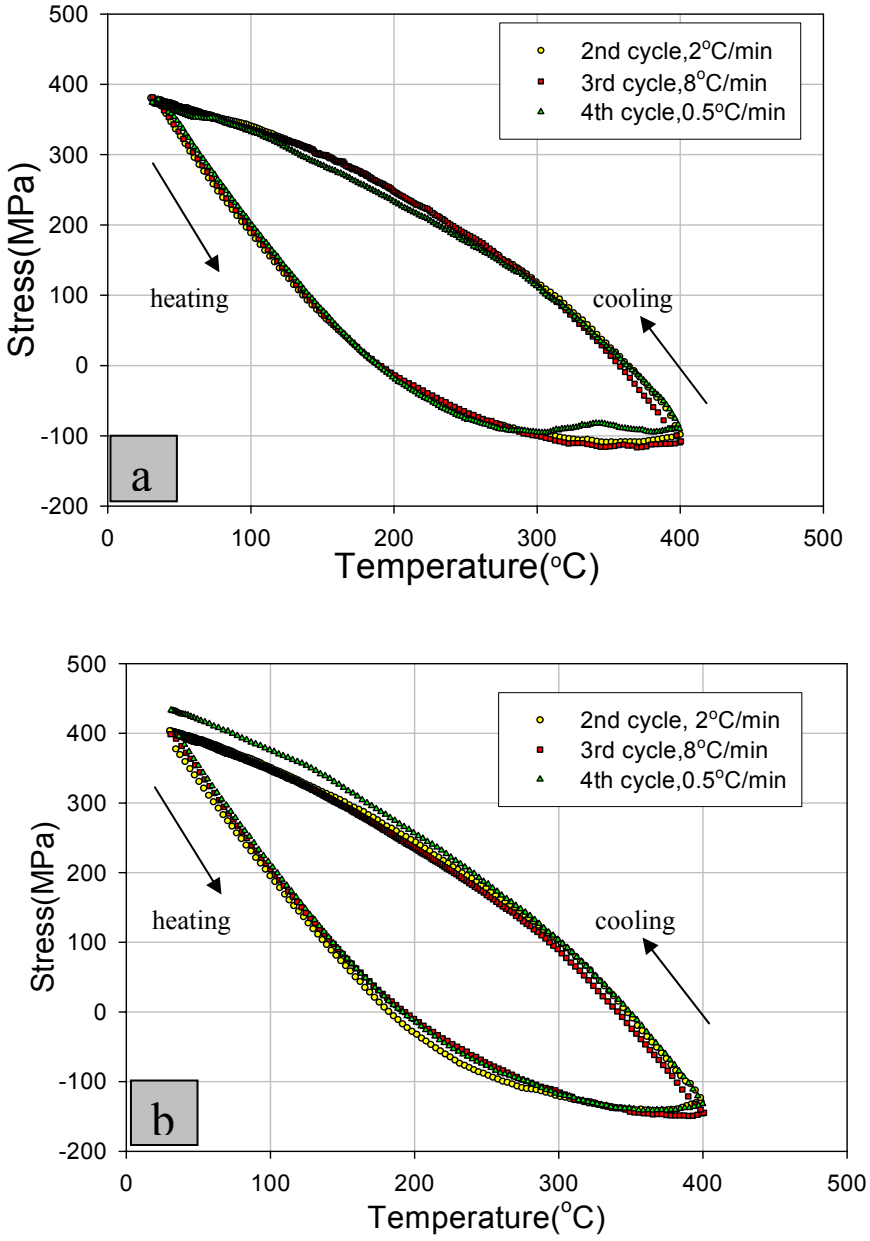


Figure 3.3. Thermal stresses in 3 thermal cycles with different ramp rates of 2°C /min, 8°C /min and 0.5°C /min. in the a) unpassivated Cu film and b) passivated Cu film

## 3.3. RESULTS AND DISCUSSION

### 3.3.1 Thermal stress and strain rate of the EP Cu films during thermal cycling

Figure 3 shows the thermal stress of the EP Cu films in the 2nd, 3rd and the 4th thermal cycles. During initial heating, the stress in both films decreased linearly with temperature, but deviated from the elastic behavior before it reached zero. Further increase of the temperature resulted in stress change from tensile to compressive, indicating stronger plastic deformation. Upon cooling down, the compressive stress also decreased thermoelastically in the initial stage, but the elastic behavior of unpassivated Cu film soon disappeared. Finally, the stress came back to almost the same value at room temperature but followed a different loop from heating, resulting in a hysteresis when a thermal cycle is completed. The residual stresses in the passivated Cu film at RT and 400ºC are higher than those in the unpassivated film. The stress-temperature curves of the unpassivated Cu film in the three thermal cycles almost overlap, except a drop in the temperature range between 310ºC and 380ºC upon heating at ramp rate of 0.5ºC/min. The "drop" did not happen to passivated Cu film upon heating at the same ramp rate of 0.5ºC/min. Interestingly, the stresses in the passivated Cu film below 250ºC upon cooling were higher than those in the previous two thermal cycles at the same temperature with the ramp rates of 2ºC/min and 8ºC/min.

As mentioned above, determining the strain rate of the Cu films helps identify the dominant deformation mechanism during thermal cycling. Figure 4 illustrates the method to deduce the relative plastic strain rate from a stress-temperature curve. In this

figure, two arbitrarily adjacent data points with values of temperature, time and stress are chosen for analysis. When plastic deformation is absent during thermal cycling, the stress in the film decreases thermoelastically from $\sigma_1$ to $\sigma_e$ when the temperature increases from $T_1$ to $T_2$ in a time interval $\Delta t=t_2-t_1$, otherwise, the stress will be $\sigma_2$, the measured stress, instead of $\sigma_e$ at $T_2$. Thus, the total stress relaxed during $\Delta t$ can be described as

$$\sigma_{relax} = \sigma_e - \sigma_2 = M\varepsilon_p \tag{1}$$

where $M$ is the film bi-axial modulus and $\varepsilon_p$ is the plastic strain, which is given by

$$\varepsilon_p = \int_{t_1}^{t_2} \dot{\varepsilon}_p dt = \dot{\varepsilon}_{avg}\Delta t \tag{2}$$

where $\dot{\varepsilon}_p$ is the plastic strain rate and $\dot{\varepsilon}_{avg}$ is the average plastic strain rate from $t_1$ to $t_2$. If $\Delta t$ is small enough, the plastic strain rate $\dot{\varepsilon}_p^{\,T}$ at temperature $T$ between $T_1$ and $T_2$ can be estimated by combining equation 1 and equation 2 as

$$\dot{\varepsilon}_p^{\,T} \cong \dot{\varepsilon}_{avg} = (\sigma_e - \sigma_2)/M\Delta t \tag{3}$$

in which, the elastic stress is given by

$$\sigma_e = M\,\Delta\alpha\,(T_2-T_1) + \sigma_1 \tag{4}$$

where $\Delta\alpha$ is the CTE difference between the Si substrate and the Cu film.

Combining equations 3 and 4 yields the following equation to deduce the strain rate during thermal cycling from a measured stress-temperature curve

$$\dot{\varepsilon}_p^{\,T} = [\Delta\alpha(T_2-T_1) + \frac{\sigma_1-\sigma_2}{M}]/(t_2-t_1) \tag{5}$$

However, the bi-axial modulus of copper films varies with the microstructure due to the mechanical anisotropy of copper crystal. For example, the bi-axial modulus in a 100% <100> textured film is about 115 GPa and <111> film is 261 GPa, suggesting that the published modulus of the bulk copper may not be equal to that of a particular copper

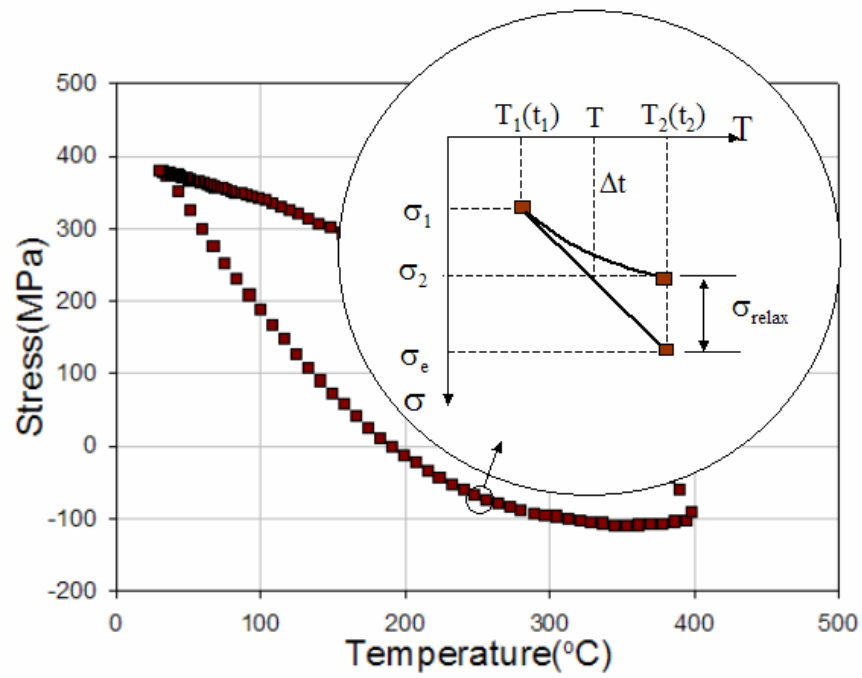


Figure 3.4 Schematic of the deduction of the plastic strain rate from the thermal stress curve.

film. Thus, the measured bi-axial modulus of the film was used to determine the strain rate.

The bi-axial modulus correlates to *S*, the slope of the thermoelastic section of a stress-temperature curve as

$$S = M\Delta\alpha \tag{6}$$

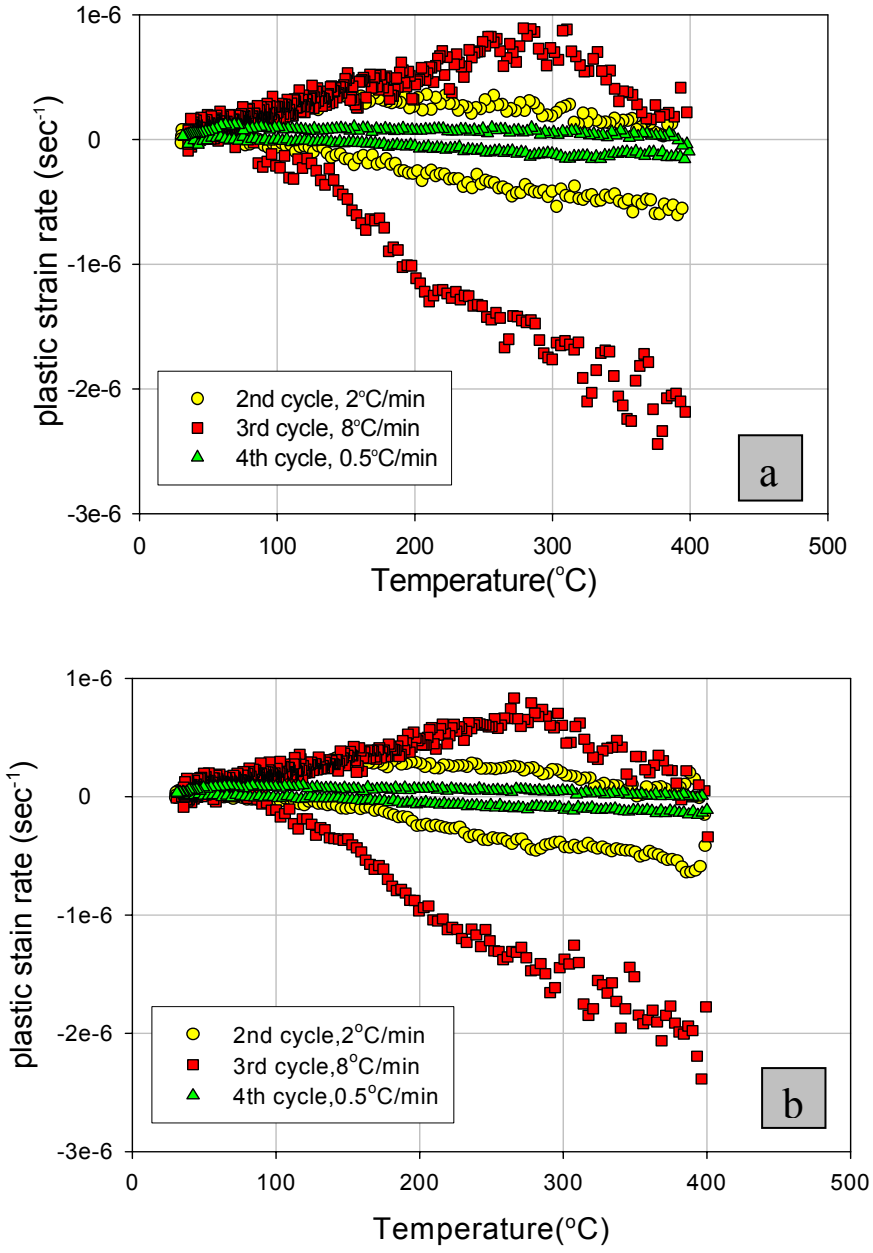


Fig 3.5 Plastic strain rates of the Cu films in 3 thermal cycles with different ramp rates in the a) unpassivated Cu film and b) passivated Cu film.

where $S$ was determined to be –2.8MPa/°C for the EP Cu films used in this study. Using $17.7\times10^{-6}$ /ºC [3.14] and $2.61\times10^{-6}$ /ºC [3.15] as the CTE of Cu and Si, respectively, the bi-axial modulus of the Cu films was determined to be about 185GPa.

The plastic strain rates of the unpassivated and passivated Cu films in these three thermal cycles were determined using equation 5 and are shown in Fig.5. The signs of the strain rate and the stress represent particular thermal stress behaviors of the Cu films. If both the strain rate and the stress are of the same sign, the plastic deformation will respectively result in the decrease of a tensile or compressive stress. On the other hand, if the signs of strain rate and the stress are opposite, an increase of the stress will be the result of the inelastic deformation. This is called the "abnormal" plastic deformation, in contrast to the common understanding that the plastic deformation will relax a stress. Accordingly, a zero strain rate correlates to thermoelastic behavior. For example, as shown in Fig.5, in the third thermal cycle, the strain rate of the unpassivated Cu film was zero from room temperature to about 100ºC upon heating up, indicating thermoelastic behavior in this temperature range. The strain rate became negative and increased with further increase of temperature with the "abnormal" plastic deformation in the temperature range from about 100ºC to 190ºC. Upon cooling down, the thermoelastic behavior occurred only in a very narrow temperature range before the "abnormal" plastic deformation appeared until about 355ºC, and then the strain rate increased before the temperatures decreased to about 300ºC. Below 300 ºC upon cooling, the plastic strain rate decreased until room temperature was reached.

For the passivated Cu film, the strain rate had similar behavior during thermal cycling except that it was smaller than that of the unpassivated Cu film in most of the temperature range and the thermoelastic behavior lasted longer. Besides the effect of the passivation layer, figure 5 shows the strong dependence of the strain rate on the ramp rate. A faster ramp rate resulted in a faster strain rate at the same temperature at about the same stress level. The observed decrease of the strain rate with the decrease of temperature upon cooling down was found to be due to the decrease of the ramp rate, as suggested by the comparison of these strain rate curves with those of the actual ramp rate shown in Fig.2. This observation leads to the conclusion that the plastic strain rate of the Cu films during thermal cycling was proportional to the ramp rate at the ranges of temperature and the ramp rate in this study

$$\dot{\varepsilon}_p \approx C\dot{T} \tag{7}$$

where $C$ is a conversion factor which is a function of temperature but independent of the ramp rate. The conversion factor of the unpassivated film in the three thermal cycles is shown in Fig.6, where the overlap of the $C$-temperature curves in these thermal cycles with different ramp rates supports the relationship described by equation 7. Combining equation 7 and equation 1 leads to

$$\frac{d\sigma}{dT} = M\Delta\alpha - C \tag{8}$$

which suggests that the slope of the measured thermal stress vs. temperature curve should be independent of the ramp rate. However, if the steady-state plastic strain rate is used to

model the thermal stress behavior of a film during thermal cycling, the differential equation should be:

$$\frac{d\sigma}{dT} = M(\Delta\alpha - \frac{\dot{\varepsilon}_p}{\dot{T}}) \tag{9}$$

in which the steady-state strain rate $\dot{\varepsilon}_p$ is a function of stress and temperature, independent of time or ramp rate. This equation implies that the slope of the stress-temperature curve depends on the ramp rate, which is not consistent with the above experimental results, indicating that the steady state strain rate equation does not account for the plastic deformation of the Cu films during thermal cycling.

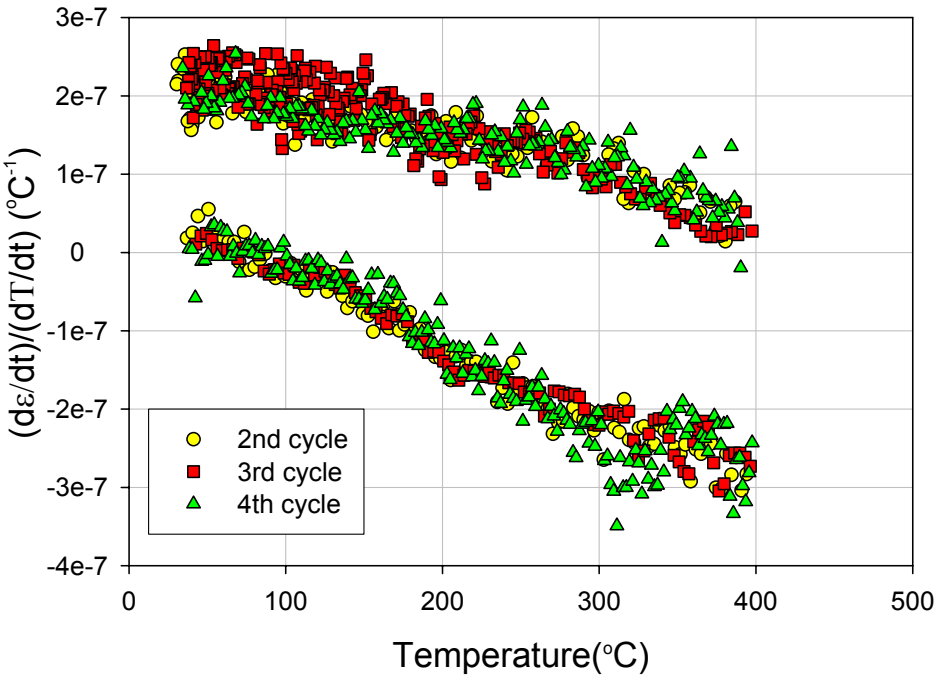


Figure 3.6 the ratio of strain rate to ramp rate of the unpassivated Cu film in the 3 thermal cycles

### 3.3.2 Plastic yield and creep of the EP Cu films during thermal cycling

Generally, plastic deformation can be divided as plastic yield and creep. Plastic yield is due to dislocation glide and creep is a diffusional process. During thermal cycling, the total strain rate of plastic deformation in a film should be

$$\dot{\varepsilon}_p = \dot{\varepsilon}_y + \dot{\varepsilon}_c \tag{10}$$

where $\dot{\varepsilon}_y$ is the yield strain rate and $\dot{\varepsilon}_c$ is the creep rate. The strain rate due to the glide of dislocations can be expressed as [3.16]

$$\dot{\varepsilon}_y = \rho_m b \bar{v} \tag{11}$$

where $\rho_m$ is the density of mobile dislocations, moving through a field of obstacles with an average velocity $\bar{v}$, and $b$ is the magnitude of the Burger's vector of the dislocation. The velocity $\bar{v}$ depends on the force per unit length on the dislocation

$$F = b\tau = b(\tau_a + \tau_i) \tag{12}$$

where $\tau$ is the shear stress acting on the dislocation, a combination of the applied stress $\tau_a$ and the stress $\tau_i$ from the internal of the material itself, such as from the other dislocations, grain boundaries or interfaces. In non-climb plastic deformation, a dislocation moves almost instantaneously in response to the shear stress $\tau > \tau_r$ but otherwise most sluggishly, where $\tau_r$ is the resolved shear stress required to move an isolated straight dislocation under the same circumstances [3.17]. As a result, if we consider the applied stress needed to move dislocations as the strength of a film, the dominant deformation mechanism will be plastic yield when the applied stress larger than the strength of the films, otherwise, it should be creep.

Since it is the thermal expansion mismatch that causes thermal stress in thin films, the stress-temperature curve of Cu films represents a particular kind of stress-strain curve during thermal cycling. Continued temperature change results in continued loading of the film with the loading rate given by

$$\dot{\varepsilon}_e = (\alpha_{Si} - \alpha_{Cu})\dot{T} \tag{13}$$

where α is CTE and T is temperature. The relationship between $\dot{\varepsilon}_e$ and $\dot{\varepsilon}_c$ will determine the contribution from plastic yield or creep on the plastic deformation of the film. In the case where the loading rate is larger than the creep rate during thermal cycling, $\dot{\varepsilon}_e > \dot{\varepsilon}_c$, there is a net loading strain that drive the film stress increase before plastic yield occur. Due to plastic yield, the stress can only increase to the level of the strength of the film. If the strength of the film (yield point) does not depend on the loading rate, the shape of the stress-temperature curve will not change with increasing loading rate. Consequently, the relationship of Eq.7 is observed and the contribution on plastic deformation from creep is not shown in the stress-temperature curve. Figure 7 shows the schematic of the thermal stress behavior in this condition, including the thermoelastic and the "abnormal" plastic behaviors, as well as yield and hardening. In particular, the "abnormal" plastic deformation is shown in the temperature range from $T_1$ to $T_{01}$ during heating up and from $T_2$ to $T_{02}$ in cooling down. The “abnormal” yielding behavior may be explained based on the dislocation-based “Bauschinger” effect [3.12] that the deformation in the reverse direction is easer than the forward direction based on the theory of dislocation movement.

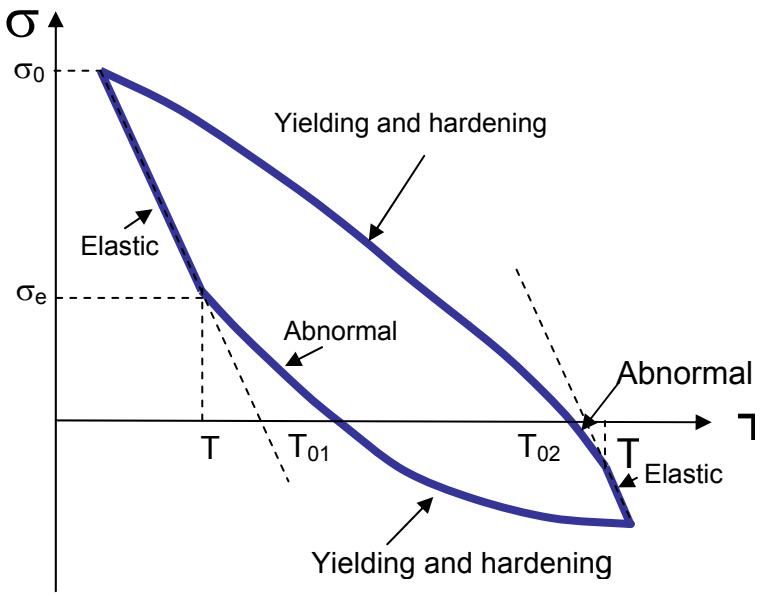


Figure 3.7 schematic of the thermal stress behavior of Cu films during thermal cycling

In Fig.7, the film has an initial stress $\sigma_0$ built up in the previous cooling down due to the strain hardening. At that situation, a dislocation is subjected a total force

$$F = b(S\sigma_0 - \tau_i) = b\tau_r \tag{14}$$

where $S$ is the Schmid Factor for a particular slip system in the film and other parameters have the same meanings in equation 11. The internal stress $\tau_i$ is opposite to the applied stress from the substrate. During heating up, the applied stress of the film from the substrate decreases thermoelastically until it reaches a value of $\sigma_e$ when the dislocation is subjected a total force of

$$F = b(S\sigma_e - \tau_i) = -b\tau_r \tag{15}$$

Further increase of temperature will result in a continual decrease of the applied stress while the internal shear stress remains almost unchanged. This causes the movement of a dislocation in the direction of the internal shear stress when the net stress on a dislocation reaches the critical resolved shear stress $\tau_r$, resulting in the "abnormal" plastic deformation shown in Fig.7. Combining equations 12 and 13, the resolved shear stress $\tau_r$ becomes

$$\tau_r = \frac{S(\sigma_0 - \sigma_e)}{2} \tag{16}$$

in which the Schmid Factor is defined as $\cos\lambda\cos\phi$, where $\lambda$ is the angle between the slip direction and the stress axis while $\phi$ is the angle between the slip plane and the stress axis. The value of the Schmid factor depends on the microstructure and the stress state. Cu films consist of two main texture components, (111) and (100), and some minor texture components such as (511) and (5,7,13) due to the twinning of Cu (111) grains. Since Cu has fcc structure with slip systems of {111} <110>, the maximum value of the Schmid factors for both the (111) and (100) textured films is $\sqrt{6}/6$ when the films are subjected in-plane bi-axial stresses from the substrate. Since Cu crystals are mechanically anisotropic and a Cu film may have different texture components, the "abnormal" deformation may also be in part due to the different plastic deformation behavior among grains with different orientations [3.18].

With decrease of the ramp rate and increase of temperature, the creep rate of a film would become larger than the loading rate during thermal cycling. In this case, there is a net strain that drives the stress deviating from the strength of the film to a lower level. When the film stress is less than the strength, plastic yield does not contribute to the plastic deformation of the film. The observed plastic deformation is then contributed by creep. That results in the "drop" of the curve of the unpassivated Cu film upon heating up with a ramp rate of 0.5ºC/min in the temperature from 310 to 380ºC as shown in Fig.3. The formation of the "drop" can be explained by the “diffusion wedge” creep model developed by Gao et al [19], which predicts that the diffusion of atoms from the film surface into grain boundaries or from grain boundaries to the surface results in the insertion or removing of a wedge shape of material in grain boundary, relaxing the film tensile or compressive stress, respectively. Since the model assumes that there is no interfacial sliding in the film bottom interface, the film stress does not relax to zero, as it predicts the “drop” of the stress curve upon heating up [3.6]. This diffusional creep mechanism seems to be suppressed by a passivation layer, which disables the fast surface diffusion on Cu films. As a result, a "drop" was not formed on the stress curve of the passivated Cu film even with a ramp rate of 0.5ºC/min.

Furthermore, because of the passivation layer, the "hardening" behavior of the Cu film also depends on the ramp rate. Shown in Fig.3, the stress with a ramp rate of 0.5ºC/min is higher than those with a ramp rate of 2ºC/min and 8ºC/min upon cooling down after the temperature was less about 250ºC, in contrast to the general understanding that in bulk material that a faster loading rate makes a harder material. The underlying

mechanism may be related to the annealing effect on the density of the mobile dislocations and the densification of the film due to anneal out of defects inside the passivated film. This may be a special characteristic of EP Cu films due to the incorporation of additives and densification of the film, as discussed in the following section.

### 3.3.3 Effect of impurity on the stress behavior of EP Cu films

Electroplating is the general choice in Cu metallization. With the scaling of the feature size and increasing of the aspect ratio of trenches, additives are needed for a better plating performance [3.20]. Generally, the commercially available additives fall into three categories, brightener or accelerator, suppressor or carrier and leveler, named according to their functionality and cathode polarization behavior. Various additive systems, the mixtures of these three kinds of additives are used to achieve bottom-up filling and a flat topography of the Cu overburden on a patterned wafer. During electroplating, additives are absorbed to the Cu surface and a small amount of them would co-deposit with Cu into the film. Some of them may not be rinsed out or not be decomposed during the subsequent cleaning or annealing processes, therefore becoming impurities in the Cu film. The impurities include Cl, S, and C etc. Concentrations of the organic additives were found to strongly affect the grain growth of EP Cu films at room temperature [3.21]. It is important to understand the effects of the impurity on the thermal stress behavior of Cu metallization.

One set of 0.95μm thick EP Cu samples, passivated with a bi-layer of silicon nitride and silicon oxide were electroplated in the solutions with different accelerator concentrations of 0%, 2.5%, 3.8% and 5%. The impurity concentration in the Cu film was higher when a higher accelerator concentration was used, shown in table 3.1 [3.22], dramatically increasing of the impurity concentrations of S, Cl, and C in the Cu films. Figure 8 shows the thermal stress of the Cu films in the 2$^{nd}$ cycle from RT to 420°C with a ramp rate of 4°C/min while in the 1$^{st}$ cycle, the samples were annealed at 430°C for 30 minutes to stabilize the film microstructure before cooling down.

Table 3.1 Impurity concentration levels for copper deposited with different chemistries.

| Impurity (ppm) | High Purity | Medium Purity | Low Purity |
|---|---|---|---|
| S | 0.3 | 7.4 | 16.5 |
| Cl | 2.1 | 28.4 | 61.4 |
| C | 4.1 | 42.5 | 135.6 |
| O | 2 | 1.7 | 2.4 |
| N | 11.7 | 25.3 | 15.5 |
| Ag | 0.4 | 0.6 | 0.5 |
| Others | <1 | <1 | <1 |

The concentration of the accelerator in the electroplating bath is shown to play an important role during the thermal stress evolution of the EP Cu films during thermal cycling. The use of the accelerator results in the decrease of the film residual stress at RT. With the increase of the concentration, the stress hysteresis becomes smaller and the shape of the curve changes. Specifically, the abnormal yielding becomes more pronounced upon heating up and the hardening rate upon cooling down becomes slower

at elevated temperature range. For the Cu films with the concentration of 3.8% and 5%, a "tail" is observed in the stress curve at the high temperature range.

The XRD 2θ scan of the Cu films and the intensities of the (111) and (200) peaks after the thermal stress measurement in Figure 9 clearly indicate that adding accelerator into the bath affects the texture development of the Cu films. Without the accelerator, the film has a medium strength of (111) texture, which decreases and then increases with the increase of the accelerator concentration while the development of (200) texture is observed in an opposite trend. The XRD result also suggests that the difference of the microstructures may not account for the difference of thermal stress.

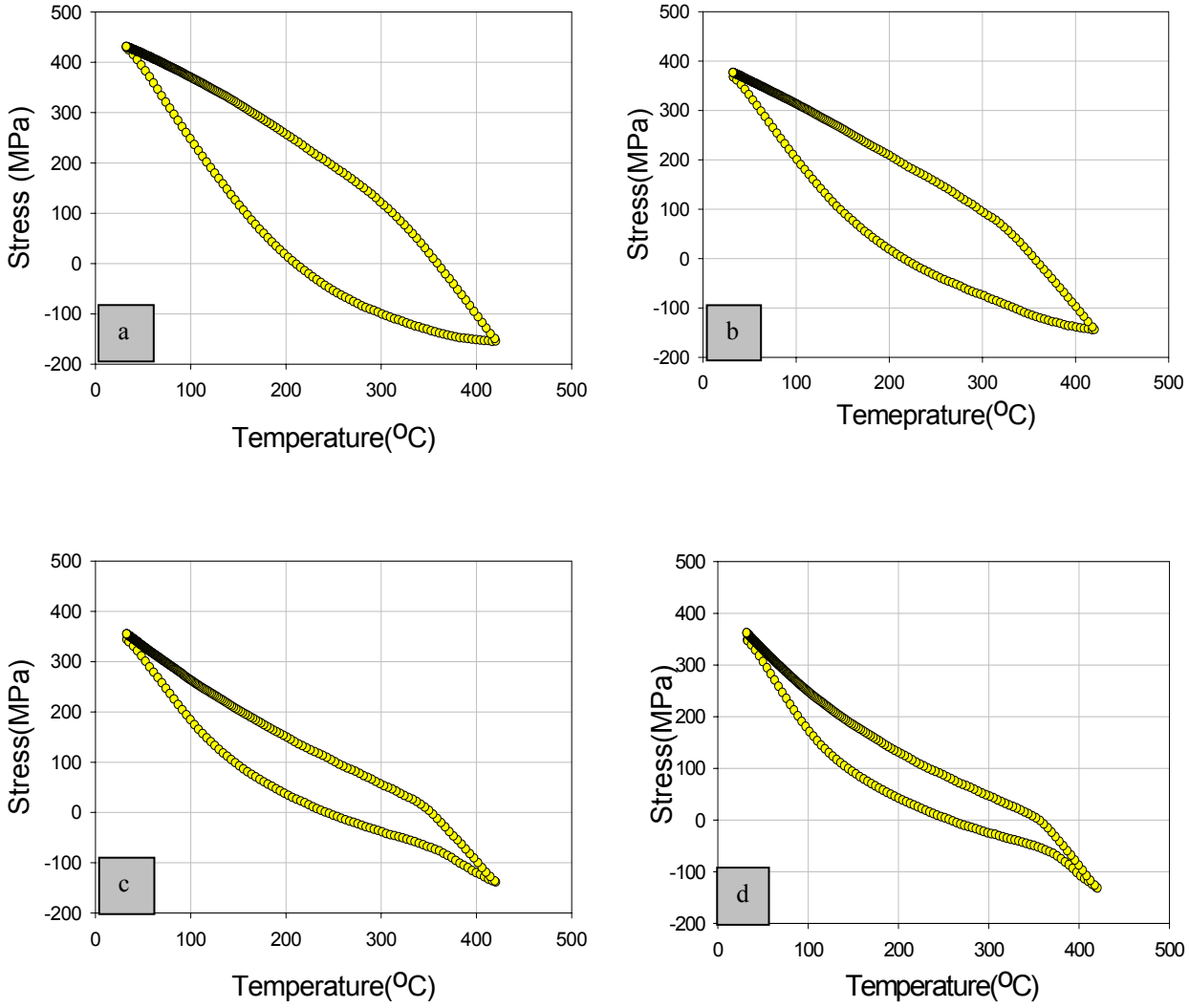


Figure 3.8. Thermal stress of EP Cu films deposited with different concentrations of accelerator a) 0% b) 2.5% c) 3.8% and d) 5%.

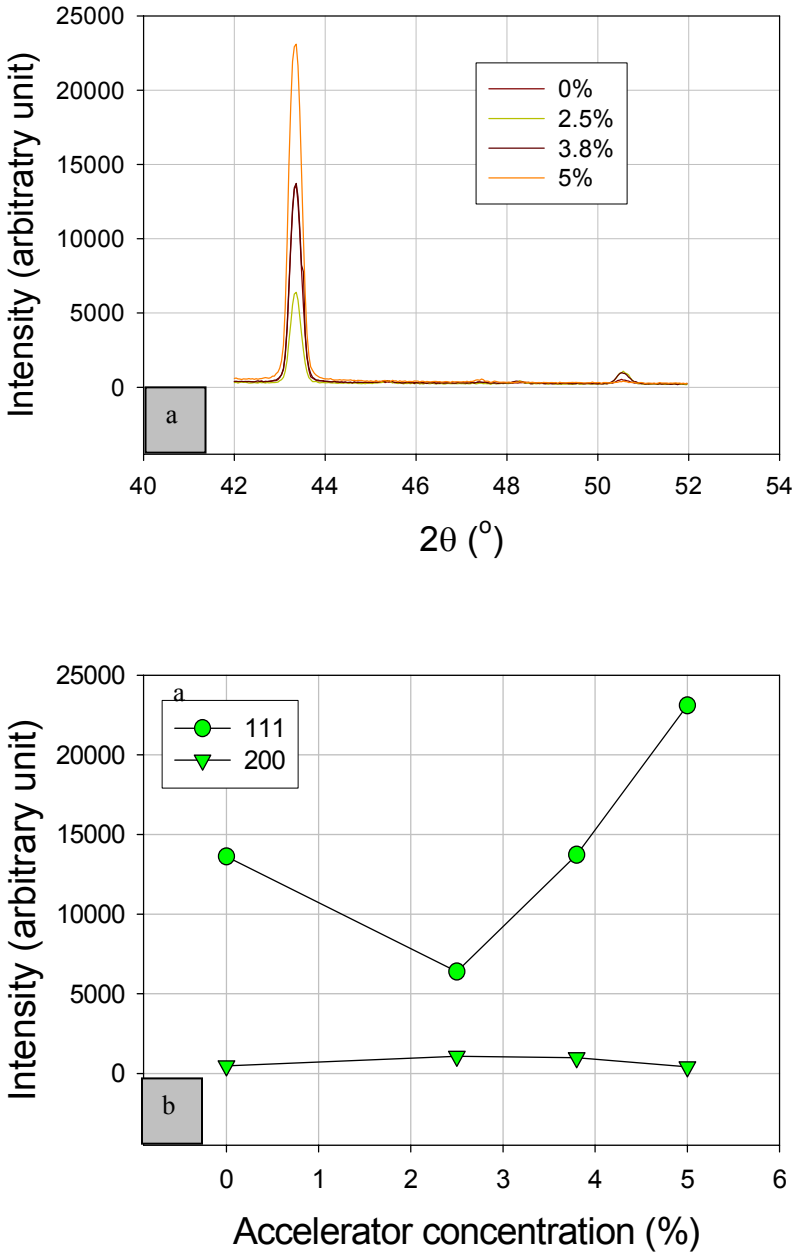


Figure 3.9. XRD result of the effect of the accelerator concentration on the texture development of EP Cu films, a) 2θ scan result b) intensity of the (111) and (200) peaks

Baker at al [3.12] also observed the aggressive "abnormal" yielding behavior in the sputtered Cu films if exposed to the oxygen ambient during film preparation, suggesting that the impurities, Cl, S or C have the similar effect of O on the "abnormal" yielding of Cu films, but it is yet to be identified which impurity has greater effect.

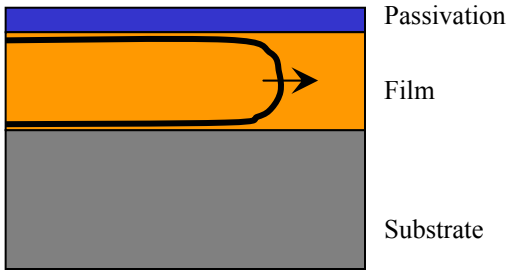


Figure 3.10. Schematic of a threat dislocation glide through a passivated film, leaving misfit dislocations at interfaces.

According to Nix [3.23], when a threading dislocation travels through a passivated thin film, additional dislocation lines (misfit dislocation) are left at the interfaces and create certain energy barrier (Figure 3.10) that increases the strength of the film due to the passivation layer. Upon heating up, the threading dislocations with misfit dislocations at the interfaces pileup in the previous cooling down will move in the opposite direction due to the internal force as mentioned above. In this case, the interaction between the interfaces and the misfit dislocations would be critical for this movement. If the segregation of the impurity at the interfaces undermines the attractive force or enhances the repulsive force of the interfaces to the misfit dislocations, the more aggressive "abnormal" yielding will be observed. While the previous pileup dislocations are consumed, the pileup of the dislocation under the applied force in the opposite stress

will enhance the film strength again, resulting in the strain hardening observed at the elevate temperature range and the formation of "tail".

## 3.4. SUMMARY

In summary, thermal stresses of both passivated and unpassivated EP Cu films were measured during thermal cycling with different ramp rates, and the correlated strain rates during thermal cycling were calculated. The plastic strain rate was found to be approximately proportional to the ramp rate, suggesting that the steady-state creep equations could not account for the plastic deformation of the Cu films during thermal cycling in the temperature range from RT to 400ºC. Both plastic yield and creep would contribute to the observed plastic deformation of the Cu films during thermal cycling, but that depends on the relationship between the loading rate and creep rate. A passivation layer is able to effectively suppress the diffusional creep of the Cu film. Impurity in EP Cu films was shown to be a critical factor affecting the thermal stress of the Cu films that might be attributed to the segregation of the impurity at the interfaces, which modified the interface properties and the interaction between the interfaces with the misfit dislocations.

# Chapter 4 Thermal stress in copper interconnects

## 4.1 INTRODUCTION

High-performance interconnects use Cu wires to connect devices and supply power. Filling the space between wires are dielectrics. Different from the process of Al alloy based interconnects, the Cu damascene interconnect structures require complex processes and structural elements, including Cu electroplating, barrier/seed layers, chemical-mechanical polishing (CMP) and passivation, as well as new materials such as low-k dielectrics and etch stops. The shrinking of the integrated circuits also requires multi-level interconnects. Figure 1 shows the cross-section of an Intel multi-level interconnect structure with eight layers of Cu metallization.

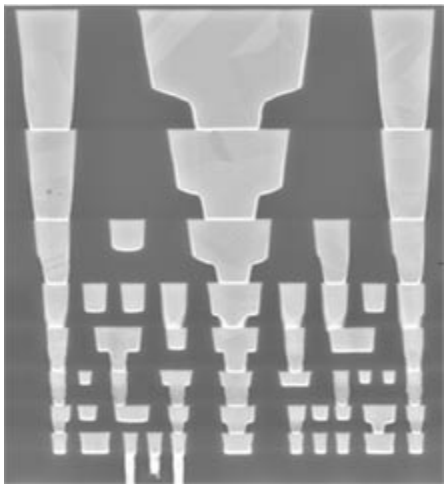

Figure 4.1 Cross section of Intel multi-level copper/low-k interconnect structure (ftp://download.intel.com/technology/silicon/65nm_logic_press_briefing_0804.pdf, 2005)

During the process of forming Cu interconnects, the Cu wires generally undergo thermal cycles from room temperature (RT) to 350-450°C during anneal and dielectric deposition. The more metal layers, more thermal cycles are needed which induce thermal stress due to the thermal expansion mismatch between Cu and surrounding materials. Since the stress may cause stress migration, delamination and cracks, it has been a major reliability concern for Cu interconnects. Therefore it is important to study the thermal stress in Cu metallization.

Differences between Cu films and Cu lines are obvious. The thickness of a Cu film could be small, but its in-plane dimension is relatively large, resulting in a bi-axial stress state. In a Cu line, a tri-axial stress state is expected since the sidewalls of the line are confined by the diffusion barrier and the IMD. Furthermore, plastic deformation behavior is also different due to much smaller dimension of Cu lines. Therefore thermal stress behavior of Cu films might not be a suitable model system to analyze the stress-related failure mechanisms in Cu lines. Thermal stress of Cu interconnects has to be directly evaluated.

Structural integrity of copper interconnects integrated with low-k materials is another major reliability concern. Compared to $SiO_2$, low k ILD's are significantly softer and expand more during thermal processing. The thermal stress behavior of Cu/low k damascene line structures has been measured using x-ray diffraction methods [4.1-2]. The barrier and the cap layer were found to play an important role in confining thermal deformation of Cu lines, resulting in a stress state distinctly different from that of AlCu/low k lines not embedded in the damascene structure [4.3]. These studies raise two

basic questions concerning thermal stress behavior of Cu/low k damascene structures. The first question concerns the effects of the diectric material, particularly when the linewidth reduces below 0.25 μm. The second question concerns the deformation and stress characteristics of the low-k ILD. The stress behavior of the ILD in the confined sub-micron geometry of the damascene structure is also expected to be quite different from that measured on blanket films or large pad structures.

This chapter reports a study on the effects of anneal, ILD and line width on the thermal stress in Cu interconnects. Thermal stresses were measured in Cu lines using x-ray diffraction method. FEA was performed to evaluate the stress behavior of the Cu lines to examine the effect of scaling in linewidth. After being verified with the experimental results, FEA was extended to evaluate the stress behavior of the low k dielectrics.

## 4.2 SAMPLE PREPARATION

The samples with the schematic structure shown in Fig 2 were fabricated at Intel. A 105nm thick etch stop was deposited on a 12-inch Si wafer followed by the deposition of a 690nm or 500nm thick ILD film, into which parallel trenches were etched. The trenches were then filled with electroplated Cu after the deposition of a 5nm thick PVD Ta barrier and a PVD Cu seed layer. Chemical mechanical planarization (CMP) was then used to remove the Cu overburden and the extra barrier. Finally, samples were capped separately with three types of passivation layer each about 105nm thick. They are SiC, SiN and a novel ES. In this study, the thickness of the Cu lines is about 0.35μm, less than

the total thickness of ILD, so that there is a layer of ILD beneath the Cu lines, different from the test structures used in the previous study [4.1-2]. Samples with two sets of Cu width/pitch, 0.4μm/0.8μm and 0.2μm/0.4μm, and three kinds of ILD, SiOF, carbon doped oxide (CDO) and a polymeric low-k dielectric named SiLK™ were prepared for this study.

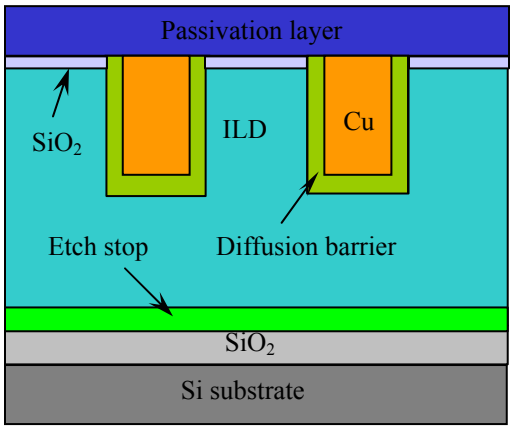


Figure 4.2 Cross-section of the line structure for stress evaluation

## 4.3 EFFECTS OF ANNEAL ON THERMAL STRESSS IN COPPER LINES

### 4.3.1 XRD stress measurements

In this study, samples of the Cu/ CDO (500nm) structure with three kinds of passivation conditions were used: 105nm thick $SiN_x$ cap layer, 105nm thick SiC cap layer and no passivation. In order to study the effects of anneal, the as-received samples were annealed by different thermal cycles with a ramp rate of 4°C/min from room temperature (RT) to 250°C, 300°C, 350°C, 400°C, 450°C and 490°C, respectively, and held for one

minute at the peak temperature. After the samples were cooled down to RT, the residual stress in the Cu lines was measured using the XRD method and the results are shown in Fig. 3, where $\sigma_x$, $\sigma_y$ and $\sigma_z$ are the principle stresses along, across and normal to the line, respectively. The precision of stress measurement is ±40 MPa. The stress state of the lines is shown to be tri-axial with the highest component along the line. In the unpassivated Cu lines, the principal stresses are shown to increase almost linearly with the annealing temperature. As a result, after being annealed at 490°C, the sample's principal stresses $\sigma_x$, $\sigma_y$ and $\sigma_z$ are about 750MPa, 284MPa, and 198MPa, dramatically larger than those of 340MPa, 70MPa and 115MPa, respectively when the annealing temperature was 250°C. The stress of the passivated lines shows different responses to annealing temperature, with the stress components $\sigma_y$ and $\sigma_z$ almost unchanged. It is shown that $\sigma_x$ of the $SiN_x$ passivated lines did not change until the annealing temperature was above 400°C, while the stress in the SiC passivated sample began to change at 350°C. After the anneal at 490°C, $\sigma_x$ in both the passivated samples can reach a value of more than 700MPa, indicating that thermal cycling can increase the residual stresses in Cu lines both in the passivated and unpassivated interconnects.

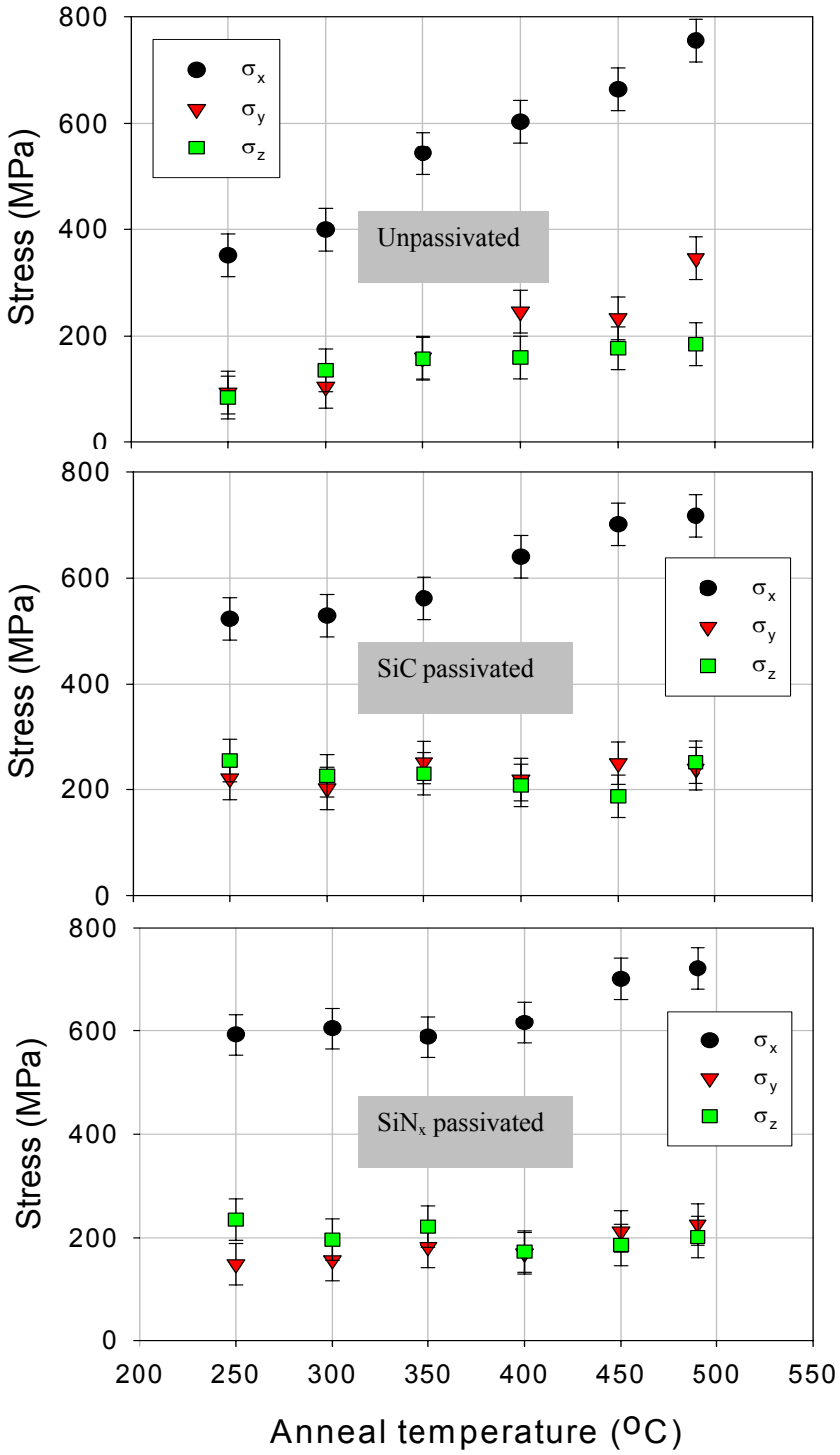


Figure 4.3 Effects of annealing temperature in the residual stress at room temperature in Cu lines with different passivation conditions.

### 4.3.2 Bending beam stress results during thermal cycling

In order to investigate the effect of annealing on the stress in Cu lines, the bending beam method was used to measure the thermal stress in the interconnect layer. Results of thermal cycles from room temperature to 450°C are shown in Fig.4, where $\sigma_x$ is along the lines and $\sigma_y$ across. The measured stresses are the average values of the whole stack above the thermal oxide on the Si wafer, including the etch stop, CDO, barrier, Cu and the passivation layer for the passivated samples. The stress normal to the surface of the wafer $\sigma_z$ is assumed to be zero. The data presented includes those in the first cycle and the 2$^{nd}$ heat up. Although the thermal stress in Cu lines may be tensile in a particular temperature range, the average stresses measured are compressive. Upon the 1$^{st}$ heat up, the thermal stresses as a function of temperature differ significantly between the samples with different passivation conditions. The thermal stresses of the unpassivated sample are shown to decrease with temperature in the 1$^{st}$ heat up, but deviate from the linear behavior after the temperature is above 100°C. With further increase of temperature, the stress curves flatten and even show a fast drop of the compressive stress. For the SiC passivated sample, $\sigma_x$ deviates from linear behavior at about 300°C and $\sigma_y$ at 100°C, compared to about 350°C and 180°C for the sample passivated by $SiN_x$. In the higher temperature range in the 1$^{st}$ heating up, both SiNx and SiC passivated samples showed a fast drop of compressive stress. Upon the 1$^{st}$ cooling down, the stresses of all the three samples decrease with temperature and this behavior is believed to be approximately linear at the temperature range of RT to 400°C, as evidenced by the absence of

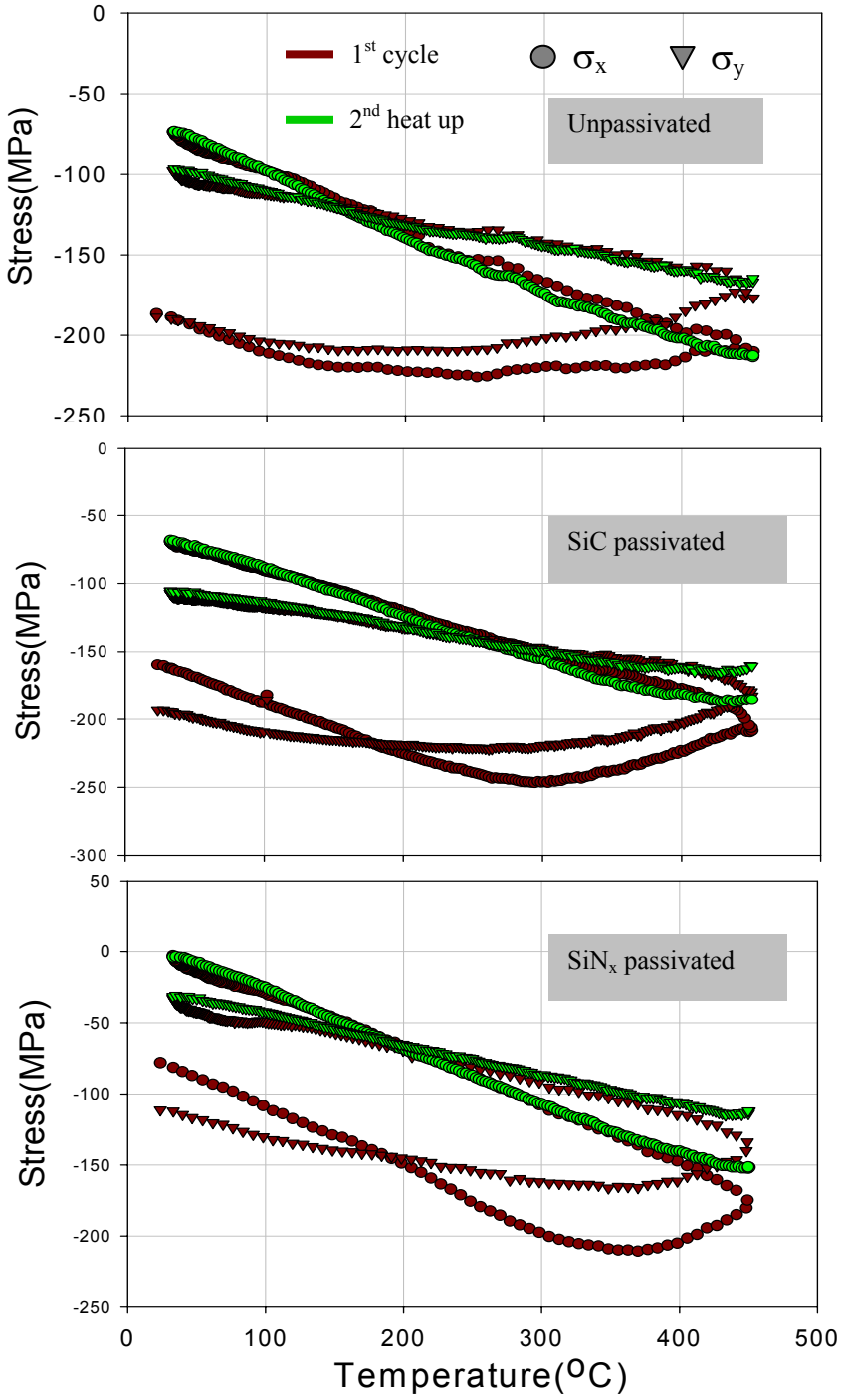


Figure 4.4 Bending beam results of the thermal stress of Cu interconnects during thermal cycling.

discernible stress hysteresis in the thermal cycle found from the 1st cooling down and 2nd heating up. The slopes of the stress-temperature curves of the linear parts in x and y directions are different for all the three samples, indicating the bi-axial modulus and/or the CTE of the interconnect layers are anisotropic in the directions along and across the Cu lines. It is also shown in Fig.4 that the thermal stresses in the layers at room temperature are quite different after the samples underwent a thermal cycle. By comparing Fig. 3 with Fig. 4, we can find that the temperatures correlating to the deviation of the linear behavior of $\sigma_x$ in the 1st heat up in Fig.4 are consistent with those, above which $\sigma_x$ will increase when the sample was annealed in Fig.3. They are 300°C for the SiC and 350°C for $SiN_x$ passivated samples.

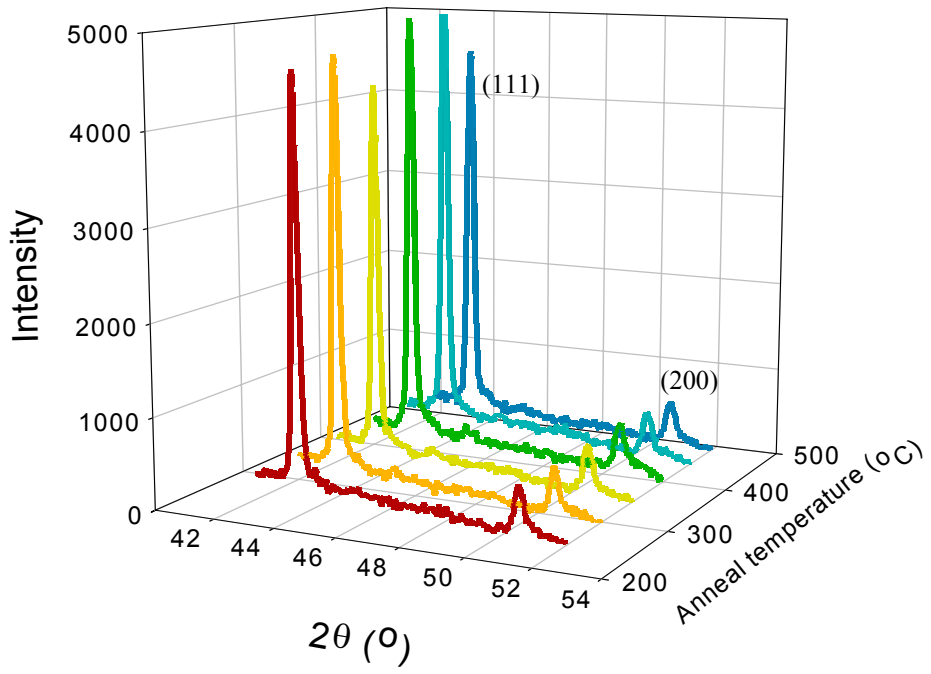


Figure 4.5 XRD 2θ scan of the unpassivated samples with different annealing temperatures.

### 4.3.3 XRD analysis of the effect of anneal on the texture in Cu lines

Figure 5 shows the XRD 2θ scans from 41° to 52° of the unpassivated line sample under the above annealing conditions. It is shown that the annealing temperature did not strongly affect the (111) and (200) textures in the Cu lines, evidenced by the obtained similar densities of the (111) and (200) peaks, in spite of the different annealing temperatures from 250°C to 490°C. Since Cu crystals are mechanically anisotropic, the change of the texture of a Cu line would result in the change of its stress, therefore the XRD result suggests that the increase of stress in the Cu lines after annealing was not due to the change of the texture.

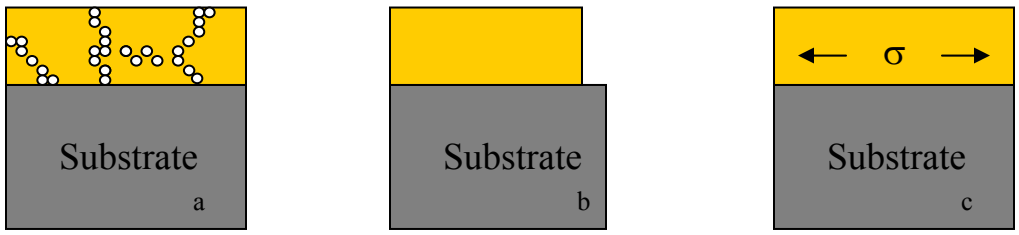


Figure 4.6 Schematic of the stress induced due to the grain growth.

### 4.3.4 Discussion

The densification of the Cu lines due to the annihilation of grain boundaries during grain growth is expected to be one reason for the increase of the residual stress in Cu lines after annealing. Figure 6 is the schematic of the stress induced by grain growth. Shown in Fig.6 (a), the Cu contains a certain amount of grain boundary, a source of vacancy, with the stress assumed to be zero. After the grain boundaries annihilate during grain growth upon annealing, the volume of the Cu shrinks as shown in Fig.7 (b). Since

Cu is confined by the substrate and the Cu/substrate adhesion is strong, the densification of Cu by annihilation of the grain boundaries builds a tensile stress in the Cu, shown in Fig.7 (c). Electroplating at room temperature results in a very small grain size of the as-deposited Cu in damascene Cu interconnects, with correspondingly high concentration of grain boundary free volume in the Cu lines. Some grain growth could occur at room temperature in the as-deposited Cu lines, and continue at higher temperatures. Although grain growth is expected to be dependent on time and temperature, temperature was shown to be the dominant factor during thermal cycling. Since pre-CMP annealing is performed at a low temperature to achieve a balance between CMP performance and the post-CMP defects, grain growth may not happen in the later annealing at a lower temperature. This explains the linear behavior, which usually indicates no grain growth, shown in the 1$^{st}$ heating up below 100°C in Fig. 4 for the unpassivated sample. Generally the deposition of passivation layers is at elevated temperatures, and Cu lines in the passivated samples undergo aggressive grain growth, hence the high residual stress. Thus, the following anneal at a lower temperature does not change the stress in the Cu lines in the passivated samples. Based on the data shown in Fig.3 and Fig.4, the deposition temperature of the SiC passivation layer is estimated to be 300-350°C and that for the $SiN_x$ is 350-400°C.

Plastic deformation or creep of the Cu lines upon heating up is another possible reason for the increase of tensile stress in the Cu lines upon cooling down after annealing. Figure 7 illustrates how the tensile stress is induced due to the plastic deformation. Assuming the Cu stress is zero at $T_0$, shown in Fig.7 (a), it becomes compressive if the

temperature increases to T (Fig.8 (b)) since the CTE of Cu is larger than that of Si substrate. If the stress and temperature are in the proper ranges, inelastic deformation could happen under the compressive stress, resulting in the shrinkage of the Cu when the temperature is cooled down to $T_0$ again. Since the Cu/substrate interface is well bonded, tensile stress arises in the Cu due to the confinement from the substrate, as shown in Fig.7 (d). A condition that must be satisfied in order to generate of tensile stress is that the plastic deformation occurring when the temperature increases from $T_0$ to T is not totally reversible when the temperature decreases to $T_0$ again. Generally, this condition can be satisfied as following.

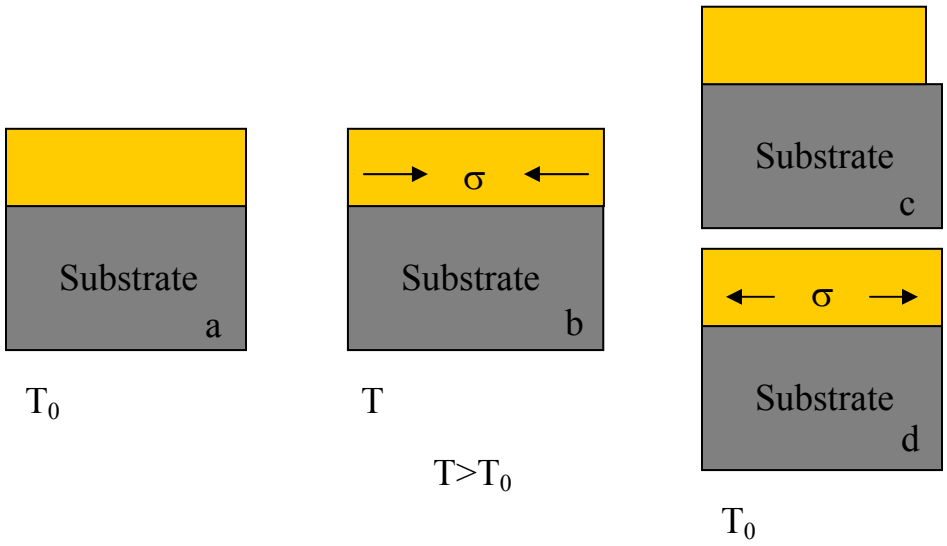


Figure 4.7 Schematic of the induction of stress due to plastic deformation

Electroplating results in a low tensile stress level, which may not be zero, in the as-deposited Cu. The stress level may become higher due to grain growth at room temperature. A low initial tensile stress at room temperature will result in a higher

compressive stress as the temperature increases, shown in Fig.8, since the CTE of Cu is larger than that of the Si substrate. When the temperature is high enough, inelastic deformation in the Cu line will occur by yielding or creep. Upon cooling down, the

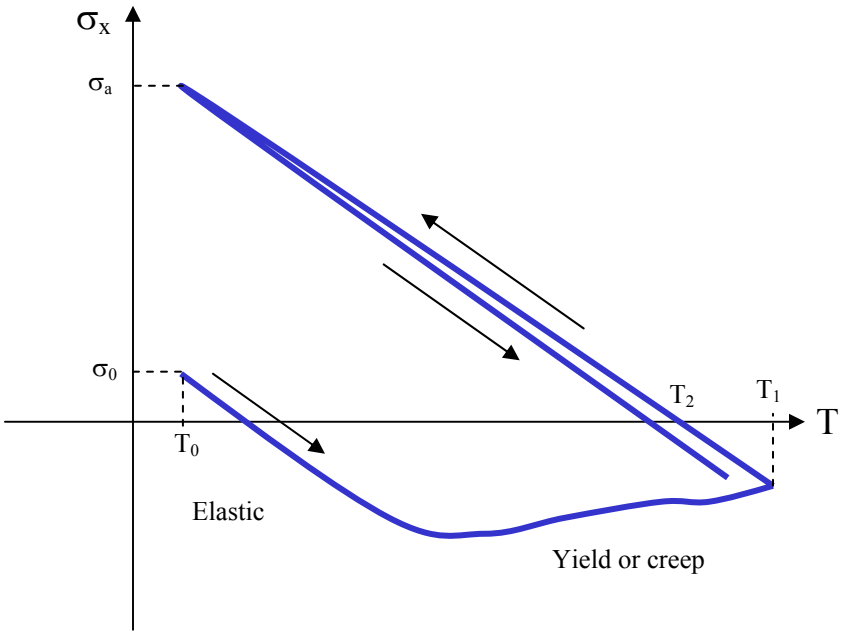


Figure 4.8 Schematic of $\sigma_x$ of a Cu line during thermal cycling

compressive stress decreases elastically to zero from $T_1$ to $T_2$. Further temperature decreases build-up the tensile stress in the Cu line. The magnitude of the tension depends on the temperature difference from $T_2$ to $T_0$, as well as on any stress relaxation process that occurs upon cooling down. Figure 8 indicates that a higher $T_1$ will be correlated to a higher zero stress temperature $T_2$, resulting in a larger temperature difference from $T_2$ to $T_0$ and thus a higher residual stress is built up at $T_0$. With a higher initial stress at $T_0$, the stress-temperature curve in the subsequent heating cycle will be different and plastic deformation may not occur since the compressive stresses may not become high enough

before higher end-point temperature, $T_1$ , is reached. Figure 8 also indicates that the conditions combining temperature and stress in the 1st heating up and cooling down are not symmetric. Upon heating up, the stress is higher at the high temperature range but lower at the low temperature range compared to that upon cooling down, so that the plastic deformation upon heating up is not canceled by that upon cooling down.

### 4.3.5 Summary

In summary, thermal processes such as annealing treatments and the deposition of dielectrics will result in the build-up of tri-axial residual stress at room temperature in Cu lines, and higher end-point temperatures give higher residual stress. Grain growth and plastic deformation of the Cu lines upon heating up are considered to be the dominant reasons for the build-up of the residual stress upon cooling down.

## 4.4 EFFECTS OF ILD AND LINE WIDTH ON THERMAL STRESS OF COPPER LINES DURING THERMAL CYCLING

In this study, structures with three kinds of ILD, SiOF, CDO and SilK™, and two sets of line width/pitch, 0.4μm/0.8μm and 0.2μm/0.4μm, were used for comparison. The ILD thickness was 0.69μm and the height of the Cu lines was 0.35μm. All the structures were passivated by a $SiN_x$ layer. XRD stress measurements were performed in-situ in two thermal cycles from RT to 400°C at a ramp rate of 2°C/min. Since in the first heating up, the Cu lines might undergo the change of microstructure and aggressive plastic deformation, only the results from the second cycle are presented.

### 4.4.1 XRD stress measurements in Cu lines

The tri-axial stress characteristics of the Cu lines measured by XRD in the Cu/SiOF, Cu/CDO and Cu/ SilK™ structures with line widths of 0.4μm and 0.2μm are presented in Figs. 9-11, where $\sigma_x$, $\sigma_y$ and $\sigma_z$ are along, across and normal to the line, respectively. In these interconnect structures, the principal stresses of the Cu lines are shown to decrease almost linearly with temperature, without noticeable stress hysteresis, from a high tensile stress at RT to a compressive stress at 400°C. The decrease of the stress with temperature is believed to be due to the larger CTE of Cu (17.7ppm) than that of Si substrate (2.61ppm) that provides the dominant confinement on the Cu lines. At room temperature, the stress along the lines ($\sigma_x$) is the largest principal stress component,

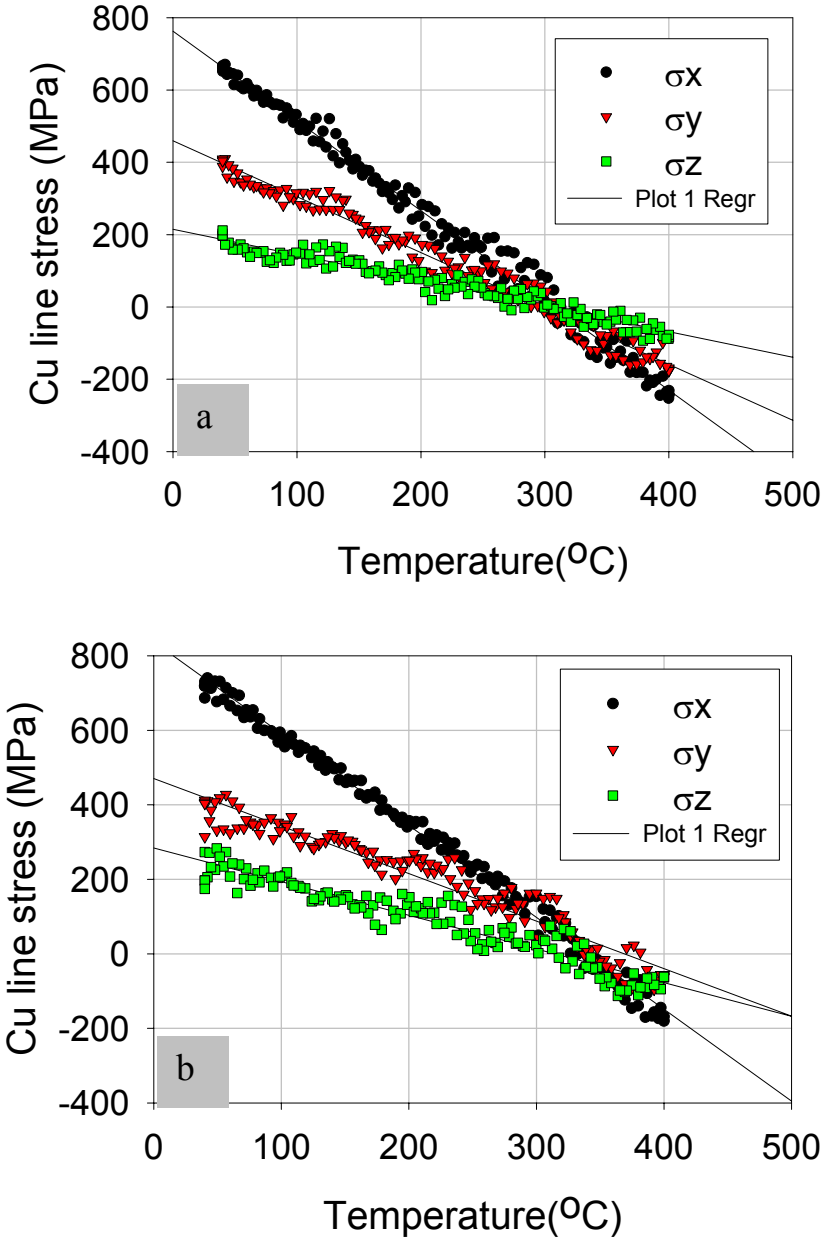


Figure 4.9 XRD results of the thermal stresses in Cu lines in the Cu/SiOF structure with the line widths of: (a) 0.4μm and (b) 0.2μm.

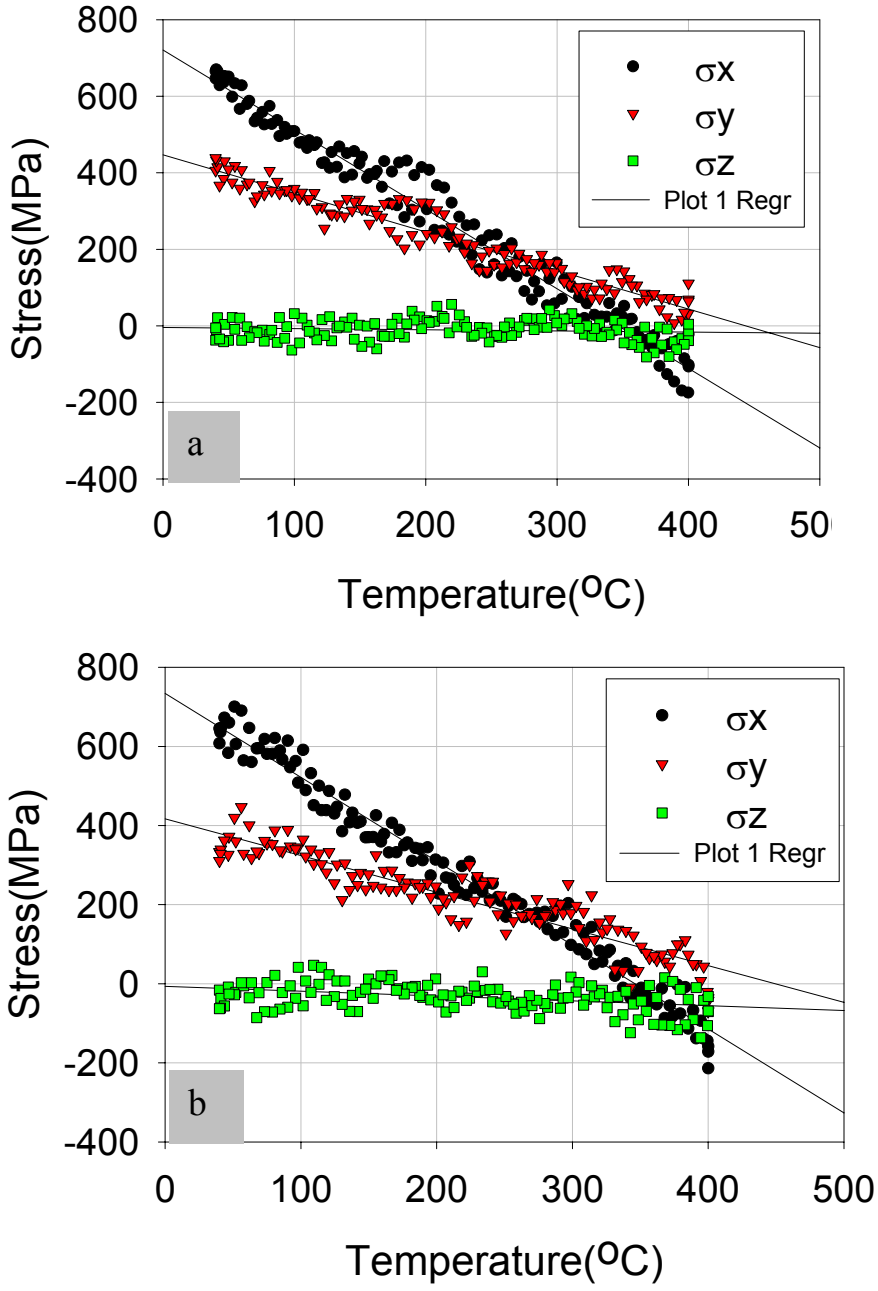


Figure 4.10 XRD results of the thermal stresses in Cu lines in the Cu/CDO structure with the line widths of (a) 0.4μm and (b) 0.2μm.

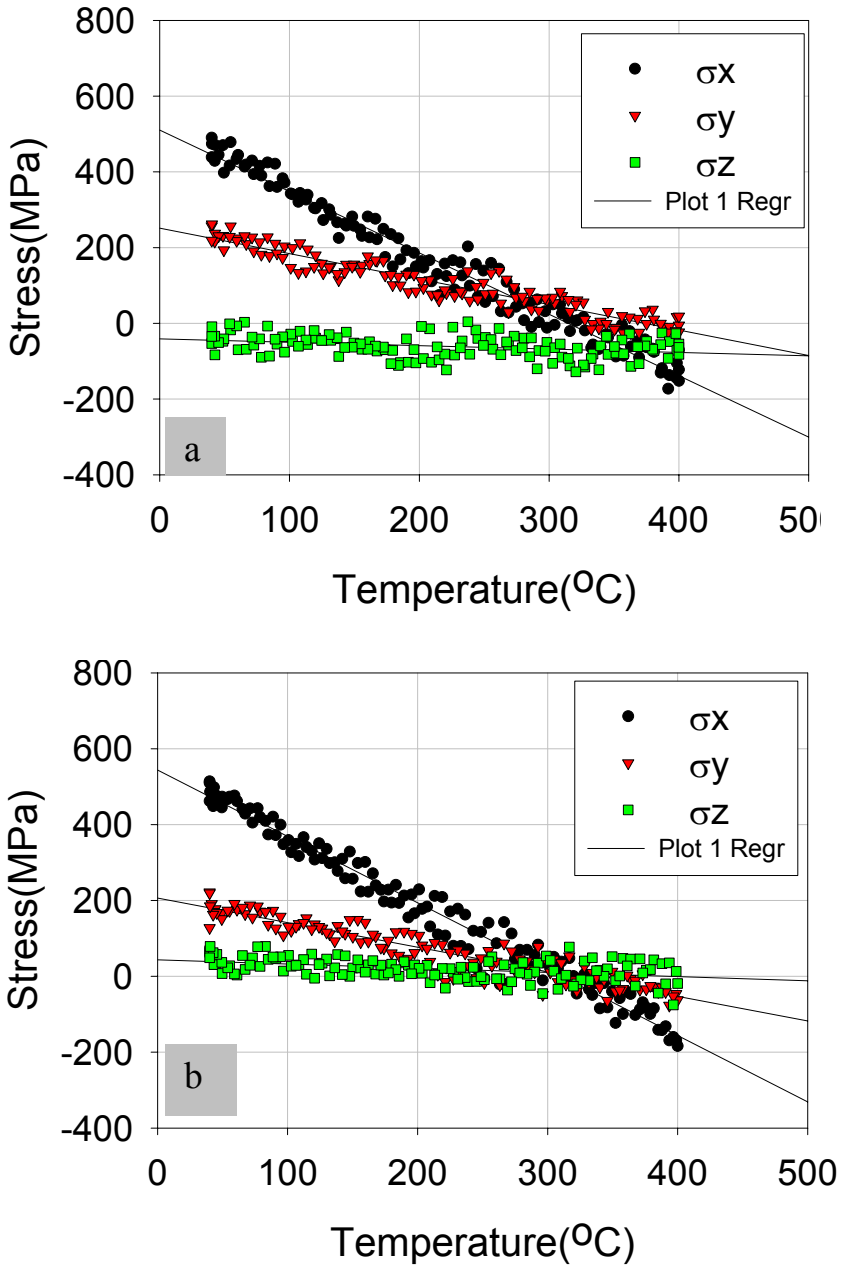


Figure 4.11 XRD results of the thermal stresses in Cu lines in the Cu/SiLK™ structure with the line widths of (a) 0.4μm and (b) 0.2μm.

followed by the stress across ($\sigma_y$) and normal ($\sigma_z$) to the lines. Compared to the principle stresses in the SiOF structure, the slopes of $\sigma_y$ and $\sigma_z$ plots for the CDO structure are obviously smaller. In particular, the slope of $\sigma_z$ decreases to about zero. For the SiLK™ structure, there is a further decrease of the slope of $\sigma_y$, and a decrease of the slope of $\sigma_x$. As a result, the hydrostatic stress in the Cu lines, calculated as $(\sigma_x+\sigma_y+\sigma_z)/3$, a driving force for stress-induced void formation, is highest in the SiOF structure, followed by the CDO and SiLK™ structures. Comparing the stress in (a) with that in (b) in Figs 9-11, no clear trend of the effect of line width on the stress in Cu lines is evident.

During thermal cycling, the stress in the Cu lines at a given temperature T could be described as

$$\sigma_T = \sigma_0 + \Delta\sigma_{th} - \sigma_p \qquad (1)$$

where $\sigma_0$ is the initial stress at $T_0$; $\Delta\sigma_{th}$ is the elastic stress change due to the thermal expansion mismatch of the Cu lines with the surrounding materials from the temperature excursion, while $\sigma_p$ is the stress relaxed due to the plastic deformation of the Cu lines in the period of the temperature change. Equation 1 indicates that the absolute value of the stress in Cu lines depends not only on the confinement from the surrounding materials ($\Delta\sigma_{th}$), but also on the processing of the interconnects ($\sigma_0$) and the plastic deformation behavior of the Cu lines ($\sigma_p$). For example, new ILD materials introduced for Cu interconnects will change the confinement on Cu lines as well as the process of the Cu interconnects, resulting in the change of the stress in the Cu lines. When the plastic deformation is ignored based on the linear behavior of the stresses in Figs.9-11, the slope

of a stress-temperature curve of the Cu lines is determined by the confinement from the surrounding materials. For this reason, the following discussion on FEA modeling of Cu lines will be based on the stress slope instead of the stress itself.

### 4.4.2 FEA modeling of the stress in Cu lines

A finite element analysis (FEA) code, called ABAQUS was used to set up the 3D elastic model with 8-node linear brick elements. The model includes half of a pitch combining the passivation layer, the Cu line, the ILD, the diffusion barrier and part of the Si substrate. Since the samples contain thousands of parallel Cu lines with the length much larger than the width, a mirror symmetry condition was then applied to the front and the right planes of the structure. The back and left planes were constrained by the CTE of Si while remaining straight to ensure the periodicity of the structure and the bending of the substrate was ignored. The calculation was performed under the linear elastic assumption with a thermal loading of -360K from an initial state of zero stress. Table 1 lists the material properties used in the calculation.

Table 4. 1 Mechanical properties of the related materials at 25°C

| Material | E (GPa) | $\nu$ | $\alpha$ (ppm/°C) |
|---|---|---|---|
| Copper | $C_{11}$, $C_{12}$, $C_{44}$ | | 17.7 |
| Silicon | 130.2 | 0.28 | 2.61 |
| SiOF | 71.7 | 0.16 | 0.94 |
| CDO | 4.47 | 0.30 | 12.9 |
| SiLK™ | 2.45 | 0.35 | 66.0 |
| Ta | 185.0 | 0.34 | 6.5 |

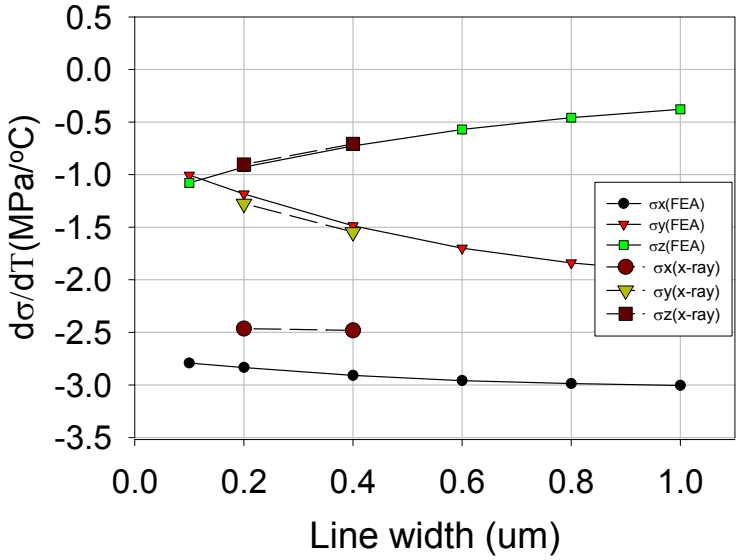


Figure 4.12 Comparison of the XRD and FEA results of the stress slope in Cu lines in the Cu/SiOF structure.

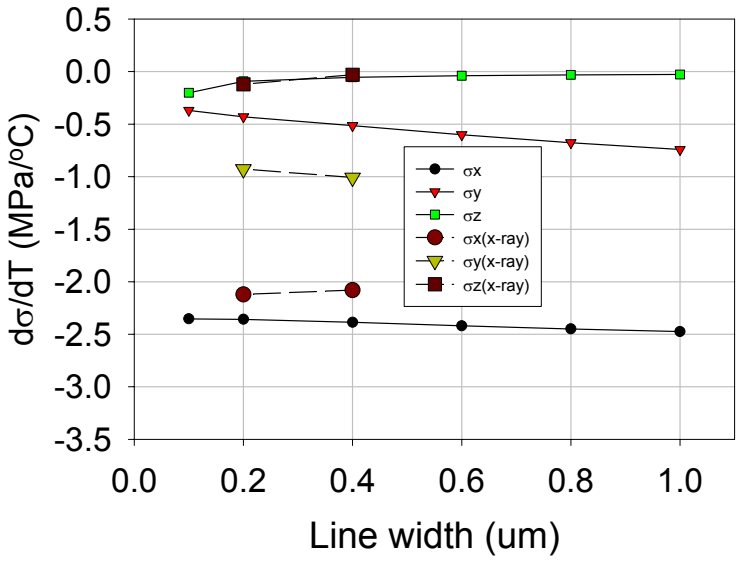


Figure 4.13 Comparison of the XRD and FEA results of the stress slope in Cu lines in the Cu/CDO structure.

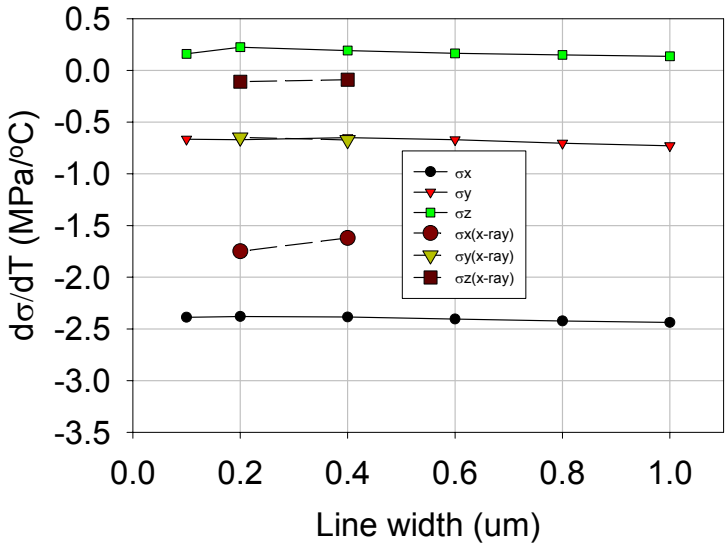


Figure 4.14 Comparison of the XRD and FEA results of the stress slope in Cu lines in the Cu/SiLK™ structure.

The slopes of the stress-temperature curves of the Cu lines calculated by the FEA modeling are shown in Figs 12-14 as functions of line width for the SiOF, CDO and SiLK™ line structures, respectively, compared with the XRD results of the measured stress slopes for the 0.4 and 0.2 μm line structures. In the SiOF structure, the shrinking of the linewidth caused an increase of the absolute value of the stress slope along z direction, but decreases of those along the x and y directions, indicating that the confinement normal to the line direction was enhanced while those along and across the line are weakened. A good agreement between the measured and calculated stress slopes in all directions is observed. It is interesting to note that the slopes of the stress-temperature curves for the two low-k dielectrics do not seem to vary much as the linewidth decreases. It is shown later that the stresses in the ILD change considerably with linewidth, suggesting that the thermomechanical interaction between Cu and ILD does change.

Therefore, the constant stress slopes with linewidth suggests that, compared with the contribution from the barrier and cap layers, the contribution to stress confinement of Cu lines from these soft low-k materials is relatively small.

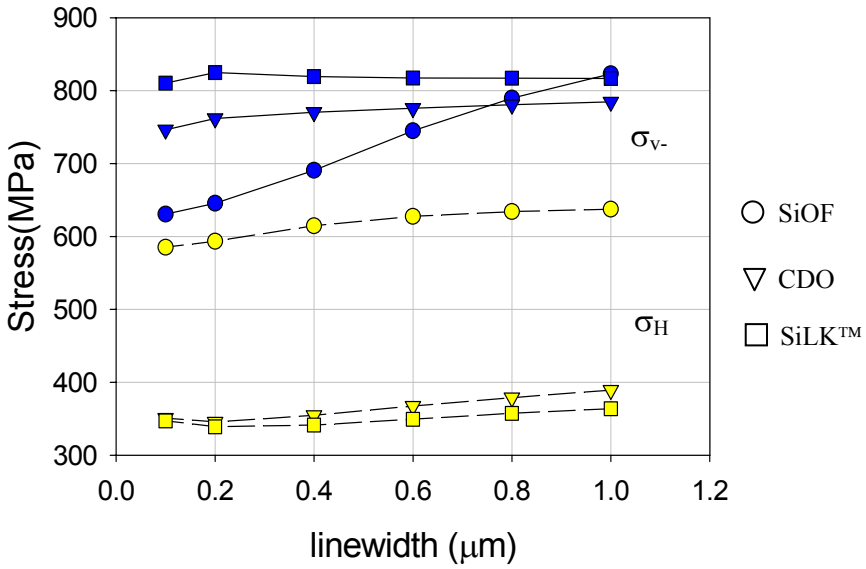


Figure 4.15 Effects of ILD and linewidth on the hydrostatic stress and Von-Miss stress in Cu lines.

Figure 15 shows the FEA results of the linewidth dependence of the hydrostatic stress and von-Mises stress in Cu lines in the SiOF, CDO and SiLK™ structures. The hydrostatic stress in the SiOF structure slightly decreases from 635MPa to 585MPa as the line width shrinks from 1.0 to 0.1μm. Those in the CDO structure and the SiLK™ structures are similar, slightly decreasing with line width from 1.0 to 0.2μm, but then increasing with further decrease of line width. The increase at small linewidths occurs because the confinement from the diffusion barrier plays a more important role for small linewidths.

The hydrostatic stress in the Cu lines is shown to dramatically decrease when the low-k materials replace SiOF as ILD. In other wards, the von-Mises stress in the Cu lines in the low-k ILD structures is much higher than that in the SiOF structure when the line width is smaller than 0.8μm. While the von-Mises stress in the low-k structures slightly changes with the line width from 1.0 to 0.1 μm, the one in the SiOF structure is shown to decrease dramatically as the line width shrinks. Since hydrostatic stress is considered to be the driving force for stress-induced void formation and the von-Mises stress drives the plastic yield, the Cu lines in the CDO or SiLK™ structures are expected to be safer from stress-induced void formation but more prone to plastic yielding than those in the SiOF structure.

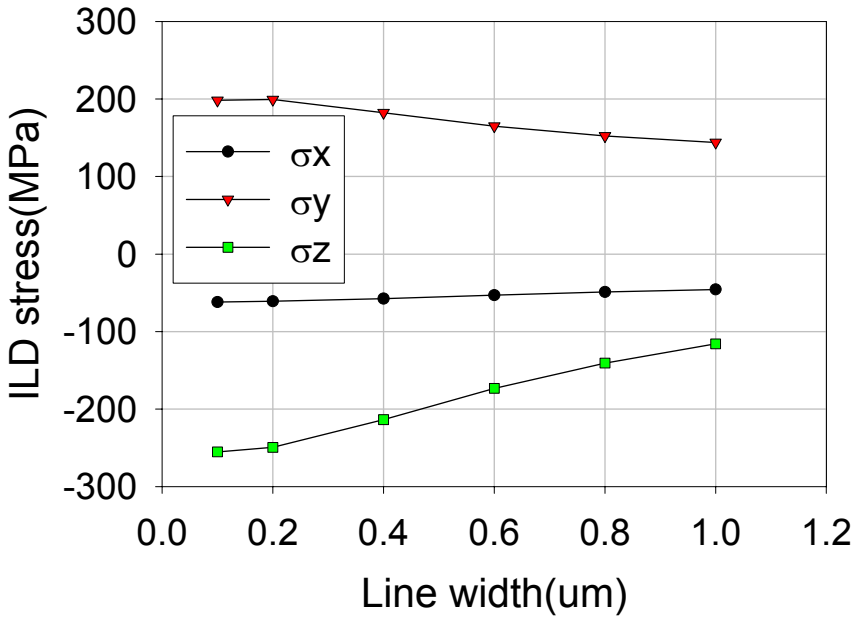


Figure 4.16 FEA results of the effect of line width on the stress in the ILD in the Cu/SiOF structure.

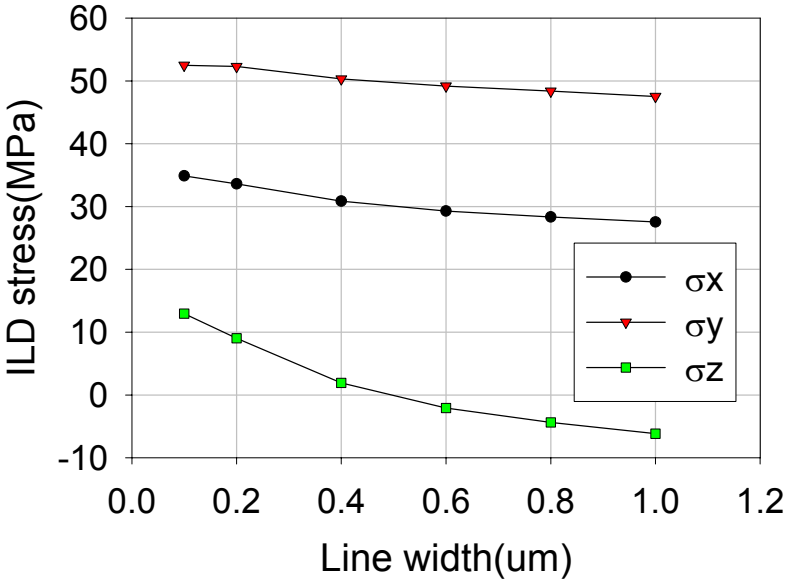


Figure 4.17 FEA results of the effect of line width on the stress in the ILD in the Cu/CDO structure.

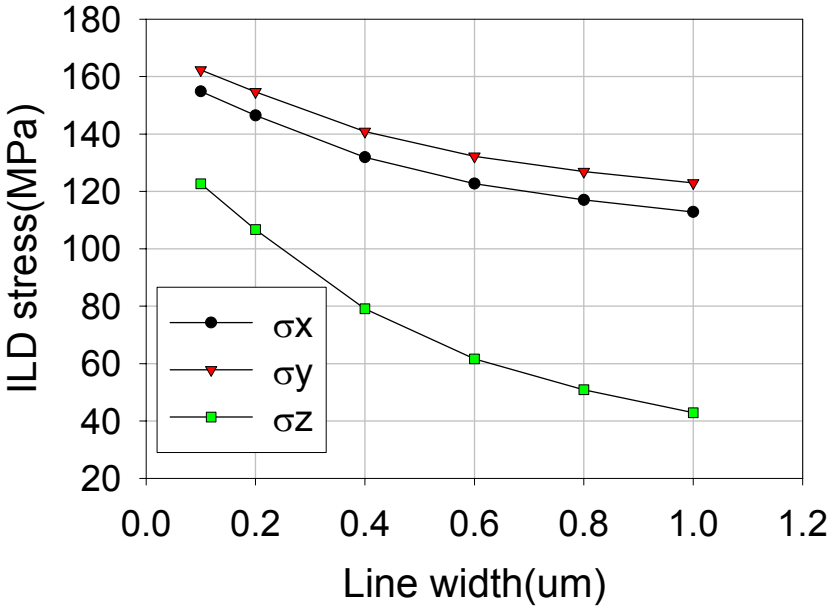


Figure 4.18 FEA results of the effect of line width on the stress in the ILD in the Cu/SiLK™ structure.

### 4.4.3 FEA modeling of the stress in ILD

FEA was extended to calculate the stress in the low k dielectrics. The results are presented as a function of the Cu linewidth in Figs. 16-18 for the ILD of SiOF, CDO and SiLK$^{TM}$ respectively. The stresses plotted here represent the stress values obtained by averaging over the ILD cross section between the Cu lines. All the stress levels vary considerably with the Cu linewidth, suggesting that the confinement on the ILD from the surrounding materials such as Cu line, the barrier and cap layers varies with the line

width. For a strong material such as SiOF with a low CTE, the confinement induces the stresses with opposite signs along y vs. x and z directions. For a soft material such as SiLK$^{TM}$ with a large CTE, the stress state becomes more hydrostatic with the decrease of the Cu linewidth. Such a stress state is significantly different from that observed in the SiOF structures. Since the channel cracking in ILD is becoming a reliability concern in Cu interconnects due to the introduction of the mechanically weaker low-k materials to replace silicon oxide, the high tensile stress state may raise the risk of failure in the low-k ILD's.

### 4.4.4 Summary

Thermal stress in Cu lines was evaluated using XRD method and a 3D FEA model. The low-k ILD's with smaller modulus and higher CTE values were found to provide less confinement on Cu lines and to modify residual stresses in Cu lines following thermal cycling, giving lower hydrostatic stresses but higher von-Mises stresses. These results suggest that the introduction of low-k ILD should mitigate the risk

of stress-induced void formation, but increase the possibility of plastic yielding in the Cu lines. While the stress in the Cu lines in the low-k structures only showed slight changes with e line width in the sub-micron range, the stress in the low-k ILD's became higher and more hydrostatic with the decrease of the line width, aggravating the risk of channel cracking in ILD's and interfacial delamination in interconnects.

# Chapter 5 Stress induced void formation in passivated Cu films

## 5.1 INTRODUCTION

Stress voiding, also known as thermal voiding and creep voiding in metallization has become an increasingly important concern in the microelectronic industry since 1984, when it was first reported by Curry et al [5.1]. It is believed to be one of the mechanisms to relax the stress in metal lines. These voids, named stress-induced voids (SIVs), cause serious yield and reliability issues in metallization.

The formation of SIV during the processing of interconnects may increase the defect density and reduce the yield of interconnects, which undergo thermal cycling for annealing or deposition of dielectrics. Stress voiding happens in the suitable stress and temperature ranges during thermal cycling. In aluminum metallization, it was shown that the nucleation and growth of SIVs occurred upon cooling down after the annealing of the structure at an elevated temperature [5.2]. Visible voids could be found after the dielectric deposition in Al lines [5.3-4]. Fast initial void growth while cooling was found to result in a void volume of 0.35% [5.5]. Void formation was also observed in Cu films [5.6] and Cu via structures [5.7] after thermal cycling. The increasing density of VLSI microcircuits requires the dimension of interconnect system shrink and that more levels of metallization to be added [5.8]. During the processing of the higher-level metallizations, the SIVs in lower levels were believed to nucleate and grow [5.9]. The greater the thermal loading, the higher the density of the SIV related defects in the multilevel interconnects.

In addition, during storage and service of the chips at elevated temperatures and even at room temperature, SIVs can grow steadily, increasing the resistance of the interconnect structures [5.10-14] and ultimately affecting the functionality of a circuit. More seriously, a void can grow big enough to cause an open circuit. Further more, SIVs would influence the electromigration (EM) behavior in interconnects. It has been found that the electromigration failure time was reduced and the time to failure decreased with increasing stress voiding severity [5.15]. Current crowding and joule heating around the initial SIVs were believed to cause the EM degradation [5.16]. A large pre-existing stress void in the metal line was shown to be more prone to growth during electromigration than a small one due to the stress gradient along the line generated by the void [5.17]. The current density exponent in Black's Equation was found to decrease in metal lines with pre-existing SIVs [5.14]. Stress voiding was also considered to be one of the reasons for early failure in the electromigration tests [5.18]. Although more research work is needed, it is quite natural to conjecture that SIVs can serve as nucleation sites and sources of vacancies for electromigration voiding and thus accelerate the electromigration failure during operation.

Recently, Cu/low-k interconnect systems are widely used to replace Al/$SiO_2$ interconnects in order to reduce the resistance-capacity (RC) delay in the continually shrinking integrated circuits. While better electromigration and stress migration (SM) performance of Cu interconnect is also expected for its much higher melting point (1083 °C) than Al (660 °C), the use of new materials and interconnect structures in Cu metallization brings new yield and reliability concerns that would undermine the

expected benefits. Easily oxidized, Cu does not form a rigid, impervious oxide layer, as Al does. Diffusion barriers and passivation layers are used to encapsulated Cu lines in interconnects in order to prevent Cu from diffusing into the inter-level dielectrics (ILD), making the interfaces the critical diffusion paths. In addition, Cu crystals show mechanical anisotropy with the bi-axial modulus of 261GPa in the (111) plane, 2.28 times the bi-axial modulus in the (100) plane. The corresponding ratio is 1.15 for Al crystals for which the bi-axial modulus in the (111) plane is 114.8GPa. Local stress gradients thus form in Cu films among grains with different orientations, as well as in Cu lines, resulting in local stress migration. Furthermore, electroplating technology is chosen for Cu deposition. Since the process of electroplating is done at room temperature and has a fast deposition rate, the as-deposited Cu has very small grain size that can drive a remarkable grain growth or recrystallization even at room temperature [5.19-21]. The grain boundary area in the EP Cu can provide extra free volume, enhancing void formation.

In order to study the fundamental behavior of stress voiding in Cu metallization, this chapter reports the study of void formation in passivated Cu films during thermal cycling and isothermal annealing, with its focus on the void nucleation and the kinetics of void growth. As a key factor affecting stress-induced voiding, the thermal stress of the Cu film was measured using the bending beam method. Furthermore, the local stress gradients due to the mechanical anisotropy and void formation were evaluated using finite element analysis (FEA).

## 5.2 SAMPLES AND EXPERIMENTAL METHODS

The **c**opper film was prepared on a 720-micron thick (100) silicon wafer following a sequence similar to that used in a damascene line structure. A layer of $SiN_x$ was deposited on the wafer by chemical vapor deposition (CVD), followed by subsequent depositions of a diffusion barrier layer and a Cu seed layer. The rest of the Cu film was deposited using an electroplating (EP) process to yield a total thickness of 0.6μm. The film was finally passivated with a bi-layer of 50nm $SiN_x$ and 200nm TEOS. All samples in this study were cut from the same wafer.

*In situ* observation of void formation during thermal cycling was performed under an optical microscope OLYMPUS AH-2 equipped with a camera. The samples were supported on a heating stage, which made it possible to control the temperature of the sample. Under the optical microscope, voids appeared as dark spots. Pictures of the film surface were taken at selected temperatures during thermal cycles to record the void density, which was obtained by dividing the number of voids in a randomly selected area of 5x5 $cm^2$ on the pictures by the actual area of the observed surface. SEM was used for the void size measurement, which was defined as the average value of the longest and the shortest distances cross the center of the void between two points at the edge of a void. Furthermore, an AFM was employed for topography analysis of the void after the passivation layer was etched off using HF acid. The thermal stress of the film was measured using the bending beam system. A FEA code, called ABAQUS was used to evaluate the stress gradient with the elastic models set up using 20-node quadratic brick elements. In this model, only 2μm instead of the real 720μm thick Si substrate was

included since the results showed that further increase of the Si thickness in the model did not affect the stress result in the Cu film when suitable boundary conditions were used.

## 5.3 RESULTS AND ANALYSIS

### 5.3.1 Thermal stress of the Cu film during thermal cycling

Figure 1 shows the thermal stress of the Cu film during the first two consecutive thermal cycles from room temperature (RT) to 450°C with a ramp rate of 5°C/min. Similar to the results in the previous chapters, the stress decreased linearly before it reached the zero point upon heating up and underwent a change from tension to compression at about 120°C and 210°C respectively in the 1st and the 2nd cycles, compared to 370°C for the change of compression to tension upon cooling down in both cycles. It is interesting that although the thermal stress of the film followed different curves upon heating, it followed almost the same curve upon cooling down in the two cycles with a large stress hysteresis.

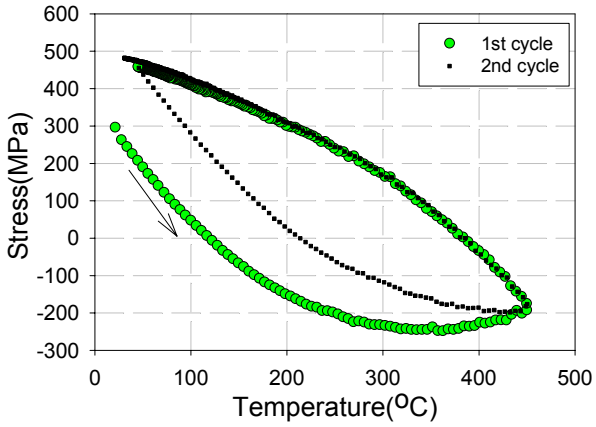


Figure 5.1Thermal stress of Cu film in the 1st and 2nd thermal cycles

Figure 2 shows a comparison of the thermal stress of the Cu film in two thermal cycles. In contrast to Fig.1, both the cycles in Fig.2 were the 1st cycles but with different cycling temperature ranges, RT to 400°C and RT to 450°C. Increasing the end-point temperature was found to increase the thermal stress in the film upon cooling down. Shown in the figure, the film stress is about 60MPa and 150MPa higher at 50°C and 350°C, respectively, when the film cooled down from 450°C, compared to 400°C. The stress difference is later shown to strongly affect the void formation in the Cu film during thermal cycling.

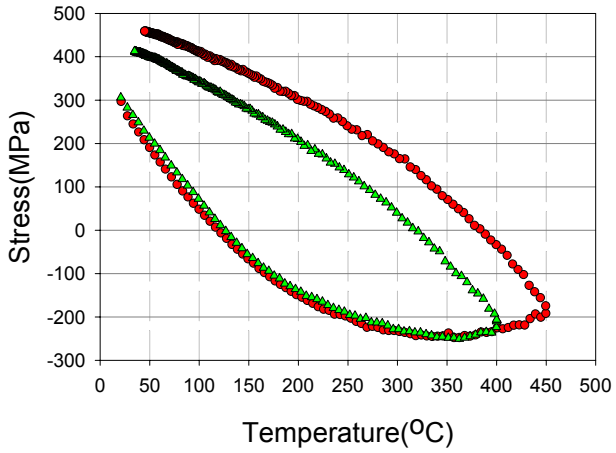


Figure 5.2 Thermal stress of Cu film in the 1st cycle with different end-point temperatures

### 5.3.2 Void formation during thermal cycling

Under the same thermal condition as the stress measurement shown in Fig 1, void formation in the first two thermal cycles was recorded under the optical microscope, as shown in Fig.3. A dark spot at the left-upper corner of each image, believed to be contamination of the sample surface, was helpful for taking the pictures in the same location of the sample surface. In the 1st thermal cycle, no void was observed until the

sample was cooled from 450°C to about 315°C. After that, voids began to appear and the void density increased until the temperature decreased below 150°C.

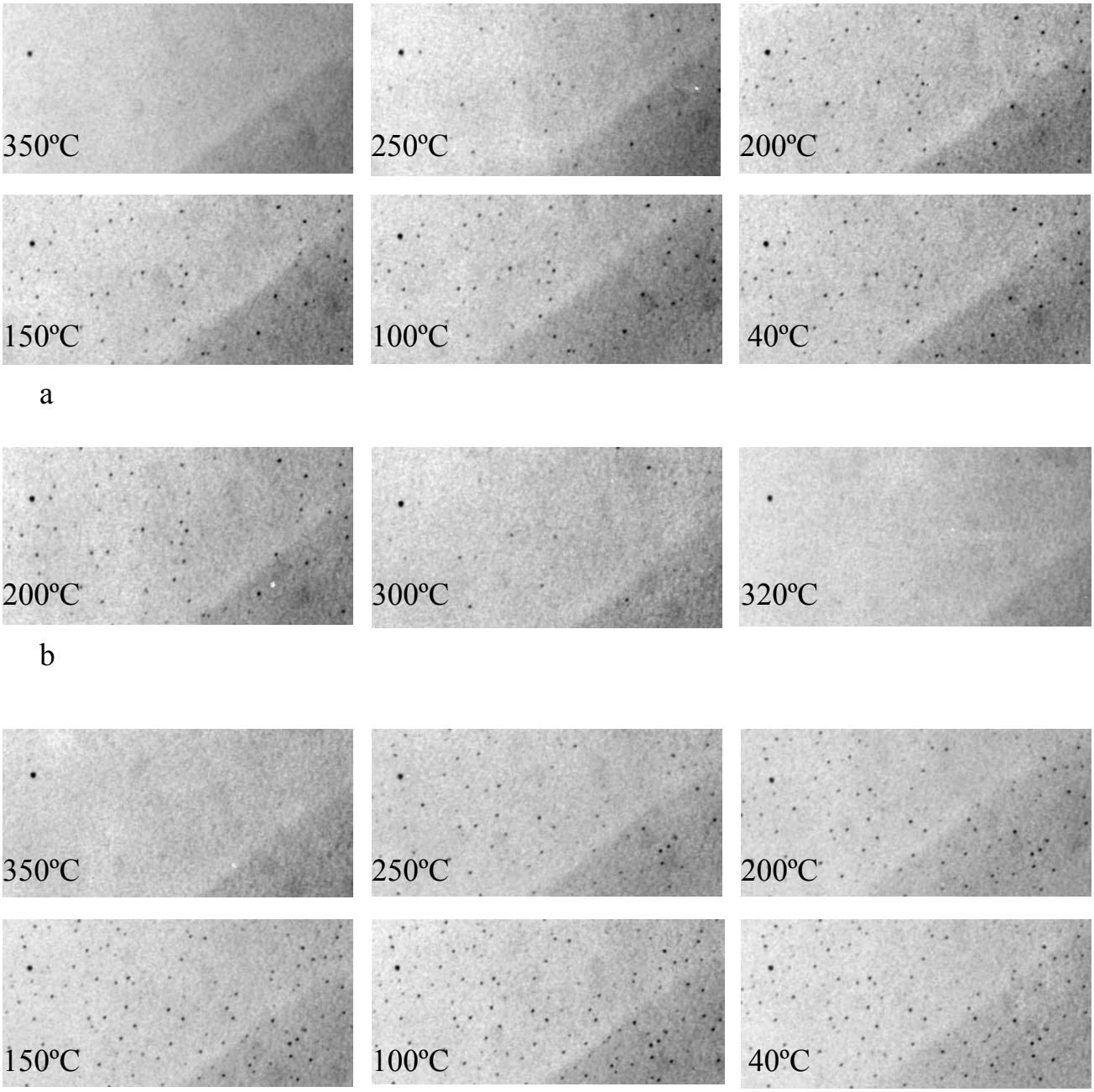


Figure 5.3 Optical microscope images of the film surface upon a) the 1st cooling down b) the 2nd heating up and c) the 2nd cooling down.

Upon heating for the 2nd cycle (Fig.3b), the void density remained unchanged until the temperature reached 280°C, at which temperature the thermal stress became compressive, as shown in Fig.1. Upon further temperature increase, the voids gradually became faint and disappeared. This behavior indicates that the voids were stress-induced, since the change occurred under compressive stress. Finally, no voids were observed after the temperature increased beyond 330°C. Voids formed again as shown in Fig.3c upon the 2nd cooling below 320°C. The void densities as functions of temperature during cooling in the two thermal cycles are shown in Fig.4. These data indicate that the void density increased upon cooling but it was higher at a given temperature in the 2nd cycle than in the 1st cycle despite the same stress in the film. Difference in the void formation sites can be observed by comparing the images at 40°C in the 1st and 2nd cycles, as shown in Fig.2a and Fig.2c receptively. The majority of the voids forming in the 1st cycle appeared again in the 2nd cycle, but a few disappeared or became faint under the microscope. Many voids formed at new sites in the 2nd cycle.

During the 1st cooling cycle, the ramp rate was found to affect the void formation as shown in Fig.5. A higher ramp rate was found to result in a lower temperature where the first void appeared and a lower void density at a given temperature. As shown in Fig. 5, the void density at room temperature after the 1st cycle with a ramp rate of 8°C/min was found to be only about 3/5 of that with a ramp rate of 2°C/min. In chapter 3, the ramp rate was shown to have a negligible effect on the thermal stress in Cu films upon cooling down, suggesting that the difference in the void density was not due to the

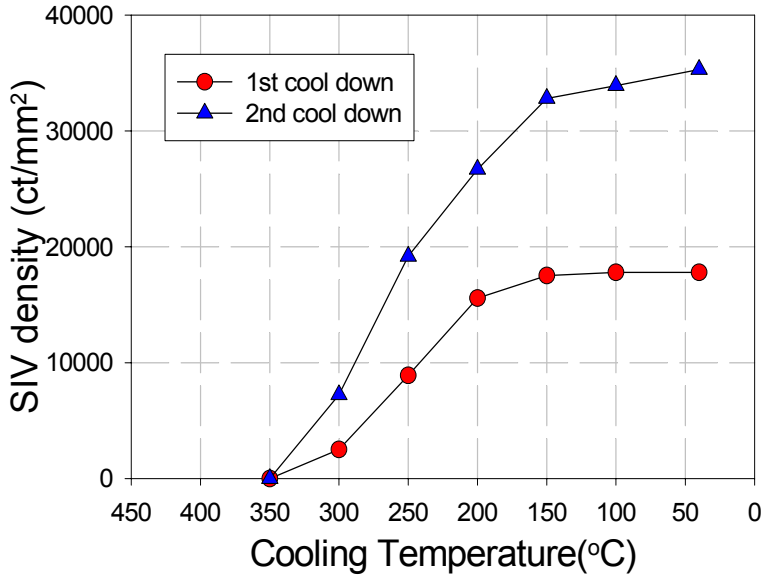


Figure 5.4 Void densities as a function of temperature upon cooling down in the two thermal cycles

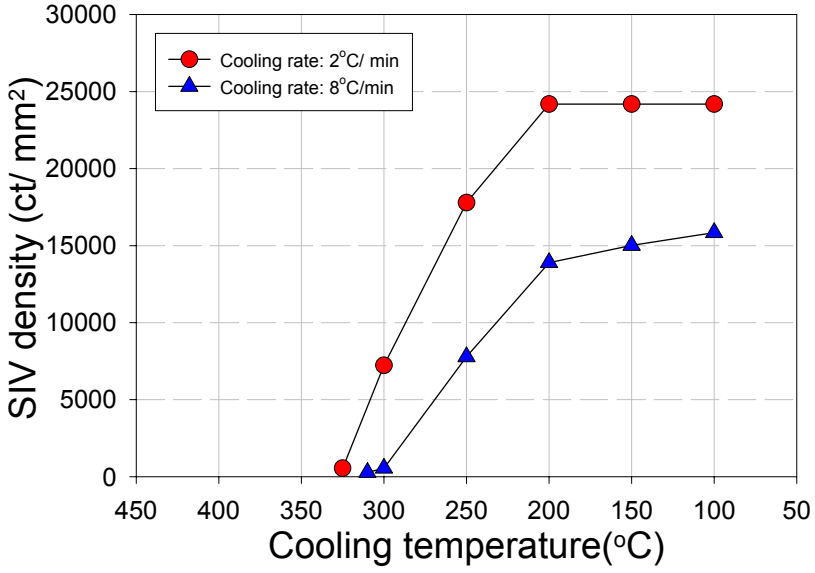


Figure 5.5 Ramp rate dependence of the void density upon cooling down

difference of stress. Further more, it was found that if the sample was cooled from 450°C to room temperature (RT) with a fast cooling rate (in air), no voids were observed.

The end-point temperature, which determines the film stress following cooling, was also an important factor affecting the void formation. When it was 400°C instead of 450°C, no voids were observed upon cooling down to room temperature. The absence of voids was believed to result from the decrease of the stress in the film upon cooling down when a lower end-point temperature was used, as shown in Fig. 2.

The above results suggest that the factors affecting the void formation in Cu film not only included thermal stress and temperature, but time and thermal history as well.

### 5.3.3 Void formation in isothermal annealing

In order to study the dependence of the void formation on thermal stress and temperature, isothermal annealing was performed at different temperatures from 100°C to 300°C with an interval of 50°C after the samples were cooled down from 400°C. 400°C was chosen as the end-point temperature instead of 450°C because that void formation did not occur in the passivated Cu film upon cooling from 400°C. As a result, the initial void size and void density of the isothermal annealing could be considered to be zero. The void density determined from the optical microscope and the void size measured using SEM are shown in Fig.6 after the samples were annealed for 20 hours at different temperatures, indicating that both the void density and void size have peak values but at different temperatures. The peak value of the void density at 150°C is about five times

and more than fifteen times higher than that at 100°C and 300°C respectively. At 250°C, the void size has its peak value, which is four times bigger than the sizes both at 100°C and 300°C.

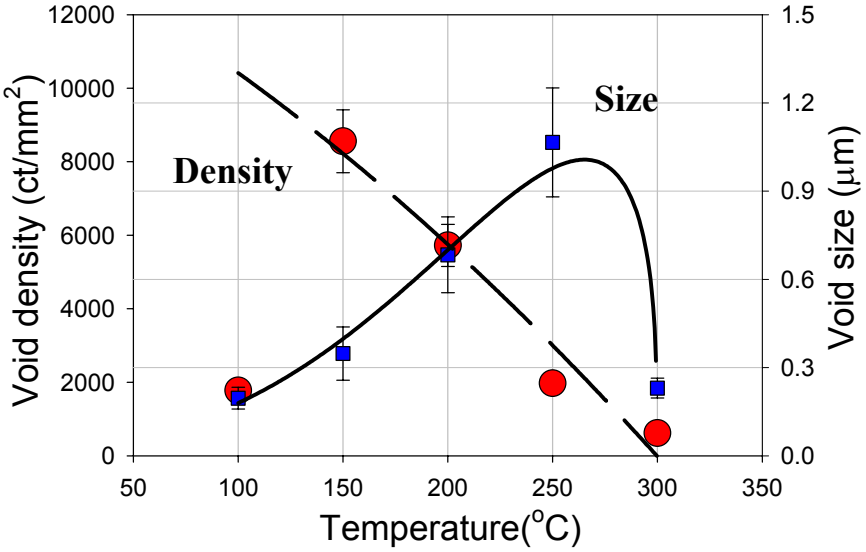


Figure 5.6 Temperature dependence of the void density and void size in isothermal annealing

During void growth under isothermal annealing, atoms diffuse away from the void with the atomic flux driven by a stress gradient as given by the Nernst-Einstein equation:

$$J = -\frac{D_{eff}}{kT}\nabla\sigma \tag{5.1}$$

where $D_{eff}$ is the effective diffusivity, depending on the diffusion paths involved, $k$ the Boltzmann's constant, $T$ the absolute temperature while $\nabla\sigma$ is the stress gradient driving the mass transport. McPherson and Dum [5.22] first proposed a power-law creep as the

mechanism for stress relaxation driving void growth in Al lines. Accordingly, the void growth rate can be expressed as:

$$R = C(T_0 - T)^N \exp(-\frac{Q}{kT}) \tag{5.2}$$

where R is the void growth rate, $T_0$ the stress-free temperature, $T$ the annealing temperature, $N$ the "creep exponent", and $Q$ is the activation energy. This model was used to study stress voiding in Cu interconnect structures where the creep rate was deduced by measuring the resistance increase of the interconnect structures [5.23].

Generally, power-law creep is related to diffusion through dislocation cores [5.24]. In this study, most of the voids were found to locate at the junctions of grain boundaries and the Cu/passivation interface, shown later in the SEM and AFM images. That suggests that the grain boundaries and interfaces were the dominant diffusion paths for the void growth. Thus a linear diffusional creep instead of a power-law creep as a driving force for void formation in Cu films was proposed, giving the following void growth kinetics:

$$V \propto d^3 = A\frac{(\sigma - \sigma_0)}{T}\exp(-\frac{Q}{kT}) \tag{5.3}$$

where $V$ is the volume of the void, which is proportional to the cube of $d$ , the measured one-dimension size. $A$ is a material constant, $\sigma$ the film stress, $\sigma_0$ the threshold stress for void growth and Q is the activation energy for void growth. Equation 3 is similar to the Nabarro-Herring or Coble strain rate equations for the diffusional creep, but with a different meaning of the material constant A. Using the stress determined in Fig.2 and the size in Fig.6, equation 3 was deduced to be

$$d^3 = 8.838 \times 10^7 \frac{(\sigma - 40.7)}{T} \exp(-\frac{0.747}{kT}) \quad (5.4)$$

where σ is in MPa and *d* is in μm. By curve fitting, we found a threshold stress of 41MPa and an activation energy of 0.75eV for void growth. The growth kinetics as described by equation 4 is plotted in Fig.6 as a solid line which agrees well with the observed void size *d* as a function of annealing temperature. The activation energy of 0.75eV for void growth is consistent with that of EM lifetime in Cu lines, suggesting that the interface diffusion plays an important role contributing to void growth in passivated Cu films.

At the temperature range of 150°C to 300°C, the void density was found to be proportional to the film stress. Using the same threshold stress for the void growth, the relationship can be fit as

$$N = 34.4(\sigma - 40.7) \quad (5.5)$$

where the void density N is in counts/mm$^2$ and the stress σ is in MPa. Equation 5.5 is plotted in Fig.6 as a dash line for comparison with the experimental data. It is clear that the relationship in equation 5.5 does not hold at the temperatures below 150°C, where the void density dramatically decreases. This may suggest a threshold temperature, below which no voids nucleate. Another possible reason may rely on the fact that to be visible under the optic microscope, the voids need to be bigger than a minimum size that can be resolved by the microscope, but if the temperature was too low to drive the diffusion fast enough for the void growth to reach the minimum size in the 20 hours, voids would not be visible and the density determined under the optic microscope should be reduced

dramatically. This is consistent with the observation that void formation became very slow after cooling down to below 150°C during thermal cycling.

Void formation induces damage in Cu films. In line structures, the damage due to void formation can be evaluated by measuring the resistance increase of the Cu line, which may relate to the number of voids, the void size, the void shape and the geometric location of voids etc. In the Cu film, if the damage is defined as the product of the void density with the one-dimension (1D) void size, the 2D void size and the 3D void size, shown in Fig.7, the temperature correlated to the peak value of the damage will be approximately 190°C, 215°C and 240°C, respectively. From equation 5.3, if the activation energy was evaluated by measuring the damage of the film, the deduced values will be about one third of, two thirds of, and equal to 0.75eV, respectively. That means measuring the damage of the film may not be able to accurately evaluate the activation energy for void formation.

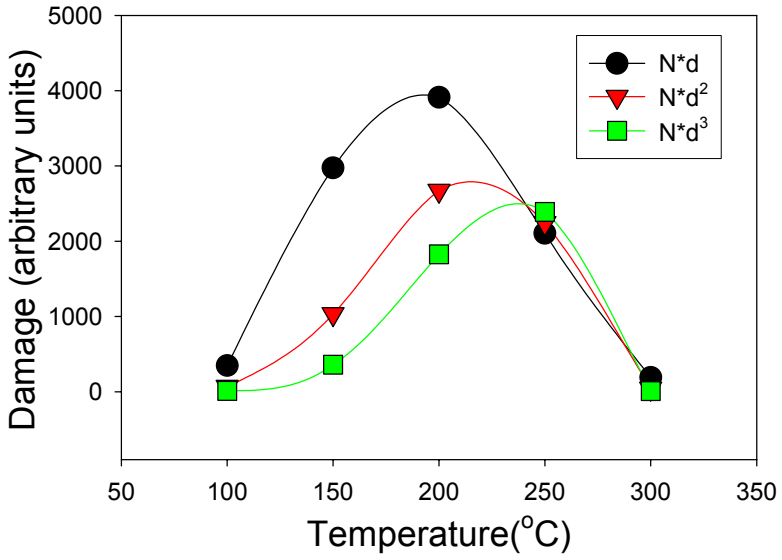


Figure 5.7 Temperature dependence of the damage by voiding with different definitions

### 5.3.4 Void growth under isothermal annealing

In this study, void growth during isothermal annealing was investigated. Cu film samples were cut from the same wafer and then put into a chamber with 50mtorr $N_2$ ambient for annealing at 250°C. At certain time of interest, one of them was taken out. The void size of the samples was determined under SEM after etching off the passivation layer by HF acid. For each sample, the sizes of 20 voids randomly selected were measured. The void size as a function of annealing time was shown in Fig. 8, where the error bar of each data point is the standard deviation of the measured values. On the samples taken out as soon as the temperature reached 250°C cooling from 400°C, no voids were observed that means the initial void size for the isothermal annealing was believed to be zero. The curve indicates a fast growth rate at the beginning of the annealing, which then decreased with time. After annealing for 20 hours, the void size can reach more than 1 micron.

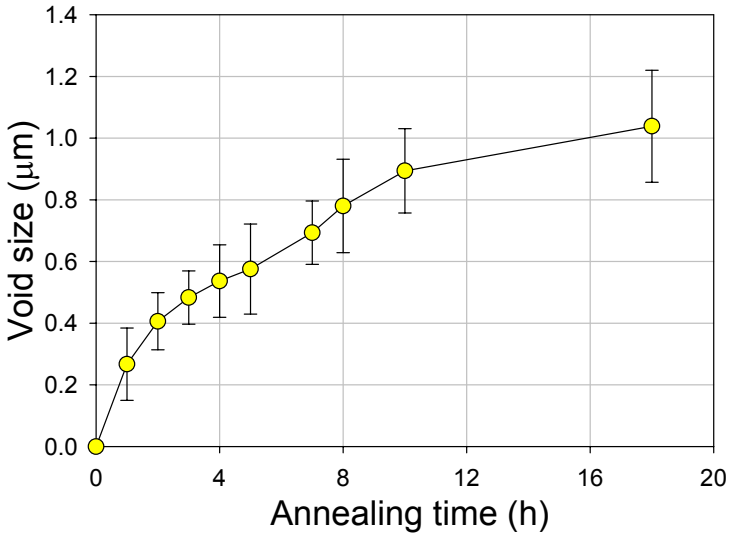


Figure 5.8 Void size as a function of annealing time at 250°C

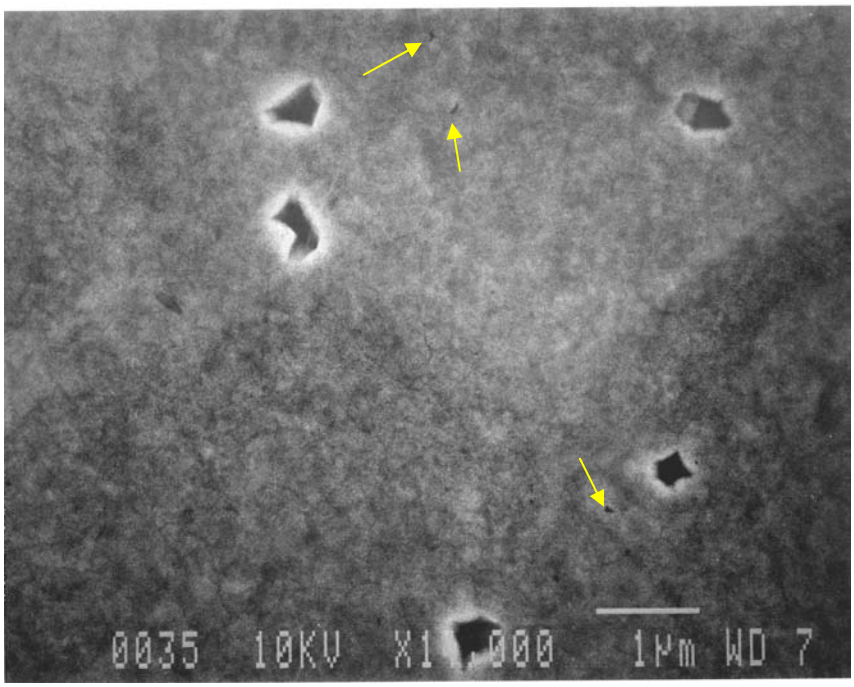


Figure 5.9 SEM image of the SIVs on a passivated Cu film after thermal cycling from RT to 450°C with the passivation etched off by HF acid. Yellow arrows point to small voids.

### 5.3.5 Voids under SEM and AFM

Figure 9 is an SEM image showing the SIV's on the passivated Cu film after thermal cycling from RT to 450°C with the passivation layer etched off. The voids appear to be multi-edge shaped, suggesting that the void growth was not isotropic and might depend on the grain orientation. Besides the big ones, there are several small voids on the film surface, some of which are indicated by the yellow arrows. The small voids may suggest that voids nucleated continuously during thermal cycling or that some sites were not favorable for void growth even though they were effective nucleation sites. Figure 10 shows the AFM images of a multi-edge void and a tri-angle void. Figure 11 shows the

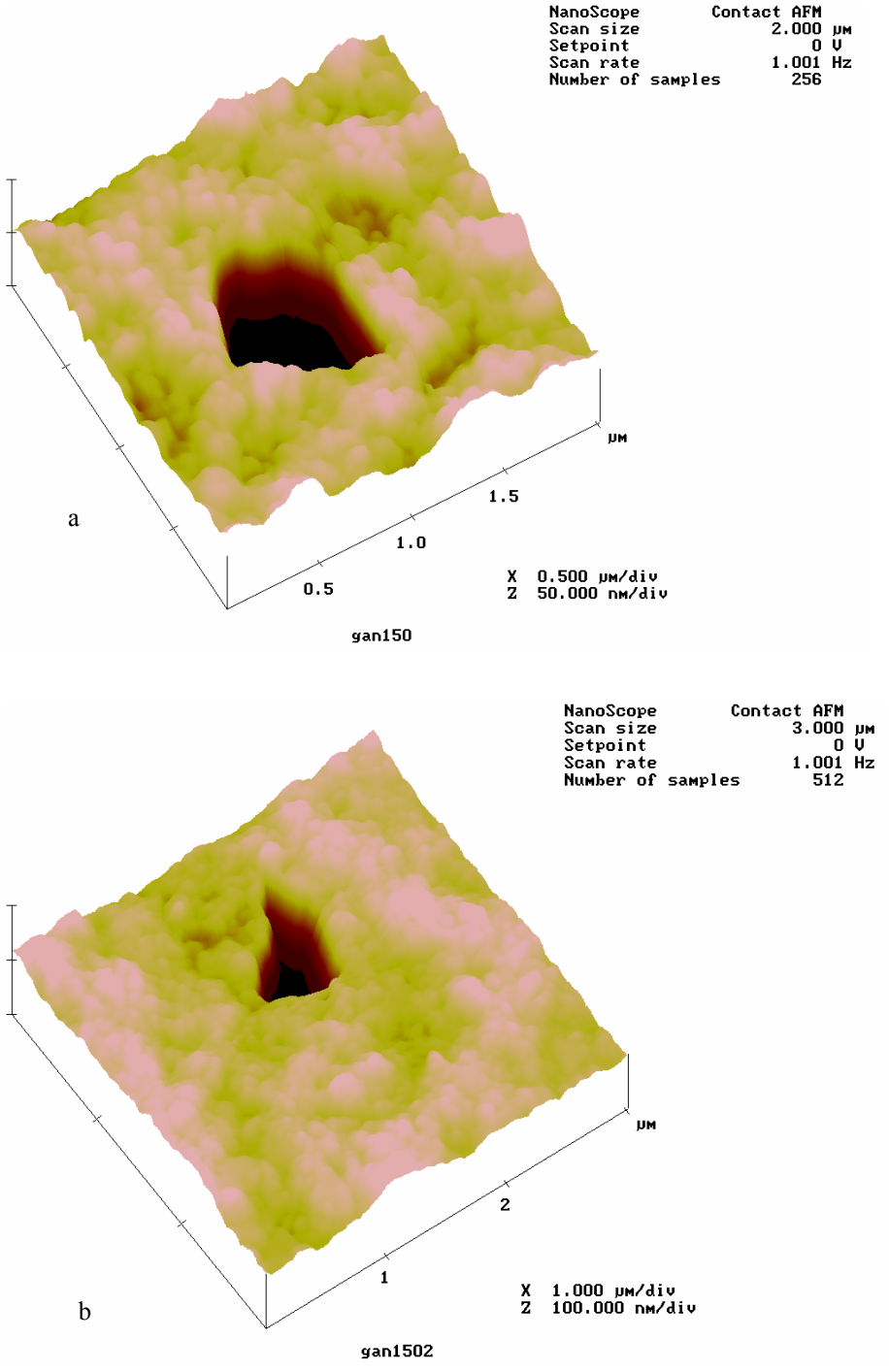


Figure 5.10 AFM images of (a) a multi-edge void and (b) a triangle void.

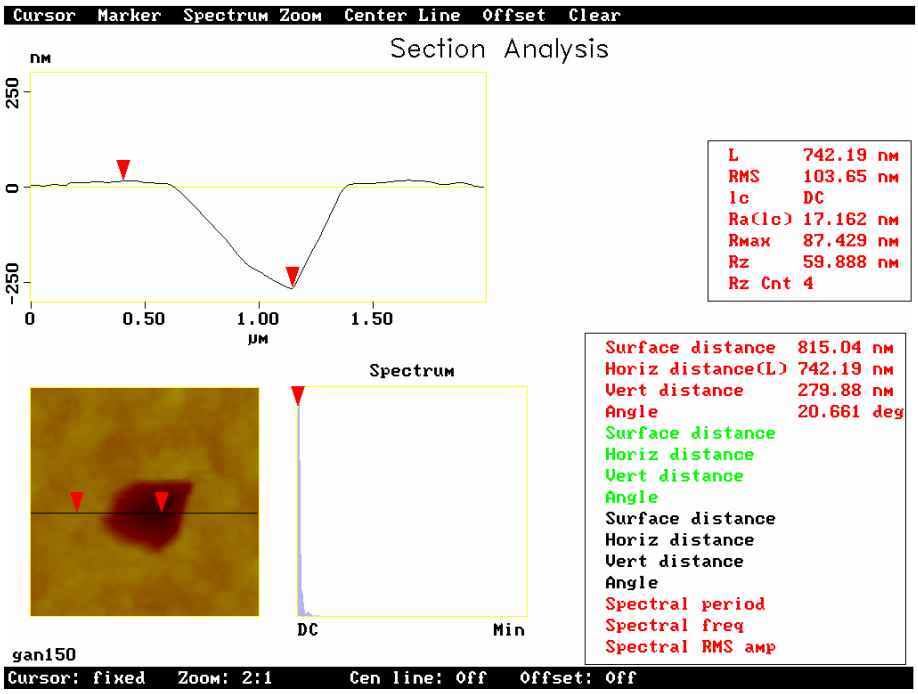


a

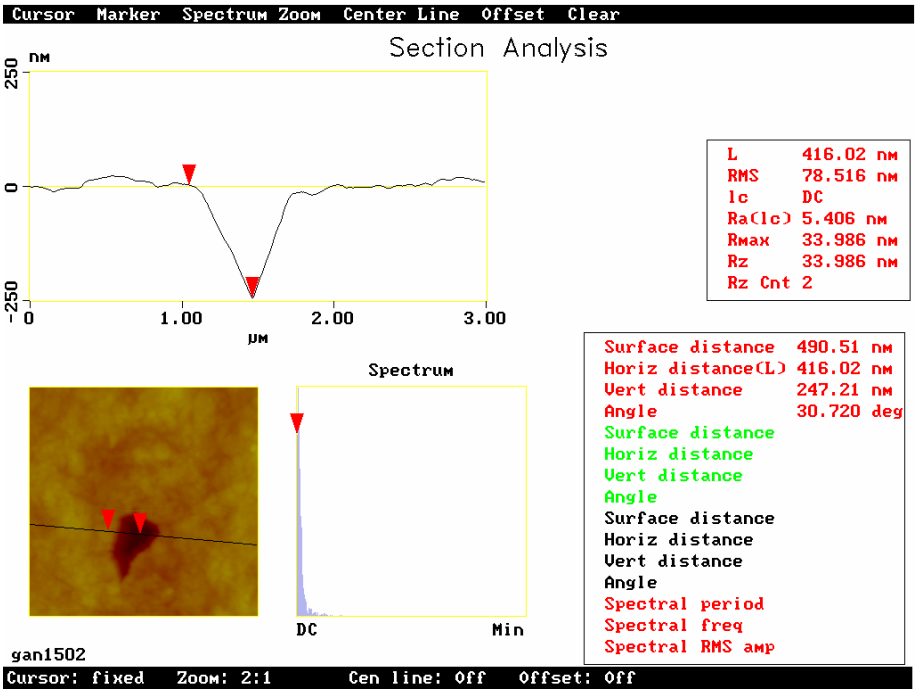


b

Figure 5.11 AFM cross-section analysis of (a) a multi-edge void and (b) a triangle void.

cross-section analysis of the multi-edge shape and the triangle shape void. The void depths are about 250nm, less than half of the film thickness (600nm). It was found that a deeper cross-section of the void with multi-edge shape was also triangle shaped, implying that the triple point of grain boundaries played an important role in the void formation.

## 5.4 DISCUSSION

### 5.4.1 Void nucleation and growth

Void nucleation and growth relies on the diffusion of vacancies and atoms. Generally, the vacancy source may include grain boundaries, dislocations and interfaces. As mentioned above, the as-electroplated Cu has a very small grain size. Ogawa et al [5.23] suggested that the annihilation of grain boundaries during grain growth provides supersaturated vacancies in the constrained interconnect structures, which would migrate to the sinks driven by thermal stress gradients and form voids. In our study, before void formation during cooling or in isothermal annealing, the samples underwent a heating cycle from RT to 450°C or 400°C. In this cycle, grain growth might not be very fast since the film was already subjected to thermal annealing during the deposition of dielectric layers (300°C to 400°C). In addition, compressive stress and plastic flow were expected to cause Cu atoms to occupy the vacancies and dramatically reduce the concentration of the vacancy from grain growth. This suggests that grain growth was not the major vacancy source for the void formation in this study.

Void formation is believed to be a mechanism to relax hydrostatic stress in metals. In Fig. 12 (a), a metal is subjected a hydrostatic stress and confined at the boundary.

Since the stress is hydrostatic without shear components, plastic yield would not happen to relax the stress. Voids will nucleate (Fig. 12 b) and grow (Fig. 12 c) at proper temperatures. As a result, the stress of the metal relaxes and thus part of the strain energy is released. It is clear shown that void grows by reducing the elastic strain of the metal.

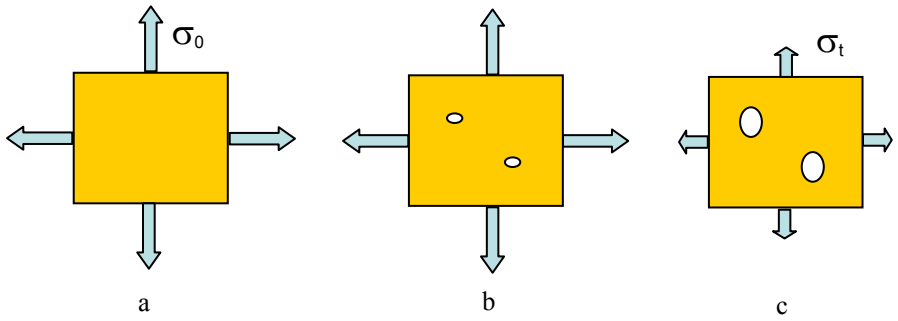


Figure 5.12 Schematic of void formation to relax hydrostatic stress in a metal: a) a metal is subjected a hydrostatic stress b) voids nucleate in the metal c) Voids grow and the stress relaxes. ($\sigma_0<\sigma_t$)

During the above voiding process, the generation of vacancies can be thermally activated with the concentration given by:

$$C_v = C_0 \exp(-\frac{Q}{kT}) \tag{5.6}$$

where $C_0$ is a constant, Q is the activation energy and $kT$ has the usual meaning. If there is a stress applied on the metal, equation (5.4) will be modified as:

$$C_v = C_0 \exp(-\frac{Q-\sigma\Omega}{kT}) \tag{5.7}$$

where Ω is the effective volume of the atom. From this equation, it is clear that a tensile stress will enhance the generation of the vacancy but the compressive stress will deplete it. This also supports the previous statement that a high supersaturation of vacancies from

grain growth would not exist in the Cu film due to the compressive stress upon heating up. Equation 5.7 also suggests that a local stress gradient will result in a local gradient of vacancy concentration, a driving force for vacancy migration.

Voids would nucleate in a metal at high temperature under tensile stress through different mechanisms [5.25]. Nucleation of an SIV can occur when vacancies accumulate in the sinks such as dislocations, grain boundaries and interfaces after migration driven by the local chemical potential gradients. During creep or plastic yielding of poly-crystals at elevated temperatures, grains may rotate or move through grain boundary sliding if there is a deformation incompatibility among them. The boundary sliding may result in cracking or voiding along grain boundaries when the movements of the adjacent grains are not well accommodated. Grain boundary or interface debonding is believed to be another mechanism for void nucleation if the stress is high enough. Void nucleation has also been found at the twin boundaries due to stress concentrations in Cu films [5.6].

SEM and AFM analysis indicated that the majority of the voids were located at grain boundaries, and the triple-point of the grain boundary was shown by AFM to be an important site for void formation. Since a grain boundary is a fast diffusion path in the Cu film, the formation of a void at a grain boundary may suggest diffusion controlled void nucleation and growth. As shown in Fig. 12, a passivated Cu film with columnar grains is subjected to an in-plane tensile stress. The stress would relax under favorable conditions by Cu diffusion from the Cu/passivation interface to the grain boundaries, resulting in the triaxial tensile stress state at the junction of the interface and the grain boundary (details of the analysis of stress relaxation in Cu films will be given in the next

chapter). Since the bottom Cu / diffusion barrier interface is believed to be well bounded in the Cu metallization, the diffusion through this interface is ignored. The junctions in triaxial stress tension are good sinks of vacancies and favorable sites for void nucleation. Once the atomic flux into the grain boundary is larger than that from the interface, a void

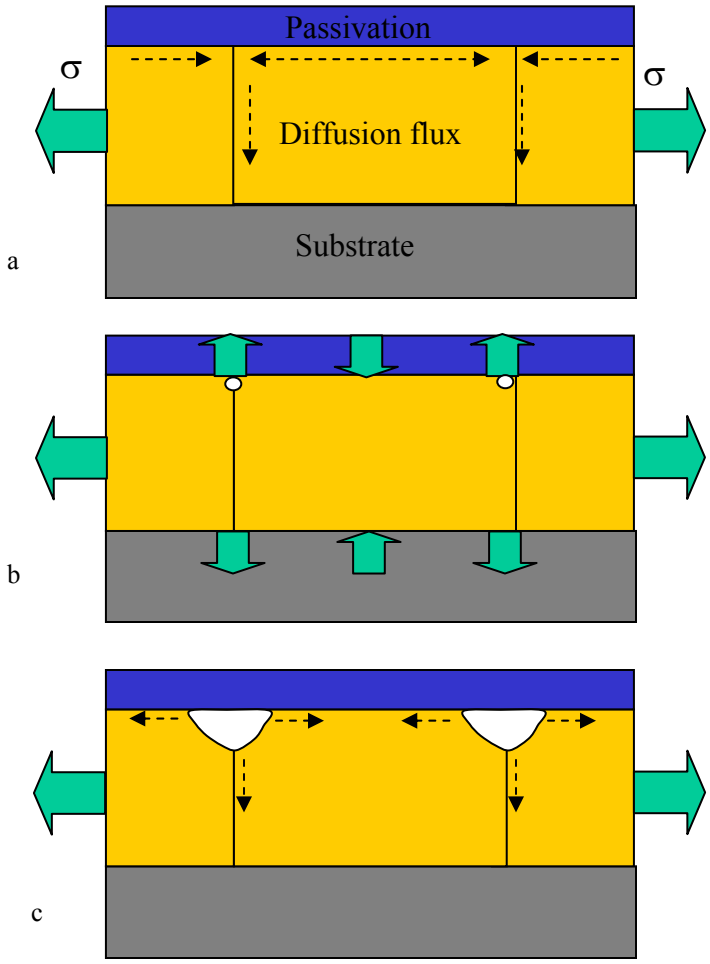


Figure 5.13 Schematic of void formation in Cu films. a) Stress relaxation of Cu films by diffusion of atoms from interface into grain boundary. b) The diffusion results in triaxial stress at the junctions of the interface and grain boundary, a favorite site for void nucleation. c) Void grows by diffusion of atoms driven by the stress gradients in the void vicinity.

forms at that point. When a void forms, the local stress state will change, resulting in stress gradients from the void surface into the grains (FEA analysis of the stress gradients in void vicinity will be provided in following). The stress gradients are believed to be one of the driving forces for void growth. Based on this analysis, grain boundary groove will be the result of the relaxation. Since individual voids not the groove along grain boundaries were observed, only some weak points along a grain boundary form voids.

Although dark contrast can only be seen under the optical microscope when the void size is big enough, it is believed that the trend of the density of the dark spots on the film surface still represents the trend of the overall void density. The higher void density upon cooling down in the $2^{nd}$ cycle than the $1^{st}$ cycle shown in Fig.4 was not due to the thermal stress since the stresses as a function of temperature shown in Fig.1 are the same in the two cycles. This phenomenon is believed to be related to a high plastic deformation and strain hardening of the Cu film upon the $1^{st}$ cooling down, which is evidenced by the large stress hysteresis in a thermal cycle. The strain hardening must induce a high density of dislocations terminating at the interfaces or grain boundaries, providing sinks and sources of vacancies for void nucleation, although part of these dislocations may disappear due to the anneal effect in the $2^{nd}$ heat up. The evidence that most voids formed again upon the $2^{nd}$ cool down at the same sites forming voids in the $1^{st}$ cool down suggests that although these voids disappeared upon heating up due to the compressive stress, some kinds of defect remained at these sites and made these sites be more prone to the void nucleation and growth. In this way, part of the sites with piling-up dislocations following the $1^{st}$ cooling cycle might leave defects for the $2^{nd}$ heating cycle and become

favorable sites for void formation, resulting in an increase of the void density in the 2nd cycle.

It was observed that voids nucleated continuously upon cooling after the first void appeared under the optical microscope. Moreover, a critical temperature of about 150°C was also found, below which the void nucleation rate dramatically decreased to almost zero. In addition, with a ramp rate of 2°C/min during cooling, no new voids were found under the microscope for temperatures below 200°C, although the tensile stress in the Cu film continually increased with decreasing temperature. During isothermal anneal, a sharp decrease of void density was also shown in Fig. 6 after the annealing temperature below 150°C. These observations suggested that the void formation in the Cu film both during thermal cycling and isothermal annealing was thermally activated. It was therefore not the result of high stress induced debonding along boundaries or interface.

### 5.4.2 FEA analysis of stress gradients in Cu films

Once a void nucleates, it grows by diffusion of atoms out of the void or diffusion of vacancies to the void. The flux of atoms or vacancies is driven by chemical potential gradients, one of which would be the of stress gradient, shown in equation 5.1. As a driving force for diffusion, a local stress gradient in a Cu film can be induced by several reasons, such as the mechanical anisotropy of Cu, defects, nonuniform geometry confinement, stress concentration etc. As an example, stress gradients induced by the mechanical anisotropy of the Cu crystals and in a void vicinity will be analyzed using

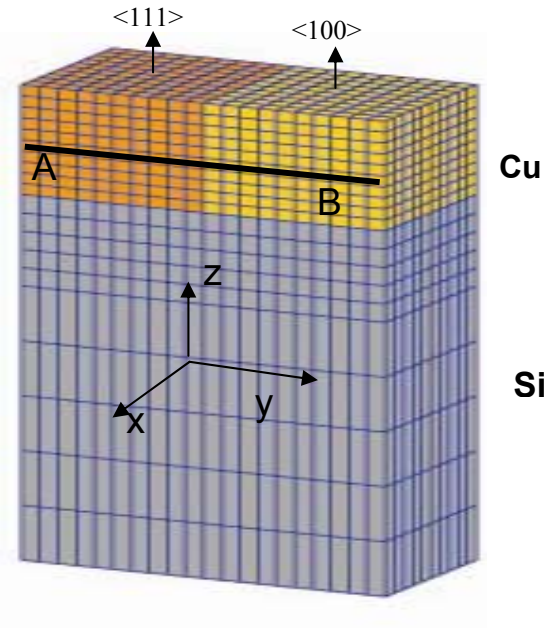


Figure5.14 Schematic of a 3D FEA mesh for analysis of stress gradients due to mechanical anisotropy of Cu crystal, including a <111> and a <100> grain with the x, y and z coordinate system as shown.

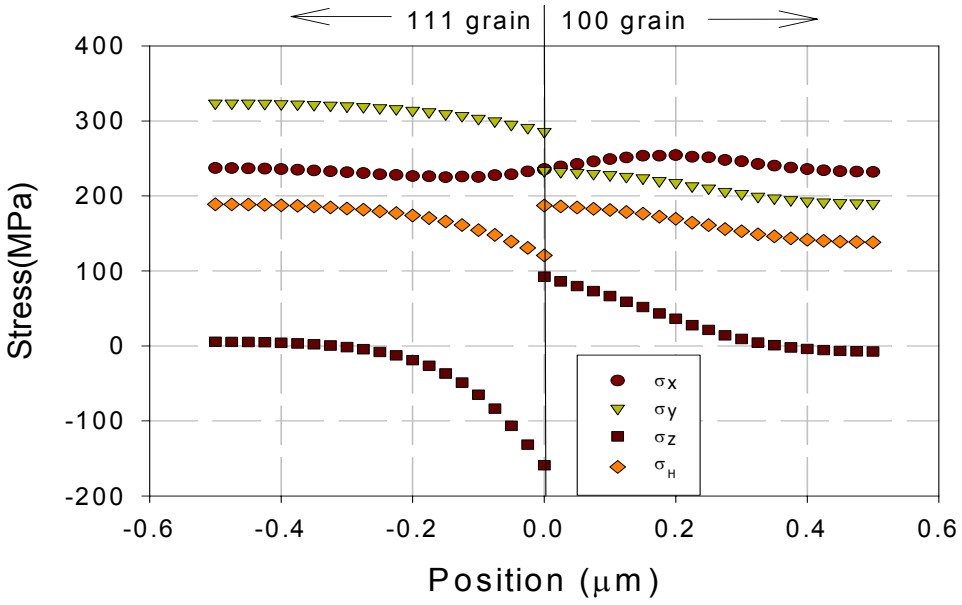


Figure 5.15 FEA result of the local stresses in the vicinity of a grain boundary formed between (111) and (100) grain.

FEA modeling. As mentioned previously, EP Cu films generally have strong (111) texture and (100) annealing textures. Due to the formation of twins, other texture components such as (511) are also found in Cu films. If grains with different orientations share a grain boundary and are confined by the Si substrate in a Cu film, a thermal stress gradient would be induced between the grains. To illustrate this effect, a model containing one <111> line and one <100> line was simulated. A finite element analysis (FEA) code, called ABAQUS was used to set up the 3D elastic model with 20-node quadratic brick elements. The width of the line is 1 micron; the thickness is 0.6 micron and the length is set to be infinite. Based on symmetry considerations, 0.5 micron is used for the length and the width in the modeling shown in the meshing scheme of the copper lines in Fig. 14. A mirror symmetry condition was applied to the front and the right planes of the structure. Since the thickness of the Si substrate was much larger than that of the structure its top, the back and left planes were constrained by the CTE of Si while remaining straight to ensure the periodicity of the structure and the bending of the substrate was ignored. The calculation was performed under the linear elastic assumption with a thermal loading of -100K from an initial state of zero stress. Figure 15 shows the FEA result of the principal stresses and the hydrostatic stress in the (111) and the (100) lines along their central line AB, shown in Fig.14. This figure indicates that stress gradients exist in the vicinity of the grain boundary due to the mechanical anisotropic of the grain. Moreover, the stress state in the vicinity of the grain boundary is triaxial with a compressive $\sigma_z$ in the <111> grain and a tensile $\sigma_z$ in the <100> grain while the film is expected to have an average bi-axial stress. As a result, the hydrostatic stress, considered

the driving force for the diffusion of vacancy or atom, decreases from the central of a grain to the grain boundary in the <111> grain while it varies in the opposite direction in the <100> grain, and a jump of the hydrostatic stress is shown at the grain boundary with the higher value in the <100> grain. Equation 5.1 indicates that the atomic flux will flow from the sites with lower tensile stress to the sites with higher tensile stress or from the sites with compressive stress to the sites with tensile stress. At the same time, vacancies will migrate in the opposite direction. Driven by the hydrostatic stress shown in Fig. 15, mass will transport from the inside of the <111> grain to the grain boundary and from the grain boundary to the inside of the <100> grain. These mass migrations driven by the local stress gradients from the mechanical anisotropy of the Cu crystal should enhance void formation in Cu films. Shaw *et al.* pointed out that the local triaxial stress state due to the mechanical anisotropy of the Cu crystal was one of the reasons for the void formation in Cu wide lines [5.26]. In this sense, a strongly textured film has a higher resistance to void formation than one with mixed grain orientations.

Although equation 5.1 suggests that mass is transported from sites with lower tensile stress to those with higher tensile stress, voids might not, in fact form at sites with lower stress. The reason is that the suitable sites for void nucleation should have high concentrations of vacancies and vacancy sinks. Equation 5.7 indicates that sites with tensile stress concentrations will result in higher concentrations of vacancies, implying that the voids readily nucleate at sites with high tensile stress. Once a void nucleates and grows, stress gradients will rise in the vicinity of the void and will rebuild the driving force for the mass transport process for the void formation. In order to study this effect,

stress gradients in the vicinity of a void as a function of the void size were analyzed using FEA modeling. In order to simplify the model, a void with a rectangular cross-section and the same thickness as the film was used, as shown in Fig.16. Considering symmetry, only a quarter of the void is presented. Boundary conditions used in the analysis of the local stress gradients due to the mechanical anisotropy of the Cu crystal were again used in this model. The model includes the Si substrate, the Cu film and the passivation layer. The thickness of the Cu film was set to be 0.6μm and that of the passivation layer was 0.2μm. Only 2μm instead of the real 720μm thick Si substrate was included in the model since the calculation showed that further increase of the Si thickness in the model did not affect the stress result in the Cu film using the above boundary conditions. Figure 17 shows the distribution of the hydrostatic stress in the vicinity of a void in the Cu film with an average bi-axial stress of 125MPa, indicating the hydrostatic stress gradient around a void and the effect of void size. The hydrostatic stress gradient at the void surface, normalized by the average hydrostatic stress of the film, was deduced from Fig.17 and shown in Fig.18, indicating that the gradient decreases with void size at faster rate for smaller voids. This exponential decrease of the hydrostatic stress with void size should be one of the reasons causing the initial exponential growth [5.5] of voids. During the void growth, mass is transported through interfaces, and grain boundaries as well as lattices at sufficient high temperature. Shown in Fig. 13, stress in a film is relaxed by diffusion of atoms from the interface into grain boundaries. Once voids nucleate at the junctions of grain boundaries and the interface, the local stress gradient around a nucleation site changes as analyzed by the FEA model, and thus the directions of the

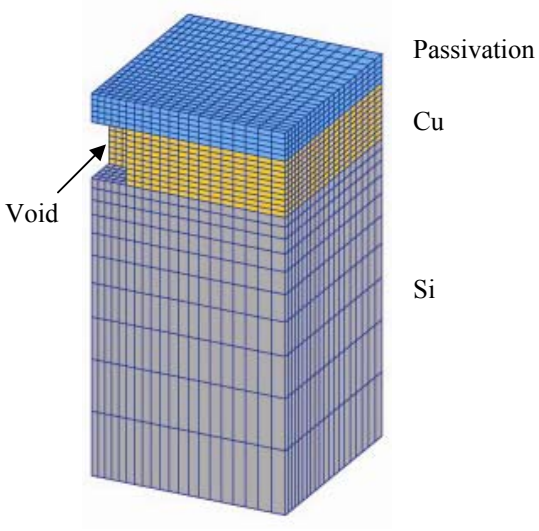


Figure 16. Schematic of a 3D FEA mesh of a void in the passivated Cu film

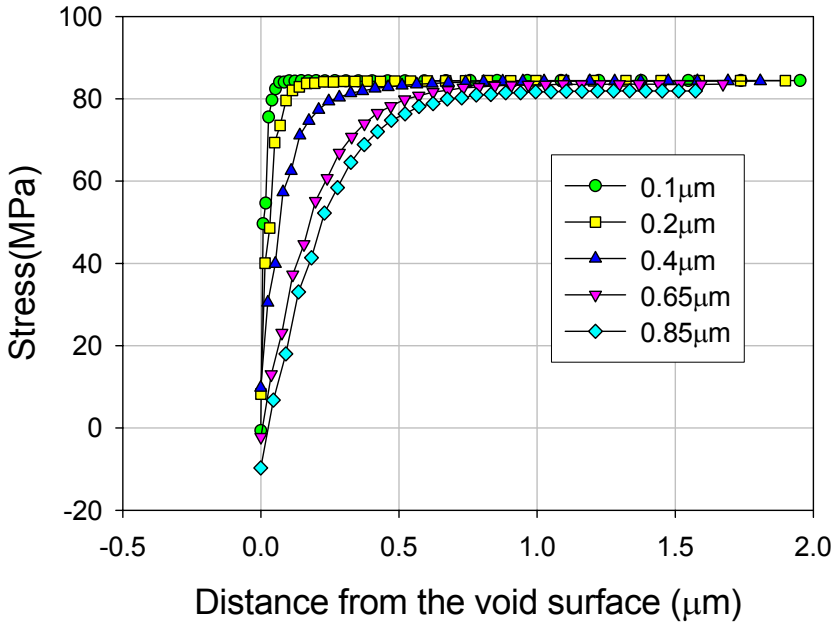


Figure 17. FEA result of the void size dependence of the hydrostatic stress in the void vicinity

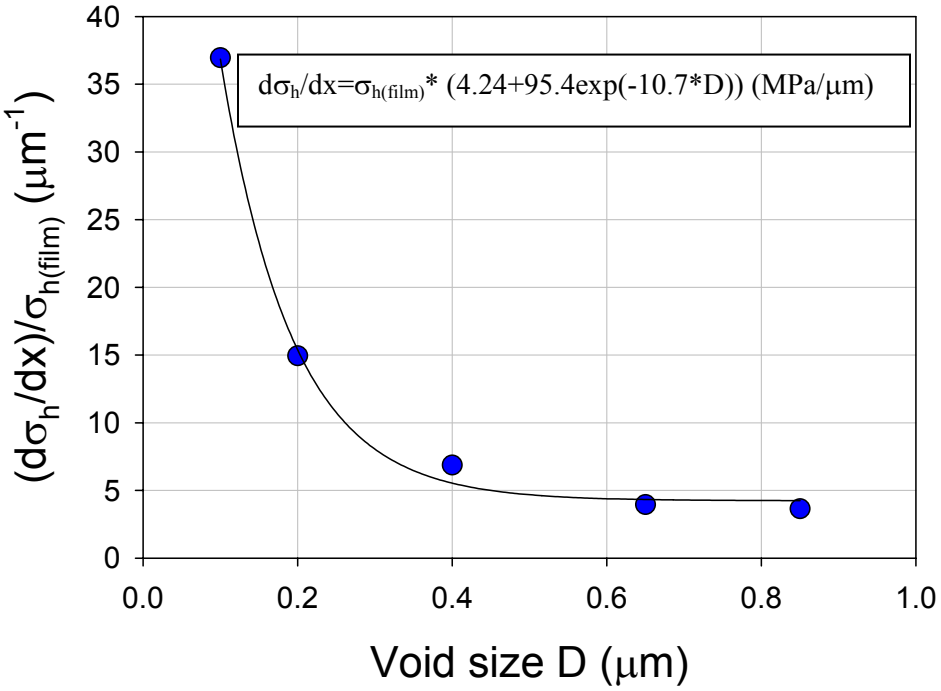


Figure 18 FEA result of the void size dependence of the stress gradient in the void vicinity

atomic fluxes in the vicinity of a void would be affected, resulting in mass transport out of the voids through the interface and/or the grain boundaries. The activation energy of 0.75eV for void growth as deduced in equation 5.2, is less than the activation energy of 1.08eV for grain boundary diffusion of Cu, implying that the mass transport involves more than just grain boundary diffusion. The relatively low activation energy suggests that the interface diffusion must play an important role in contribution to void formation in passivated Cu films.

## 5.5 CONCLUSION

Void formation in a passivated Cu film was studied by measuring the void density and the void size both during thermal cycling and isothermal annealing. During thermal cycling, voids formed upon cooling under tensile stress and disappeared upon heating under compressive stress, but a threshold stress and temperature were found for the void formation. A faster ramp rate was found to result in a lower void density upon cooling, implying that the void formation was time dependent and therefore must be a diffusion-controlled process. Moreover, not only stress and temperature, but also plastic yielding or strain hardening in the thermal history is also believed to enhance void formation, partially due to the defects induced by dislocation accumulation at the Cu/passivation interface or grain boundaries. Under isothermal annealing, both the void density and void size were found to depend on film stress and temperature. There also existed a threshold stress and a threshold temperature, below which void formation was not observed. Both the void density and void size, functions of the annealing temperature in isothermal annealing, showed peak values but at different temperatures, the higher one for the void size.

The vacancies for the void formation are believed to be generated by thermally activated processes enhanced by tensile stress or pileup dislocations, but not from the annihilation of grain boundaries during grain growth observed in an other study [5.22]. Local triaxial stress state due to diffusional creep, local stress gradients due to mechanical anisotropy of Cu, and stress gradients in the vicinity of a void must play an important role in contributing to void formation in Cu films. The stress gradients were analyzed using

FEA models. The void size dependence of the stress gradient in void vicinity was believed to correlate to the exponential growth of a void. Voids were believed to nucleate at preferred sites such as grain boundary triple points, and points with tensile stress concentrations and high defect densities. Stress gradients increase in the vicinity of the void, driving the mass transport out of the void. Both grain boundaries and interfaces would be diffusion paths for void formation, but the deduced activation energy, 0.75eV, is smaller than that for grain boundary diffusion, suggesting the Cu/passivation interface to be the dominant diffusion path for the void formation in the Cu film.

# Chapter 6 Stress relaxation and mass transport in Cu metallization

## 6.1 INTRODUCTION

Aluminum alloys have been used as interconnect conductors in the microelectronic industry for about 40 years. With continuous downscaling of the interconnect size to increase chip performance, a conductor with lower resistance is needed to replace Al alloy in order to reduce the R-C delay, where R and C represent the resistance and capacitance associated with interconnect architecture. Obviously, Cu is chosen by the industry as the alternative due to its high electric conductivity. Since Cu has a much higher melting point than Al (1357K vs. 933K), it is also expected to be of higher electromigration (EM) resistance. However, the improvement in performance and reliability has been the subject of concern with new materials and technologies being exploited. The formation of Cu damascene interconnect structures requires complex processes and structural elements, including electroplating Cu, barrier/seed layers, chemical-mechanical polishing (CMP) and passivation. These processes and elements are believed to give rise to distinct defect characteristics and mass transport paths, leading to failure mechanisms of electromigration (EM) and stress voiding for Cu interconnects different from Al interconnects [6.1-3]. Unlike aluminum, copper does not form a tightly bonded oxide and the need for CMP in processing, making Cu/barrier and Cu/cap interfaces fast diffusion paths. Previous studies have shown that the activation energy values for electromigration failure of Cu interconnects are lower than that for grain boundary diffusion [6.4]. Although the barrier material was found to affect the

electromigration performance of Cu interconnect due to the diffusion through the barrier/Cu interface [6.5-6], the cap/Cu interface was believed to be the dominant diffusion path for electromigration, partially due to defects and contaminations induced by the CMP process [6.7-8]. This raised the possibility of reducing interfacial mass transport to improve EM lifetime by optimization of the chemical bonds at the Cu/cap layer interface. Recently, Lane et al. [6.9] showed that EM lifetime of Cu interconnects can be improved by optimizing the interfacial bond using different cap layers and cleaning processes, and their results were supported by a correlation between EM lifetime and interfacial adhesion. This was corroborated by Hu et al. [6.10] who demonstrated a significant improvement in EM lifetime by coating the Cu surface with a thin (20-30nm) metal layer.

Mass transport through the interface is also critical for the thermal stress related yield and reliability issues in Cu metallization. Thermal stress induced in Cu interconnects depends not only on the thermal expansion mismatch between Cu and the surrounding materials, but also on the Cu stress relaxation where interfaces serve as the dominant diffusion path or reaction sites with dislocations. Interfacial diffusion was found to be the key in the stress-induced void formation in Cu interconnects [6.11].

As interconnect scaling advances beyond the 90 nm node, the interface-to-volume ratio continues to increase, making interfacial diffusion increasingly important in contributing to mass transport and thus in controlling the EM and SM reliability of Cu interconnects. EM failure is a complex phenomenon that requires local divergence of a diffusion flux. While diffusion processes along interfaces, grain boundaries and other

paths contribute to the overall mass transport in EM, the flux divergent sites are usually associated with localized defects. Therefore, it is difficult to correlate directly the EM lifetime to mass transport and thus to deduce the diffusivity for the Cu interface. For this reason, thermal stress and stress relaxation are studied using the bending beam method. Kinetic models coupling grain boundary diffusion and interface diffusion are set up to analyze the isothermal stress relaxation behavior in Cu metallization. The combination of stress measurement and modeling is used to evaluate the grain boundary and interface diffusivities. Since both stress relaxation and electromigration are found to be dominated by interface diffusion in Cu metallization, stress relaxation measurements were verified in order to evaluate the EM performance.

Deformation mechanisms and mass transport processes have been extensively studied for metal films, including e-beam and sputter deposited Cu films [6.12-17]. Several authors have shown that, at moderate temperatures, stress in polycrystalline thin films can be relaxed by diffusion flows at the surfaces and grain boundaries [6.13,14,17]. Thouless [6.18] and Gao *et al*. [6.19] developed diffusional creep models based on coupling of grain boundary and surface diffusion to account for thermal stress behavior under thermal cycling in unpassivated Cu films. Although the stress behavior under thermal cycling is commonly used to investigate mass transport and deformation mechanisms in metal films, it is difficult to delineate diffusion mechanisms when the stress behavior is observed under relatively rapidly changing temperatures where steady states are usually not reached. It is shown that stress relaxation observed under isothermal conditions is well suited for mechanistic studies since the stress variation is observed

over a long period of time where mass transport and deformation can be examined in details from the initial transient behavior to the steady state. In order to study interconnect metallization, understanding of both transient and steady state stress characteristics is required so as to control process yield and long-term reliability.

This chapter presents the results of a study of stress relaxation in Cu thin films and line structures with a focus on the effect of the passivation layers. Stress was measured using the bending beam technique and the XRD method. Kinetic models were set up to analyze the stress relaxation behavior and to evaluate the mass transport in combination with the bending beam results. It is shown that stress relaxation measurement can be an effective method to evaluate EM performance of Cu interconnects by measuring the interface diffusion.

## 6.2 STRESS RELAXATION AND MASS TRANSPORT IN COPPER FILMS

### 6.2.1 Sample Preparation

Cu film samples were prepared on silicon wafers. A layer of silicon nitride ($SiN_x$) was deposited on one side of the wafer by a CVD process, followed by the deposition of a diffusion barrier layer to prevent the Cu atoms from diffusing into the substrate. A 100 nm thick Cu seed layer was then deposited on the barrier layer by a PVD process. The rest of the Cu film was electroplated, and the total thickness of the Cu film was 1.0 μm. Some films were further capped with 50nm $SiN_x$ and 200nm silicon oxide as passivation.

Stress in the Cu films was determined using the bending beam method. For the passivated Cu films, since the thickness of the $SiN_x$ layer is much smaller than that of the Cu film, its contribution to the curvature change was ignored. The contribution from the oxide layer was accounted for using the stress of the TEOS film alone on a Si substrate [6.20]. Because $R_0$ was measured after the film was etched off, the relocation of the sample beams and other uncertainties would induce a system error estimated to be about 5%.

The samples were cut into 5x40mm$^2$ stripes. The surface curvatures were monitored as a function of time and temperature as the samples were thermally loaded in a vacuum chamber under a nitrogen atmosphere at a pressure of 50 torr. In this study, stresses in the Cu films were first measured under thermal cycles, and then isothermal stress relaxation tests were performed at selected temperatures with various initial stresses based on the thermal cycling stress behavior.

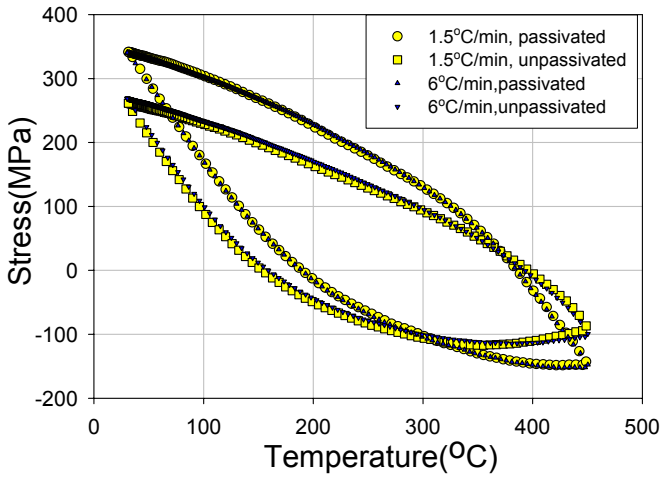


Figure 6.1 Thermal stresses of the passivated and unpassivated Cu films in two thermal cycles with different ramp rates.

### 6.2.2 Thermal Stress of Cu Films during thermal cycling

Figure 1 shows the measured stress behavior of the passivated and the unpassivated Cu films in two thermal cycles with different ramp rates. In the 1st cycle (not shown in the figure), the temperature range was from room temperature (RT) to 460ºC where the films were annealed for 30 minutes to stabilize their microstructures. Subsequently, the temperature cycles run from RT to 450ºC with the ramp rates of 1.5ºC/min and 6ºC/min. The thermal stress behaviors of these Cu films are similar to those shown in chapter 3, including the effect of the passivation layer and the effect of the ramp rate. As described in chapter 3, plastic yielding is the dominant mechanism for the plastic deformation of the Cu films during thermal cycling at a rate much faster than the strain rate due to the thermal mismatch. At high temperatures, it may be expected that diffusional creep as a result of mass transport would contribute to stress relaxation. However, no significant difference was observed in the stresses of the Cu films for temperatures up to 450ºC in two thermal cycles, implying that within the range of the ramp rates, the contribution from diffusional creep is negligible, making it difficult to extract any information about diffusional creep and the associated mass transport. The effect of the cap layer observed under thermal cycling is thus most likely due to the confinement effect on plastic yielding [6.21], rather than diffusional mass transport. Furthermore, the plastic strain rate was shown in chapter 3 to be approximately proportional to the ramp rate. For these films, the same result is held that implies any steady-state deformation mechanisms would thus be unable to account for such behavior. While such strain rate provides no obvious connection to the kinetics of mass transport,

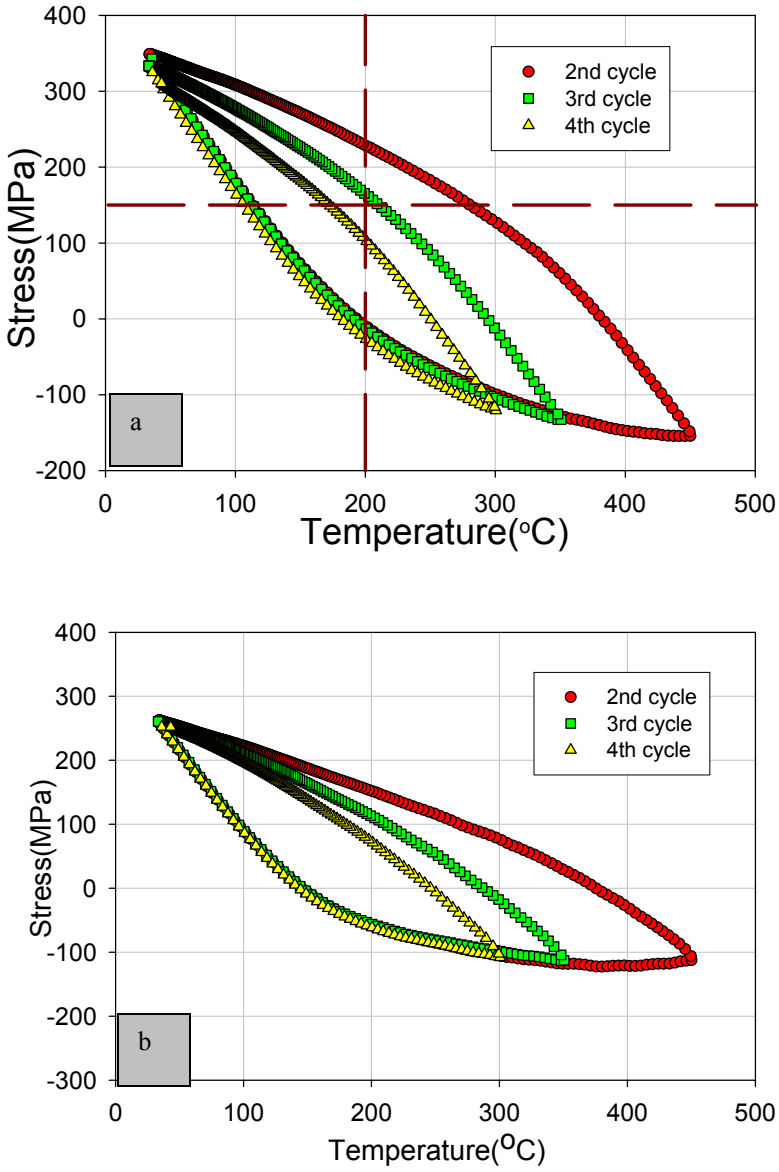


Figure 6.2. Stress hysteresis in different thermal cycles of (a) the passivated Cu film (b) the unpassivated Cu film

the measured stress, except the elastic part, under thermal cycling may be considered as the "yield strength" of the film, which is independent on the ramp rate but is a function of the temperature and the accumulated plastic strain (strain hardening). Isothermal stress relaxation measurement may be a better alternative to study the mass transport in Cu metallization.

As shown in Fig. 2, by varying the peak temperature, different stress hysteresis can be obtained during thermal cycling and both the temperature and the initial stress can be adjusted for isothermal stress relaxation measurements. In this way, the effects of stress and temperature can be investigated separately. This is illustrated in Fig. 2 (a) where the vertical line indicates that different initial stresses can be obtained at the same temperature to study the stress effect on stress relaxation. Similarly, as illustrated by the horizontal line, the same initial stress at different temperatures can be used to study the effect of temperature. This allows us to obtain suitable stress and temperature ranges to study a particular relaxation mechanism. For such studies, the microstructures of the film should remain about the same and not be changed after the 1$^{st}$ cycle. This was supported by the observation using transmission electron microscopy by Dehm *et al.* [6.22].

The hysteresis loop of the stress-temperature curves can be roughly divided into four regimes: a low-temperature elastic regime upon heating, an inelastic regime under compression, a high-temperature elastic regime upon cooling, and an inelastic regime under tension. Each of these regimes may be associated with different deformation mechanisms in isothermal annealing, although it was shown that plastic yield is the dominant plastic deformation mechanism in cycling. The stress level and the temperature

range for initial tensile stress states seem to be most suitable for analysis using the coupled diffusion model that will be reported later.

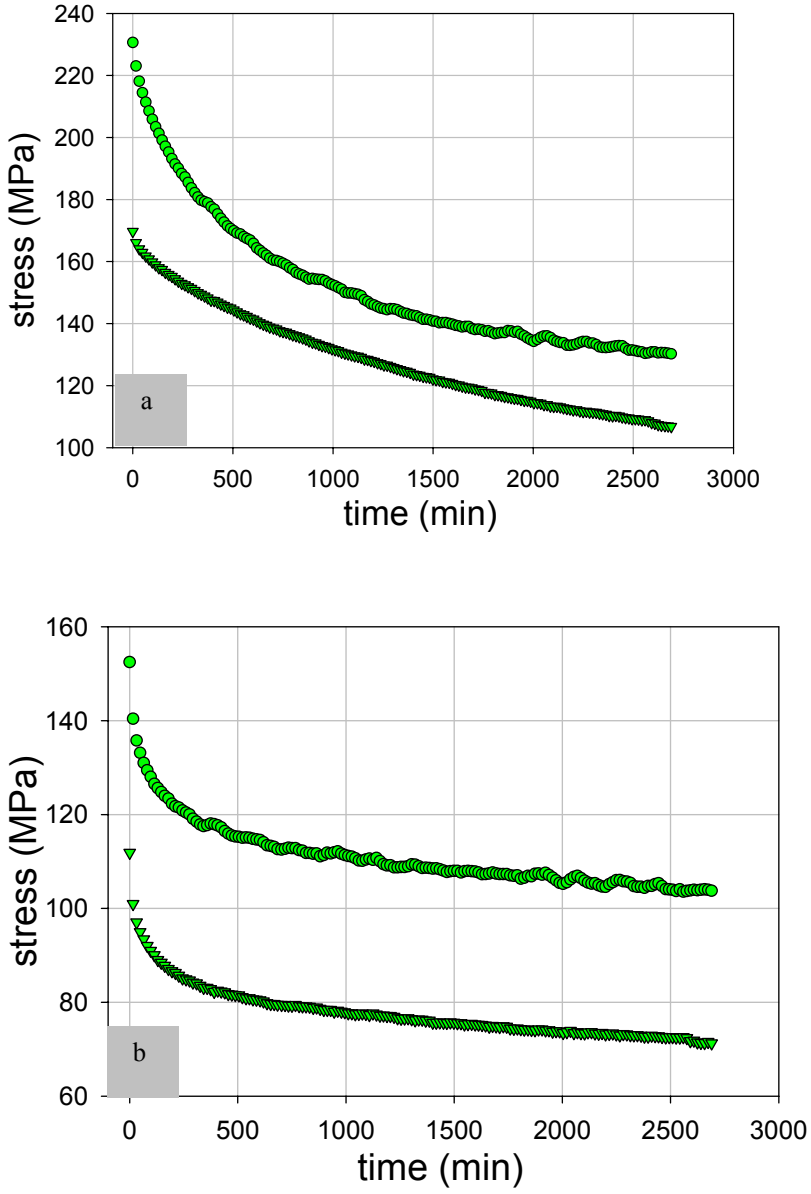


Figure 6.3 Stress relaxation of the Cu films at 200°C from different initial stresses: a) passivated Cu film and b) unpassivated Cu film

### 6.2.3 Isothermal Stress Relaxation of Cu Films

***A. Effect of initial stress***

Figure 3 shows the measured stress relaxation curves of the passivated and unpassivated Cu films for 45 hours, starting from different initial stresses at 200ºC. The initial stresses for the passivated film are 230MPa and 170MPa, and those for the unpassivated film are 152MPa and 112MPa. The higher initial stress was achieved by cooling the films from 450ºC, and the lower from 350ºC. A higher initial stress resulted in more stress being relaxed within a period of 45 hours but still retained a higher stress at the end for both the passivated and unpassivated films. Each curve shows an initial transient behavior with a sharp decrease of stress with time followed by a steady relaxation. The significance of the transient behavior will become clearer by considering the change in the strain rate as described below.

The total strain in the film consists of an elastic strain and an inelastic strain, and the stress is related to the elastic strain via Hooke's law. Under an isothermal condition, the total strain remains constant as the film is constrained by the substrate. Over time, the inelastic strain increases and the elastic strain decreases. Consequently, the stress relaxes. The rate of stress relaxation is related to the rate of inelastic deformation as follows:

$$\dot{\sigma} = -M\dot{\varepsilon}_p , \tag{2}$$

where $\dot{\varepsilon}_p$ is the inelastic strain rate, $\dot{\sigma}$ is the measured stress relaxation rate, and $M$ is the biaxial modulus of the film. Accordingly, one can deduce the inelastic strain rate from the stress relaxation curve. The modulus of Cu thin films strongly depends on the film texture due to the mechanical anisotropy of Cu. It may vary from film to film and differ

from that of the bulk Cu. The biaxial modulus of the Cu films used in this study was determined from the slope of the elastic regime of the stress-temperature curves. Their relationship is described as

$$S = M^* \Delta\alpha \tag{3}$$

where $S$ is the slope of the elastic regime of the stress-temperature curve of the Cu film, and $\Delta\alpha$ is the CTE mismatch of the Cu film and Si substrate, about 15.09 x$10^{-6}$/ºC (Cu: 17.7 x$10^{-6}$/ºC and Si: 2.61 x$10^{-6}$/ºC). Figure 6.4 shows the thermal stress curve of the passivated Cu film during thermal cycles, from which the film bi-axial modulus as a function of temperature was deduced as

$$M = 197.7 - 0.0515\ T + 7.59x10^{-5}\ T^2, \tag{4}$$

where the biaxial modulus $M$ is in GPa and the temperature $T$ is in K.

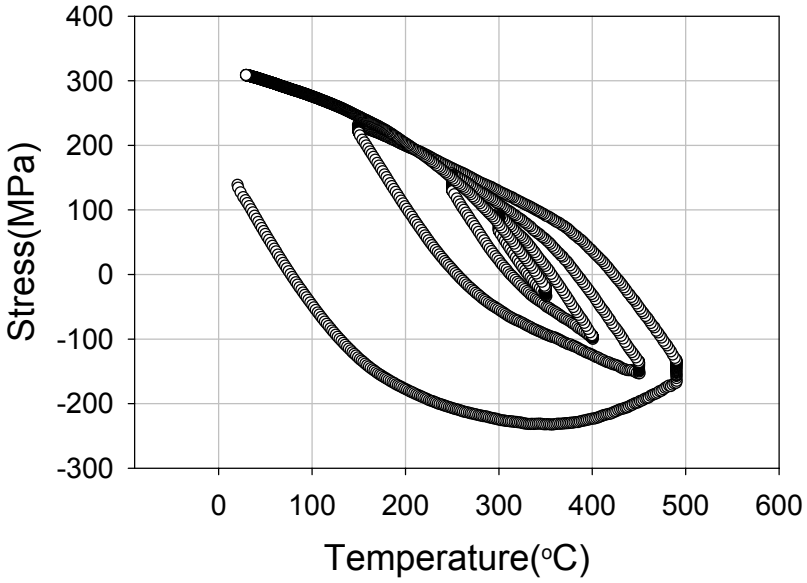


Figure 6.4 Thermal stress of the passivated Cu film during thermal cycling for the bi-axial modulus measurement.

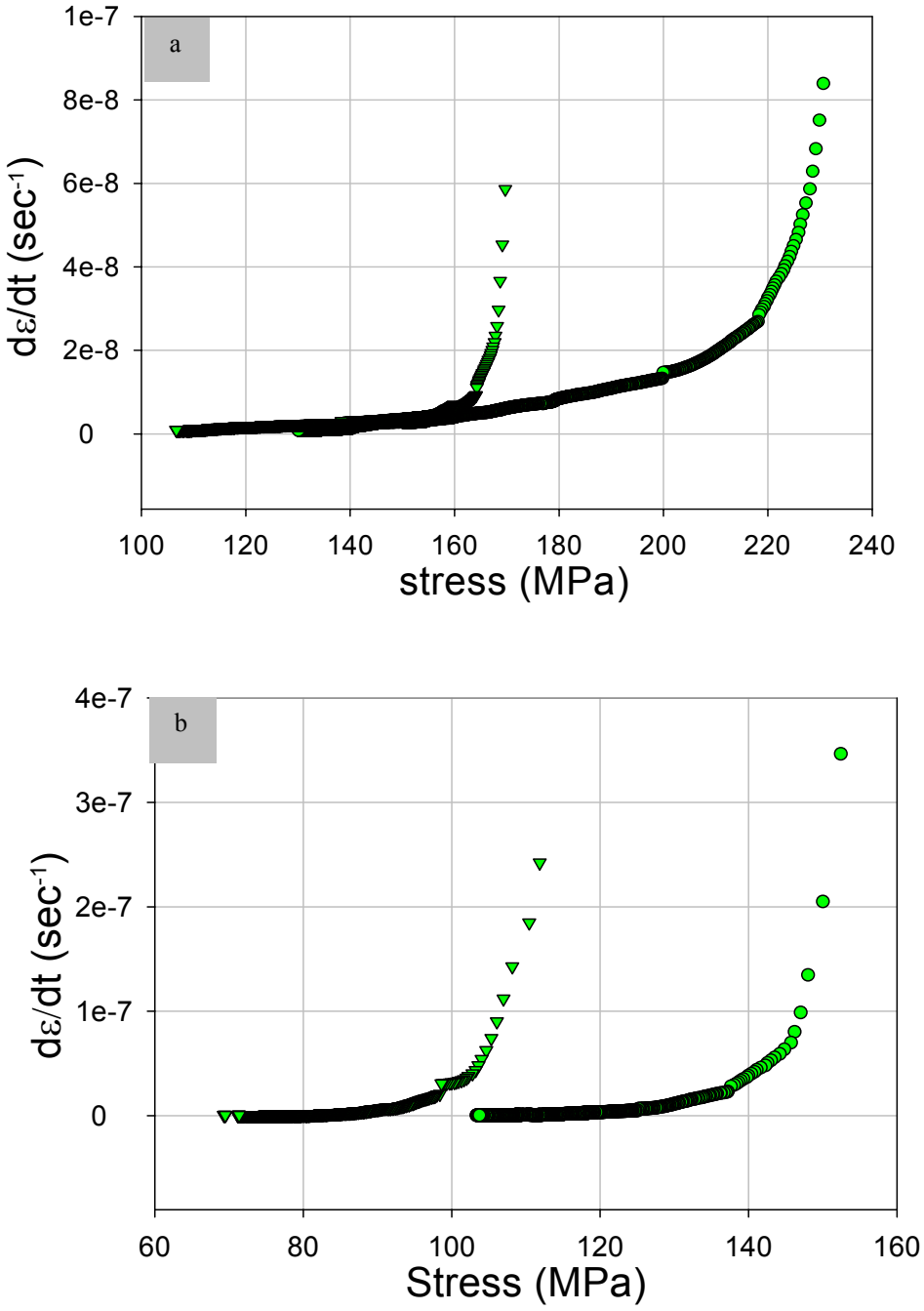


Figure 6.5 Creep rate as a function of stress at 200°C for a) the passivated Cu film and b) the unpassivated Cu film

The stress relaxation rate was obtained from the measured relaxation curve using a linear regression fitting. The inelastic strain rate was then calculated using Eq. 2 and plotted in Fig. 5 as a function of stress. A transient behavior of stress relaxation was clearly observed for both passivated and unpassivated films, where the inelastic strain rate was found to depend on the initial stress and the time since the relaxation started. Each curve in Fig. 5 can be roughly divided into an initial transient regime and a steady-state regime, a typical creep behavior. As the starting points of these relaxation measurements were taken from thermal cycling experiments, it confirms that, during thermal cycling, the films had not reached the steady state of inelastic deformation. It is clear that the time to reach the steady state is much longer than that expected from previous studies. Consequently, the transient behavior can significantly affect the thermomechanical behavior under thermal cycling. It is noted that, compared with the passivated Cu film (Fig. 5a), the unpassivated Cu film (Fig. 5b) took much longer time to reach the steady state and, although the initial stresses were lower, the unpassivated film had higher initial creep rates, which can be qualitatively explained by a kinetic model described in a later section.

**B.** ***Effect of annealing temperature***

Figure 6 shows the isothermal stress relaxation of the Cu films in 45 hours at different temperatures, 176ºC, 215ºC and 290ºC, but with similar initial stress for each film. Increase of the annealing temperature, shown in Fig.6, results in a faster stress relaxation rate that makes the film stress relaxed more quickly to the zero-creep stress

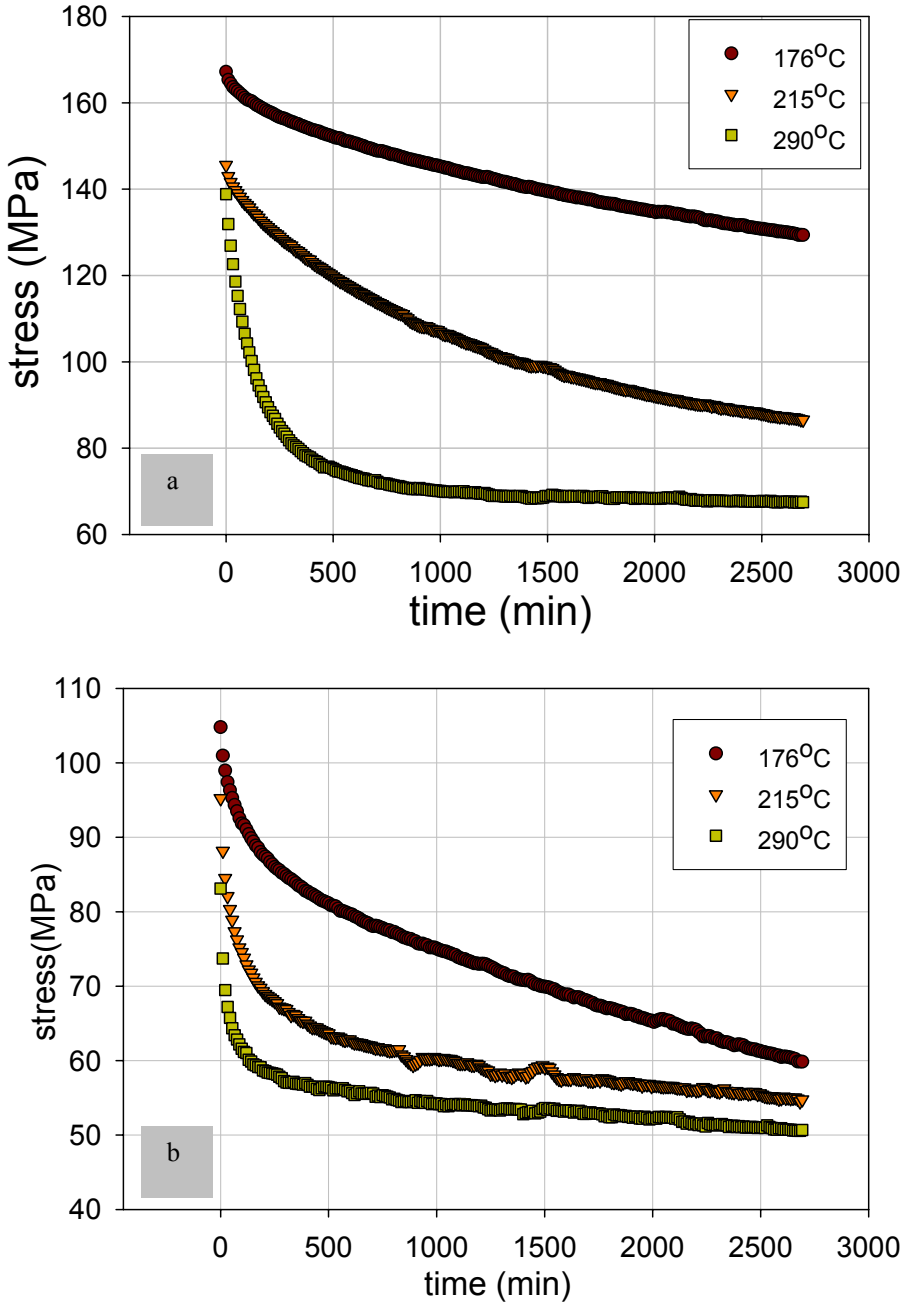


Figure 6.6 Temperature dependence of the isothermal stress relaxation of (a) the passivated Cu film and (b) the unpassivated Cu film.

below which plastic deformation does not occur. These measurements enable the extraction of the temperature dependence of inelastic deformation and in particular, the activation energy of mass transport. One interesting phenomenon is that, for all the stress relaxation measurements, the stresses did not relax to zero within the period of measurements and at 290ºC, the stresses in the films seem to saturate at some moderate stress levels without further relaxing.

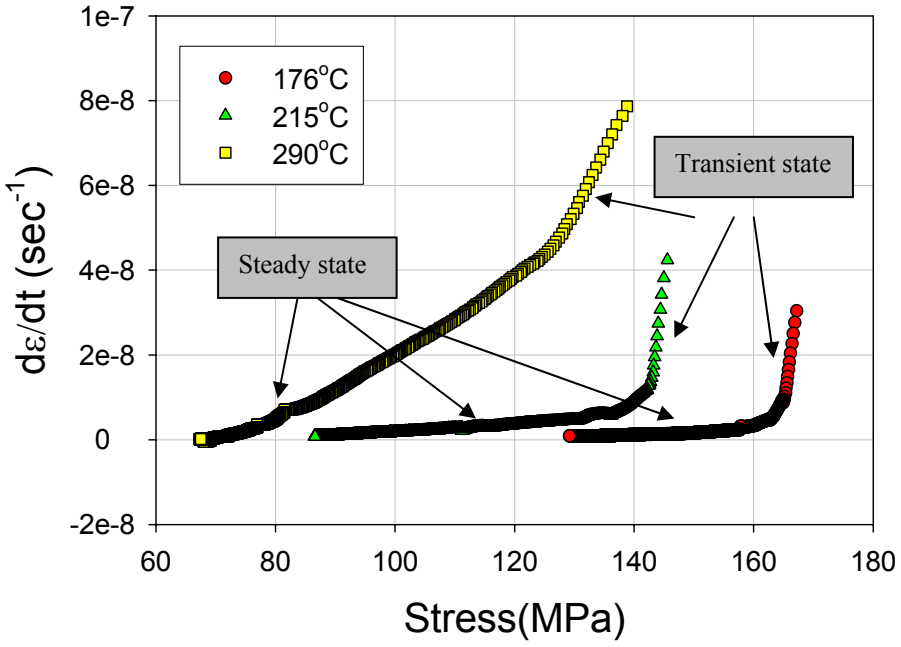


Figure 6.7 Creep rate as functions of stress in stress relaxation at different temperatures for the passivated film.

Figure 7 shows the creep rate as functions of stress of the passivated Cu film in isothermal stress relaxation at different temperatures. In the temperature range of the measurements, the relationship of the creep rate with the stress indicates that the stress relaxation of the passivated Cu film may be divided into a transient state and a steady

state. In the steady state, linear relationships between the creep rate and the film stress are shown, suggesting diffusion-controlled stress relaxation processes. Figure 8 shows the result for the unpassivated Cu film, where the transient behavior is also clearly indicated in the temperature range. Similar to the passivated Cu film, an increase the annealing temperature resulted in the increase of the initial creep rate in the unpassivated Cu film, and the initial creep rates are higher than those of the passivated, but the boundary between a transient and a steady state is not clear as that in the passivated Cu film.

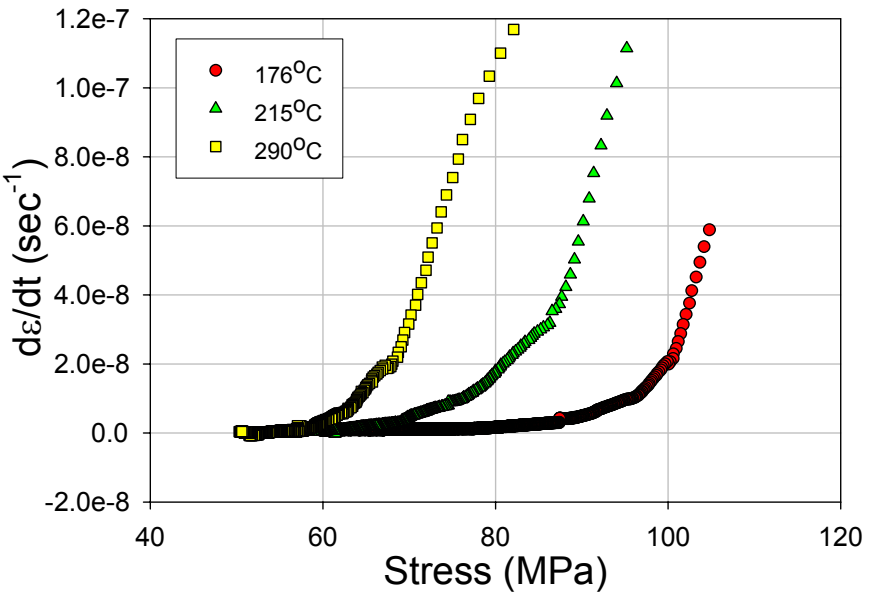


Figure 6.8 Creep rate as functions of stress in stress relaxation at different temperatures for the unpassivated film.

**C.** ***Relaxation of compressive stress***

Figure 9 shows the stress relaxation results for the Cu films at 290ºC for 45 hours (the oscillation was due to the instability of the optical sensors in the BB system). Different from the previous measurements, the initial stresses of these curves are compressive rather than tensile. The creep rates in both films are shown to decrease sharply after about 1 hour annealing. After 500 minutes, the stress in the unpassivated Cu film seems to be stable, although the stress is still high (~ -83MPA) compared to the initial stress (~ -103MPa), while the creep rate becomes much smaller for the passivated Cu film and left a high residual stress after annealing. This behavior is quite different from that of the relaxation of a tensile stress shown in Fig .6. Without in-depth understanding of reasons for the difference, further study will focus on the mass transport during relaxation of tensile stress since it is the tensile stress not the compressive stress causing void formation in metallization.

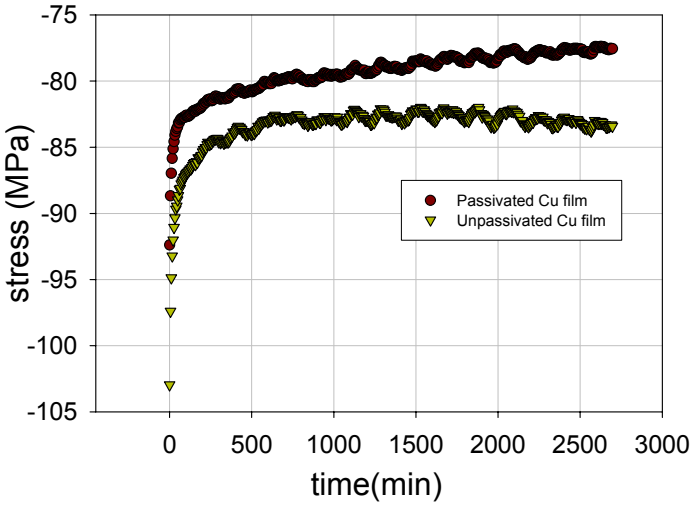


Figure 6.9 Relaxation of compressive stress of the Cu films at 290°C.

### 6.2.4 Modeling Analysis

#### *A. Empirical creep analysis*

At a given temperature, the total strain of the film in isothermal stress relaxation is a constant, depending on the thermal expansion mismatch between the film and the substrate. Upon annealing, plastic strain in the film increases, by various mechanisms depending on temperature as well as the stress level. The behavior is broadly termed as creep. As a result, the elastic strain decreases and the stress in the film relaxes as a function of time given by

$$\sigma(t) = \sigma_0 - M\int_0^t \dot{\varepsilon}_p dt\,, \tag{5}$$

where $\sigma_0$ is the initial stress and $\dot{\varepsilon}_p$ is the creep rate. Here we consider the average stress only and neglect the effect of film texture and anisotropy.

As in bulk materials, creep deformation can be divided into three stages: primary creep, steady-state creep, and ternary creep. The primary creep is often ignored, as the transient stage is short compared to the steady-state stage. For the steady-state creep, the strain rate of a given material is a function of stress and temperature. Various creep laws exist. In particular, most diffusion mechanisms lead to linear creep, such as Coble creep, Nabarro-Herring creep, and their modified forms for thin films [6.22]. According to linear creep, the strain rate is given by

$$\dot{\varepsilon}_p = \frac{\sigma}{\eta}, \tag{6}$$

where $\eta$ is the creep viscosity, which is a function of temperature and depends on the dominant diffusion path. Substituting (6) into (5), one can solve for the stress as a function of time

$$\sigma_t = \Delta\sigma \exp(-t/\tau) + \sigma_\infty \tag{7}$$

where $\tau = \eta/M$ is a time constant of stress relaxation and $\sigma_\infty$ represents a zero-creep stress, at which the strain rate is zero.

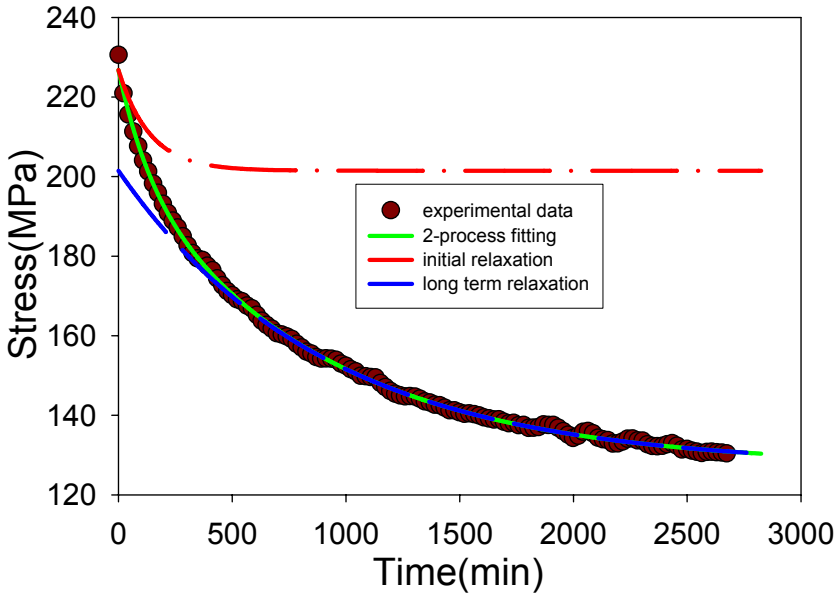


Figure 6.10 Schematic of the 2-process fitting of the stress relaxation curve of the passivated Cu film at 200°C.

The strain rate of steady state linear creep is proportional to the stress. However, our experiments showed that the strain rates in both passivated and unpassivated Cu films also depended on the thermal history, especially at the initial stage of relaxation. Evidently, the transient behavior is important for understanding stress relaxation. The

experimental results showed that in both sections of the relaxation, fast relaxation at the initial stage and slow relaxation at the second stage, the strain rate is approximately a linear function of the stress. Based on this observation, the relaxation curves would be fit in the form of

$$\sigma_t = \Delta\sigma_1 \exp(-t/\tau_1) + \Delta\sigma_2 \exp(-t/\tau_2) + \sigma_\infty, \quad (8)$$

which consists of two exponential terms with different time constants, corresponding to the two processes, short-term and long-term behaviors, respectively. As an example, the two-process fitting for the stress relaxation curve of the passivated Cu film at 200°C with an initial stress of 230MPa is shown in Fig.10, which includes the relaxation curves for each process and their combination, indicating that the faster process contributed the initial fall of the stress and the other contributed to the later relaxation in a longer time. A very good agreement between the experimental data and the fit curve is shown, except for the initial about 10 minutes.

Since the stress relaxation in the passivated Cu film reaches a steady state in the period of annealing, the activation energy of the relaxation process can be deduced. According to Coble creep or Nabarro-Herring creep, the strain rate of a diffusional-controlled creep is given by,

$$\dot{\varepsilon} \propto \frac{\sigma D_{eff}}{kT} = \frac{A\sigma}{T} \exp(\frac{-Q}{kT}) \quad (9)$$

where $D_{eff}$ is the effective diffusivity, $A$ the material constant, $Q$ the activation energy for the diffusion while the other parameters have the usual meanings. Equation 9 can be modified as

$$\ln(Td\dot{\varepsilon}/d\sigma) = -\frac{Q}{kT} + \ln A \tag{10}$$

Table 6.1 Parameters from the strain rate-stress curves of the passivated Cu film

| T (°C) | 176 | 200 | 215 | 290 |
|---|---|---|---|---|
| $d\dot{\varepsilon}/d\sigma$ ($sec^{-1}MPa^{-1}$) | $4.17x10^{-11}$ | $5.92\ x10^{-11}$ | $8.62\ x10^{-11}$ | $8.09\ x10^{-10}$ |

From the measured strain rate-stress curves, $d\dot{\varepsilon}/d\sigma$ were deduced and listed in table 1 and the linear relationship between $\ln(Td\dot{\varepsilon}/d\sigma)$ and 1/kT is shown in Fig.11, which yields the steady state creep rate of the passivated Cu film

$$\dot{\varepsilon} = \frac{0.2\sigma}{T}\exp(\frac{-0.635}{kT}) \tag{11}$$

where the stress is in $MPa$ and the activation energy for the stress relaxation in the steady state of the passivated Cu film is deduced to be about $0.64\,eV$ .

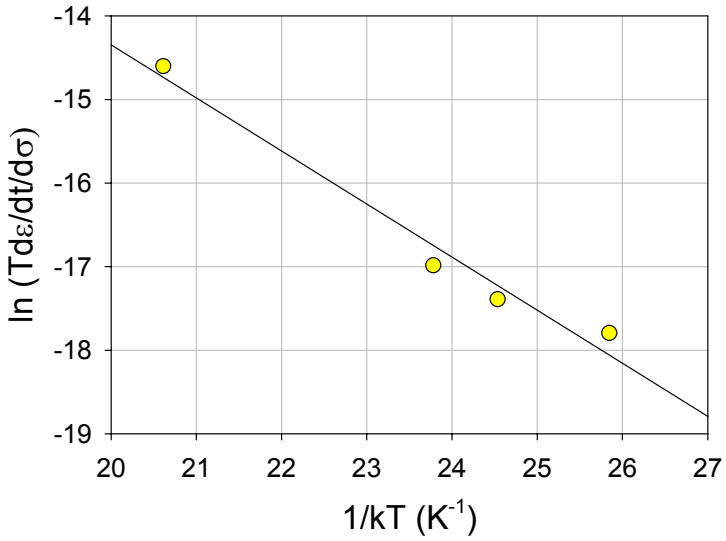


Figure 6.11 Temperature dependence of the steady-state strain rate of the passivated Cu film in isothermal stress relaxation.

***B. A kinetic model for stress relaxation***

Although the steady-state equations would be used to deduce the activation energy for the stress relaxation as described in section A, the information for the interface mass transport can not be directly obtained since the process of stress relaxation might couple with diffusion through grain boundaries, lattice, and dislocations as well as interfaces. In order to evaluate the mass transport through the interface, models that can define the role for each diffusion path are needed. Huang *et al*. [6.23] developed a diffusion model for isothermal stress relaxation based on coupling of grain-boundary diffusion and interface diffusion, for both passivated and unpassivated polycrystalline films. Similar models have also been developed by Thouless [6.18] and Gao *et al*. [6.19,24], both for unpassivated films only. As Cu films in interconnect structures are

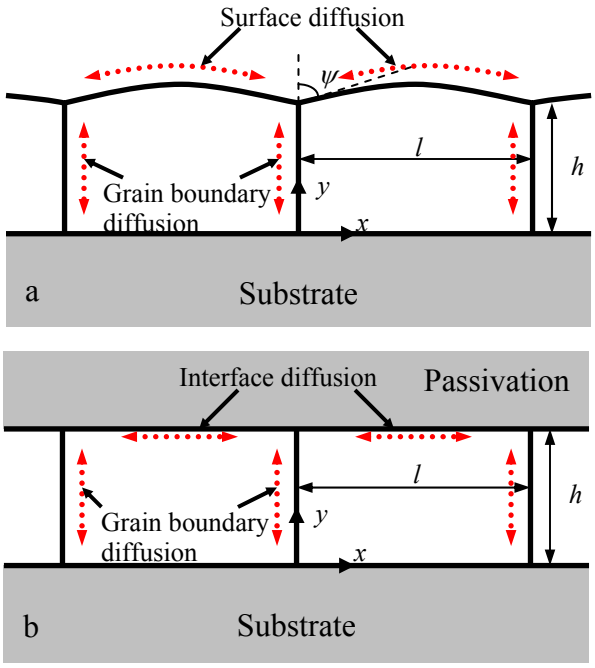


Figure 6.12 Schematics of polycrystalline thin films: a) an unpassivated film and b) a passivated film.

always passivated, the interface diffusion through the Cu/cap layer interface is of particular interest for electromigration studies. Here we briefly outline the model first and then focus on comparisons between the model and the experiments.

Figure 12 schematically illustrates the model structures for unpassivated and passivated thin films. For unpassivated films (Fig. 12a), we consider mass transport by diffusion along the free surface and the grain boundaries, but neglect lattice diffusion and diffusion along the film/substrate interface. The chemical potential is defined by the local curvature for the surface and the normal stress for the grain boundaries. The gradient of chemical potential drives atoms to diffuse into or out of grain boundaries, relaxing the average stress in the film. For the unpassivated films, assuming infinitely fast surface diffusion, we have

$$\frac{\partial \sigma_B}{\partial t} = \frac{M\Omega\delta_B D_B}{lkT}\frac{\partial^2 \sigma_B}{\partial y^2} \tag{12}$$

$$\left.\frac{\partial \sigma_B}{\partial y}\right|_{y=0} = 0 \tag{13}$$

$$\sigma_B\left(y = h\right) = \kappa_0 \gamma_S \tag{14}$$

where $\sigma_B$ is the normal stress at the grain boundary, $M$ the biaxial modulus of the film, $\Omega$ the atomic volume, $\delta_B$ the grain boundary width, $D_B$ the grain boundary diffusivity, $l$ the grain size, $h$ the film thickness, $k$ the Boltzmann's constant, $T$ the absolute temperature, $\gamma_S$ the surface energy density, $\kappa_0$ the surface curvature at equilibrium, while $y$ is the coordinate along the grain boundary. Boundary condition (13) is used to disable the diffusion flux flowing from grain boundary into the bottom interface.

Solving Eq. (12) with the boundary conditions (13) and (14), we obtain that

$$\sigma_B(y,t) = \kappa_0\gamma_S + \sum_{n=0}^{\infty} A_n \cos(k_n y)\exp\left(-\overline{D}_B k_n^2 t\right), \tag{15}$$

where $\overline{D}_B = \dfrac{M\Omega\delta_B D_B}{lkT}$ , $k_n = \dfrac{(2n+1)\pi}{2h}$ , $A_n = \dfrac{(-1)^n}{2n+1}\dfrac{4}{\pi}\left(\sigma_0 - \sigma_{EQ}\right)$ and $\sigma_{EQ} = \dfrac{\gamma_S}{h}\left(\kappa_0 h + \sin\psi\right)$. The effective film stress as a function of time is given by

$$\sigma(t) = \sigma_\infty + \frac{1}{h}\int_0^h \sigma_B(y)dy = \sigma_\infty + \left(\sigma_0 - \sigma_\infty\right)\frac{8}{\pi^2}\sum_{n=0}^{\infty}\frac{\exp\left(-t/\tau_n\right)}{(2n+1)^2} \tag{16}$$

where $\tau_n = \dfrac{4kTh^2 l}{(2n+1)^2\pi^2 M\Omega\delta_B D_{B0}}\exp\left(\dfrac{Q_B}{kT}\right)$ and $D_{B0}$ is the pre-exponential factor for grain boundary diffusivity. In addition, $\sigma_0$ is the initial stress and $\sigma_\infty$ is the zero-creep stress. The zero-creep stress by this model is a result of surface tension and the local equilibrium at the junction of the surface and a grain boundary i.e.,

$$\sigma_\infty = -\frac{2\gamma}{h}\cos\psi + \frac{\gamma}{h}\sin\psi\,, \tag{17}$$

where $\gamma$ is the surface energy density and $\psi$ is the dihedral angle at the junction.

Equation (16) consists of infinite exponential terms, each decaying at a different time scale. Similar solution was obtained by Gao et al [6.19]. The empirical Eq. 8 can be considered to be a special case of this solution including only two exponential terms. This form of solution exhibits a transient behavior of stress relaxation in that the stress relaxes faster initially as the high order terms decays exponentially at high rates and then slows down with only the first term remaining effective. Figure 13 shows the inelastic strain

rate, calculated by inserting Eq.16 into Eq.2, as a function of the stress for the unpassivated film relaxing from two different initial stresses at 200°C. Table 2 lists the parameters used for this calculation. Comparing to Fig. 5b, the agreement between the model and the experiments is reasonably good. In particular, the transient behavior is clearly shown by the different strain rates at the same stress and the same temperature from the two different initial stresses.

Table 2 Structure and Material parameters for the electroplated Cu films

| | |
|---|---|
| Film thickness | $h$ = 1μm |
| Average grain size | $l$ = 1.3μm |
| Pre-exponential grain-boundary diffusivity | $\delta_B D_{B0}$=1.1×10$^{-14}$m$^3$/s |
| Activation energy for grain-boundary diffusion | $Q_B$=1.07eV |
| Atomic volume | Ω=1.18×10$^{-29}$m$^3$ |
| Boltzmann's constant | k=8.617×10$^{-5}$ eV/K |

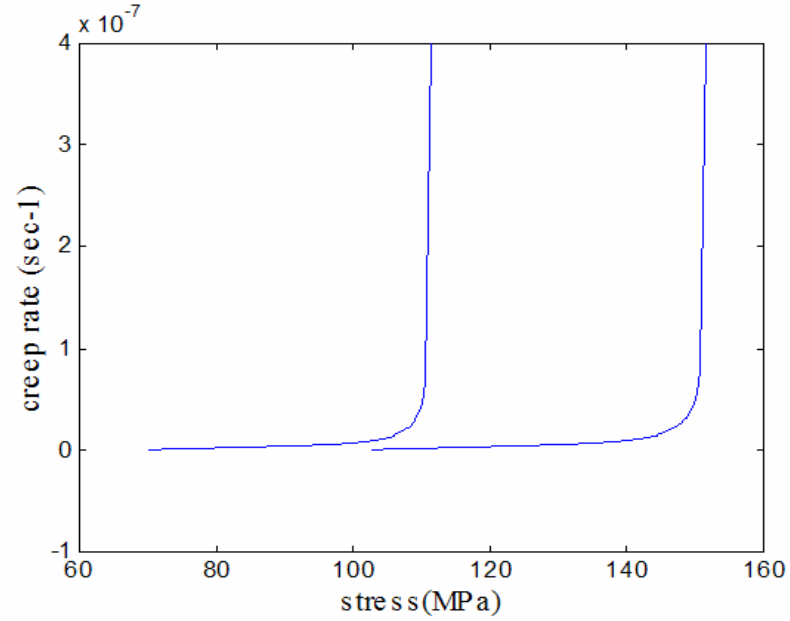


Figure 6.13 The stress -creep rate relationship of the unpassivated Cu film at 200°C predicted by the model indicates a transient behavior in stress relaxation.

For passivated films, we consider grain boundary diffusion coupled with interface diffusion between the Cu film and the cap layer (Fig. 12b). In contrast to the case of the free surface for unpassivated films, the interface is assumed to remain flat due to the constraint of the cap layer. Mass transport along the interface induces nonuniform local normal stresses, which define the chemical potential and drive interface diffusion, and we have

$$\frac{\partial \sigma_I}{\partial t} = \frac{M\Omega \delta_I D_I}{hkT} \frac{\partial^2 \sigma_I}{\partial x^2} + \frac{2M\Omega}{hl} J_0(t) \tag{18}$$

where $\sigma_I(x)$ is the locally normal stress at the interface, $x$ is the coordinate along the interface and $J_0(t)$ is the atomic flux rate at the junction between the interface and a grain boundary.

The following boundary conditions are used.

$$\left. \frac{\partial \sigma_I}{\partial x} \right|_{x=l/2} = 0 , \tag{19}$$

$$\left. \frac{\partial \sigma_I}{\partial x} \right|_{x=0} = \frac{\delta_B D_B}{2\delta_I D_I} \left. \frac{\partial \sigma_B}{\partial y} \right|_{y=h} , \tag{20}$$

$$\sigma_I(0,t) = \sigma_B(h,t) . \tag{21}$$

Equation (19) implies no flux at the center, and Eqs. (20) and (21) ensure continuity of the flux and the chemical potential at the junction between the interface and a grain boundary. As before, the grain boundary diffusion is governed by Eq. (12) plus the boundary condition, Eq. (13), for no flux at the film-substrate interface. The coupled

problem is then solved numerically. Figure 14 shows the numerical solution of the evolution of the interface stress and the film stress, where the stress is normalized by the

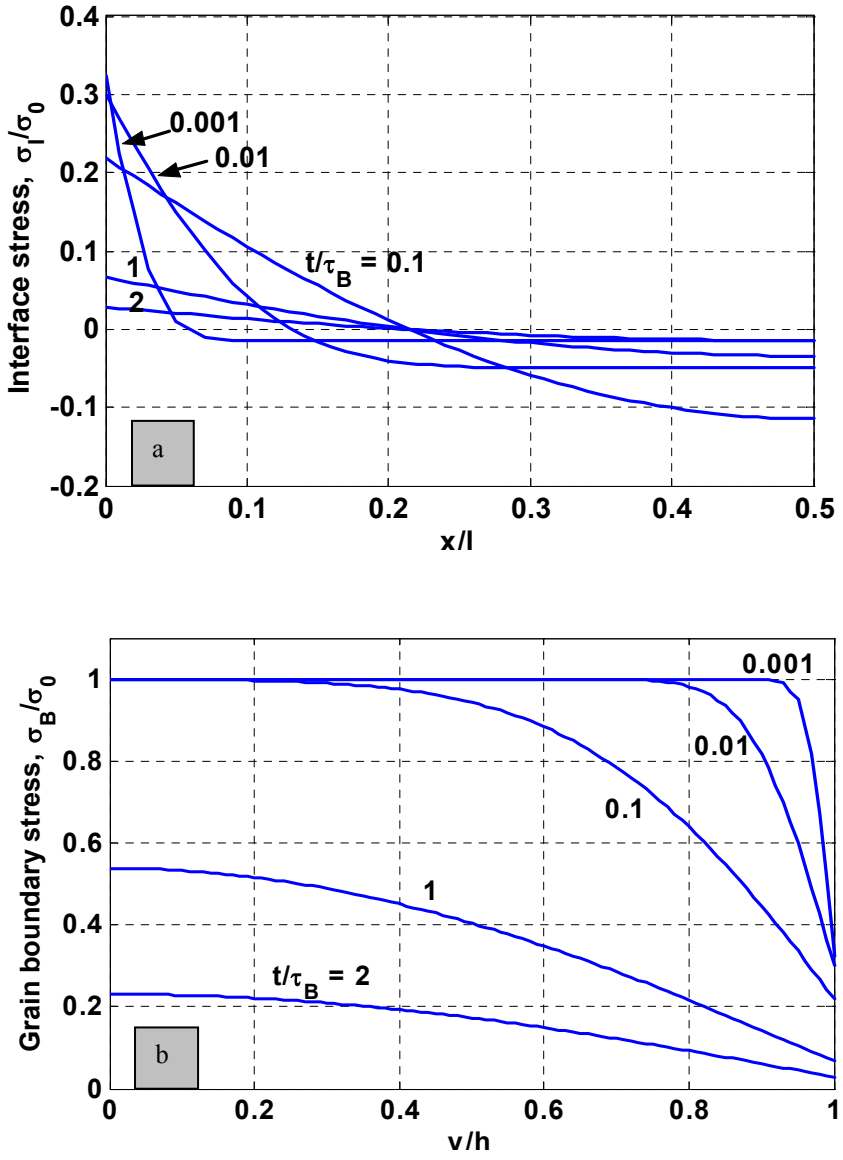


Figure 6.14 Simulated evolution of (a) the interface stress and (b) the grain boundary stress during isothermal relaxation of a passivated film with $\frac{\delta_I D_I}{\delta_B D_B} = 1$.

initial stress and the time is normalized by a time scale characterizing the grain boundary diffusion

$$\tau_B = \frac{4kTh^2 l}{\pi^2 M\Omega\delta_B D_B} \tag{22}$$

In this study, we consider the sensitivity using the stress relaxation measurement to evaluate the interface mass transport in Cu metallization. Figure 15 shows the predicted stress relaxation in unpassivated and passivated films with different ratios between the diffusivities. Figure 15(a) shows that, for unpassivated films, the stress relaxation curve is insensitive to the surface diffusivity as long as surface diffusion is faster than grain boundary diffusion, while in Fig.15 (b), the stress relaxation is shown to be much more sensitive to the interface diffusivity for passivated films than it is to the surface diffusivity for unpassivated films, especially if the diffusivities follow the general trend, $\delta_S D_S > \delta_B D_B > \delta_I D_I$. The sensitivity of the stress relaxation to interface diffusion allows quantitative characterization of the kinetics of mass transport along the interface, which can then be used to evaluate selected passivation layers for improving electromigration reliability of Cu interconnects.

Figure 16 shows comparison of the experimental data with the modeling results for the stress relaxation of the passivated Cu film at 200°C with different initial stresses. It is noted that, while the agreement between the model and the experiment is excellent for the case with the lower initial stress ($\sigma_0$ = 170 MPa), the agreement is poor for the case with the higher initial stress ($\sigma_0$ = 230 MPa). This suggests the existence of different deformation mechanisms at a high stress level and the diffusion mechanism considered in

this model should only be effective within a certain range of temperature and stress levels. With a high initial stress level, for example, the dislocation plasticity may be activated, especially at the initial stage.

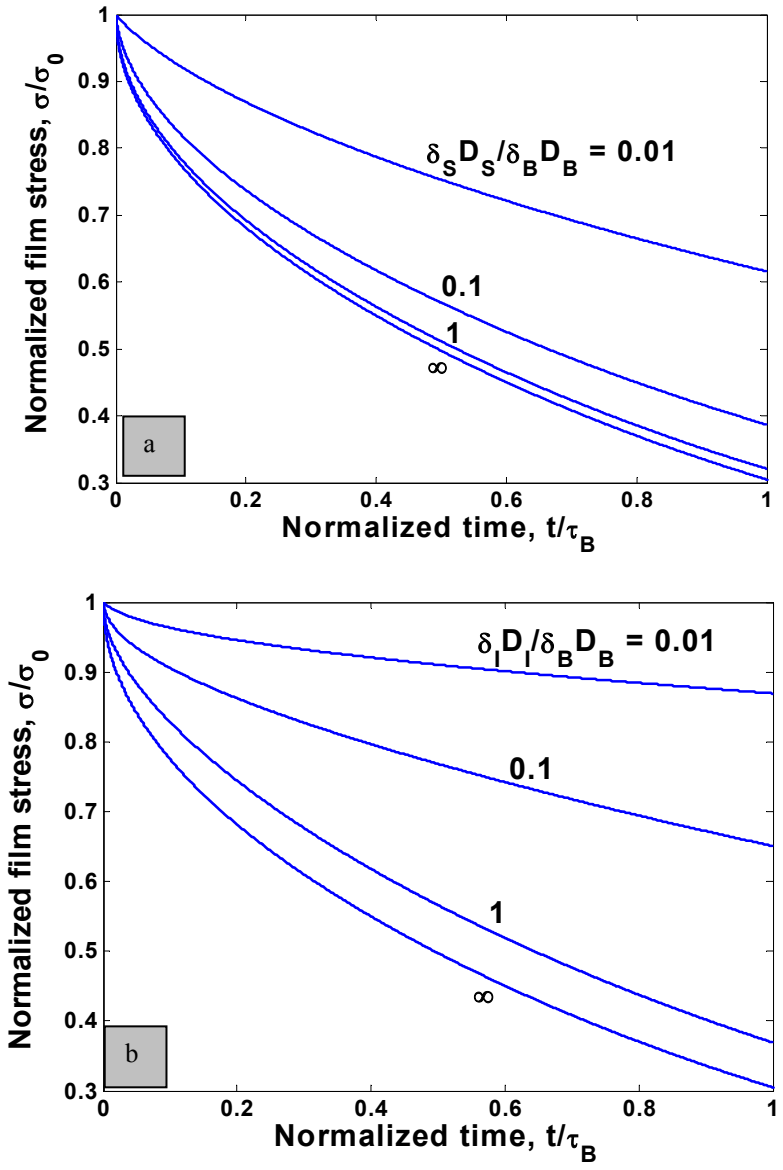


Figure 6.15 Effects of (a) surface diffusivity and (b) interface diffusivity on stress relaxation of unpassivated and passivated films, respectively.

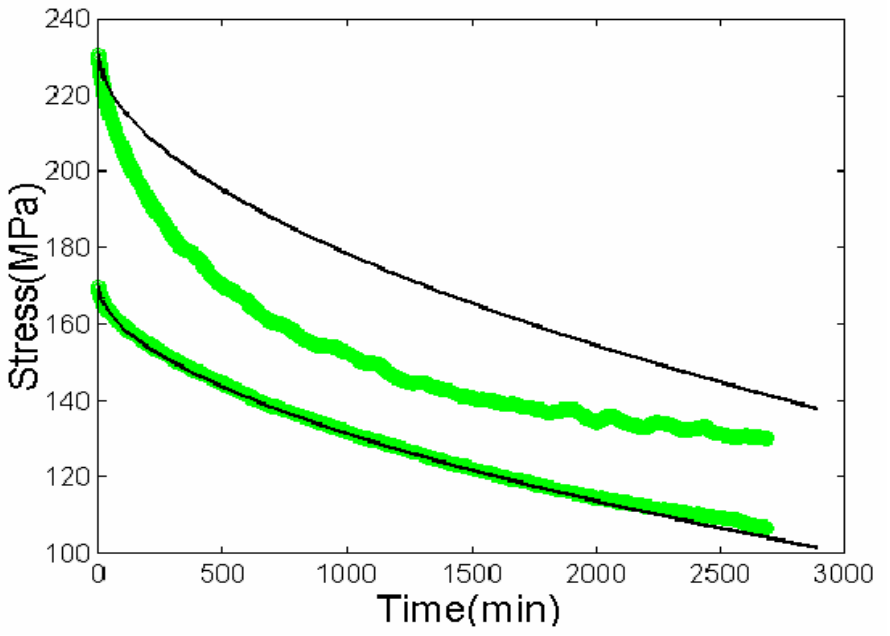


Figure 6.16 Comparison of the experimental and modeling results of the stress relaxation of the passivated Cu film at 200°C with different initial stresses.

### 6.2.5 Extraction of Grain Boundary and Interface Diffusivities

The isothermal stress relaxation experiments and the diffusion model together allow for the extraction of grain boundary and interface diffusivities. The corresponding activation energies can then be deduced from the temperature dependence of the diffusivities within the proper temperature range. In this study, the stress relaxation curves at 176ºC, 200ºC and 215ºC are used to evaluate the grain boundary and interface diffusivities as functions of temperature. The procedure is illustrated as follows.

First, the grain boundary diffusivity at various temperatures can be obtained from the stress relaxation curves of unpassivated films by comparison to the model prediction, i.e., Eq. (16) under the assumption that surface diffusion is typically faster than grain

boundary diffusion. The zero-creep stress, $\sigma_\infty$, however, is not well understood. The model predicts a negligible zero-creep stress for Cu films of 1.0 μm thickness from Eq. (17), while the experimental data suggests a significant zero-creep stress. For this reason, the zero-creep stress was deduced by fitting the experimental data with Eq.(8) and the results are listed in table 3.

Table 3 Zero-creep stress of the unpassivated Cu film in isothermal annealing deduced by curve fitting

| T (°C) | 176 | 200 | 215 |
|---|---|---|---|
| $\sigma_\infty$ (MPa) | 32.8 | 69.5 | 54.3 |

Then, the grain boundary diffusivity is varied to minimize the fitting error between Eq. (16) and the experimental data with the error defined as

$$error = \sqrt{\sum_{i=1}^{n} (\sigma_{mi} - \sigma_{ei})^2} \tag{23}$$

where the subscript "m" stands for the modeling data and "e" for the experimental data while "n" denotes the data size. Figure 17(a) shows the stress relaxation curves at three different temperatures, 176ºC, 200ºC and 215ºC, and the fitting results. The grain boundary diffusivities ($\delta_B D_B$) of the Cu film were deduced to be $9.5\text{x}10^{-27}\text{m}^3/\text{s}$, $5.5\text{x}10^{-26}\text{m}^3/\text{s}$ and $8.1\text{x}10^{-26}\text{m}^3/\text{s}$, respectively. The three diffusivities were then fitted into an Arrhenius plot as shown in Fig. 17(b), assuming $\delta_B D_B = \delta_B D_{B0} \exp(-Q_B / kT)$, from which we obtain the activation energy and the pre-exponential factor for the grain

boundary diffusion: $Q_B$ = 1.07eV and $\delta_B D_{B0}$ = 1.1 × $10^{-14}$ $m^3/s$, which are listed in Table2.

Next, the interface diffusivities at various temperatures are deduced similarly from the stress relaxation curves for the passivated Cu film by varying the ratio between the interface diffusivity and the grain boundary diffusivity. The grain boundary diffusivity deduced above was used to determine the interface diffusivity. Figure 18(a) shows the stress relaxation curves of the passivated Cu film at 176ºC, 200ºC and 215ºC and the fitting results. A finite difference method was used to obtain the numerical solutions for the coupled diffusion model. The interface diffusivities were deduced to be $4.94x10^{-28}$, $4.94x10^{-28}$ and $1.47x10^{-27}$ at 176ºC, 200ºC and 215ºC, respectively, shown in Fig. 18(b), from which we obtain the activation energy and the pre-exponential factor for the interface diffusion: $Q_I$ = 0.54eV and $\delta_I D_{I0}$ = 6.4 × $10^{-22}$ $m^3/s$. In the temperature range of the present study, the deduced Cu/$SiN_x$ interface diffusivity is about two orders of magnitude smaller than the deduced grain boundary diffusivity.

Some previous studies have assumed Cu films have the same grain boundary diffusivity as in bulk Cu, for which the activation energy is 1.08eV [6.25]. Other studies have reported grain boundary diffusivities measured directly in Cu polycrystals. For example, Gupta *at al*. [6.26] reported that $Q_B$ = 0.95eV and $\delta_B D_{B0}$ = 2.9 × $10^{-15}$ $m^3/s$. Compared to these results, the grain boundary diffusivity extracted in the present study seems to be reasonable. For the interface diffusivity, we are not aware of any previous report. In this study, the extracted interface diffusivity also depends on the grain

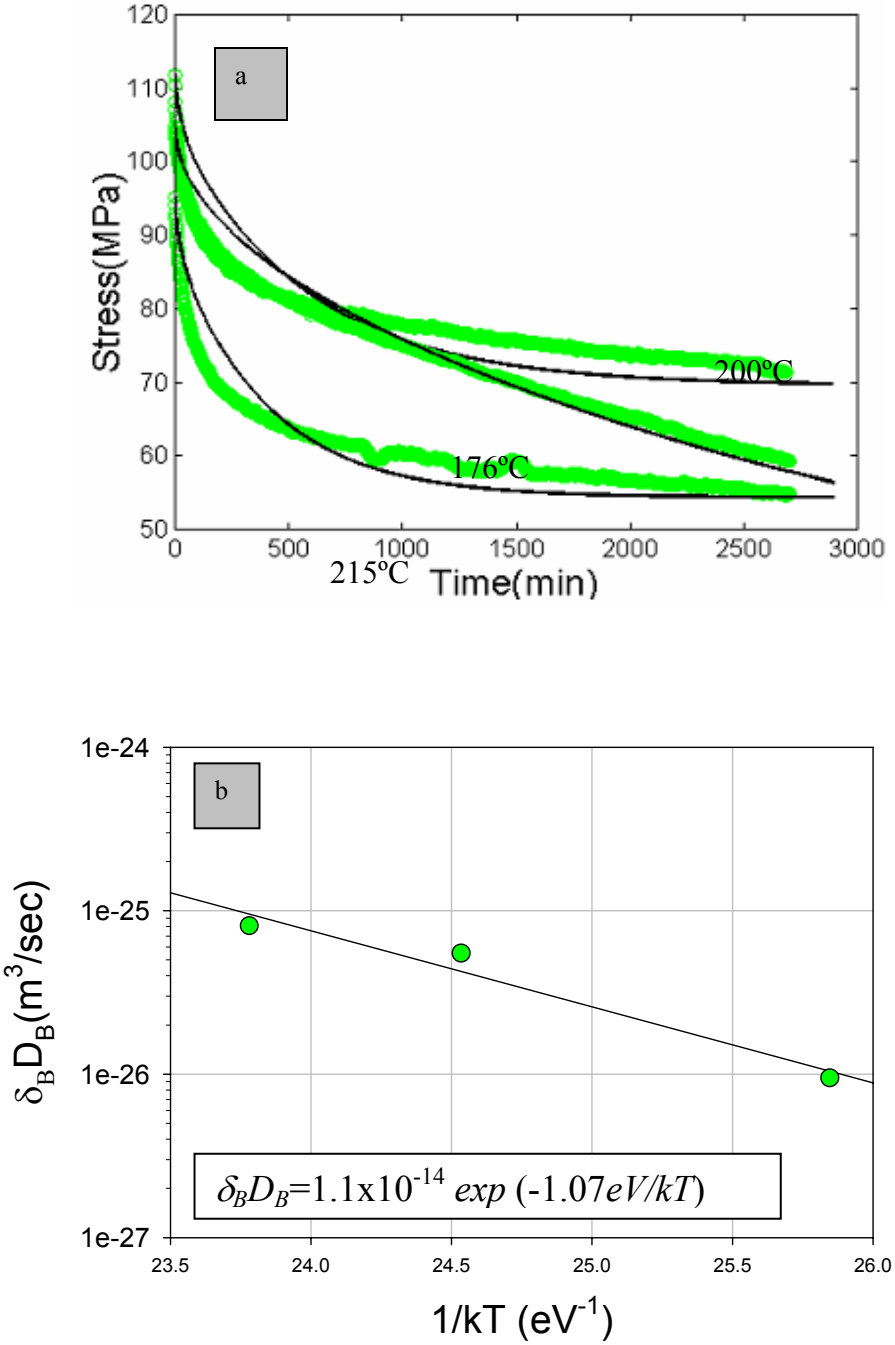


Figure 6.17. Deduction of the grain boundary diffusivities from the stress relaxation measurements: (a) experimental data and the fitting by the diffusion model; (b) the deduced grain boundary diffusivity as a function of temperature.

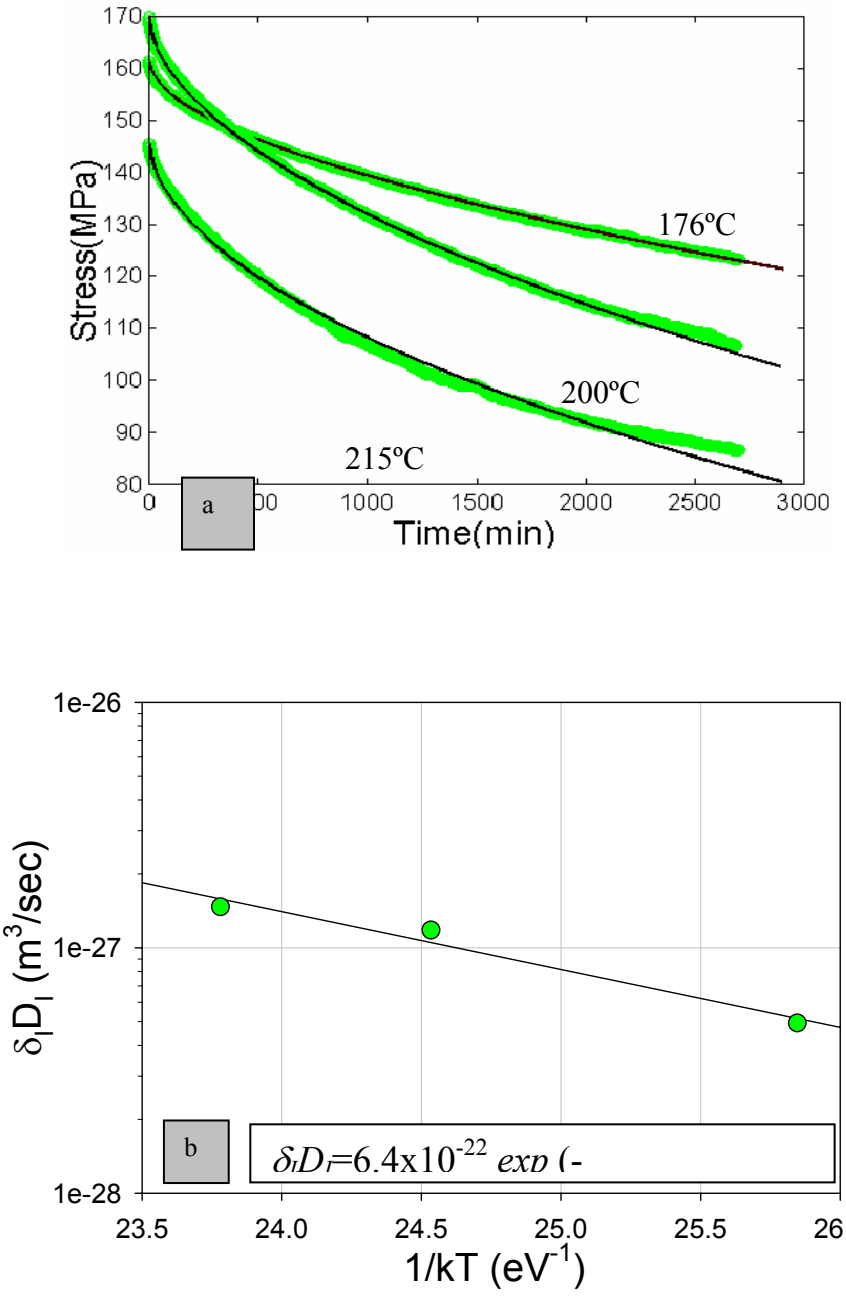


Figure 6.18. Deduction of the Cu/SiN interface diffusivity from the stress relaxation measurement: (a) experimental data and the fitting by the coupled diffusion model (numerical solutions); (b) the deduced Cu/SiN interface diffusivity as a function of temperature.

boundary diffusivity, due to the coupling of the two diffusion processes. Using the grain boundary diffusivity by Gupta *at al.* [6.26], we obtain that $Q_I$ = 0.66eV and $\delta_I D_{I0}$ = 1.0 $\times 10^{-20}$ $m^3/s$. In Fig. 19, we compare the two sets of interface diffusivities as well as the grain boundary diffusivities of the Cu film with the published results by Frost and Ashby [6.25], Gupta *et al*. [6.26], and Surholt and Herzig [6.27]. In the temperature range of this study, the interface diffusivity in the Cu film is about two orders of magnitude smaller than the grain boundary diffusivity, which qualitatively explains the higher strain rates in the unpassivated films (Fig. 5b) in comparison with those in the passivated films (Fig. 5a).

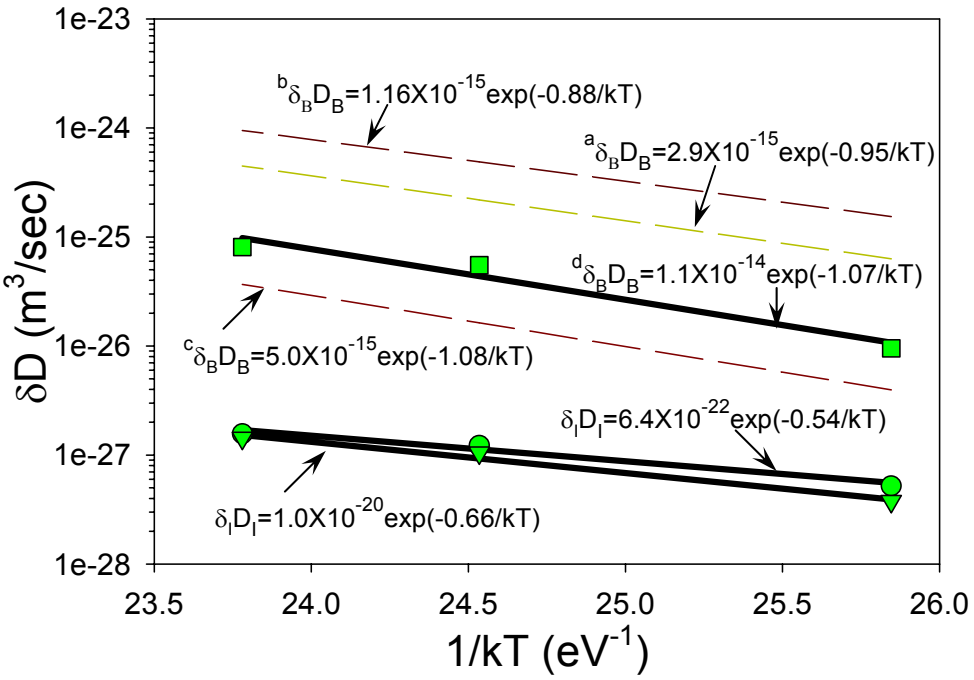


Figure 6.19 Comparison of the grain boundary and interface diffusivities with previous studies ([a]Gupta at al[6.26], [b]Surholt et al [6.27], [c]Frost at al [6.25] and [d]this study).

In sub-micron Cu lines with a bamboo-like microstructure, the Cu/cap layer interface is believed to be the dominant diffusion path for electromigration and the activation energy was determined from the EM lifetime to be between 0.8eV and 1.2eV [6.7]. Obviously, the activation energy, 0.54 or 0.66 eV, deduced in this study is lower than the values measured by electromigration test. Reasons for this discrepancy may be related to the properties of the interface in the passivated Cu film used in this study. EM lifetime is controlled by the mechanism of damage formation, a complex process where the diffusivity is only one of the controlling factors. It may not be surprising that the EM activation energy differs from that obtained for interface diffusion. The limitation of the modeling may be one of the reasons, which will be discussed in following.

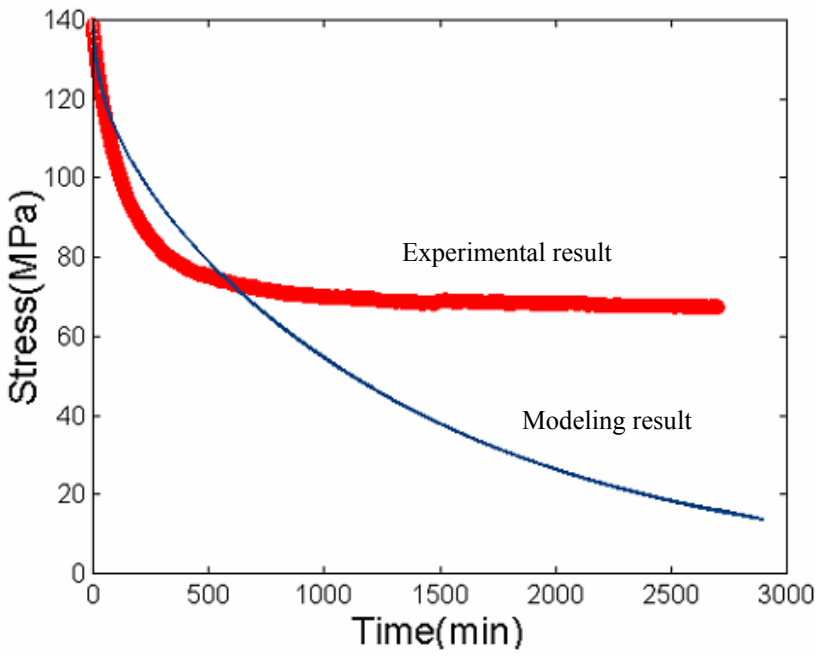


Figure 6.20. Comparison of the experimental and the modeling results of the stress relaxation of the passivated Cu film at 290°C, using the deduced interface diffusivity in Fig.18.

### 6.2.6 Modification of the Kinetic Model

***A. Change the boundary condition***

Figure 20 shows a comparison of the experimental and modeling results of the stress relaxation of the passivated Cu film at 290°C. The modeling curve is predicted using the interface diffusivity deduced by fitting the relaxation curves of 176°C, 200°C and 215°C. Compared to the fittings in Fig.18, the modeling result in Fig.20 does not agree well with the experimental data. In particular the predicted zero-creep stress is much lower than the experimental result which is about half of the initial stress. This suggests that the model may be applicable in limited stress and temperature ranges.

Although this model uses the boundary condition (13), which suggests that no diffusion flux flows from the grain boundary into the bottom interface, the stress of the film at the interface does relax, as shown in Fig. 14(b), and will relax to about zero with the relaxation rate of the bottom interface being comparable to that of the upper interface when the annealing time is longer than $0.1\tau_B$. In the passivated Cu film structure, the bottom interface is a Cu/Ta interface, which is supposed to be well bonded, compared to the upper Cu/SiNx interface. For this reason, the relaxation rate of the bottom interface is expected to be very slow and may be considered to be zero. Thus the stress of the bottom interface can approximately be considered constant during the stress relaxation

$$\sigma_B\big|_{y=0} = \sigma_0 \tag{24}$$

If Eq. 24 replaces Eq. 13 as one of the boundary condition for the stress relaxation of the

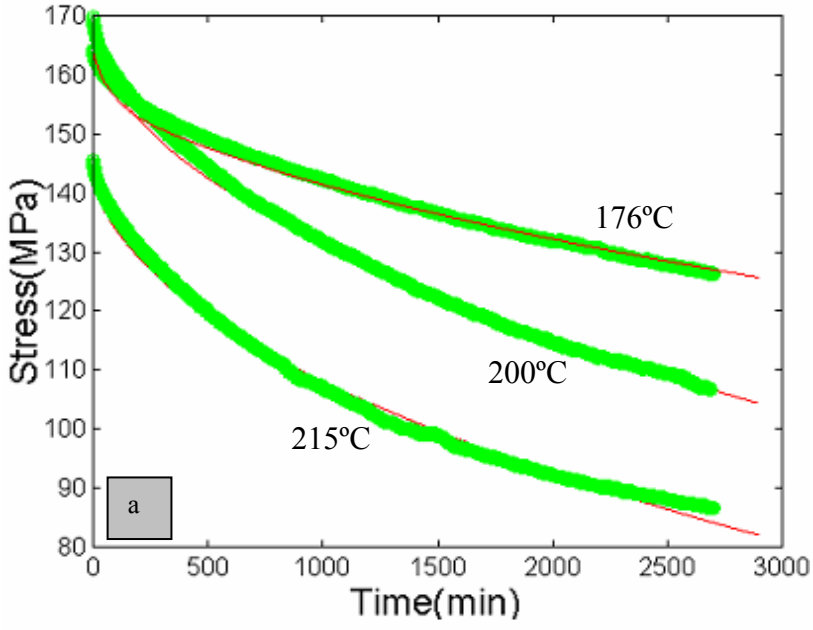


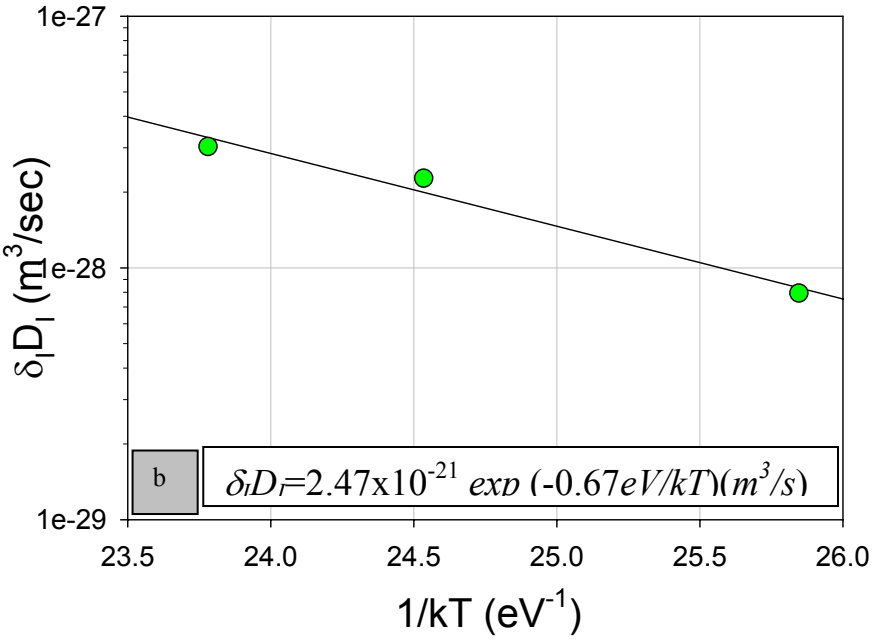


Figure 6.21. Deduction of the Cu/SiN interface diffusivity from the stress relaxation measurement: (a) experimental data and the fitting by the coupled diffusion model with modified BC (24); (b) the deduced Cu/SiN interface diffusivity as a function of temperature.

passivated Cu film, the time scale characterizing the grain boundary diffusion will be (details will be in section B)

$$\tau_B = \frac{kTh^2 l}{\pi^2 M\Omega\delta_B D_B} \tag{25}$$

In this case, the stress of the film will reach a stable state after relaxing for a very long time. There will be a linear stress distribution along the film thickness direction at the stable state with the stress in the upper interface relaxing to zero and the stress in the bottom interface being constant. This implies that zero creep stress of the film is half of the initial tensile stress, agreeing well with the experimental data. But this replacement also raises some details which are not well understood, such as that the final stress distribution of the film results in a stress gradient that may cause diffusion along grain boundary, but the model predicts a stable state. More details must be studied in the future.

Using the modification, we can deduce the interface diffusivity following the curve fitting process described in the above section. Figure 21 (a) shows the experimental and the modeling stress-time curves, and the deduced interface diffusivities are shown in Fig.21 (b), where The interface diffusivities were deduced to be $7.94x10^{-29}$, $2.27x10^{-28}$ and $3.03x10^{-28}$ at 176ºC, 200ºC and 215ºC, respectively. From these data, we obtain the activation energy and the pre-exponential factor for the interface diffusion: $Q_I = 0.67eV$ and $\delta_I D_{I0} = 2.47 \times 10^{-21}$ m$^3$/s. The activation energy is higher than the previous result of $0.54eV$, and this model predicts a higher residual stress in the Cu film, which is consistent with the experimental results.

### *B. A semi-phenomenological (SP) model*

According to Fig.12 (b), mass transport within grain boundaries will not result in the relaxation of the average stress of the film. The total stress relaxation depends on mass transports between the interface and grain boundaries: from grain boundaries to interfaces under tensile stress and conversely for compressive stress. Thus, the stress relaxation rate depends on the stress gradient between the interface and the grain boundary that governs the rate of mass transport between grain boundaries and the interface. It is reasonable to assume that the stress relaxation of the film depends on the stress relaxation of the interfaces, which is expected to be a function of bonding property or the interface diffusivity. Funn and Dutta [6.28] set up experiments and a model of a periodic interface to study interfacial sliding under shear creep. By modifying the classical model for grain boundary sliding [6.29], they gave the interface shear strain rate of

$$\dot{\gamma} \approx \frac{4\delta_I D_I \Omega}{kTh^3}\left[\tau_I + 2\sigma_R\left(\frac{\pi h}{\lambda}\right)^3\right] \tag{26}$$

where $\tau_I$ and $\sigma_R$ are respectively the shear stress and the normal stress acting on the interface while $h$ and $\lambda$ are the width (*i.e.*, twice the amplitude) and the morphological periodicity of the interface. Eq.26 indicates a linear relationship between the creep rate of the interface and the stress acting on it, which will cause the stress to relax exponentially as described in Eq. 7. Without considering the details, we assume that the relaxation of the interface stress is a diffusion-controlled process that follows the linear creep law and the stress decreases exponentially during the isothermal annealing. We have

$$\sigma_B\big|_{y=0} = \sigma_{10}\exp(-\frac{t}{\tau_1}) + \sigma_{1\infty} \tag{27}$$

$$\sigma_B\big|_{y=h} = \sigma_{20}\exp(-\frac{t}{\tau_2}) + \sigma_{2\infty} \tag{28}$$

and

$$\sigma_B\big|_{t=0} = \sigma_0 \tag{29}$$

where '1' stands for the bottom interface and '2" for the upper interface, $\sigma_0$ the initial stress, $\tau$ time scale characterizing the interface diffusion, while $\sigma_\infty$ is the zero-creep stress of the interfaces. Using Eq.27 and Eq.28 as boundary conditions and Eq.29 as the initial condition, Eq.12 can be solved and yield

$$\sigma(y,t) = (\sigma_{1\infty} - \sigma_{2\infty})\left(1 - \frac{y}{h}\right) + \sigma_{2\infty} + \sum_n C_n \exp\left(-A\left(\frac{n\pi}{h}\right)^2 t\right)\sin\left(\frac{n\pi}{h}y\right)$$
$$+ \frac{\sigma_{10}}{\sin\left(\frac{h}{\sqrt{A\tau_1}}\right)}\exp\left(-\frac{t}{\tau_1}\right)\sin\left(\frac{h-y}{\sqrt{A\tau_1}}\right) + \frac{\sigma_{20}}{\sin\left(\frac{h}{\sqrt{A\tau_2}}\right)}\exp\left(-\frac{t}{\tau_2}\right)\sin\left(\frac{y}{\sqrt{A\tau_2}}\right) \tag{30}$$

where $A = \frac{M\Omega\delta_B D_B}{lkT}$ and

$$C_n = 2\left[\frac{\sigma_{10}}{n\pi}\left(1-(-1)^n\right) + \frac{(-1)^{n+1}(\sigma_{1\infty}-\sigma_{2\infty})}{n\pi} - \frac{\sigma_{10}n\pi}{\left((n\pi)^2 - \frac{h^2}{A\tau_1}\right)} - \frac{(-1)^{n+1}\sigma_{20}n\pi}{\left((n\pi)^2 - \frac{h^2}{A\tau_2}\right)}\right]$$

Thus, the stress of the film is given by

$$\sigma_f(t) = \frac{1}{h}\int_0^h \sigma(y,t)dy$$

$$= \frac{(\sigma_{1\infty} + \sigma_{2\infty})}{2} + \sum_n C_n \exp\left(-A\left(\frac{n\pi}{h}\right)^2 t\right)\frac{\left(1-(-1)^n\right)}{n\pi} + \sigma_{10}\frac{\sqrt{A\tau_1}}{h}\exp\left(-\frac{t}{\tau_1}\right)\frac{\left(1-\cos\left(\frac{h}{\sqrt{A\tau_1}}\right)\right)}{\sin\left(\frac{h}{\sqrt{A\tau_1}}\right)}$$

$$+ \sigma_{20}\frac{\sqrt{A\tau_2}}{h}\exp\left(-\frac{t}{\tau_2}\right)\frac{\left(1-\cos\left(\frac{h}{\sqrt{A\tau_2}}\right)\right)}{\sin\left(\frac{h}{\sqrt{A\tau_2}}\right)}$$

(31)

where the time scale characterizing the grain boundary diffusion is $\tau_B = \frac{h^2}{\pi^2 A} = \frac{h^2 kTl}{\pi^2 M\Omega\delta_B D_B}$, which is used in section **A** with the modified boundary condition. Eq.31 also predicts the transient behavior of the stress relaxation in passivated films.

Figure 22 (a) and (b) show the stress distribution along the grain boundary as a function of time from $0.01\tau_B$ to $100\tau_B$ during stress relaxation with the interface properties being: $\sigma_{10}=\sigma_0$, $\sigma_{1\infty}=0.01\sigma_0$, $\tau_1=100\tau_B$ (for Fig. (b), $\tau_1=1000\tau_B$), $\sigma_{20}=0.8\sigma_0$, $\sigma_{2\infty}=0.01\sigma_0$, and $\tau_2=10\tau_B$. The correlated stress-time curves are shown in Fig. 23, which indicates that the residual stress of a passivated film for stress relaxation strongly depends on the property of the interface that increases with a longer time scale characterizing the interface diffusion. By comparing the geometry locations of the grain boundaries and the

interfaces in the passivated film structure shown in Fig. 13, the time scale characterizing the interface diffusion can be given by

$$\tau_I = \frac{cl^2 kTh}{\pi^2 M\Omega\delta_I D_I} \tag{32}$$

where $c$ is a constant which may be used to make adjustments. In this study, we take $c$=1 as approximation.

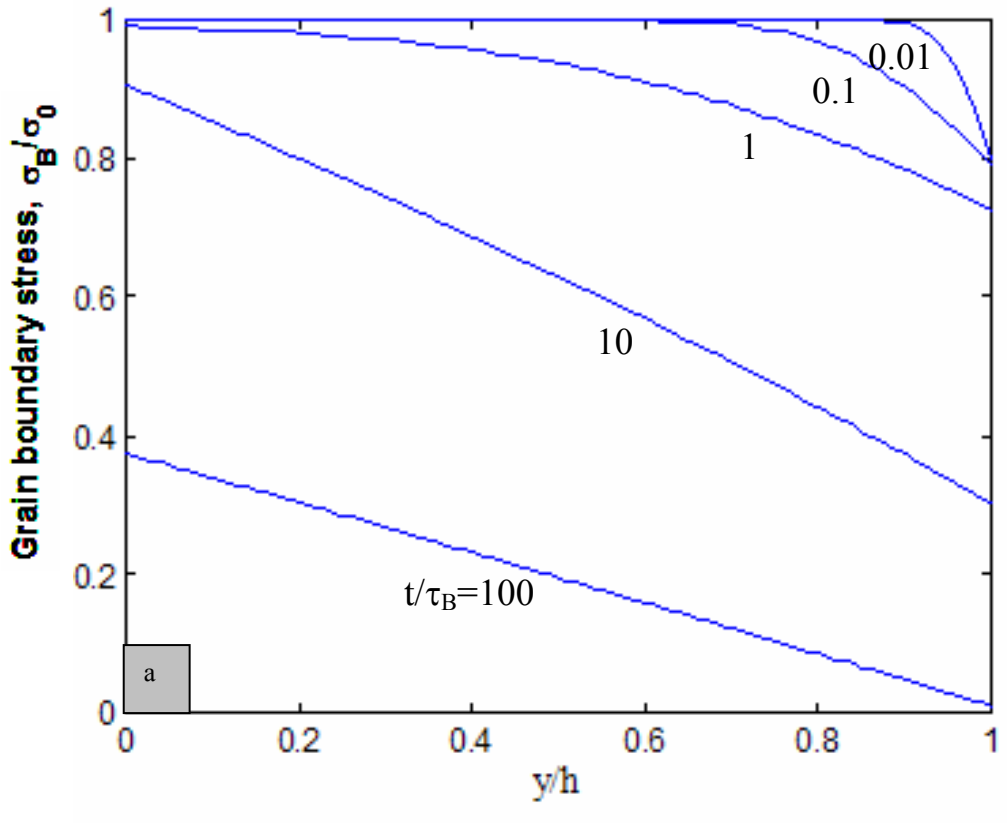


Figure 6.22 Effect of the interface property on the stress distribution along the grain boundary during stress relaxation of passivated films (a) $\tau_1=100\tau_B$, $\tau_2=10\tau_B$ (b) $\tau_1=1000\tau_B$, $\tau_2=10\tau_B$.

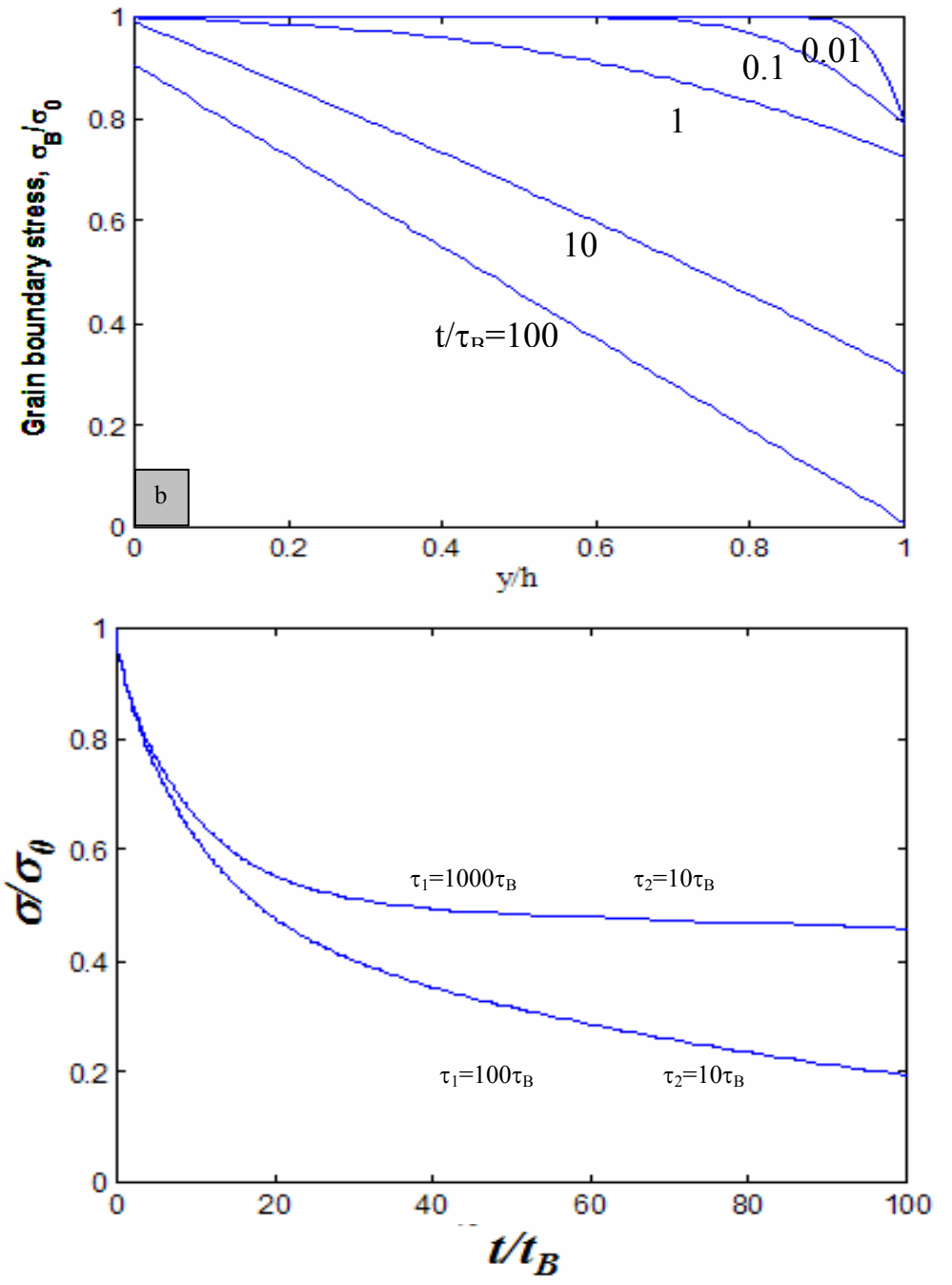


Figure 6.23 Effect of the interface property on stress relaxation of passivated films

Combination of the model and the experiment curves can also be used to deduce the interfacial diffusivity. The curve fitting results and the deduced interface diffusivity are shown in Fig. 24. The parameters were chosen as following. Without available values for the diffusivity of the Ta/Cu interface, the bottom interface was assumed to be well bonded and with the initial stress $\sigma_{10}$ being equal to the film stress $\sigma_0$ at the beginning of the stress relaxation at each temperatures. The time scale characterizing the bottom interface diffusion $\tau_1$ was set to be 300 times of that of the upper interface $\tau_2$ since this value caused the best fitting of the curve at 290°C. It was found that the change of the ratio of $\tau_1$ to $\tau_2$ does not significantly affect the fitting results at other temperatures when it was larger than 100, thus in this fitting, the ratio was also used for other temperatures. Once the above parameters were determined, by varying $\sigma_{20}$ and the upper interface diffusivity, the best fits were obtained and thus the correlated interface diffusivities were deduced, which were $1.6x10^{-27}$, $4.8x10^{-27}$, $6.7x10^{-27}$ and $7.46x10^{-26}$ $m^3$/sec with the $\sigma_{20}$ to $\sigma_0$ ratio of 0.75, 0.82, 0.85 and 0.95 at the temperature of 176°C, 200°C, 215°C and 290°C, respectively. Shown in Fig. 24(b), the activation energy and the pre-exponential factor for the interface diffusion are: $Q_1 = 0.73$eV and $\delta_1 D_{10} = 2.38 \times 10^{-19}$ $m^3$/s.

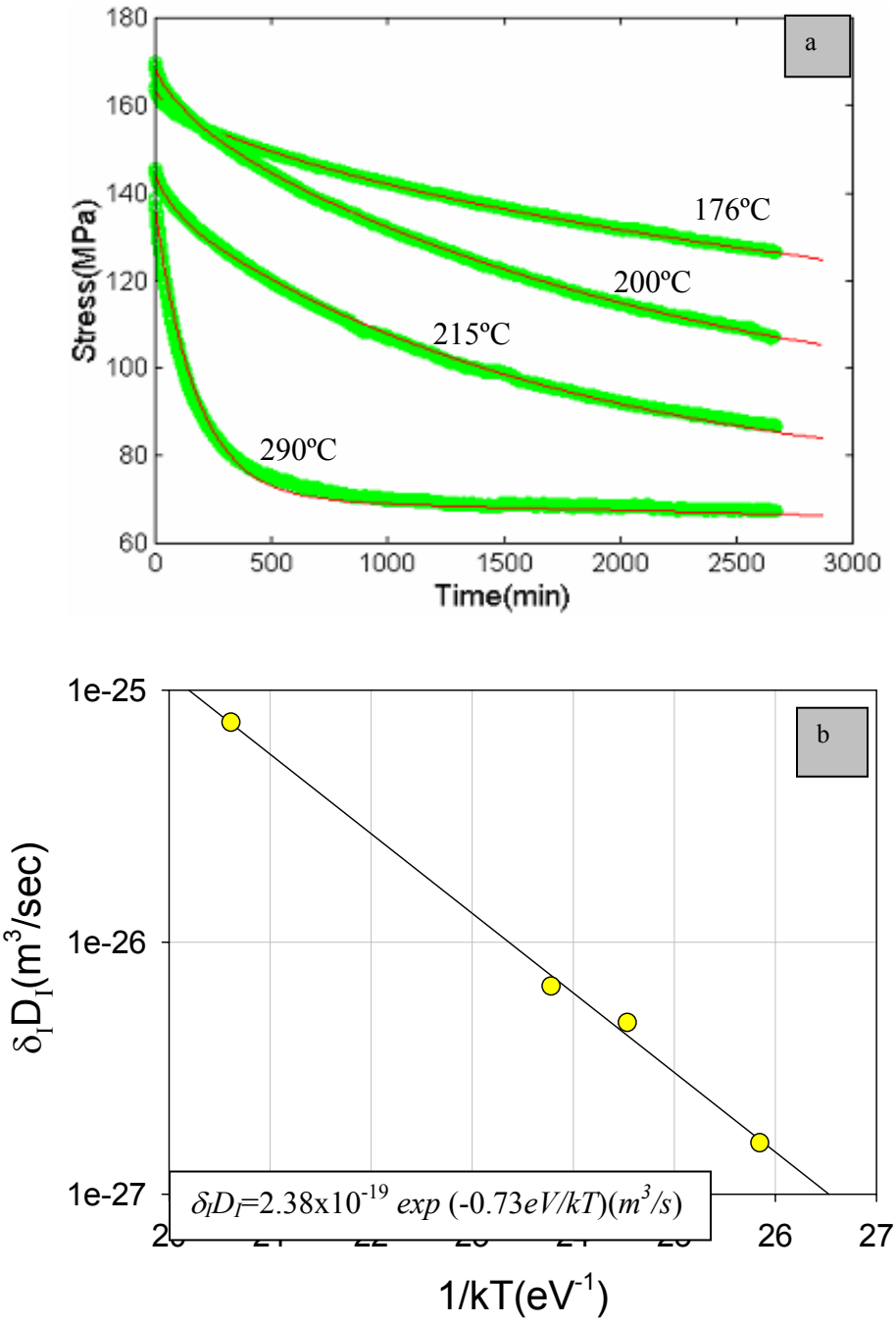


Figure 6.24. Deduction of the Cu/$SiN_x$ interface diffusivity from the stress relaxation measurement: (a) experimental data and the fitting by the semi-phenomenological diffusion model, (b) the deduced Cu/$SiN_x$ interface diffusivity as a function of temperature.

It is interesting to show that the $\sigma_{20}$ to $\sigma_0$ ratios are not equal to one for the best fit of the modeling results with the experimental data. The possible reasons may be the following. First, the initial stress of the Cu film was obtained by thermal cycling, during which, the interface stress would have been relaxing before the beginning of the isothermal stress relaxation at a given temperature. Second, the boundary conditions of Eq. 27 and 28 may not perfectly describe the behavior of the stress change of the interface. They can be considered as approximate solutions since the behavior of the interface may include a fast initial relaxation state as the transient relaxation state of the film. This could be adjusted in modeling when the ratio less than 1 is used. In addition, the ratio less than one suggests that the initial stress relaxation of the film is controlled by the grain boundary diffusion without the influence from the interface, shown in Fig.22,

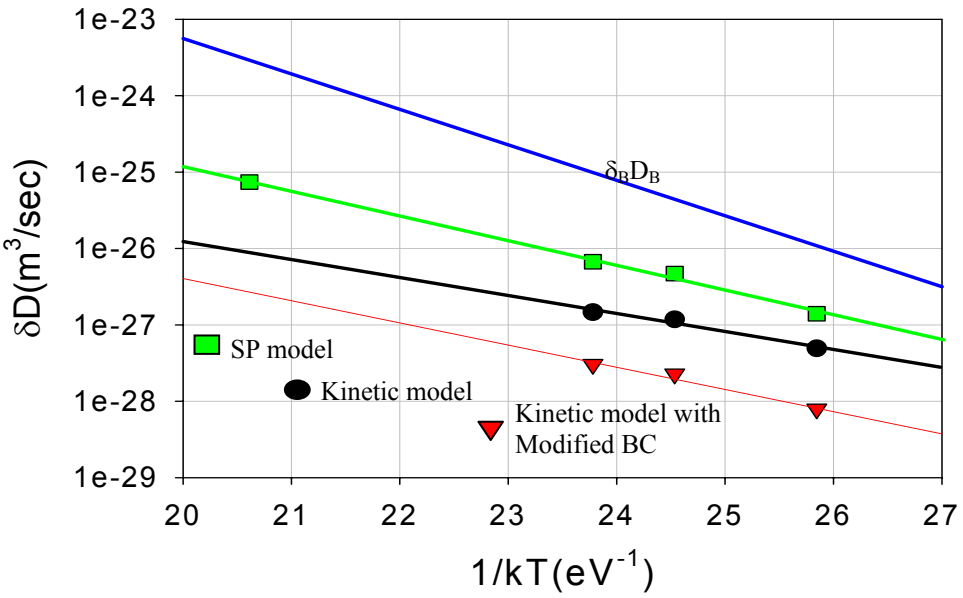


Figure 6.25. Comparison of the grain boundary diffusivity with the interface diffusivities deduced using different models.

resulting in a very fast initial relaxation rate. That is supported by the isothermal stress relaxation result of the Cu films with different passivation layers in the next section. Without in-depth understanding of the initial fast relaxation of the film that may also relate to the accumulated dislocation besides the grain boundary diffusion, using the ratio less than one is believed to be a good approximation.

Figure 25 shows the comparison of the deduced interface diffusivities using different models and correlated with the grain boundary diffusivity. All the deduced interface diffusivities are shown smaller than the grain boundary diffusivity in the test temperature range. Since the semi-phenomenological model provides an analytical solution of the stress relaxation of passivated films, it becomes feasible to combine the stress relaxation measurement and modeling to evaluate the interface diffusivity in a wide range of temperature, particularly at high temperatures, where it takes long time to have the numerical solution for the other two models, for example, using the MATLAB code running in a PC takes almost 5 days to draw a curve at 290°C. Furthermore, the semi-phenomenological model predicts a very small creep rate when the bottom interface dominates the stress relaxation of the film, which agrees well with the experimental observation (i.e. relaxation at 290°C). The activation energy deduced using this model is also consistent with that deduced in chapter 4 from the stress-voiding data. But the semi-phenomenological model is believed to be an approximation to describe the stress relaxation behavior of the passivated thin films. In-depth study of the involved mechanisms is needed but that is not the objective of this study.

### 6.2.7 Effect of the passivation layer

In this study, the Cu film samples were prepared in Intel. Figure 26 shows the schematic of the film stack. Different from the samples used in the previous studies, the Cu films were deposited on a 450nm thick CDO layer and subjected to a CMP process before being passivated by the layers of SiN, Novel SiC (N-SiC) or standard SiC (S-SiC). In addiction, a sample with a metal cap layer (M-cap) before being further passivated by a SiNx layer was prepared that added a Cu/(M-cap) interface with the Cu/$SiN_x$, Cu/N-SiC and Cu/S-SiC interfaces for this study.

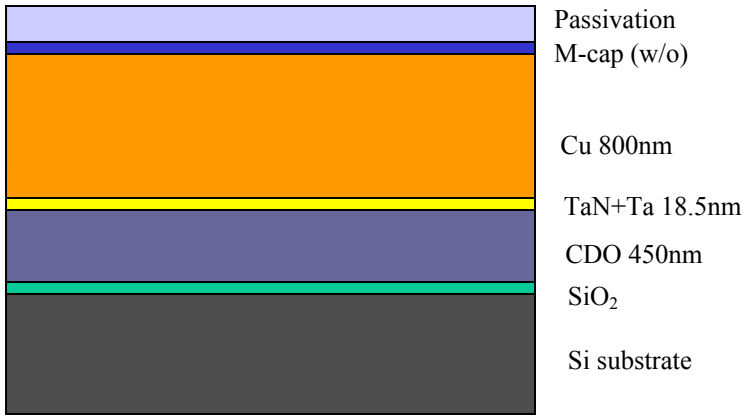


Figure 6.26 Schematic of the film stack of the Intel sample

**A. *Thermal stress during thermal cycling***

The thermal stress of the Cu films was measured during thermal cycling with a ramp rate of 4 °C/min. In the 1st cycle, the temperature range was from room temperature to 450°C where the sample was annealed for 20 minutes. Since the 1st cycle was used to stabilize the microstructure of the films, only the data from the subsequent three cycles

with the cycling temperatures of 400°C, 350°C and 300°C, respectively are shown for each sample. Figure 27 shows the result of the unpassivated Cu film, where the stress behavior is significantly different from that in Fig. 2 by showing inflection points upon both heating up and cooling down. That means the diffusional creep contributed more in this film to the inelastic deformation at the high temperature range during thermal cycling. This might be due to the effects of the CMP on the Cu surface or due to different Cu film properties from different chemistries used for electroplating.

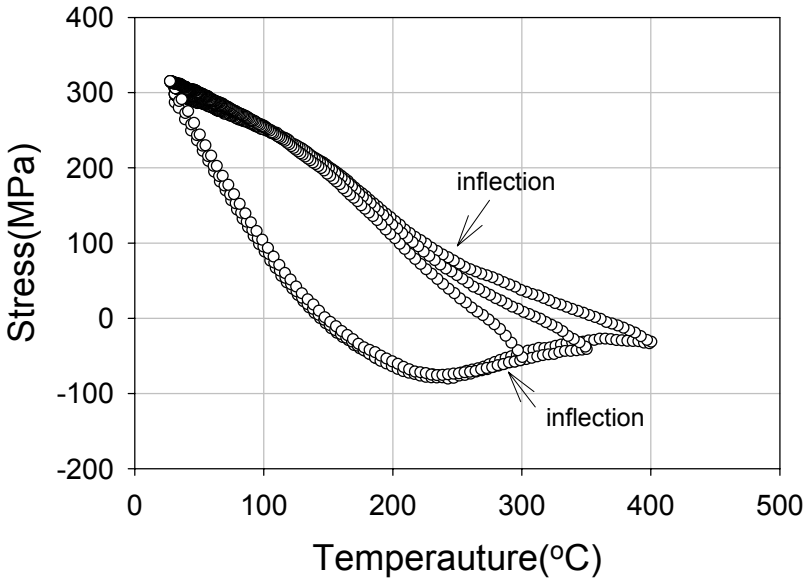


Figure 6.27 Thermal stress of the 0.8μm thick unpassivated Cu film

The thermal stress of the Cu films passivated by metal/$SiN_x$, $SiN_x$, novel SiC and old SiC during thermal cycling are shown in Fig 28-31, respectively. Different from that of the unpassivated Cu film, the stress-temperature curves of the passivated Cu films show higher residual tensile stresses in room temperature and higher compressive stresses in the elevated temperature range. In addition, no sinks occur upon heating and cooling in

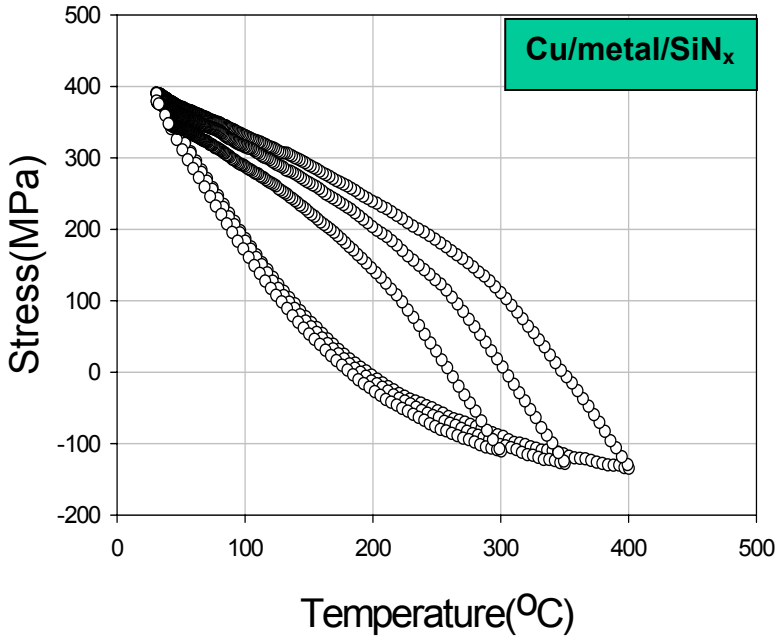


Figure 6.28 Thermal stress of the 0.8μm thick Cu film capped with metal/$SiN_x$ .

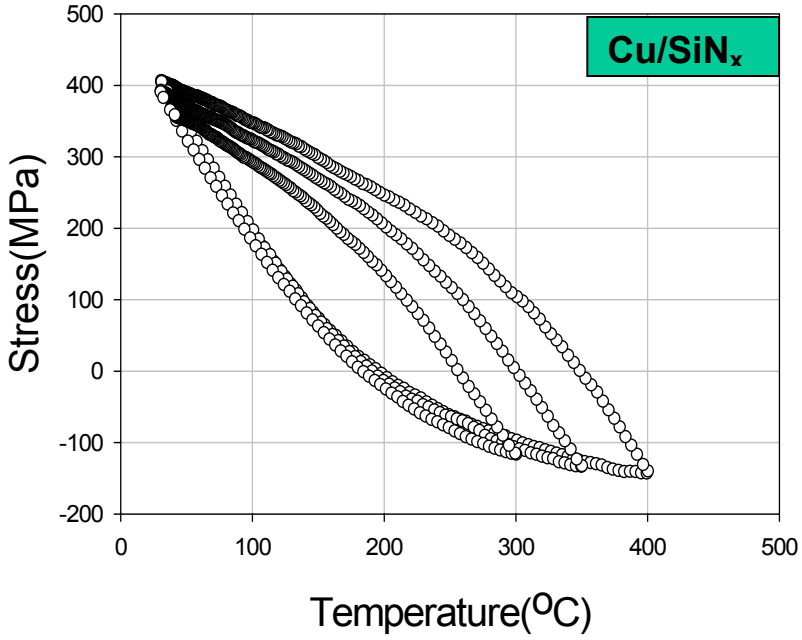


Figure 6.29 Thermal stress of the 0.8μm thick Cu film capped with $SiN_x$ .

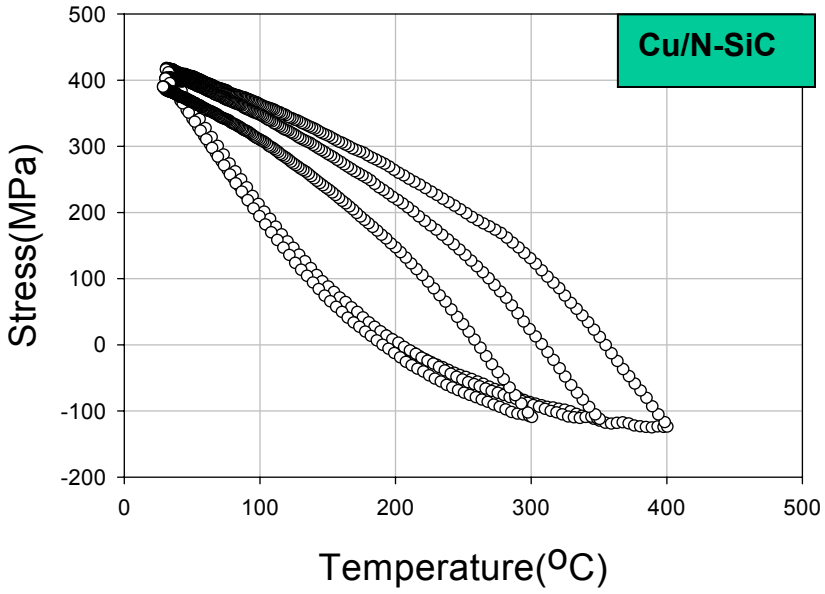


Figure 6.30 Thermal stress of the 0.8μm thick Cu film capped with N-SiC

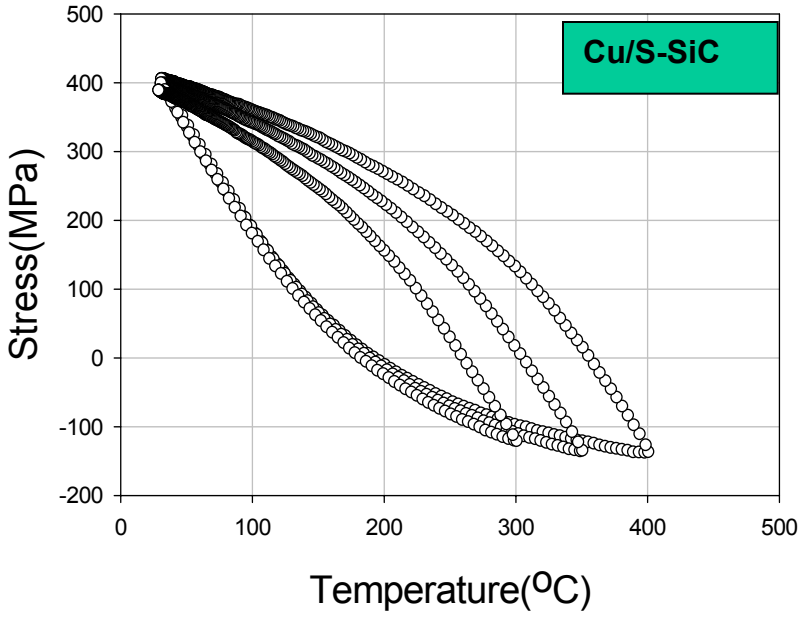


Figure 6.31 Thermal stress of the 0.8μm thick Cu film caped with S-SiC

these curves of the passivated Cu films. Compared to these significant differences between the stress curves of the unpassivated and the passivated films, the differences among the curves of the passivated Cu films seem to be negligible. These curves are shown to have similar shapes and the stress values in the temperature range for each thermal cycle. This observation supports our previous conclusion that thermal stress of the Cu films during thermal cycling is not suitable to evaluate mass transport through the Cu/cap interface.

**B.** ***Isothermal stress relaxation***

Isothermal stress relaxation measurements were set up from the same initial stress, about 192 MPa in this study but at different temperatures, 179°C, 210°C and 247°C. Based on the thermal stresses of the Cu films during thermal cycling shown in Figs. 28-31, the above temperatures for isothermal stress relaxation with an initial stress of 192MPa in the Cu films were achieved when the films were cooled down from 300°C, 350°C and 400°C, respectively in the $2^{nd}$ cycle. All the samples were annealed and were believed to develop similar microstructures in the $1^{st}$ cycle, from room temperature to 450°C, which was held for 30 minutes before cooling down. Figure 32-35 show the stress relaxation curves at different temperatures for the films passivated by the metal/$SiN_x$, $SiN_x$, N-SiC and S-SiC, respectively. It is indicated that stress relaxation of the Cu films strongly depends on the passivation layer while increase of the annealing temperature resulted in more stress relaxed in the 35 hour period. It is interesting to be noted that the relaxation of the initial several-MPa stress was not affected by the type of the passivation

layer, although the rest of the stress relaxation strongly depended on the passivation layer. As mentioned above, the initial part of the stress relaxation was believed to be controlled by the diffusion inside the film through grain boundaries. To account for that, the semi-phenomenological model was used to fit the stress relaxation curves, shown in the correlative figures as red lines. The grain boundary diffusivity of $\delta_B D_B$=1.1x10$^{-14}$ *exp* (-1.07*eV/kT*) ($m^3/s$) and the bi-axial modulus of 196MPa deduced from the elastic part of the stress-temperature curve upon heating were used for modeling. The other fitting parameters and the deduced interfacial diffusivities are listed in table 4. The modeling curves were shown to agree well with the experimental data.

Table 4. The parameters for least-square fitting of the stress relaxation curves

| Passivation | *T (℃)* | $\sigma_{10}$ | $\sigma_{20}$ | $\delta_I D_I$ ($m^3/s$) |
|---|---|---|---|---|
| Metal/$SiN_x$ ($\tau_1=20\tau_2$) | 179 | $\sigma_0$ | $0.93\sigma_0$ | 7.7x10$^{-29}$ |
| | 210 | $\sigma_0$ | $0.91\sigma_0$ | 1.5x10$^{-28}$ |
| | 247 | $\sigma_0$ | $0.90\sigma_0$ | 4.2x10$^{-28}$ |
| $SiN_x$ ($\tau_1=100\tau_2$) | 179 | $\sigma_0$ | $0.92\sigma_0$ | 2.1x10$^{-28}$ |
| | 210 | $\sigma_0$ | $0.91\sigma_0$ | 5.2x10$^{-28}$ |
| | 247 | $\sigma_0$ | $0.91\sigma_0$ | 2.1x10$^{-27}$ |
| N-SiC ($\tau_1=100\tau_2$) | 179 | $\sigma_0$ | $0.88\sigma_0$ | 5.2x10$^{-28}$ |
| | 210 | $\sigma_0$ | $0.90\sigma_0$ | 9.6x10$^{-28}$ |
| | 247 | $\sigma_0$ | $0.92\sigma_0$ | 2.8x10$^{-27}$ |
| | 295 | $\sigma_0$ | $0.95\sigma_0$ | 1.25x10$^{-26}$ |
| S-SiC ($\tau_1=100\tau_2$) | 179 | $\sigma_0$ | $0.83\sigma_0$ | 9.8x10$^{-28}$ |
| | 210 | $\sigma_0$ | $0.84\sigma_0$ | 2.4x10$^{-27}$ |
| | 247 | $\sigma_0$ | $0.88\sigma_0$ | 7.3x10$^{-27}$ |
| | 295 | $\sigma_0$ | $0.90\sigma_0$ | 1.6x10$^{-26}$ |

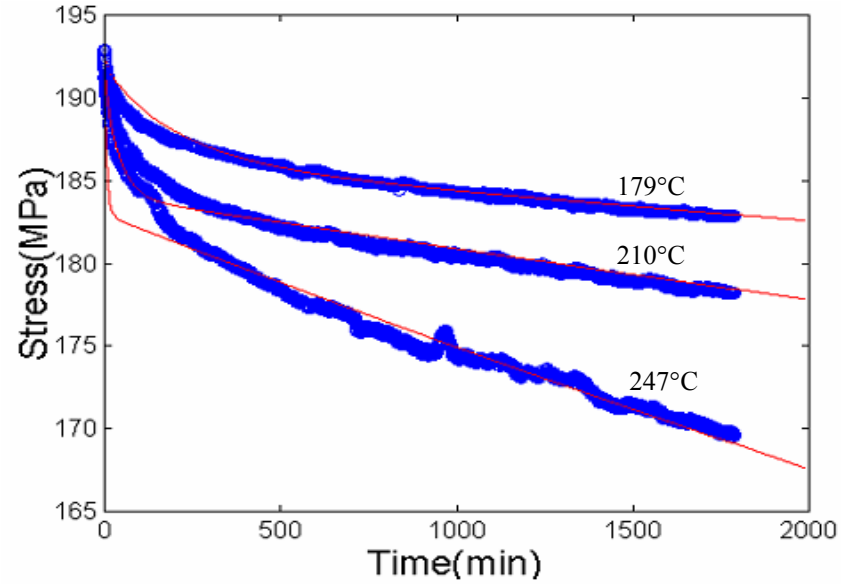


Figure 6.32 Isothermal stress relaxation of the Cu film caped with metal/SiN

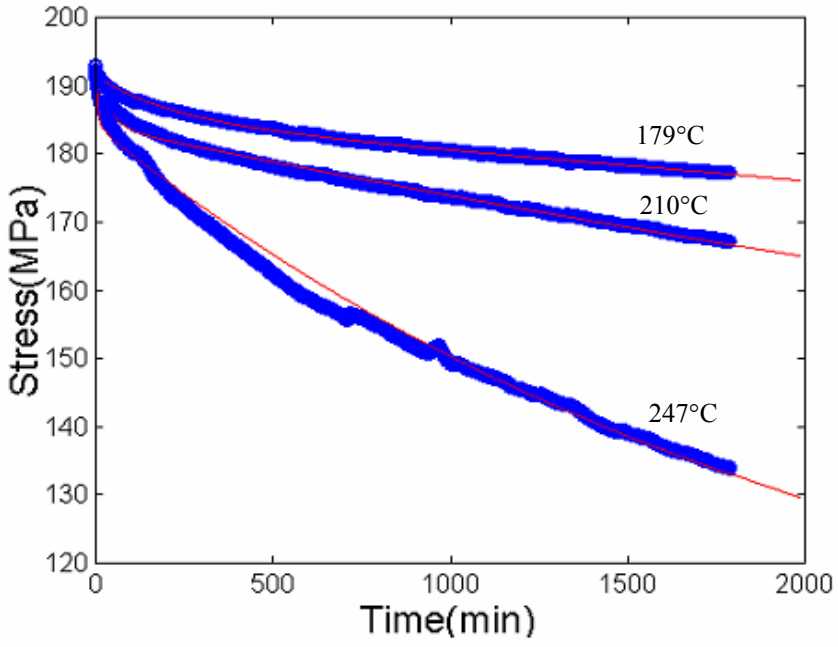


Figure 6.33 Isothermal stress relaxation of the Cu film capped with $SiN_x$

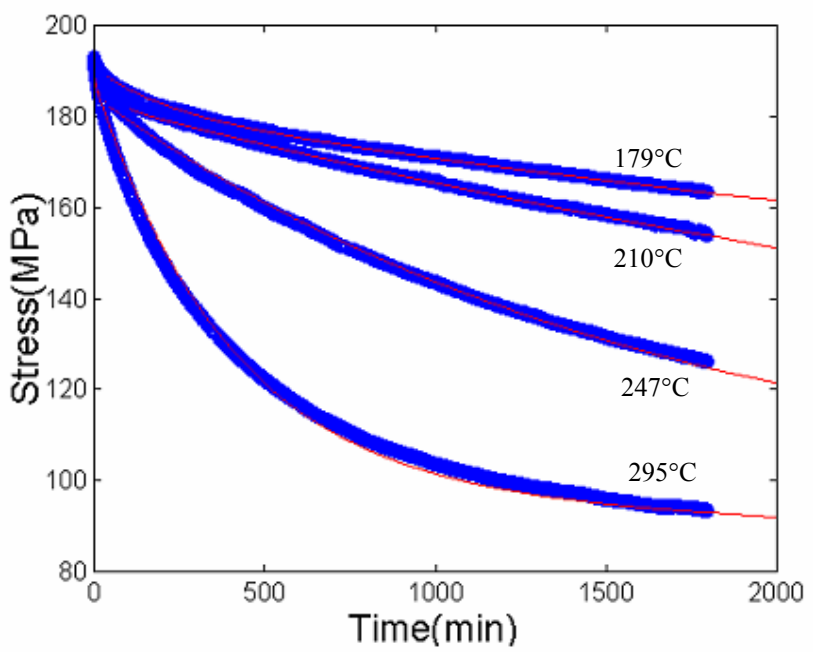


Figure 6.34 Isothermal stress relaxation of the Cu film capped with N-SiC

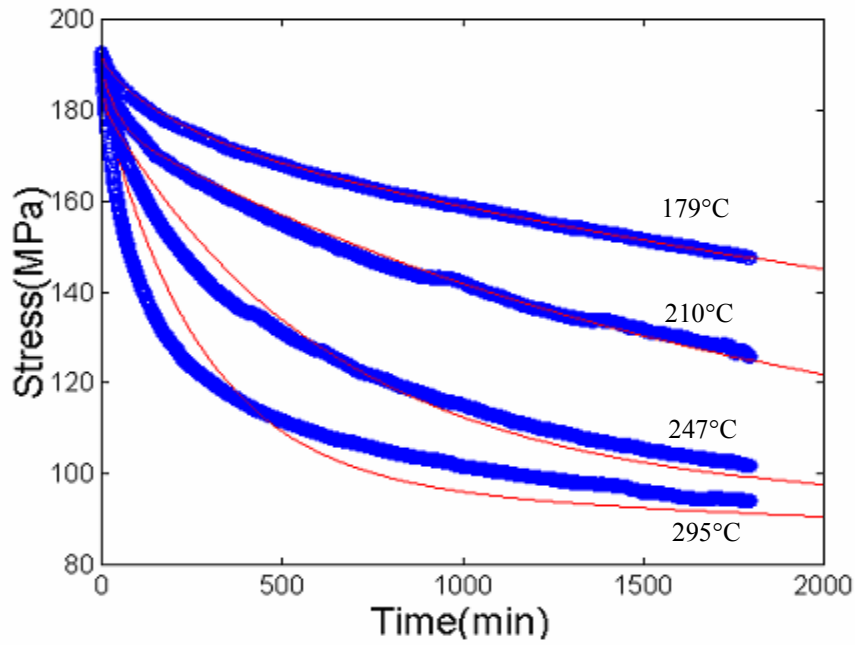


Figure 6.35 Isothermal stress relaxation of the Cu film capped with S-SiC

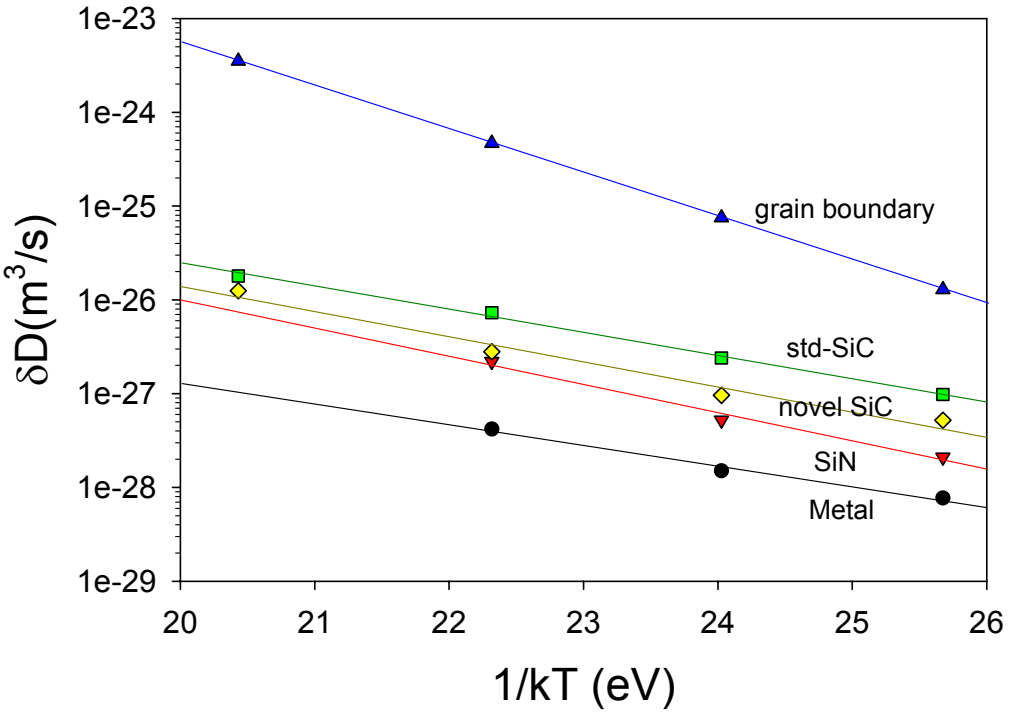


Figure 6.36 Comparison of the deduced interfacial diffusivities with the grain boundary diffusivity

The interfacial diffusivities listed in table 4 were then fitted into Arrhenius plots as shown in Fig.36 compared with the grain boundary diffusivity. Using linear regression, the interfacial diffusivities as functions of temperature were deduced to be

$\delta_I D_I = 3.18 \times 10^{-23} \exp(-0.51/kT)$ for Cu/metal

$\delta_I D_I = 1.25 \times 10^{-20} \exp(-0.70/kT)$ for Cu/$SiN_x$

$\delta_I D_I = 2.79 \times 10^{-21} \exp(-0.61/kT)$ for Cu/N-SiC

$\delta_I D_I = 1.91 \times 10^{-21} \exp(-0.56/kT)$ for Cu/S-SiC

In the temperature range of this study, the interfacial diffusivities are shown to decrease in the order of S-SiC > N-SiC > $SiN_x$ > metal, and all of them are smaller than

the grain boundary diffusivity. This order is consistant with the result reported by M. Lane *et al* [ 9] that the electromigration life time of the Cu interconnects passivated with different cap layers decreased in the order of metal > $SiN_x$ > SiC. Although the interfaces in this study may not be exactlly the same with those in M.Lane's study since interfaces are highly process dependent, the results indicates that stress relaxation measurement is an effective method to evaluate the interfacial mass transport corelated to EM lifetime.

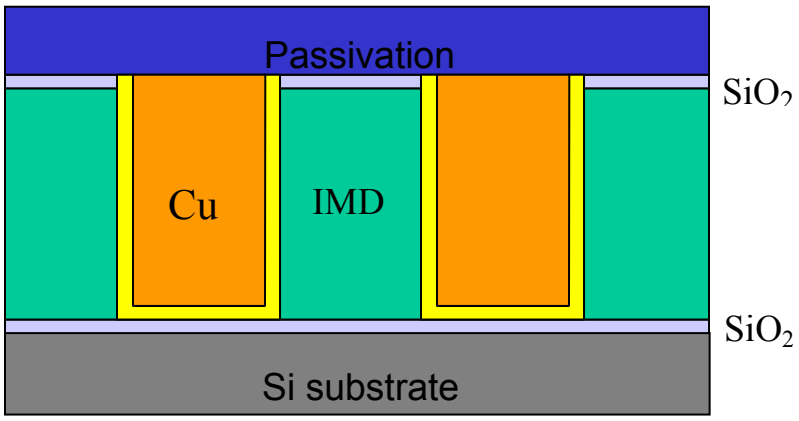


Figure 6.37 cross-section of the line structure for stress relaxation study

## 6.3 STRESS RELAXATION IN COPPER INTERCONNECTS

In this study, the effect of passivation layers on stress relaxation of Cu interconnects was investigated and correlated to the EM lifetime and interfacial adhesion. The samples particularly designed for this study were fabricated in Intel. Figure 37 shows a schematic of a cross-section of the line structure, referred to as a "landed" structure in which there is no low-k ILD beneath the Cu lines. The thickness of the barrier is about 7-10nm on the sidewalls while that on the bottom is much thicker. The line width/pitch is

0.2μm /0.4μm and the aspect ratio of the Cu lines is about 3 with two kinds of IMD, SiOF and SiLK™, and two kinds of passivation layer, $SiN_x$ and SiC. Another set of damascene Cu/CDO line structure, referred to as a "hanging" structure as shown in Fig.4.2, was also used in this study with the line width/pitch being 0.2μm /0.4μm and the aspect ratio of 2. Besides the $SiN_x$ and SiC passivation layers, an additional passivation layer named ES#1 was also used in the Cu/CDO structure. For comparison, the unpassivated Cu line structure was subjected to the same stress relaxation measurement.

The stress relaxation of the line structures was measured using the bending beam method. Since the interconnect layers on the wafer were elastically anisotropic, modified Stoney's equations, equation 2.1-4a and 2.1-4-b were used to calculate the stress of the layer from the measured curvature changes of the substrate in the directions parallel and perpendicular to the Cu lines. In this case, two kinds of the sample configuration shown in Fig. 38 were used for measurement. The Si substrate was thinned down to about 300μm by mechanical polishing to increase the ratio of signal to noise of the curvature measurement.

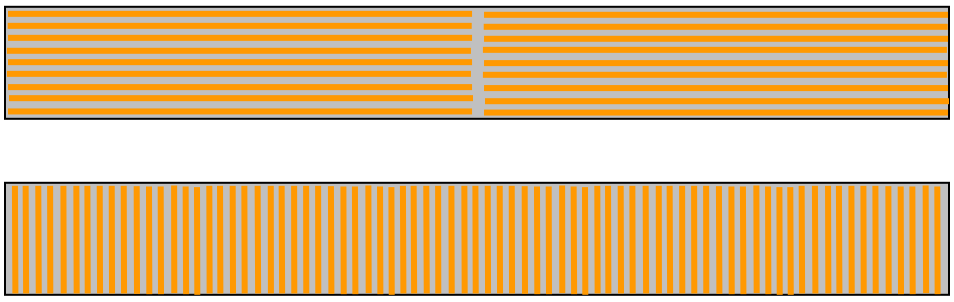

Figure 6.38 Sample configurations of Cu line structures for bending beam stress measurement

The purpose of this study was to investigate the effect of the passivation layer on stress relaxation of Cu interconnects. Since stress relaxation strongly depends on the initial stress and the microstructure of the materials, in order to show the effect of the passivation layer, it is quite important to set other conditions to be the same for different samples except the passivation layer. During the deposition of passivation, the Cu interconnects were subjected to thermal loading, which would result in different microstructures and residual stresses in Cu lines capped by different passivation layers. That is clearly shown in the study of annealing effect on the residual stress in Cu lines in chapter 4. Thus, in this study, all samples were annealed at 430°C for 30 minutes before being cooled down to the selected temperatures for stress relaxation measurement.

Samples were cut into beams 5mm in width and 5cm in length. The sample beams with the two configurations shown in Fig.36 were simultaneously put in the vacuum chamber of the BB system. The chamber was filled with 50 torr $N_2$. With a ramp rate of 4°C /min, the samples were first heated up from RT to 430°C, then held hold for 30 minutes to stabilize the microstructure of the Cu lines as mentioned above. Then the samples were cooled down to 200°C for stress relaxation, where the curvature change of the beams was recorded as a function of time, from which the stress was calculated using equation 2.1-4a and 2.1-4b.

### 6.3.1 Experimental results

**A.** ***Effect of passivation layer on thermal stress in Cu lines***

The thermal stress of the Cu lines in the Cu/SiOF and Cu/CDO interconnect structures with different passivation layers was measured using XRD during thermal cycling from room temperature to 400ºC with a ramp rate of 2ºC/min. The 1$^{st}$ cycle was used to stabilize the samples and only the results from the 2$^{nd}$ thermal cycle were shown in Fig.39 and Fig.40 for the Cu/SiOF and Cu/CDO line structures, respectively, where $\sigma_x$, $\sigma_y$ and $\sigma_z$ was the stress along, cross and normal to the Cu lines. The results indicate that thermal stress characteristics of the Cu lines passivated with different passivation layers were similar in either Cu/SiOF or Cu/CDO structures, indicating that different passivation layers have similar effects on the thermal stress in Cu lines.

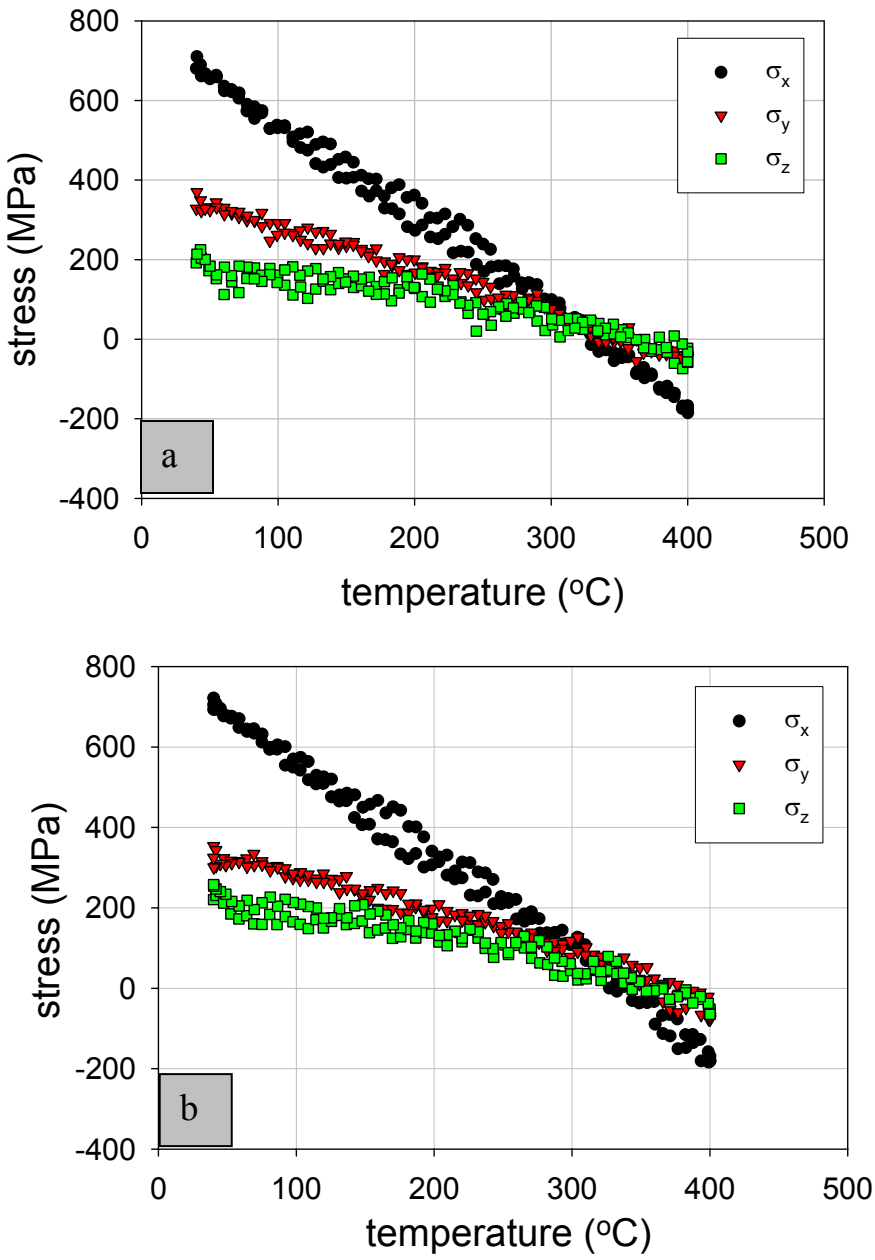


Figure 6.39 Thermal stress of Cu lines in Cu/SiOF structures passivated with a) SiN and b) SiC.

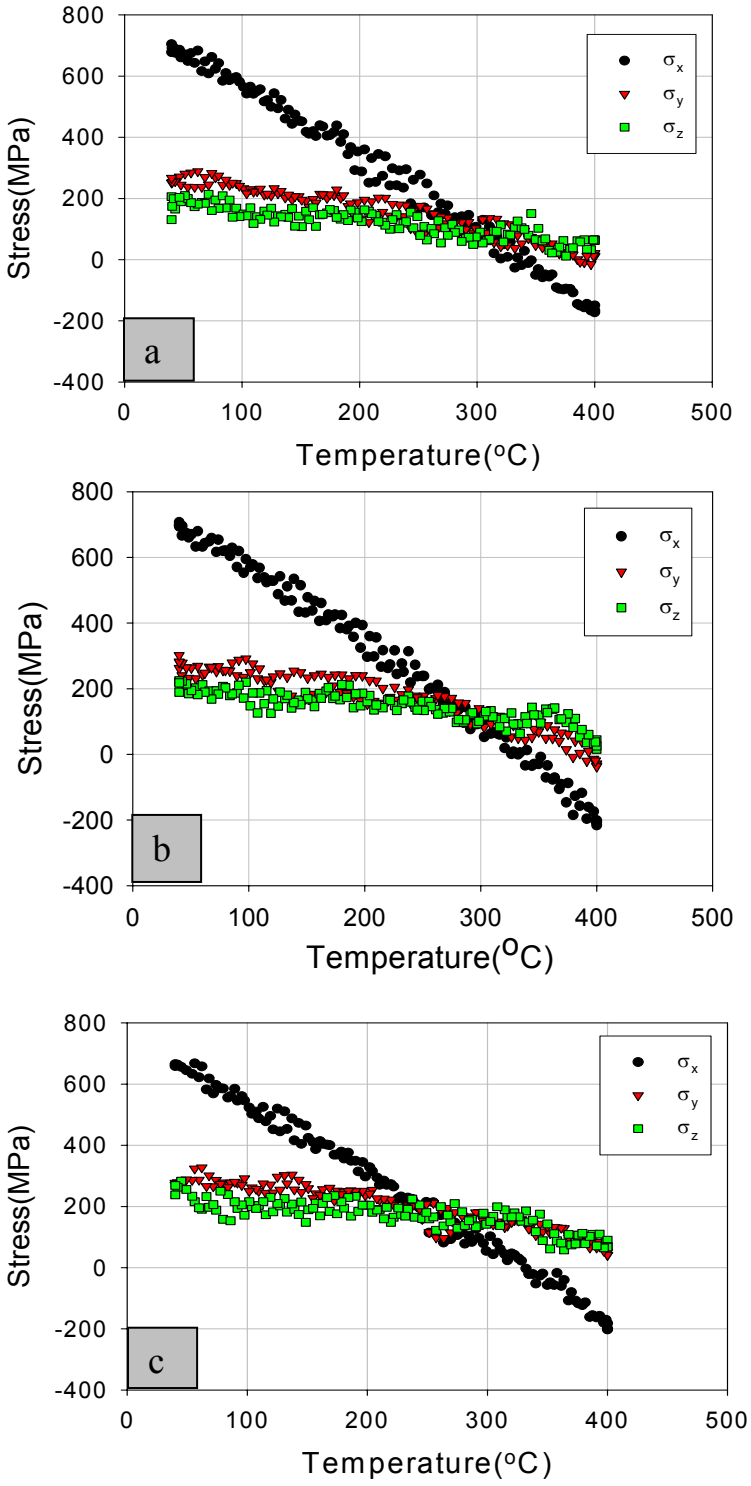


Figure 6.40 Thermal stress of Cu lines in Cu/CDO structures passivated with a) ES#1 b) $SiN_x$ and c) SiC

**B.** ***Effect of passivation layer on stress relaxation of Cu interconnects***

Isothermal stress relaxation measurements were performed at 200°C on Cu/SiOF, Cu/SiLK™ and Cu/CDO structures, and the results are shown respectively in Fig.42, Fig.43 and Fig.44, where the initial stresses along ($\sigma_x$) and across ($\sigma_y$) the lines were set to be zero and the curves record the stress change as functions of time. Since the bending beam results showed that the stress in a bare passivation layer did not relax in the same thermal condition, the recorded stress relaxation was believed to come from the interconnect layer including the Cu lines, the IMD and the barrier between them, shown in Fig. 41, where x and y directions are defined to be along and across the Cu lines, respectively. These figures indicate that the stress relaxation rate of the Cu line structures was strongly dependent on the passivation condition including different passivation layers and being unpassivated. In these line structures, the stress relaxation rate was shown to decrease as a function of passivation in the order of unpassivated > SiC > $SiN_x$ and the ES#1 passivation resulted in the slowest relaxation rate in the Cu/CDO structure, with $\sigma_x$ relaxing faster than $\sigma_y$ for all test structures.

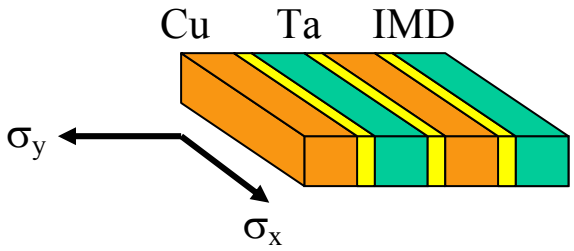


Figure 6.41 Schematic of the average stress measured by the bending beam method in the Cu interconnect layer

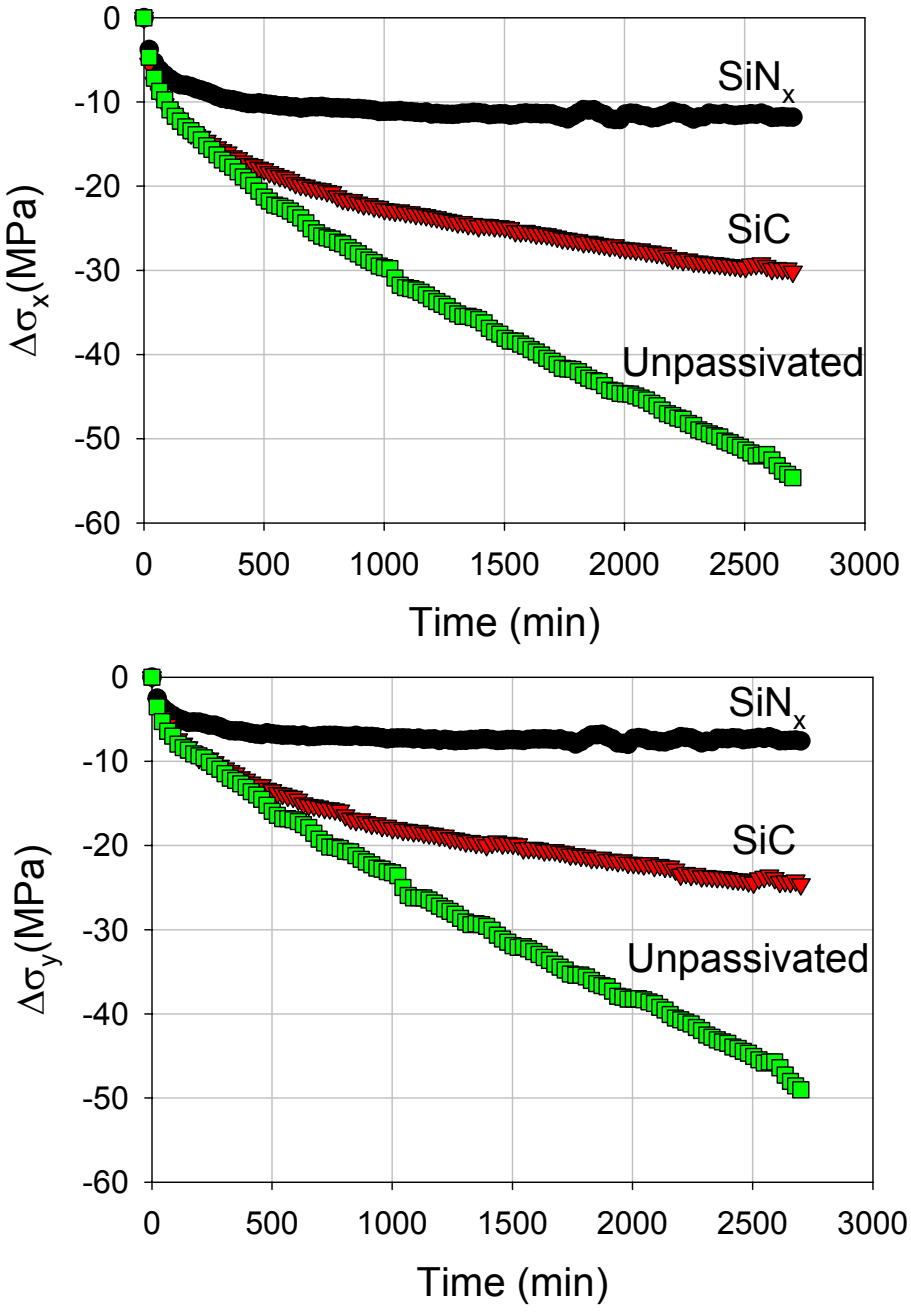


Figure 6.42 Effect of passivation condition on isothermal stress relaxation of Cu/SiOF structure

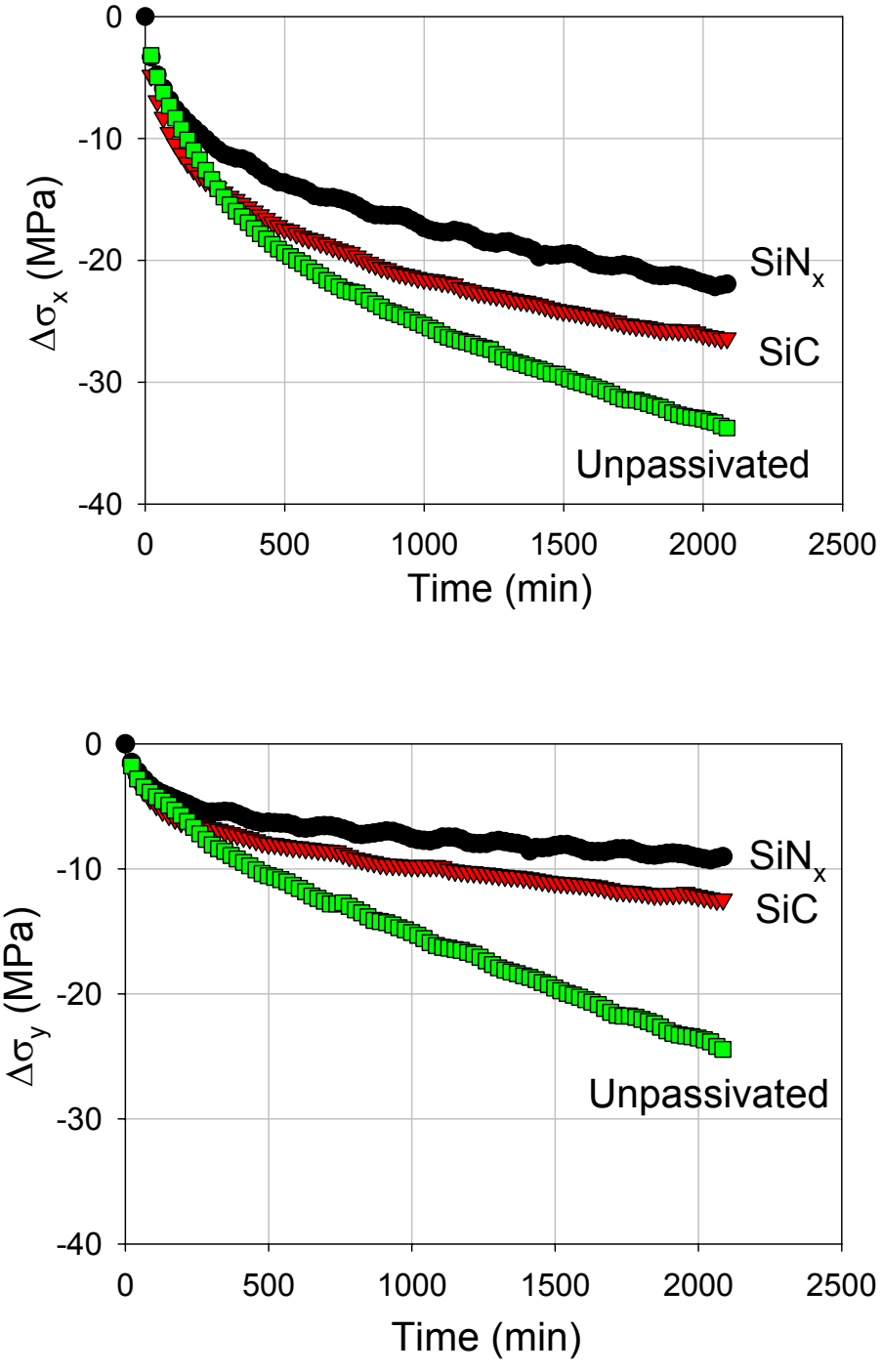


Figure 6.43 Effect of passivation condition on isothermal stress relaxation of Cu/SiLK™ structure

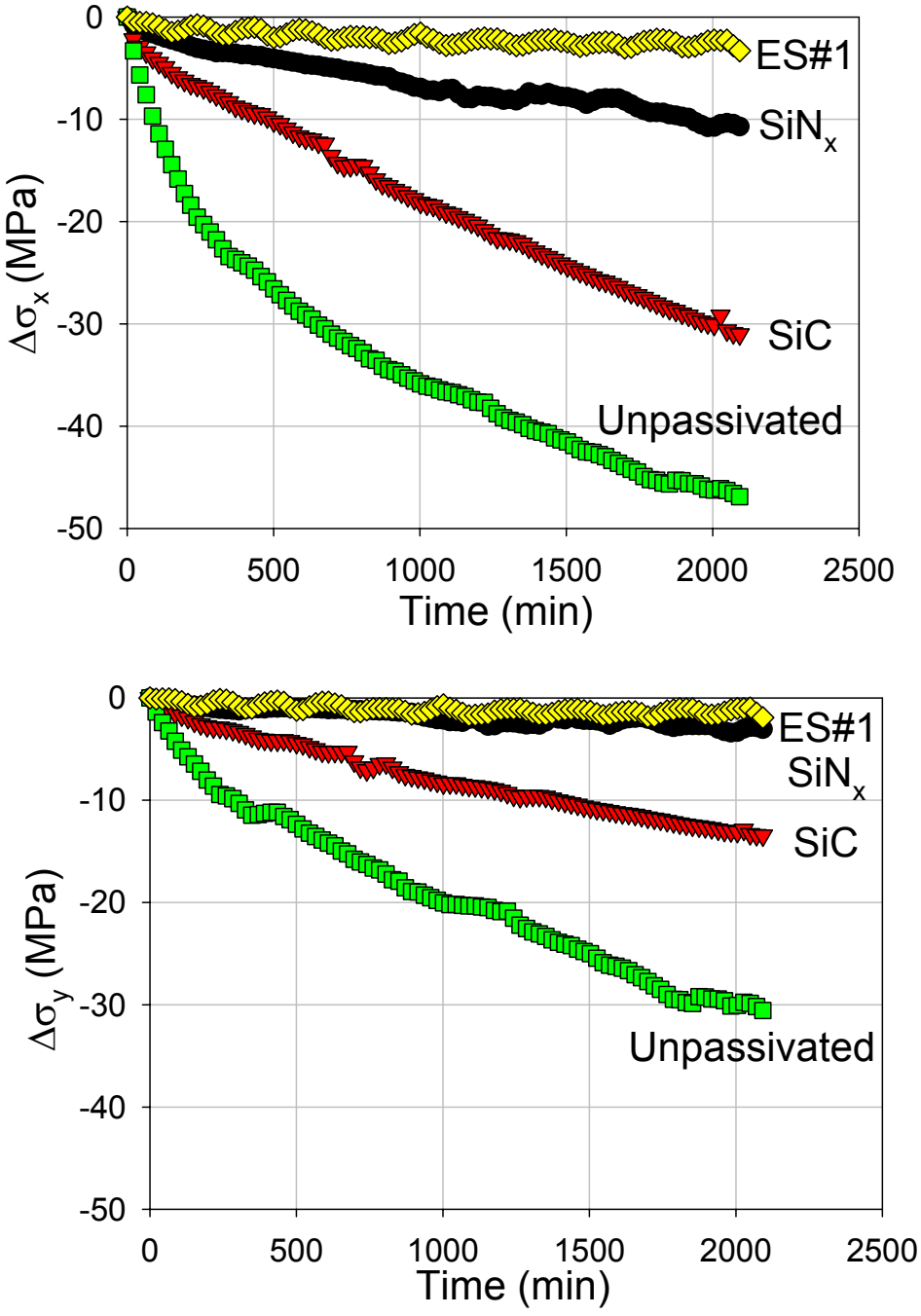


Figure 6.44 Effect of passivation condition on isothermal stress relaxation of Cu/CDO structure

The corresponding interfacial adhesion and electromigration (EM) lifetime of the Cu/CDO interconnects were measured at Intel and the normalized results are listed in Table 1, where the interfacial adhesion was determined using a 4-point bending technique [30]. Both the Cu/passivation interfacial adhesion and the EM lifetime of the line structures are shown to be dependent on the passivation material. Larger interfacial adhesion energies corresponded with longer EM lifetimes. The results are in good agreement with those of the stress relaxation such that the novel ES exhibits the lowest relaxation rate, the highest adhesion energy and the longest EM lifetime. The Cu/ passivation layer interface must be one of the dominant factors for the stress relaxation in the line structures.

Table 6.5 Adhesion energy of passivation/Cu interface and electromigration lifetime for various passivation layers in Cu/CDO structures with comparison of stress relaxation results

| Passivation Layer | Interfacial Adhesion ($J/m^2$) | Electromigration MTTF, hrs (normalized) | $\Delta\sigma_x$(MPa) | $\Delta\sigma_y$ (MPa) |
|---|---|---|---|---|
| SiC | 4 | 1 | 31 | 13.5 |
| SiN | 10 | 2.0 | 10 | 3.1 |
| Novel ES | 12 | 3.1 | 3.3 | 2.0 |

### *C. Stress relaxation of Cu lines*

Since the bending beam method can only be used to measure the stress relaxation of the interconnect layer, in order to know the stress relaxation behavior of Cu lines, XRD method can be used. Figure 45 shows the strain and stress relaxation at 200°C of the Cu lines in the Cu/SiOF structrure. With a ramp rate of 4°C/min, the sample was heated up from RT to 430°C and annealed for 30 minutes at 430°C before it was cooled

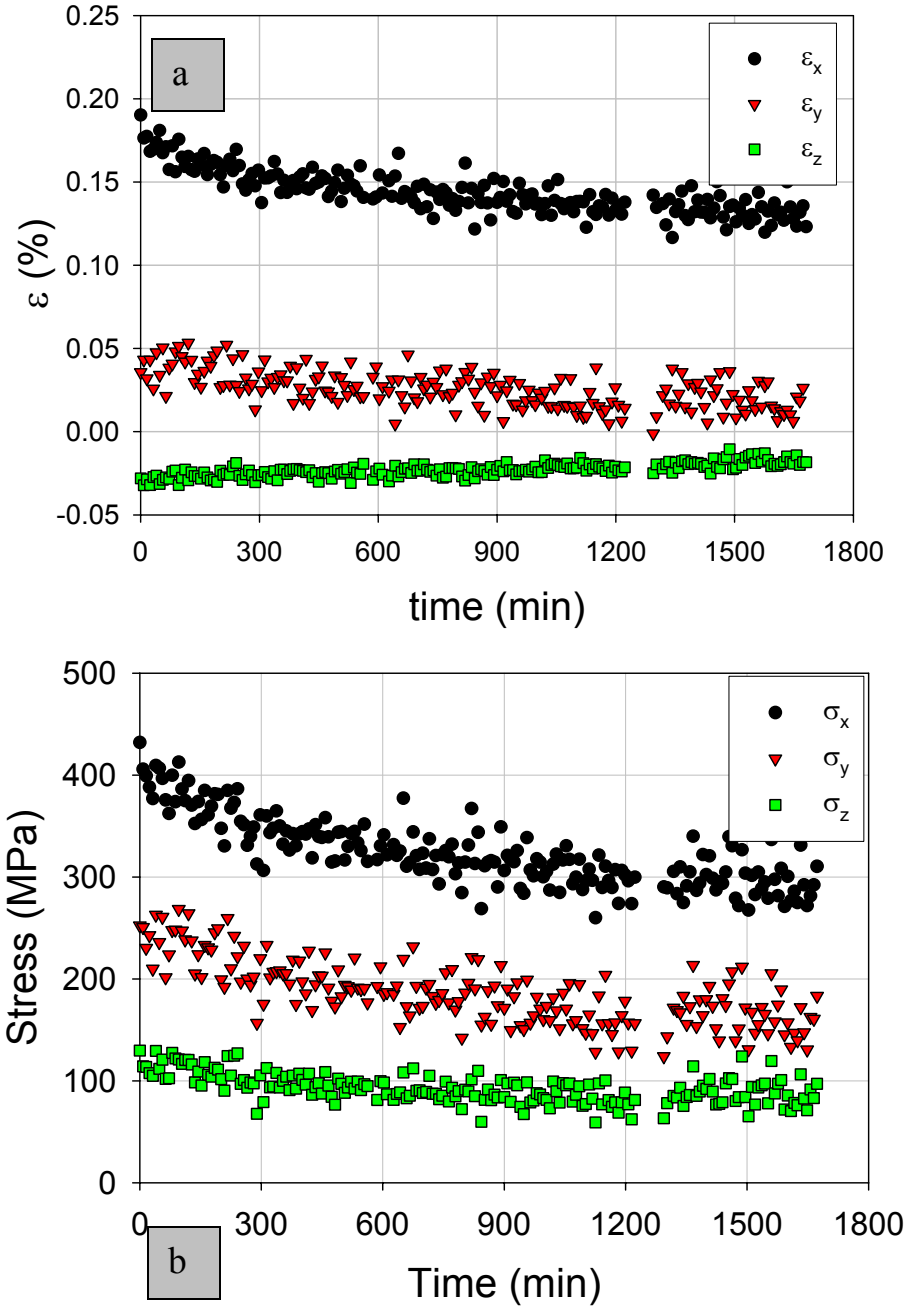


Figure 6.45 Strain (a) and stress (b) relaxation of the Cu lines passivated by SiC in the Cu/SiOF structure at 200°C

down to 200°C for stress relaxation measurement.

After the sample was cooled down to 200°C, the initial stresses of the Cu lines, $\sigma_x$, $\sigma_y$ and $\sigma_z$ were tensile while the strains in x and y directions, $\varepsilon_x$ and $\varepsilon_y$ were positive and that in z direstion, $\varepsilon_z$ was nagative. During stress relaxation, both the tensile ($\varepsilon_x$ and $\varepsilon_y$ ) and the compresive ($\varepsilon_z$ ) strains decreased as a function of time. As a result, the tensile principle stresses of the Cu lines relaxed during the isothermal annealing.

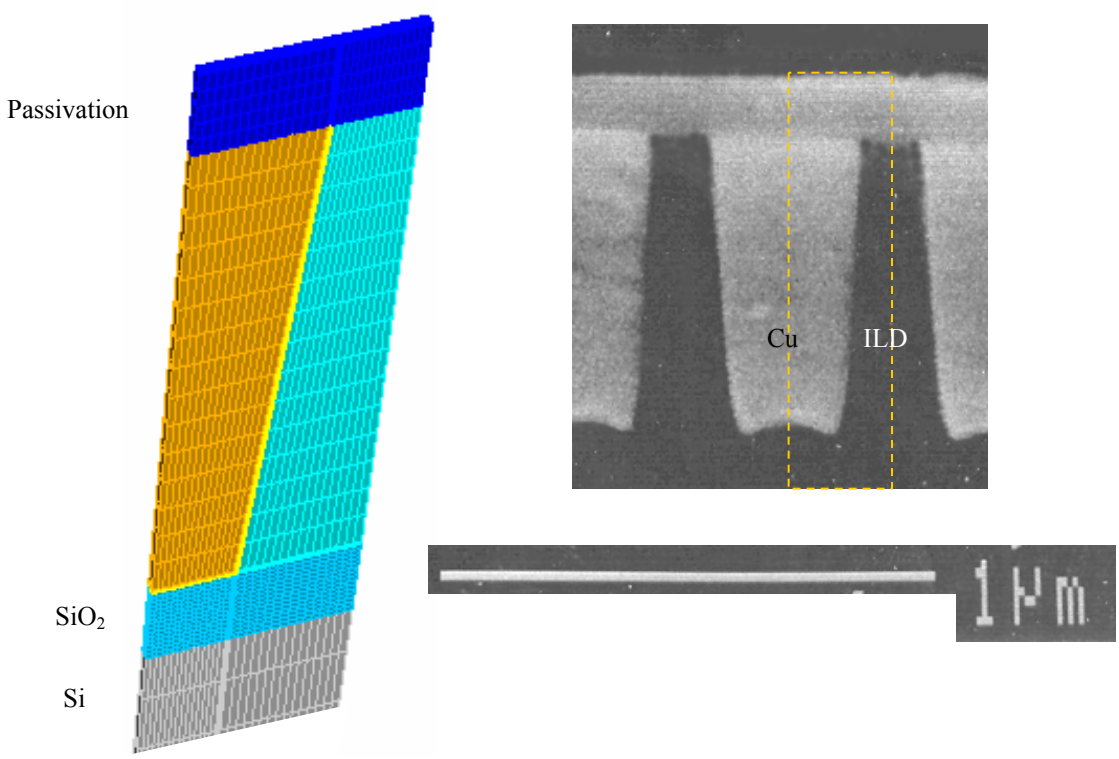


Figure 6.46FEA elements and SEM imagine of the cross section of the damascene line structure

### 6.3.2 FEA modeling

A finite element analysis (FEA) code, called ABAQUS was used to set up the 3D elastic model with 20-node quadratic brick elements. The model includes half of a pitch

combining the passivation layer, the Cu line, the ILD, the diffusion barrier and part of the Si substrate, as shown in Fig. 46. The corresponding SEM image of the line cross section is included for comparison. A mirror-symmetry condition was applied to the front and the right planes of the structure and the back and left planes were constrained by the CTE of Si while remaining straight to ensure the periodicity of the structure and the bending of the substrate was ignored. Table 6 lists the material properties used in the calculations.

Table 6.6 Mechanical properties of the used materials in the FEA calculation at 25°C

| Material | E (GPa) | ν | α (ppm/°C) |
|---|---|---|---|
| Copper | $C_{11}$, $C_{12}$, $C_{44}$ | | 17.7 |
| Silicon | 130.2 | 0.28 | 2.61 |
| SiOF | 71.7 | 0.16 | 0.94 |
| SiLK™ | 2.45 | 0.35 | 66.0 |
| SiN | 300 | 0.24 | 3.3 |
| SiC | 440 | 0.17 | 4.5 |
| Ta | 185.0 | 0.34 | 6.5 |

### *A. Effect of passivation on thermal stress and stress gradient in Cu lines*

The FEA model was used to evaluate the thermal stress of Cu lines in Cu/SiOF and Cu/SiLK™ structures. The calculation was performed under the linear elastic assumption with a thermal loading of -100K from an initial state of zero stress and the results are shown in Fig.47, including the principle stresses and the von Mises stress of the Cu lines. In both structures, the stresses in Cu lines are found to be similar although different passivation conditions were used. This result is consistent with the XRD results that the passivation condition did not significantly affect the thermal stress of the Cu lines

during thermal cycling, shown in Fig. 39 and Fig. 40. Since the stress relaxation rate strongly depends on the magnitude of the stress, different initial stress may results in different stress relaxation rates. It is indicated by the FEA and XRD result that the mechanical confinement from the passivation layer has a negligible effect on the thermal stress of the Cu lines. This confirms that the different relaxation rates were not from different initial stresses, not due to the different mechanical confinements from the passivation layer.

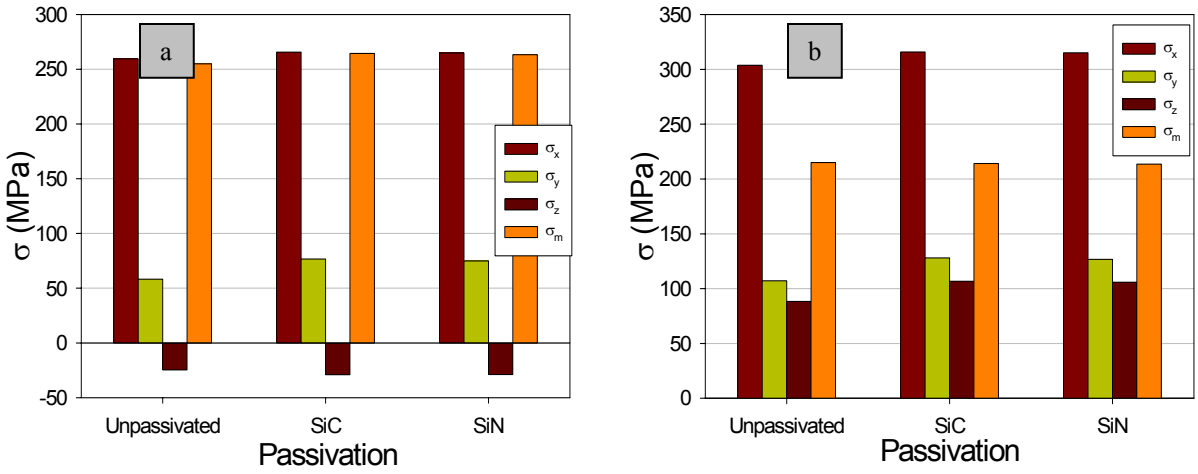


Figure 6.47 FEA analysis of the effect of passivation condition on the thermal stress in Cu lines in (a) Cu/SiLK™ structure and (b) Cu/SiOF structure

Fig.48 shows the hydrostatic stress contours in the Cu lines with different passivation layers in Cu/SiLK™ and Cu/SiOF structures. These contours indicate that the distribution of the stress in the line is not uniform, resulting in stress gradients. Different passivation layers result in different stress contours and the stress gradients are larger in the vicinity near the top and the bottom interface of the Cu lines. The hydrostatic stress

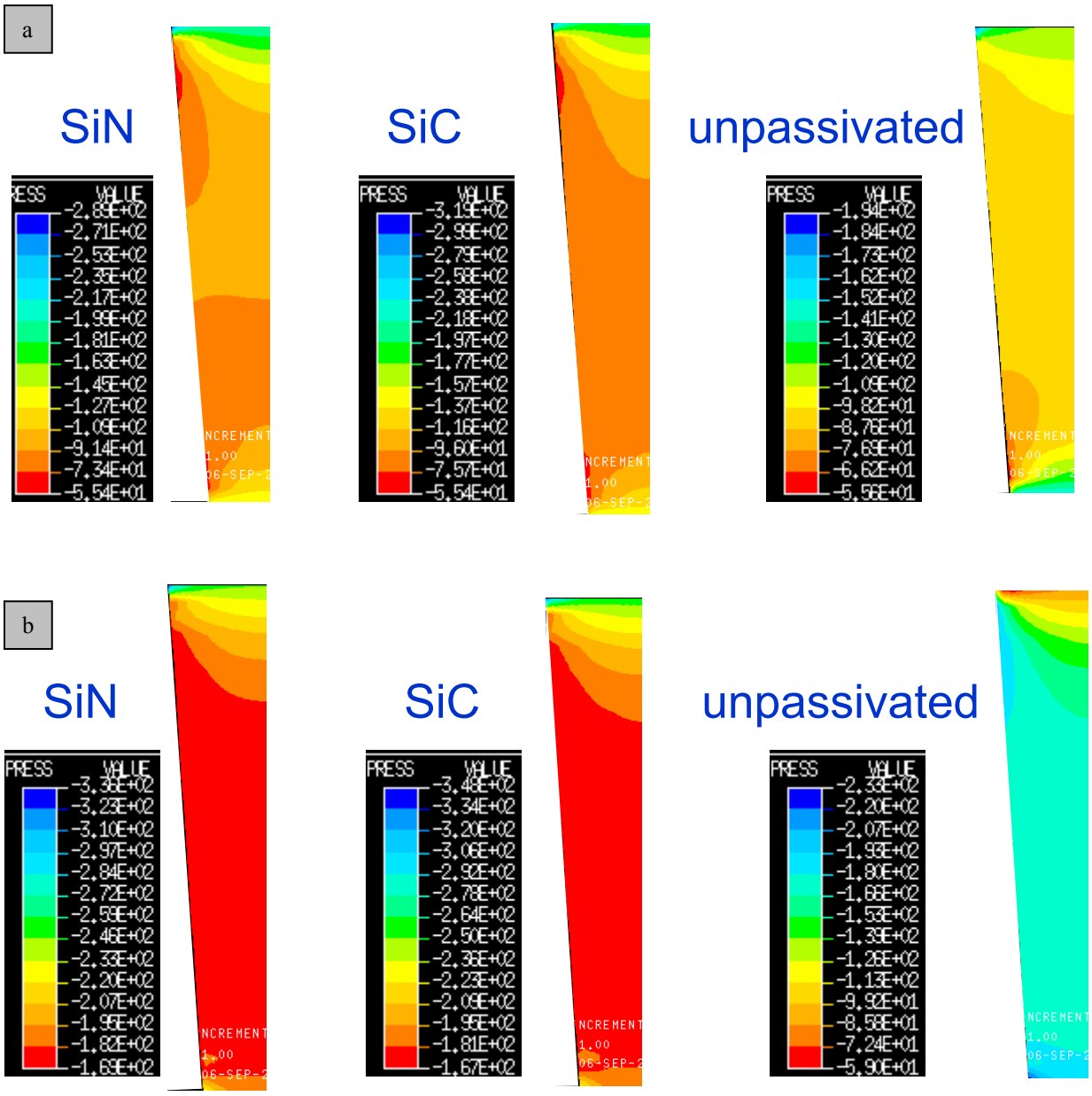


Figure 6.48 FEA analysis of the hydrostatic stress contours in Cu lines with different passivation conditions in (a) Cu/SiLK™ structure and (b) Cu/SiOF structure

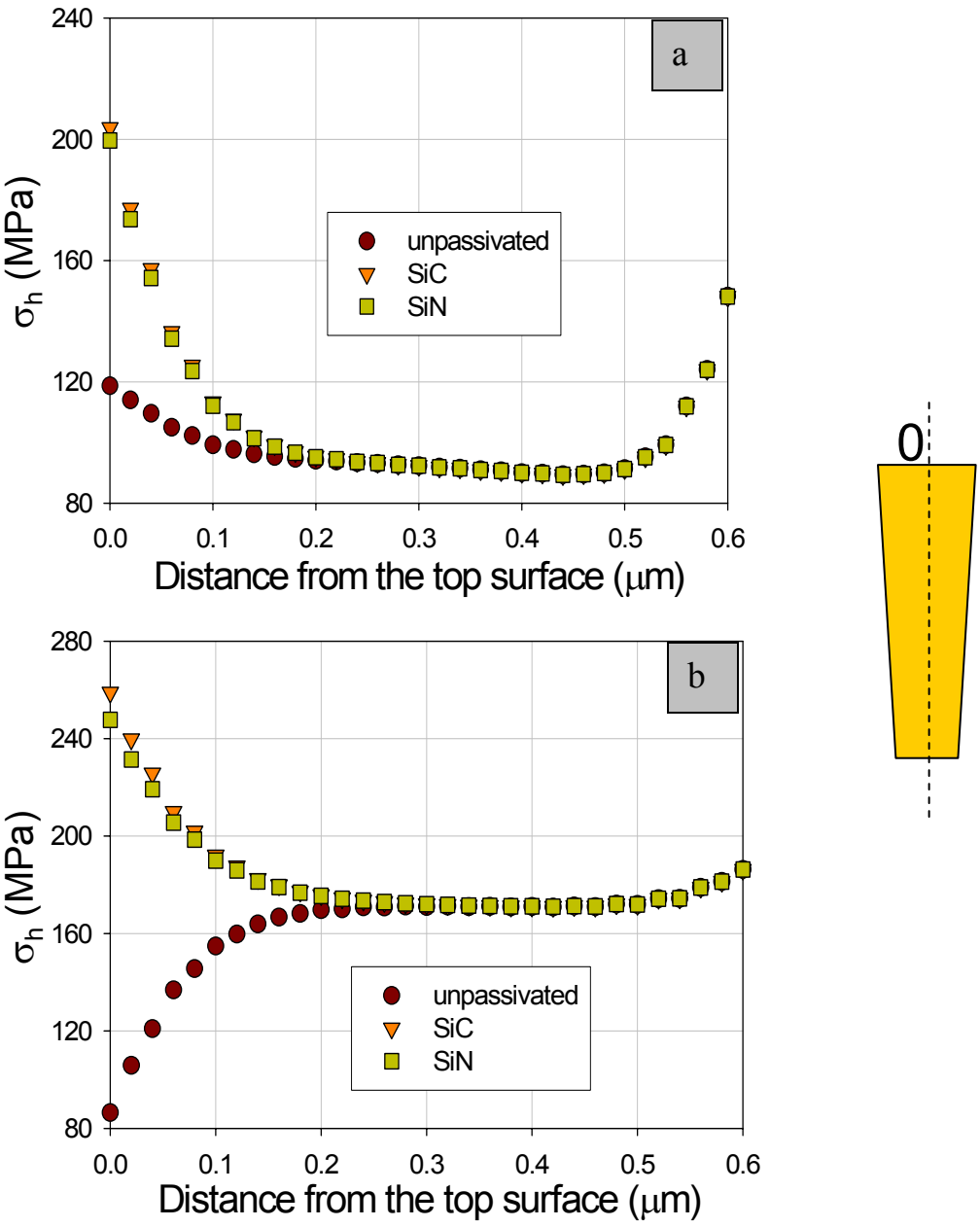


Figure 6.49 FEA analysis of the hydrostatic stress distribution along the central line of Cu lines with different passivation conditions in (a) Cu/SiLK™ interconnect and (b) Cu/SiOF interconnect

distribution along the central line from the top to the bottom in a Cu line is shown in Fig. 49. Although in the unpassivated structures, the stress in the top surface is much smaller than those in the passivated structures, similar stress distributions are shown in the SiNx and SiC passivated structures in both the Cu/SiOF or Cu/SiLK™ interconnects. This observation implies that the mechanical confinement should not be the reason to cause the difference of the stress relaxation behavior in SiNx and SiC passivated structures.

### *B. Effective modulus (B) of Cu line structure*

Effective modulus (B) of a interconnect structure can be used to evaluate the confinement on the metal lines from the surrounding materials. B is defined as

$$\frac{dC}{C} = -\frac{d\sigma}{B} \tag{32}$$

where $dC$ is the change of the available lattice sites per unit volume and $dC/C$ is the relative density change in the metal lines[6.31]. σ would be principle stresses, hydrostatic stress and other stress components. $B$ depends not only on the elastic properties and geometry of the line and the surrounding materials, but also on the location of the depletion and deposition of atoms or the mass transport if the confinement on the metal lines is anisotropic. Figure 50 shows three kinds of location for mass transport: (1) the top interface, (2) the sidewall interfaces and (3) the grain boundaries in the Cu lines. The effective moduli of the structure are different for the three conditions, as shown in following.

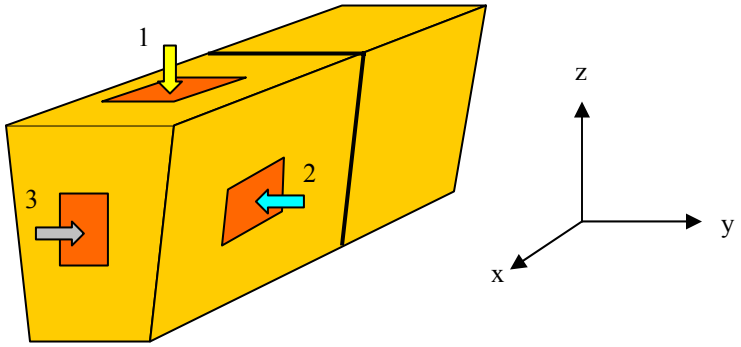


Figure 6.50 Schematic of the locations for the changed lattice sites in a Cu line at: (1) the top interface (2) the sidewall interface and (3) the grain boundary

In this study, FEA was used to calculate the effective modulus of the metal lines in the Cu/SiOF interconnects with the same mesh shown in Fig. 46 and the mechanical properties listed in Table 6.6. The CTE of the Cu was set to be anisotropic, and those of the other materials were set to be zero in order to simulate the change of lattice sites using thermal expansion. Figure 51 illustrates the steps to calculate the effective modulus when the lattice sites are added or removed from the top interface of the Cu line. In this case, the components of the CTE of the Cu in the x and y directions were set to zero but that in the z direction was not. When a thermal load, $\Delta T$, was applied to the system, from a zero-stress temperature $T_1$ to $T_2$, the dimension of the Cu line in the z direction will change while the others in the system remain unchanged due to the CTE settings mentioned above. As a result, if there was not any confinement on the Cu line from the surrounding materials, the stress in the system was zero and the dimension was shown in step (2). In the real situation, the interfaces were well bounded and stress was induced in the system due to the thermal loading, shown in step (3). The change of the lattice density

can be calculated using the expansion of the Cu lines and the effective moduli were deduced when the stress was known. Table 7 lists the deduced moduli in the Cu/SiOF structure, where the B with the subscribe x, y, z and h corresponds to $\sigma_x$, $\sigma_y$, $\sigma_z$ and the hydrostatic stress $\sigma_h$, respectively.

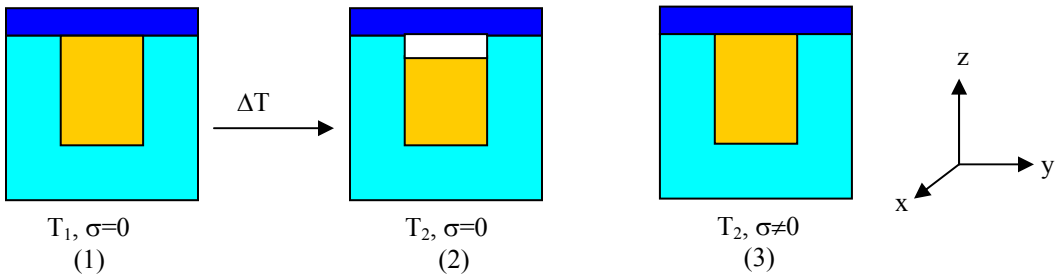


Figure 6.51 Schematic of the FEA steps to calculate the effective modulus in Cu interconnects.

Table 7 Effective moduli in the Cu/SiOF interconnect with different passivation (in GPa)

| passivation | lattice site | $B_x$ | $B_y$ | $B_z$ | $B_h$ |
|---|---|---|---|---|---|
| $SiN_x$ | Top interface | 12.4 | 2.5 | 50.9 | 21.9 |
| | sidewall | 24.6 | 62.3 | 3.0 | 30.0 |
| | grain boundary | 173.0 | 24.5 | 12.6 | 70.0 |
| SiC | Top interface | 12.5 | 2.6 | 50.9 | 22.0 |
| | sidewall | 24.8 | 62.9 | 3.0 | 30.2 |
| | grain boundary | 173.1 | 24.7 | 12.7 | 70.2 |
| None | Top interface | 9.4 | -1.6 | 44.6 | 17.5 |
| | sidewall | 22.0 | 57.0 | 0.7 | 26.6 |
| | grain boundary | 171.3 | 21.5 | 10.3 | 67.7 |

The effective modulus coresponding to a purticular stress is shown to be different for different positions where the lattice sites are added or removed, and the difference

would be more than one order of magnitude. The moduli corresponding to different principle stresses are also shown to be different, and the effect of the passivation layer is shown based on the comparson of the passivated structures with the one unpassivated, but the correlative values in the $SiN_x$ passivated and SiC passivated structrues are about the same. The negligible difference in the effective moduli in the line structures with $SiN_x$ and SiC passivation layers can not account for their different isothermal stress relaxation behavior. Thus the results indicate an effect primarily on the diffusivity due to the interfacial chemistry of the passivation layer.

### *C. A FEA kinetic model*

The results of the XRD thermal stress measurement and the FEA stress analysis indicate that the mechnical confinement from the passivation layer was not the reason causing the different stress relaxation rates of the line structures with different passivation layers. Thus, the Cu/passivation interface is believed to play an important role during the stress relaxation. To investigate the effect of the Cu/passivation interfacial diffusitivity and evaluate its values, Bower *et al*. [6.32] set up a 3D FEA kinetic model, shown in Fig. 52, for the stess relaxation in the Cu line structures. The stress relaxation was assumed to be due to the mass transport between the interfaces and grain boundaries, most likely by diffusion of Cu atoms from passivation/Cu interface into either sidewall interfaces or grain boundaries. To fit the experimental results, the involved diffusivities in the Cu line structure must have the relationship that the grain boundary diffusivity is greater than the Cu/passivation interfacial diffusivity while the Cu/barrier interfacial diffusivity is the

smallest one. The Cu/passivation interfacial diffusivity was deduced by combining the experimental data and the modeling results.

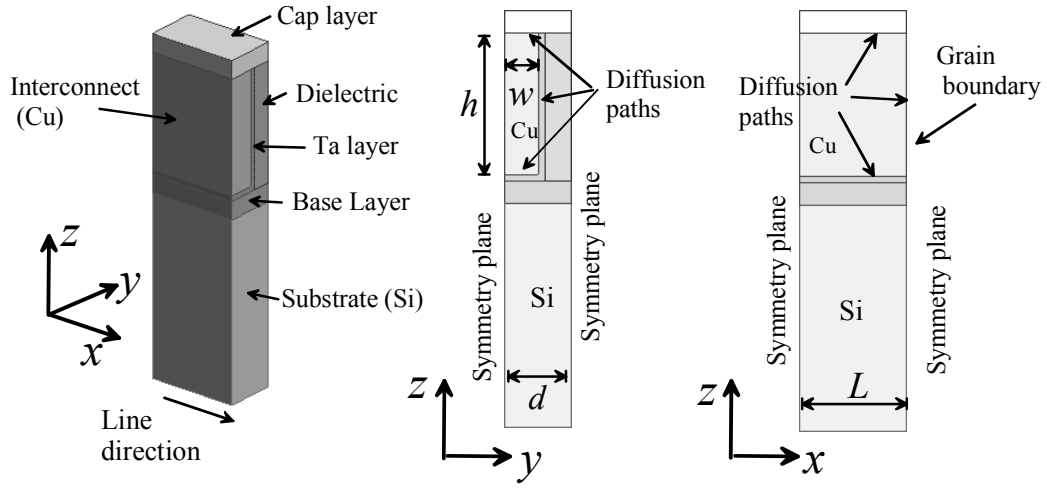


Figure 6.52 Unit cell used in finite element computations

FEA analysis indicated that the mechanical confinement of the passivation layer on the Cu lines was not the reason causing different isothermal stress relaxation behavior in the line structures with different passivation conditions. It is believed that the result was due to the difference of the Cu/passivation interfacial diffusivity, because of which, the stress relaxation rate of the line structures would correlate to the electromigration lifetime as well as the interface adhesion. In this sense, isothermal stress relaxation measurement can be used to evaluate the interfacial diffusivity and thus to evaluate the electromigration performance of a Cu interconnect structrue

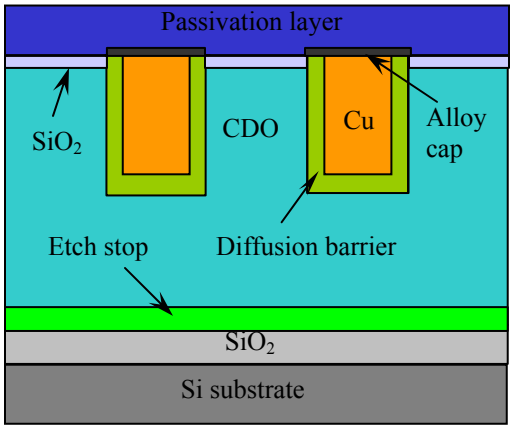


Figure 6.53 cross-section of the line structure with alloy cap layer

### 6.3.3 Effects of the process of an alloy cap layer

In this study, Cu/CDO line structures with alloy cap layers, shown in Fig.53 were used to study the effects of treatments on the stress relaxation of Cu lines. The line width /pitch is 0.32μm/0.4μm and the line thickness is 0.4μm. Two sets of samples, passivated by ES#1 or $SiN_x$ after the deposition of the alloy cap layer were prepared with different processes named #1, #1A, #1B, #1C and #1D. While #1 was the basic process, processes #1A and #1B added pretreatments with different chemistries to the Cu surface after CMP but before alloy cap deposition and processes #1C and #1D included both pretreatment and post-treatment. The post-treatment was performed after the alloy cap deposition but before passivation with annealing at 350~450ºC for about 30 minutes. *C* and *D* correlate to different annealing temperatures. Stress relaxation was performed at 200°C under the same thermal condition described previously for the line structure. The stress relaxation of the line structure without the alloy cap layer was also measured for comparison.

The stress relaxation results of the line structures passivated by ES#1 and $SiN_x$ are shown in Fig.54 and Fig. 55, respectively. For the ES#1 passivated line structures, the stress relaxation rate varies for different processes in both directions along and across the line. Correlated to the process, it increases in the order: #1A < #1 < #1B, but the values for these processes are similar while those for the processes #1C and #1D are shown much larger, indicating a stronger effect of the post-treatment than the pre-treatment. For $SiN_x$ passivated line structures, the stress relaxation rates for different processes are similar although those for #1A and #1B are shown smaller than those of #1D and #1C, and the correlative value is larger than that of the ES#1 passivated structure. Different from that in the Cu films measured previously, an alloy cap layer in the line structures did not significantly decrease the stress relaxation rate, on the contrary, the stress relaxation rates of most of the structures with the alloy cap layer dramatically increased, indicating that process conditions strongly affect the quality of the Cu/alloy cap layer interface according to the previous study on Cu films. From the SIMS data (not shown here), annealing could result in inter-diffusion between the alloy cap layer and Cu lines that was expected to enhance the interface adhesion. But oxygen was also found to diffuse from the alloy cap layer to the interface during annealing. The formation of the copper oxide at the interface was believed to cause fast stress relaxation rate [33] of the line structures. The difference between the stress relaxation behaviors between the ES#1 and $SiN_x$ passivated samples may suggest either a poor coverage on Cu or a loose alloy structure,

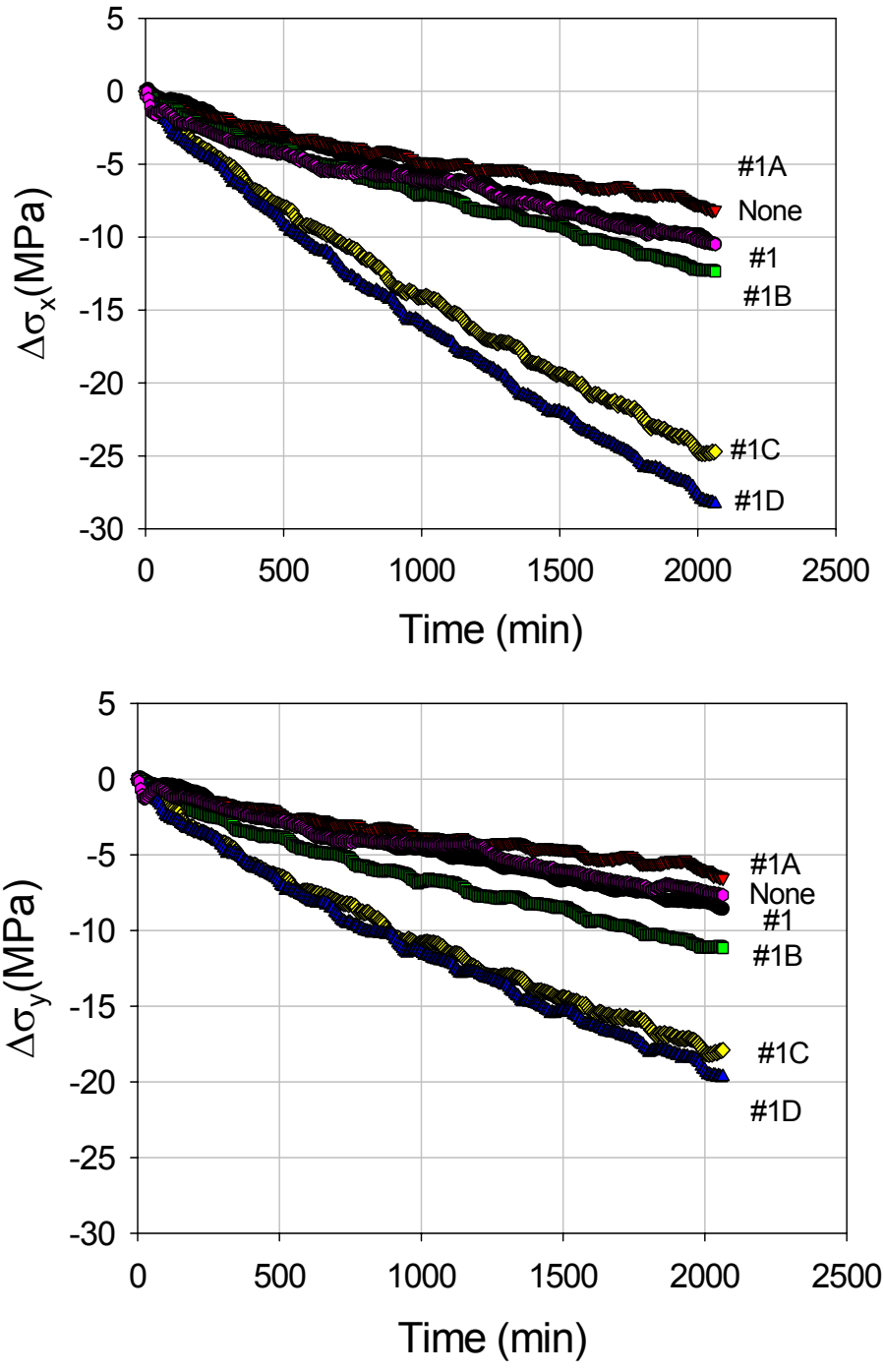


Figure 6.54 Effects of the processing of the alloy cap layer on stress relaxation of the Cu/CDO line structure passivated with SiN. *None* means no alloy cap

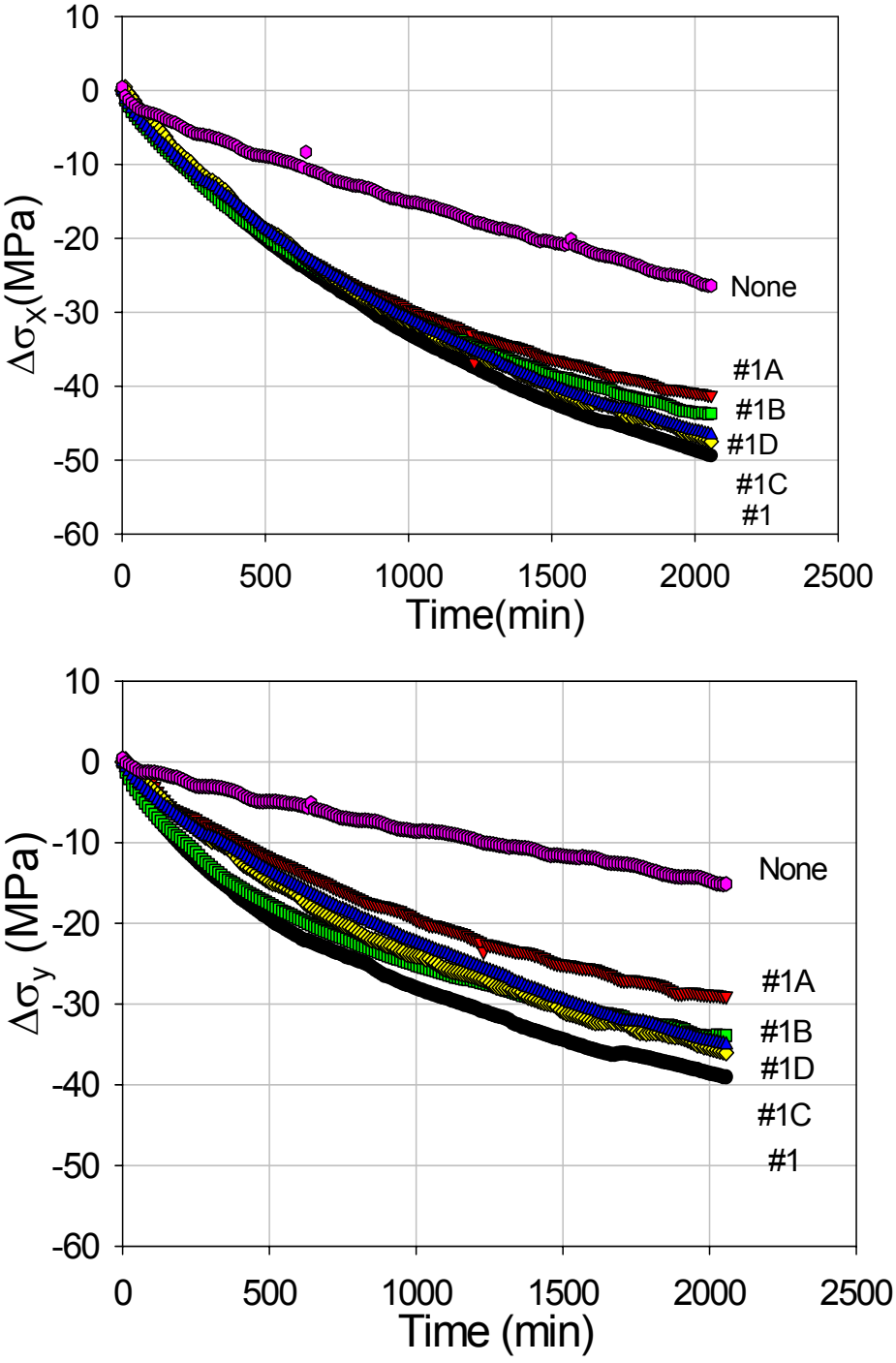


Figure 6.55 Effects of the processing of the alloy cap layer on stress relaxation of the Cu/CDO line structure passivated with ES#1. *None* means no alloy cap.

which caused the exposure of the Cu surface to the ambient of the subsequent process steps after the deposition of the alloy cap layer and thus affected the quality of the interface. How the deposition of the passivation affected the interface quality is not understood yet.

## 6.3 SUMMARY

Bending beam technique, x-ray diffraction method and finite element analysis were used to study the isothermal stress relaxation in electroplated Cu films and Cu line structures. When the initial stress, temperature and process etc. were important factors in the stress relaxation behavior in Cu films and line structures, the passivation condition was shown to be critical. XRD and FEA results indicated that the mechanical confinement of the passivation layer had a negligible effect. The change in stress relaxation rate is believed to originate from variations in the interfacial diffusivity of the Cu/passivation interface for different passivation layers. A kinetic model coupling the diffusion through the interface/surface and grain boundaries was developed for thin films and used to evaluate the grain boundary and interface diffusivities in Cu films by combining the isothermal stress relaxation results. A FEA model was also developed by Bower *et al.* [6.32] to evaluate the interface diffusivity in Cu interconnects. Although the Cu/cap layer interface is believed to be the dominant diffusion path for electromigration, the interfacial diffusivity was found in this study to be much smaller than the grain boundary diffusivity. The stress relaxation rates of the Cu films and line structures with different passivation conditions were shown to correlate well with the interfacial

adhesion and electromigration lifetime of the Cu interconnects. That makes the stress relaxation measurement an effective method to evaluate the electromigration performance of Cu interconnects.

# Chapter 7 Summary

Thermal stress and mass transport are key issues for Cu metallization yield and reliability. While the stress can be evaluated by the bending beam technique, XRD method and Finite Element Analysis (FEA), no effective methods have been reported to determine the diffusivity of Cu/passivation interface, the dominant diffusion path for electromigration in Cu interconnects. In summary, this study has made the following contributions to address these issues.

Different from the previous studies on the deformation mechanism of thin films, in Chapter 3, the strain rate of Cu films was determined experimentally from the measured stress-temperature curve. The correlation of strain rate with the ramp rate indicated that the steady-state creep equation could not account for the thermal stress behavior of Cu films during thermal cycling. In the case where the loading rate is larger than the creep rate, the shape of the stress-temperature curve does not depend on the ramp rate. The shape changes when the creep dominates the plastic deformation as the loading rate is lower than creep rate. Furthermore, the impurities in Cu films induced by the additives in plating bath were shown to be important in the stress development in thermal cycling. However, the mechanism has yet to be understood.

The thermal stress in Cu interconnects was systematically studied in Chapter 4 using both “landed” and “hanging” structures. The residual stress in the Cu lines increases with a higher annealing temperature. While this was expected as a result of the densification of the Cu lines due to grain growth, the different levels of plastic deformation of the Cu lines upon heating and cooling were identified to stem from other

reasons. In addition, the effect of mechanical confinement on the thermal stress of Cu lines was studied using two kinds of linewidth, 0.2 and 0.4μm, and three types of ILD, SiOF, CDO and SiLK™, providing a wide range of modulus and CTE. The stress of Cu lines was found to be strongly affected by ILD but not sensitive to the change of the line width in the submicron range. Besides the XRD stress measurement, FEA model was set up to study the effect of confinement on the stress in Cu lines and then used to evaluate the stress in ILD. Interestingly, the stress in SiOF and SiLK™ was quite different and that implies reliability issues of low-k ILD, such as channel cracking and interfacial delamination, therefore more in-depth studies are needed.

Stress-induced void formation in passivated Cu films in both thermal cycling and isothermal annealing was studied in Chapter 5. As the driving force, the stress in the Cu films was measured and correlated to the void formation. During thermal cycling, the voids were observed to grow upon cooling and disappear under heating within a certain range of temperature, and the void density was dependent on the film stress and the ramp rate. Interestingly, it was found that the void density was much higher upon the $2^{nd}$ cooling down than that upon the $1^{st}$ cooling down, in spite of the identical film stress and microstructure. In addition, both the void density and void size were measured in isothermal annealing as a function of annealing temperature and found to peak at different temperatures, about 150°C for void density and 250°C for void size. Similar to the diffusional creep rate, a kinetic model was established to account for the void growth as a function of temperature and the stress, yielding a threshold stress of 40 MPa and an activation energy of 0.75eV. However, a linear relationship between the void density and

the film stress was shown in the temperature range from 150°C to 300°C. SEM and AFM reveal that the voids were multi-edge shaped, indicating the growth of the void was anisotropic. Based on the observation, void nucleation and growth were discussed with the FEA models to analyze the local tri-axial stress state and stress gradients in Cu films due to the mechanical anisotropy and in the void vicinity. The plastic deformation is believed to be important in controlling void formation in Cu films. It provided the extract nucleation sites and vacancy source by pileup of dislocations, although it decreased the stress level of the film. In-depth study on this issue is needed.

In Chapter 6, the study was extended to the stress relaxation and mass transport in Cu films and line structures in order to evaluate the diffusivity of the Cu/passivation interface. For this purpose, an experimental method was developed to study the isothermal stress relaxation of Cu films that can isolate the effect of temperature and initial stress. From the stress relaxation measurement performed both in passivated and unpassivated Cu films at different initial stresses and temperatures, it was important to find that the transient behavior of the Cu films in isothermal stress relaxation can not be ignored, especially for the unpassivated Cu film where the steady-state might not be reached for as long as 45 hours. As a result, the steady-state equations are not suitable to describe the stress relaxation of the films. Although a 5-parameter exponential decay equation could be used to fit the stress relaxation curves very well, consistent interface diffusivity still could not be deduced from the fitting parameters. For this reason, a kinetic model coupling the diffusion through grain boundaries and the Cu/passivation interface or Cu surface, and a semi-phenomenological model were developed to evaluate

the grain boundary and interface diffusivity of Cu films. Interestingly, while the deduced grain boundary diffusivity agreed well with other studies, the interface diffusivity was much smaller than the grain boundary diffusivity. In addition, different passivation layers on Cu films were tested, including $SiN_x$, old SiC, novel SiC and a thin alloy cap layer. The Cu/SiC showed the largest interfacial diffusivity followed by the Cu/ modified SiC and Cu/$SiN_x$ interfaces, while the thin metal alloy layer dramatically decreased the interfacial diffusivity. The stress relaxation study was extended to the Cu line structures. Similarly, the relaxation rate of the line structures was strongly dependent on the passivation layer, regardless of the different ILD's of SiOF, CDO and SiLK™, and it correlates well with EM life time and interfacial adhesion. XRD stress measurement and FEA results justified that it is the difference of the interfacial diffusivity instead of the mechanical confinement that caused the different relaxation rates of the Cu line structures. These studies demonstrate that the stress relaxation measurement is an effective method to evaluate the electromigration performance of Cu interconnects. However, since the activation energy for the interface diffusion deduced from the stress relaxation measurement is smaller than those determined by the EM test, further study is needed to understand their relationship and to refine the kinetic stress relaxation models.

## Appendix: A semi-phenomenological model for stress relaxation of passivated thin films

For diffusion under stress gradient, we have

$$\vec{J}_C = -\frac{D}{kT}\left(\vec{\nabla}\sigma\right) \tag{A.1}$$

For the diffusion along the grain boundary shown in the Fig A.1, Eq.A.1 can be written as

$$\frac{\partial\sigma}{\partial t} - A\frac{\partial^2}{\partial x^2}\sigma = 0 \tag{A.2}$$

where A=$\frac{M\Omega\delta_B D_B}{lkT}$, $M$ the biaxial modulus of the film, $\Omega$ the atomic volume, $\delta_B$ the grain boundary width, $D_B$ the grain boundary diffusivity, $l$ the grain size. The generic solutions for A.2 are: $\exp\left(-Ak^2t\right)\cos\left(kx+\varphi\right)$, $x^2+2At$, $x$ and 1.

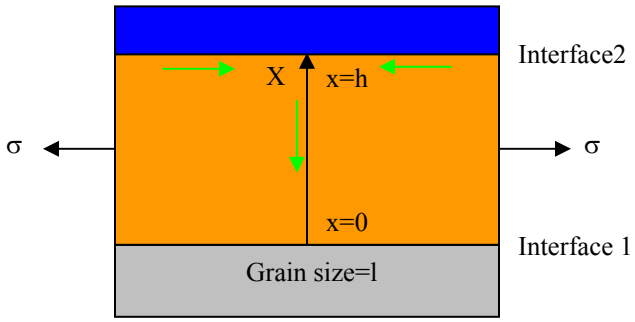


Figure A.1 Schematic of the passivated film structure

We have the asymptotic conditions

$$\sigma\left(x,t\to\infty\right) = \left(\sigma_{1\infty} - \sigma_{2\infty}\right)\left(1-\frac{x}{h}\right) + \sigma_{2\infty} \tag{A.3}$$

and

$$\sigma(x,t\to\infty)=A_1x+A_2+\sum_i C_i\exp\left(-Ak_i^{\,2}t\right)\cos(k_ix+\varphi_i)=A_1x+A_2 \tag{A.4}$$

where 1 and 2 stands for the bottom and the top interface, respectively. With the assumption that the relaxation of the interface stress is a diffusion-controlled process that follows the linear creep law and the stress decreases exponentially in isothermal annealing, the boundary conditions become

$$\sigma(0,t)=(\sigma_0-\sigma_{1\infty})\exp\left(-\frac{t}{\tau_1}\right)+\sigma_{1\infty} \tag{A.5}$$

$$\sigma(h,t)=(\sigma_0-\sigma_{2\infty})\exp\left(-\frac{t}{\tau_2}\right)+\sigma_{2\infty} \tag{A.6}$$

We have

$$\sigma_{1\infty}+\sum_i C_i\exp\left(-Ak_i^{\,2}t\right)\cos(\varphi_i)=(\sigma_0-\sigma_{1\infty})\exp\left(-\frac{t}{\tau_1}\right)+\sigma_{1\infty} \tag{A.7}$$

$$\sigma_{2\infty}+\sum_i C_i\exp\left(-Ak_i^{\,2}t\right)\cos(k_ih+\varphi_i)=(\sigma_0-\sigma_{2\infty})\exp\left(-\frac{t}{\tau_2}\right)+\sigma_{2\infty} \tag{A.8}$$

$C_i$ and $C_j$ can be deduced by following:

$$\sum_i C_i\exp\left(-Ak_i^{\,2}t\right)\cos(\varphi_i)=(\sigma_0-\sigma_{1\infty})\exp\left(-\frac{t}{\tau_1}\right)$$

$$\sum_i C_i\exp\left(-Ak_i^{\,2}t\right)\cos(k_ih+\varphi_i)=(\sigma_0-\sigma_{2\infty})\exp\left(-\frac{t}{\tau_2}\right)$$

$$Ak_i^2\neq\frac{1}{\tau_1},\ \cos(\varphi_i)=0$$

$$Ak_i^2\neq\frac{1}{\tau_2},\ \cos(k_ih+\varphi_i)=0\Rightarrow\sin(k_ih)=0\Rightarrow k_i=\frac{n\pi}{h},\ C_i\neq 0$$

$$Ak_i^2 = \frac{1}{\tau_1}, C_i \cos(\varphi_i) = \sigma_0 - \sigma_{1\infty}, \text{and } \cos(k_i h + \varphi_i) = 0$$

$$\Rightarrow C_i = \frac{\sigma_0 - \sigma_{1\infty}}{\sin\left(\frac{h}{\sqrt{A\tau_1}}\right)}, \varphi_i = \frac{\pi}{2} - \frac{h}{\sqrt{A\tau_1}} \tag{A.9}$$

$$Ak_j^2 = \frac{1}{\tau_2}, C_j \cos(\varphi_j) = 0, \text{and } C_j \cos(k_j h + \varphi_j) = \sigma_0 - \sigma_{2\infty}$$

$$\Rightarrow C_j = \frac{\sigma_0 - \sigma_{2\infty}}{\sin\left(\frac{h}{\sqrt{A\tau_2}}\right)}, \varphi_j = -\frac{\pi}{2} \tag{A.10}$$

The stress at the grain boundary is given by

$$\sigma(x,t) = (\sigma_{1\infty} - \sigma_{2\infty})\left(1 - \frac{x}{h}\right) + \sigma_{2\infty} + \sum_n C_n \exp\left(-A\left(\frac{n\pi}{h}\right)^2 t\right)\sin\left(\frac{n\pi}{h}x\right)$$
$$+ \frac{\sigma_0 - \sigma_{1\infty}}{\sin\left(\frac{h}{\sqrt{A\tau_1}}\right)}\exp\left(-\frac{t}{\tau_1}\right)\sin\left(\frac{h-x}{\sqrt{A\tau_1}}\right) + \frac{\sigma_0 - \sigma_{2\infty}}{\sin\left(\frac{h}{\sqrt{A\tau_2}}\right)}\exp\left(-\frac{t}{\tau_2}\right)\sin\left(\frac{x}{\sqrt{A\tau_2}}\right) \tag{A.11}$$

From the initial condition: $\sigma(x,0) = \sigma_0$, we have

$$\sigma_0 = (\sigma_{1\infty} - \sigma_{2\infty})\left(1 - \frac{x}{h}\right) + \sigma_{2\infty} + \sum_n C_n \sin\left(\frac{n\pi}{h}x\right) +$$
$$\frac{\sigma_0 - \sigma_{1\infty}}{\sin\left(\frac{h}{\sqrt{A\tau_1}}\right)}\sin\left(\frac{h-x}{\sqrt{A\tau_1}}\right) + \frac{\sigma_0 - \sigma_{2\infty}}{\sin\left(\frac{h}{\sqrt{A\tau_2}}\right)}\sin\left(\frac{x}{\sqrt{A\tau_2}}\right) \tag{A.12}$$

$$C_n = \frac{2}{h}\int_0^h \left(\sigma_0 - \sigma_{1\infty} + (\sigma_{1\infty} - \sigma_{2\infty})\frac{x}{h} - \frac{\sigma_0 - \sigma_{1\infty}}{\sin\left(\frac{h}{\sqrt{A\tau_1}}\right)}\sin\left(\frac{h-x}{\sqrt{A\tau_1}}\right) - \frac{\sigma_0 - \sigma_{2\infty}}{\sin\left(\frac{h}{\sqrt{A\tau_2}}\right)}\sin\left(\frac{x}{\sqrt{A\tau_2}}\right)\right)\sin\left(\frac{n\pi x}{h}\right)dx$$

$$= 2\int_0^1 \left( \sigma_0 - \sigma_{1\infty} + (\sigma_{1\infty} - \sigma_{2\infty})y - \frac{\sigma_0 - \sigma_{1\infty}}{\sin\left(\frac{h}{\sqrt{A\tau_1}}\right)} \sin\left(\frac{h(1-y)}{\sqrt{A\tau_1}}\right) - \frac{\sigma_0 - \sigma_{2\infty}}{\sin\left(\frac{h}{\sqrt{A\tau_2}}\right)} \sin\left(\frac{hy}{\sqrt{A\tau_2}}\right) \right) \sin(n\pi y) dy$$

$$= 2\left[ \begin{array}{l} \int_0^1 (\sigma_0 - \sigma_{1\infty}) \sin(n\pi y) dy + \int_0^1 (\sigma_{1\infty} - \sigma_{2\infty}) y \sin(n\pi y) dy - \\ \int_0^1 \frac{\sigma_0 - \sigma_{1\infty}}{\sin\left(\frac{h}{\sqrt{A\tau_1}}\right)} \sin\left(\frac{h(1-y)}{\sqrt{A\tau_1}}\right) \sin(n\pi y) dy - \int_0^1 \frac{\sigma_0 - \sigma_{2\infty}}{\sin\left(\frac{h}{\sqrt{A\tau_2}}\right)} \sin\left(\frac{hy}{\sqrt{A\tau_2}}\right) \sin(n\pi y) dy \end{array} \right]$$

$$= 2\left[ \frac{(\sigma_0 - \sigma_{1\infty})}{n\pi}\left(1 - (-1)^n\right) + \frac{(-1)^{n+1}(\sigma_{1\infty} - \sigma_{2\infty})}{n\pi} - \frac{(\sigma_0 - \sigma_{1\infty})n\pi}{\left((n\pi)^2 - \frac{h^2}{A\tau_1}\right)} - \frac{(-1)^{n+1}(\sigma_0 - \sigma_{2\infty})n\pi}{\left((n\pi)^2 - \frac{h^2}{A\tau_2}\right)} \right]$$

(A.13)

$$\sigma_f(t) = \frac{1}{h}\int_0^h \sigma(x,t) dx$$

$$= \frac{1}{h}\int_0^h \left[ \begin{array}{l} (\sigma_{1\infty} - \sigma_{2\infty})\left(1 - \frac{x}{h}\right) + \sigma_{2\infty} + \sum_n C_n f \sin\left(\frac{n\pi}{h}x\right) + \frac{\sigma_0 - \sigma_{1\infty}}{\sin\left(\frac{h}{\sqrt{A\tau_1}}\right)} \exp\left(-\frac{t}{\tau_1}\right) \sin\left(\frac{h-x}{\sqrt{A\tau_1}}\right) \\ + \frac{\sigma_0 - \sigma_{2\infty}}{\sin\left(\frac{h}{\sqrt{A\tau_2}}\right)} \exp\left(-\frac{t}{\tau_2}\right) \sin\left(\frac{x}{\sqrt{A\tau_2}}\right) \end{array} \right] dx$$

$$= \frac{1}{h}\left[ \begin{array}{l} \sigma_{1\infty} h - \frac{(\sigma_{1\infty} - \sigma_{2\infty})h}{2} + \sum_n C_n f \frac{h}{n\pi}\left(1 - (-1)^n\right) + (\sigma_0 - \sigma_{1\infty})\sqrt{A\tau_1} \exp\left(-\frac{t}{\tau_1}\right) \frac{\left(1 - \cos\left(\frac{h}{\sqrt{A\tau_1}}\right)\right)}{\sin\left(\frac{h}{\sqrt{A\tau_1}}\right)} \\ + (\sigma_0 - \sigma_{2\infty})\sqrt{A\tau_2} \exp\left(-\frac{t}{\tau_2}\right) \frac{\left(1 - \cos\left(\frac{h}{\sqrt{A\tau_2}}\right)\right)}{\sin\left(\frac{h}{\sqrt{A\tau_2}}\right)} \end{array} \right]$$

(A.14)

$$= \sigma_{1\infty} - \frac{(\sigma_{1\infty} - \sigma_{2\infty})}{2} + \sum_n C_n \exp\left(-A\left(\frac{n\pi}{h}\right)^2 t\right)\frac{\left(1-(-1)^n\right)}{n\pi} + (\sigma_0 - \sigma_{1\infty})\frac{\sqrt{A\tau_1}}{h}\exp\left(-\frac{t}{\tau_1}\right)\frac{\left(1-\cos\left(\frac{h}{\sqrt{A\tau_1}}\right)\right)}{\sin\left(\frac{h}{\sqrt{A\tau_1}}\right)}$$

$$+ (\sigma_0 - \sigma_{2\infty})\frac{\sqrt{A\tau_2}}{h}\exp\left(-\frac{t}{\tau_2}\right)\frac{\left(1-\cos\left(\frac{h}{\sqrt{A\tau_2}}\right)\right)}{\sin\left(\frac{h}{\sqrt{A\tau_2}}\right)}$$

# References


CHAPTER 1

[1.1] S.P.Jeng, R.H.Havemann, and M.C.Chang, MRS Symp. Proc. **337**, 25 (1994)

[1.2] G. E. Moore, Electronics, **38**, No. 8, April 9, 1965.

[1.3] B.J. Howard and Ch. Steinbruchel, Appl. Phys. Lett., **59**, 914(1991).

[1.4] *Smithell Metals Reference Book*, 6th Ed., E. A. Brandes, Butterworth & Co Ltd, London, 1983.

[1.5] SRC report

[1.6] J.Curry, G.Fitzgibbom, Y. Guan, R. Muollo, G. Nelson, and A.Thomas, in 22nd Annual Proceeding of Reliability Physics, Las Vegas, 6(1984).

[1.7] Yasushi Koubuchi, Jin Onuki, Motoo Suwa and Sin-ichi Fukada, VMIC Conference, IEEE, 419(1989).

[1.8] S. Kordic. R.A.M.Wolters, and K.Z.Troost, J. of Appl. Phys **74**, 5391 (1993).

[1.9] H.Okabayashi, Materials Science and Engineering Reports, **R11,**191(1993).

[1.10] Anke Zitzlsberger, Mathias Lehr, 99IRW FINAL REPORT, 1999 IEEE, P10-13.

[1.11] T. D. Sullivan, Stress Induced Phenomena in Metallization: 2nd International Workshop, 100(1994).

[1.12] T. Marieb, P. Flinn, J.C.Bravman and D.J. Gardner. Appl. Phys. **78**, 1026 (1995).

[1.13] S. Shingubara, T. Osaka, S.Abdeslam, and H. Sakue, Stress Induced Phenomena in Metallization: Fourth International Workshop, 159(1997).

[1.14] Y. J. Kime and P. Grach, Mat. Res. Soc. Symp. Proc. **338**, 255 (1994).

[1.15] M.D.Naeem, P.L. Flaitz and D. Chidambarrao, IEEE/CPMT Int'l Electronics Manufacturing Technology Symposium. 270(1999)

[1.16] P. A. Flinn, S. Lee, J.Doan, and T.N. Marieb, Stress Induced Phenomena in Metallization: Fourth International Workshop, 250(1997).

[1.17] In-Seok Yeo, Ph. D thesis, The Univ. of Texas at Austin, 1996.

[1.18] E.T.Ogawa, J.W.McPherson, J.A.Rosal, K.J.Dickerson, T.-C.Chiu, L.Y.Tsung, M.K.Jain, T.D.Bonifield, J.C.Ondresek, and W.R.Mckee, International Reliability Physics Symposium, Piscataway, NJ, 312(2002).

[1.19] J.A.Nucci, Y.Shacham-Diamand, and J.E.Sanchez, Jr., Appl. Phys. Lett. **65**, 3585 (1995).

[1.20] J.A.Nucci, Y.Shacham-Diamand, and J.E.Sanchez, Jr., Appl. Phys. Lett. **69**, 4017 (1996).

[1.21] A.Sekiguchi, J.Koike, S.Kamiya, M.Saka and K.Maruyama, Appl. Phys. Lett. **27**, 1264 (2001).

[1.22] T.Oshima, T. Tamaaru, K. Ohmori, H. Aoki, H.Ashihara, T. Saito, H.Yamaguchi, M.Miyauchi, K.Torii, J.Muarata, A.Satoh, H.Miyazaki and K.Hinode, IEDM, 123 (2000).

[1.23] P. A. Flinn, J. Mater. Res., **6**, 1498(1991).

[1.24] M.D.Thouless, J.Gupta, and J.M.E.Harper, J.Mater.Res., **8**, 1845(1993).

[1.25] R.P.Vinci, E.M.Zielinski, J.C.Bravman, Thin Solid Films **262**,142(1995).

[1.26] Y-L, Shen and S.Suresh, M.Y.He and A. Bagchi, O,Kienzle and M.Ruhle, A.G.Evans, J. Mater. Res., 13, 1928(1998).

[1.27] R.M.Keller, S.P.Baker and E.Arzt, Acta mater.**47**, 415(1999).

[1.28] D.Weiss, H.Gao and E.Arzt, Acta mater, **49**, 2395(2002).

[1.29] M.D.Thouless, K.P.Rodbell and C.Cabral, Jr. J.Vac. Sci. Technol .A **14**, 2154(1996).

[1.30] R.Spolenak, C.A.Volkert, K.Takahashi, S.Fiorillo, J.Miner and W.L.Brown, Mat.Res. Soc. Symp. Proc. **594**, 63(2000).

[1.31] R-M. Keller, S.P.Baker, and E.Arzt, J.Mater. Res., **13**, 1307(1998).

[1.32] J.J. Toomey, S.Hymes, and S.P.Muraka, Appl. Phys. Lett. **66**,2074(1995).

[1.33] R.P.Vinci, J. Mater. Res., **17**, 1863(2002).

[1.34] S.P.Baker, R.-M. Keller-Flaig, and J.B.Shu, Acta. Materialia, **51** 3019(2003).

[1.35] P. R. Besser, S. Brennan and J.C. Bravman, J. Mater. Res. **9,** 13(1994).

[1.36] J. Kasthurirangan, Y. Du, P. Ho, C. Capasso, M. Gall, and H. Kawasaki, AIP Conf. Proc. 491, 304(1999).

[1.37] P.R.Besser,Y.-C.Joo, D.Winter, M. Van Ngo, and R. Ortega, Mater.Res. Soc. Symp. Proc. **563**, 189(1999).

[1.38] S. H. Rhee, Y. Du and P. S. Ho, Proc. Int. Interconnect Tech. Conf. 89(2001).

[1.39] K.P. Rodbell, M.V. Rodriguez and P.J. Ficalora, J. of Appl. Phys, **61**, 2844(1987).

[1.40] J.J. Clement, E.M. Atakov and J.R. Lloyd, Digital Technical Journal, 4, 114 (1992).

[1.41] C.K. Hu, P.S. Ho, M.B. Small, J. of Appl. Phys,**72**, 291 (1992).

[1.42] C.-K. Hu, M.B. Small, P.S. Ho, J. of Appl. Phys,**74**, 969(1993).

[1.43] C.-K. Hu, Thin Solid Films, **260**, 124(1995).

[1.44] J.R. Lloyd, J.J.Clement, Thin Solid Films, **262**, 135 (1995)

[1.45] M.B. Small, C.-K. Hu, Thin Solid Films, **300**, 278 (1997).

[1.46] Pei-Hua Wang; P.S. Ho, J. Pellerin, R. Fox, J. of Appl. Phys, **84**, 6007 (1998)

[1.47] C-K, Hu, R. Rosenberg, KY, Lee, Appl. Phys. Lett. **74**, 5433 (1999).

[1.48] L. Arnaud, G. Tartavel, T. Berger, D. Mariolle, Microelectronics Reliability, 77 (2000).

[1.49] E.C.C. Yeh, K.N. Tu, J. of Appl. Phys, **88**, 5680 (2000).

[1.50] P.-C. Wang, R.G. Filippi, Appl. Phys. Lett. **78**, 3598(2001)

[1.51] Ki-Don Lee; E.T. Ogawa, Matsuhashi, H.; Justison, P.R.; Appl. Phys. Lett. **79**, 3236 (2001).

[1.52] E.T. Ogawa, Ki-Don Lee; V.A. Blaschke, P.S. Ho, IEEE Transactions on Reliability, 51, 403 (2002).

[1.53] P.S. Ho, K.-D. Lee, E.T. Ogawa, X. Lu, *In:* International Electron Devices Meeting. Technical Digest (Cat. No.02CH37358). Piscataway, NJ, USA: IEEE, 741(2002).

[1.54] E.T. Ogawa, K.-D. Lee, H. Matsuhashi, K.-S. Ko, *In:* 2001 IEEE International Reliability Physics Symposium Proceedings. 39th Annual (Cat. No.00CH37167). Piscataway, NJ, USA: IEEE, 341 (2001).

[1.55] J.R.Lloyd, J.Clemens, R.Snede, Microelectronic Reliablity **39,**1595 (1999).

[1.56] J.Proost, T.Hirato, T.Furuhara, K.Maex, and J.P.Celis, J. of Appl. Phys, **87**, 2792(2000).

[1.57] M.Hayashi, S.Nakano, T.Wada, Microelectronics Reliability, **43,** 1545 (2003).

[1.58] C.K. Hu, R. Rosenberg, and K.Y. Lee, Appl. Phys. Lett. **74**, 2945 (1999).

[1.59] P. Besser, A. Marathe, L. Zhao, M. Herrick, C. Capasso, and H. Kawasaki, IEDM, Technical Digest, Piscataway, NJ, 119 (2000).

[1.60] M.W. Lane, E.G. Liniger, and J.R. Lloyd, J. Appl. Phys. **93**, 1417 (2003).

[1.61] C.K. Hu, L. Gignac, R. Rosenberg, E. Liniger, J. Rubino, C. Sambucetti, A. Domenicucci, X. Chen, and A.K. Stamper, Appl. Phys. Lett. **81**, 1782 (2002).

CHAPTER 2

[2.1] G.G. Stoney, Proc. R. Soc. London, Ser. A **82**, 172(1909).

[2.2] R.W. Hoffman, *in Physics of Thin Films*, Edit by G. Hass and R.E. Thun, Academic Press., **69**, 1384 (1991).

[2.3] P.H. Townsend, D.M. Barnet, and T.A. Brunner, J. Appl. Phys. **62**, 4438 (1987).

[2.4] J.H. Jou and L.Hsu, J. Appl. P hys.**69**, 1384 (1991).

[2.5] I.S. Yeo, P.S. Ho, and S.G. Anderson, J. Appl. Phys. **78**, 945 (1995).

[2.6] R.W. Hertzberg, Deformation and fracture mechanics of engineering materials; John Wiley and Sons, 1989.

[2.7] W.A. Brantley. J. Appl. Phys. **44**, 534 (1995).

[2.8] J. Kasthurirangan, Ph. D thesis, The Univ. of Texas at Austin, 1998.

CHAPTER 3

[3.1] Paul A. Flinn, J. Mater. Res., **6**, 1498(1991).

[3.2] M.D.Thouless, J.Gupta, and J.M.E.Harper, J. Mater. Res., **8**, 1845(1993).

[3.3] R.P.Vinci, E.M.Zielinski, J.C.Bravman, Thin Solid Films, **262**, 142(1995).

[3.4] Y-L, Shen and S.Suresh, M.Y.He and A. Bagchi, O,Kienzle and M.Ruhle, A.G.Evans, J. Mater. Res., **13**, 1928(1998).

[3.5] R.M.Keller, S.P.Baker and E.Arzt, Acta mater. **47**, 415(1999).

[3.6] D.Weiss, H.Gao and E.Arzt, Acta mater, 49, 2395(2002).

[3.7] M.D.Thouless, K.P.Rodbell and C.Cabral, Jr., J.Vac. Sci. Technol .A **14**, 2154(1996).

[3.8] R.Spolenak, C.A.Volkert, K.Takahashi, S.Fiorillo, J.Miner and W.L.Brown, , Mat.Res. Soc. Symp. Proc. **594**, 63(2000).

[3.9] R-M. Keller, S.P.Baker, and E.Arzt, J.Mater. Res., **13**, 1307(1998).

[3.10] J.J. Toomey, S.Hymes, and S.P.Muraka, Appl. Phys. Lett. 66, 2074(1995).

[3.11] R.P.Vinci, J. Mater. Res., 17, 1863(2002).

[3.12] S.P.Baker, R.-M. Keller-Flaig, and J.B.Shu, Acta. Materialia, **51,** 3019 (2003).

[3.13] H.J.Frost, Mat. Res. Soc. Symp. Proc.**265**, 3(1992).

[3.14] *Smithell Metals Reference Book*, 6$^{th}$ Ed., E.A.Brandes Ed., (Butterworths & Co. Ltd., London, 1983.

[3.15] R.R.Reeber and K.Wang, Mater.Chem. and Phys., **46**,259 (1996).

[3.16] H.J.Frost and M.F.Ashby, Deforamtion-mechanism maps, New York, 7(1984).

[3.17] D.Kuhlmann-Wilsdorf, Philosphical Magazine A, **79,** 955(1999).

[3.18] D.Spolenak, C.A.Volkert, S.Ziegler, C. Panofen, W.L. Brown, Mat.Res. Soc. Symp. Proc. 673, 4(2001).

[3.19] H.Gao, L.Zhang, W.D.Nix, C.V.Thompson and E.Arzt, Crach-like, Acta mata. 47, 2865(1999).

[3.20] B. Zheng; R. He, B. Mikkola, J. Wang; C. Long; C. Yu; Z.W. Sun, E. Step, J. Chen, R. Emami, Z.A. Wang, R. Nayak, T.Taylor, and G. Dixit, Advanced Metallization Conference, 197(2001).

[3.21] T. Ritzdorf, L. Chen, D. Fulton and C. Dundas, International Interconnect Technology Conference, Proc. IEEE, 287(1999).

[3.22] G.B. Alers, X. Lu, J.H. Sukamto, S.K. Kailasam, J. Reid and G. Harm, Technology Conference, Proc. IEEE, 2004.

[3.23] W. D. Nix, Met. Trans. A, **20**, 2217(1989).

CHAPTER 4

[4.1] P. R. Besser, S. Brennan and J.C. Bravman, J. Mater. Res. **9,** 13(1994).

[4.2] J. Kasthurirangan, Y. Du, P. Ho, C. Capasso, M. Gall, and H. Kawasaki, in Stress Induced Phenomena in Metallization, AIP Conf. Proc. **491**, 304(1999).

[4.3] S. H. Rhee, Y. Du and P. S. Ho, Proc. Int. Interconnect Tech. Conf. 89(2001).

CHAPTER 5

[5.1] J.Curry, G.Fitzgibbom, Y. Guan, R. muollo, G. Nelson, and A.Thomas, in 22nd Annual Proceeding of Reliability Physics, Las Vegas, 6(1984).

[5.2] Yasushi Koubuchi, Jin Onuki, Motoo Suwa and Sin-ichi Fukada, VMIC conference, 419(1989).

[5.3] Anke Zitzlsberger, Mathias Lehr, 99IRW FINAL REPORT, 10(1999).

[5.4] Munir D.Naeem, Philip L, Flaitz and Dureseti Chidambarrao, IEEE/CPMT Int'l Electronics Manufacturing Technology Symposium. 270(1999)

[5.5] M.A.Korhonen, P.Borgesen, and Che-Yu Li, MRS BULLETIN, **61**, 61(1992).

[5.6] A.Sekiguchi and J.Koike, Applied Physics Letters, **27**, 1264 (2001).

[5.7] T.Oshima, T. Tamaaru, K. Ohmori, H. Aoki, H.Ashihara, T. Saito, H.Yamaguchi, M.Miyauchi, K.Torii, J.Muarata, A.Satoh, H.Miyazaki and K.Hinode, IEDM, 123 (2000).

[5.8] Michel Brillouet, Microelectronic Engineering **37/38**, 5(1997).

[5.9] M.A.Korhonen, Tao Liu, D.D.Brown, and C.-Y.Li, Mat.Res.Soc.Symp.Proc. **391** 411(1995).

[5.10] T.D.Sullicvan and L.A.Miller, Mat.Res.Soc.Symp.Proc. **308,** 169(1993).

[5.11] A.Witvrouw, K.Maex, W.De Ceunick, G.Lekens, J.D'Haen and L.DeSchepper, Microelectronics Reliability **38**, 1035(1998).

[5.12] Shinichi Domae, Ryuji Eto, Keiji Okuma, Microelectronics Reliability **39**, 507(1999).

[5.13] B.Wallace, Y.-H. Lee, D. Pantuso, K. Wu, and N.Mielke, IEEE 99CH36296, 37$^{th}$ annual international reliability physics symposium, San Diego, California, 303(1999).

[5.14] A.H. Fischer and A.E. Zitzelsberger, IEEE 01CH37167, 39th annual international reliability physkics symposium, Orlando, Florida, 334(2001).

[5.15] A.S.Oates, 1993 IEEE/IRPS P297-302.

[5.16] N.Matsunaga, H.Shibata and K.Hashimoto, 1992 symposium on VLSI technology digest of technical, IEEE, P76-77.

[5.17] C.A.Minor, Y.L.Guo and Y.L.Shen, Scripta Materialia, Vol.41, No 4, P347-352.

[5.18] James A. Walls, IEEE transaction on electron devices, Vol.44, NO.12, 1997.

[5.19] C.Lingk and M.E. Gross, Journal of Applied Physics, **84**, 5547 (1998).

[5.20] S. Lagrange, S.H.Brongersma, M.Judelewicz, A.Saerens, I.Vervoort, E.Richard, R.Palmans and K.Maex, Microelectronic Engineering, **50**, 449 (2000).

[5.21] W.H.The, L.T.Koh, S.M.Chen, J.Xie, C.Y.lI, and P.D.Foo, Microelectronics Journal, **32**, 579(2001).

[5.22] J.W. McPherson and C.F. Dunn, J. Vac. Sci.& Tech, B. **5**, 1321(1987).

[5.23] E.T.Ogawa, J.W.McPherson, J.A.Rosal, K.J.Dickerson, T.-C.Chiu, L.Y.Tsung, M.K.Jain, T.D.Bonifield, J.C.Ondresek, and W.R.Mckee, International reliability physics symposium, Piscataway, NJ, 312(2002).

[5.24] H.J.Frost and M.F.Ashby, Deforamtion-mechanism maps, New York, 1984.

[5.25] Hermann Ridedl, Fracture at high temperatures, Springer-Verlag Berlin Heidelberg, New York, 51(1987).

[5.26] T.M.Shaw, L.Gignac, X-H.Liu, and R.R.Rosenberg, Sixth International Workshop on Stress-induced Phenomena in Metallization. Ithaca, NY, USA, 25(2001).

CHAPTER 6

[6.1] R. Rosenberg, D.C. Edelstein, C.K. Hu, and K.P. Rodbell, Ann. Rev. Mat. Science **30**, 229 (2000).

[6.2] C.K. Hu, and J.M.E. Harper, Materials Chemistry Physics **52**, 5 (1998).

[6.3] E. Ogawa, K.D. Lee, and P.S. Ho, IEEE Transactions on Reliability **3,** 403 (2002).

[6.4] J.R.Lloyd, J.Clemens, R.Snede, Microelectronic Reliablity **39**, 1595(1999).

[6.5] J.Proost, T.Hirato, T.Furuhara, K.Maex, and J.P.Celis, J. of Appl. Phys, **87**, 2792 (2000)

[6.6] M.Hayashi, S.Nakano, T.Wada, Microelectronics Reliability, **43**, 1545(2003).

[6.7] C.K. Hu, R. Rosenberg, and K.Y. Lee, Appl. Phys. Lett. **74**, 2945 (1999).

[6.8] P. Besser, A. Marathe, L. Zhao, M. Herrick, C. Capasso, and H. Kawasaki, IEDM, Technical Digest, Piscataway, NJ, 119 (2000).

[6.9] M.W. Lane, E.G. Liniger, and J.R. Lloyd, J. Appl. Phys. **93**, 1417 (2003).

[6.10] C.K. Hu, L. Gignac, R. Rosenberg, E. Liniger, J. Rubino, C. Sambucetti, A. Domenicucci, X. Chen, and A.K. Stamper, Appl. Phys. Lett. **81**, 1782 (2002).

[6.11] E.T.Ogawa, J.W.McPherson, J.A.Rosal, K.J.Dickerson, T.-C.Chiu, L.Y.Tsung, M.K.Jain, T.D.Bonifield, J.C.Ondresek, and W.R.Mckee, Piscataway, NJ, 312(2002).

[6.12] P.A. Flinn, J. Mater. Res. **6**, 1498 (1991).

[6.13] M.D. Thouless, J. Gupta, and J.M.E. Harper, J. Mater. Res. **8**, 1845 (1993).

[6.14] R.P. Vinci, E.M. Zielinski, and J.C. Bravman, Thin Solid Films **262**, 142 (1995).

[6.15] Y.-L. Shen, S. Suresh, M.Y. He, A. Bagchi, O, Kienzle, M. Ruhle, and A.G. Evans, J. Mater. Res. **13**, 1928 (1998).

[6.16] R.M. Keller, S.P. Baker, and E. Arzt, Acta Mater. **47**, 415 (1999).

[6.17] R.M. Keller, S.P. Baker, and E. Arzt, J Mater Res. **13**, 1307 (1998).

[6.18] M.D. Thouless, Acta Metal. Mater. **41**, 1057 (1993).

[6.19] H. Gao, L. Zhang, W.D. Nix, C.V. Thompson, and E. Arzt, Acta Mater. **47**, 2865 (1999).

[6.20] I.-S. Yeo, Ph.D Dissertation, University of Texas at Austin, TX, 1996.

[6.21] R-M. Keller, S.P.Baker, and E.Arzt, J.Mater. Res., **13**, 1307(1998).

[6.22] H.J. Frost, Mat. Res. Soc. Symp. Proc. **265**, 3 (1992).

[6.23] R. Huang, D.W. Gan, P.S. Ho, J. Appl. Phys. **97**, 103532 (2005).

[6.24] L. Zhang, and H. Gao, Z Metallkd **93**, 417 (2002).

[6.25] H.J. Frost, and M.F. Ashby, Pergamon Press, Oxford, 1982.

[6.26] D. Gupta, C.K. Hu, and K.L. Lee, Defect and Diffusion Forum, **143-147**, 1397 (1997).

[6.27] T. Surholt, and C. Herzig, Acta Mater. **45**, 3817 (1997).

[6.28] J.V.Funn and I.Dutta, Acta mater, **47**, 149 (1999).

[6.29] R.Raj and M.F. Ashby, Metall. Trans. **2**, 1113 (1971).

[6.30] G. Kloster, T. Scherban, G. Xu, J. Blaine, B. Sun, Y. Zhou, IITC. 242(2002).

[6.31] M.A.Korhonen, P.Borgesen, K.N.Tu and Che-Yu Li, J. Appl. Phys. **75**, 3790(1993).

[6.32] A. F. Bower, N. Singh, D.W. Gan, S. Yoon, P.S. Ho, J. Leu and S. Shankar, J. Appl. Phys. **97**, 013539 (2005).

[6.33] S.P.Baker, R.-M. Keller-Flaig, and J.B.Shu, Acta. Materialia, **51**, 3019(2003).

## VITA

Dongwen Gan was born in Guangxi province, P. R. China in February, 1970, the son of Naicheng Gan and Xiuzhen Li. After completing his work at Liuzhou District High School, Guanxi province, P.R.China, in 1988, he attended Tsinghua University, Beijing, P.R.China and received the degree of Bachelor of Science in July 1993. During the following two years, he was employed as an engineer in the Fourth Construction Company of SINOPEC Corp., Tianjin, P.R.China. In September 1995, he entered the graduate school of the Tsinghua University and received the degree of Master of Science in July 1998. In August, he entered the Material Science and Engineering program of the University of Texas at Austin, working in the Interconnect and Packaging Group under the supervision of Professor Paul Ho in pursuit of a Ph.D degree. As an intern-engineer, he worked at ECP Division, Applied Materials, Inc., Santa Clara, CA, from October 2002 to January 2003 and has been working in the ATD, Intel, Chandler, AZ since February 2005. In February 1998, he was married to Ye Zhu and they now have two happy boys, Lawrence B. Gan and Ryan B. Gan.

Permanent Address: P. R. China, Guanxi Province, Wuxuanxian Shiudianju, 545900

This dissertation was typed by the author.